



**HAL**  
open science

## Increasing the porosity of zeolites

Viktoria Babic

► **To cite this version:**

Viktoria Babic. Increasing the porosity of zeolites. Catalysis. Normandie Université, 2021. English.  
NNT : 2021NORMC205 . tel-03167919

**HAL Id: tel-03167919**

**<https://theses.hal.science/tel-03167919>**

Submitted on 12 Mar 2021

**HAL** is a multi-disciplinary open access archive for the deposit and dissemination of scientific research documents, whether they are published or not. The documents may come from teaching and research institutions in France or abroad, or from public or private research centers.

L'archive ouverte pluridisciplinaire **HAL**, est destinée au dépôt et à la diffusion de documents scientifiques de niveau recherche, publiés ou non, émanant des établissements d'enseignement et de recherche français ou étrangers, des laboratoires publics ou privés.



Normandie Université

## THÈSE

**Pour obtenir le diplôme de doctorat**

**Spécialité CHIMIE**

**Préparée au sein de l'Université de Caen Normandie**

### Increasing the porosity of zeolites

**Présentée et soutenue par  
Viktoria BABIC**

**Thèse soutenue publiquement le 24/02/2021  
devant le jury composé de**

Mme TZONKA MINEVA	Directeur de recherche, ENSCM Montpellier	Rapporteur du jury
M. LUDOVIC PINARD	Maître de conférences HDR, Université de Poitiers	Rapporteur du jury
Mme SVETLANA MINTOVA	Directeur de recherche au CNRS, Université Caen Normandie	Membre du jury
M. VALENTIN VALTCHEV	Directeur de recherche au CNRS, ENSICAEN	Directeur de thèse
M. JEAN-PIERRE GILSON	Professeur des universités, ENSICAEN	Co-directeur de thèse
M. NIKOLAI NESTERENKO	Ingénieur HDR, Total Petrochemicals Research Feluy	Président du jury

**Thèse dirigée par VALENTIN VALTCHEV et JEAN-PIERRE GILSON, Laboratoire  
catalyse et spectrochimie (Caen)**





# Contents

---

<b>Chapter 1</b>	Introduction	1
<b>Chapter 2</b>	Literature review	3
<b>Chapter 3</b>	Materials and methods	39
<b>Chapter 4</b>	Comparative study of zeolite L etching with $\text{NH}_4\text{F}$ and $\text{NH}_4\text{HF}_2$ solutions	55
<b>Chapter 5</b>	Preparation of hierarchical SSZ-13 by $\text{NH}_4\text{F}$ etching	79
<b>Chapter 6</b>	Chromic acid etching of zeolites	107
<b>Chapter 7</b>	Conclusions and prospects	129
<b>Annexes</b>		133



# 1

## Introduction

## 1 Overture

Zeolites are crystalline microporous crystals with applications ranging from the petrochemical industry to chemical sensing and medicine. Zeolites face two contradictory requirements: a micropore ( $\leq 2$  nm) confinement and no diffusion limitations. The lone presence of microporous channels inescapably restricts bulky reactants' diffusivity and products towards and away from the acid sites, prompting retarded reaction rates and catalyst deactivation. Developing hierarchical zeolites that comprise of mesoporous and/or macroporous networks can overcome this problem. This enhances the mass transport of molecules while maintaining the intrinsic shape selectivity provided by the zeolite micropores.

Hierarchical zeolites can be obtained via post-synthesis or direct synthesis methods. Chemical etching has been used for years to modify the zeolite framework's composition or introduce a secondary system of pores in zeolite crystals. However, the usual treatments often result in a preferential dissolution of the framework constituents, silicon and aluminum, and change the intrinsic zeolite properties.

Chemical etching with fluoride solutions continues to develop in recent years. This solution dissolves in equal rates Si and Al, which opens up the possibility to extract framework atoms in a discrete and uniform manner from a zeolite structure, which opens the possibility to develop zeolites with new properties in terms of accessibility of the active sites, available free total pore volume, and thus to extend the possible applications of conventional aluminosilicate zeolites.

The Ph.D. work's objective is to study the key factors controlling the unbiased dissolution of zeolite framework, as special attention is paid to the kinetics of the process and the development of zeolite materials able to process bulkier molecules than their conventional counterparts.

## 2 Scopes of the thesis

In this study, fluoride solutions were mainly used to obtain hierarchically porous zeolites. Zeolite structures with relevant functions in the chemical industry were selected for developing improved catalysts. Chabazite and zeolite L were selected for the incorporation of multimodal porosity. The goal is to understand the impact of the fluoride etching on the hierarchical derivatives' morphological, textural, and acidic properties.

Chapter 4 compares the chemical etching of a commercial zeolite L with aqueous solutions of  $\text{NH}_4\text{F}$  and  $\text{NH}_4\text{HF}_2$  to generate secondary porosity. Tuning the etching conditions allows creating hierarchical zeolites without losing micropore volume. The catalytic properties of the pristine and modified zeolites are evaluated in the dealkylation of 1,3,5-triisopropylbenzene.

Chapter 5 presents  $\text{NH}_4$ -SSZ-13 subjected to etching with an aqueous solution of 40 wt/%  $\text{NH}_4\text{F}$  upon different synthesis conditions to obtain hierarchical derivatives. The etched zeolites were extensively characterized. The set of experimental data shows the temperature and high liquid-solid ratio treatments have to be carefully tuned to obtain a hierarchical material with retained basic characteristics.

Chapter 6 deals with a novel method for chemical etching of zeolites with different pore openings, 8 MR, 10 MR, and 12 MR, using chromic acid. This study expands the zeolite post-synthesis modifications to new etchant and brings insight into etchant size exclusion by the pore opening, which impacts the dissolution process.

Finally, the general results are summarized in the last section (Chapter 7) and new possible research directions are presented.

# 2

Literature review

<b>1</b>	<b>INTRODUCTION TO ZEOLITES.....</b>	<b>5</b>
<b>2</b>	<b>ZEOLITE STRUCTURE .....</b>	<b>5</b>
2.1	ZEOLITE BUILDING UNITS.....	5
2.2	PORE STRUCTURE CLASSIFICATION .....	7
2.2.1	<i>Zeolite structures employed in the present study.....</i>	<i>7</i>
2.2.1.1	SSZ-13 .....	7
2.2.1.2	ZSM-5 .....	8
2.2.1.3	Zeolite L.....	8
2.3	ZEOLITE COMPOSITION .....	9
<b>3</b>	<b>ZEOLITE SYNTHESIS.....</b>	<b>9</b>
3.1	HISTORY OF ZEOLITE SYNTHESIS .....	9
3.2	BASIC PRINCIPLES OF ZEOLITE SYNTHESIS .....	10
3.2.1	<i>Zeolite nucleation and growth.....</i>	<i>11</i>
3.3	POST-SYNTHETIC TREATMENT AND MODIFICATIONS OF ZEOLITES.....	12
<b>4</b>	<b>HIERARCHICAL ZEOLITES.....</b>	<b>12</b>
4.1	SYNTHESIS OF HIERARCHICAL ZEOLITES.....	13
4.1.1	<i>Bottom-up approach.....</i>	<i>14</i>
4.1.1.1	Dual Templating.....	14
4.1.1.1.1	Hard templating .....	14
4.1.1.1.2	Soft templating.....	14
4.1.1.2	Non-templating.....	15
4.1.2	<i>Top-down approach.....</i>	<i>15</i>
4.1.2.1	Dealumination .....	15
4.1.2.2	Desilication.....	16
4.1.2.3	Fluoride-medium treatment .....	18
<b>5</b>	<b>APPLICATIONS OF ZEOLITES.....</b>	<b>26</b>
5.1	CATALYSIS.....	26
5.1.1	<i>Properties of zeolites enabling catalysis .....</i>	<i>27</i>
5.1.1.1	Zeolites as solid acids .....	27
5.1.1.2	Shape Selective Catalysis .....	27
5.1.2	<i>Catalytic applications of hierarchical zeolites.....</i>	<i>27</i>
<b>6</b>	<b>REFERENCES .....</b>	<b>29</b>

# 1 Introduction to zeolites

Zeolites are minerals known from about 250 years ago. In 1756, a Swedish mineralogist Alex Fredrik Crönstedt discovered that a mineral (widely claimed to be stilbite[1]) exhibits swelling upon heating (intumescence) and gave off a hissing sound due to the release of steam. This new family of minerals was called *zeolite*, from the Greek words *zeo* and *lithos*, which means “to boil” and “stone”. [2–4]

Today zeolites are of great interest as heterogeneous catalysts, molecular sieves, and cation exchangers. Zeolite minerals are of limited value since nature has not optimized their properties for catalysis, and they contain impurities.[3] Therefore, natural zeolites are mainly used in agriculture. In contrast, synthetic zeolites offer uniformity in terms of chemical and phase composition, which is indispensable for high-tech applications. Nowadays, the precise engineering of their properties is possible (crystal size, composition), which illustrates the advantage of synthetic zeolites over their natural counterparts. More than 50 different types of zeolite structures have been discovered in nature, while the number of synthetically made zeolites has reached over 250 and continues to grow.[5,6]

In 1862 was the first attempt to make a laboratory synthesis of zeolites by H. E. Sainte-Claire Deville, who claimed to have made levynite (levyne).[4,7] The era of synthetic zeolites started after the Second World War with the pioneering work of Richard M. Barrer and Robert M. Milton. Zeolites revolutionized heterogeneous catalysis in the 1960s, as they showed remarkable activity and selectivity for acid-catalyzed processes.[3,8] A major event was the introduction of synthetic faujasites in the FCC (fluid catalytic cracking) catalysts in 1962. Nowadays, the zeolites are extensively used in petrochemistry and fine chemistry, and they have also found promising applications within the field of renewable energy like biomass conversion, fuel cells, thermal energy storage, and environmental improvements like pollution abatement, CO<sub>2</sub> capture, and water purification.[9]

## 2 Zeolite structure

Zeolites are microporous crystalline aluminosilicates with a three-dimensional framework structure, which is built of TO<sub>4</sub> (T = Si<sup>4+</sup>, Al<sup>3+</sup>) tetrahedra connected via shared O atoms. T sites can also be occupied by P, Ga, Ge, Ti, and to a less extent by other atoms. These structures are known as zeotypes, even though they are often referred to as zeolites in the literature.[10,11] The tetrahedra of SiO<sub>4</sub> and AlO<sub>4</sub><sup>-</sup> connected through their bridging oxygen atom form together subunits and the crystal lattice by repeating identical building blocks.[2] The general composition of the skeleton is TO<sub>2</sub> because each oxygen atom is coordinated with two T atoms.[12]

The presence of trivalent T-atoms (Al<sup>3+</sup>) introduces a negative charge in the framework, which is compensated by the presence of alkali or alkali-earth cations in the voids of the framework, which are loosely bound, and this gives zeolites their cation exchange properties. The alkali cations with their hydration spheres serve as structure-directing agents (SDAs) in the synthesis of zeolites. Organic cations, as tetraalkylammonium cations, can play the same role in zeolite synthesis.[13] Removing water and organic molecules at elevated temperatures brings about the regular porous structure of molecular dimensions, which gives zeolite materials their unique adsorption properties.[12]

### 2.1 Zeolite building units

Zeolite frameworks are complex lattice structures classified according to the smaller subunits. The basic building unit (BBU) or the primary building unit is a TO<sub>4</sub> tetrahedron; through shared oxygen, they can combine to form secondary building units (SBU). The simplest examples of SBUs are rings with a different number of T atoms. In general, a ring containing *n* tetrahedra is referred to as an *n* member ring (*n* MR).

The most common rings are formed by 4, 5, 6, 8, 10, and 12 tetrahedra, but materials with 14, 18, and up to 20 MR have been prepared. Zeolite frameworks with 3, 7, or 9 MR are rare.[14] When a ring defines the pore aperture, it is also called a window.

Secondary units can further build tertiary building units or building polyhedra. For instance, twelve tetrahedrons can be connected by sharing cube vertices, and form a double six-ring (*d6r*) polyhedra. Examples of zeolite building units are given in **Figure 2.1**. [15]

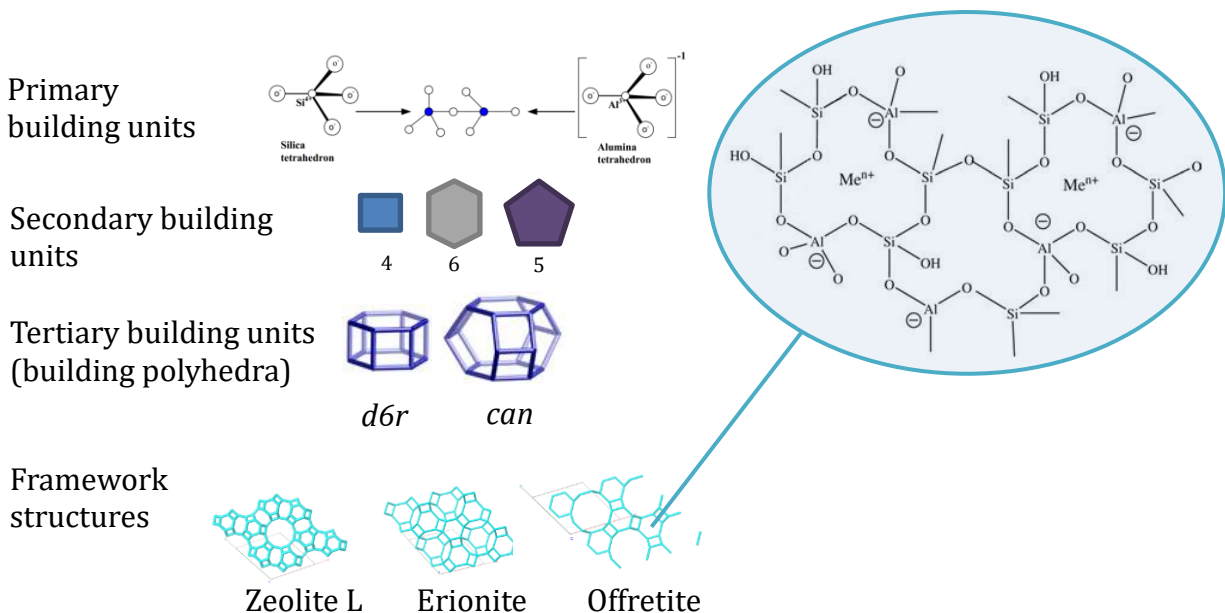


**Figure 2.1.** Examples of zeolite building units and framework types.

Polyhedral building units are often described using common names (such as cancrinite cage) and three-letter codes (*d6r* or *can*) and using descriptors  $[n_1^{m_1}, n_2^{m_2}, \dots]$  where  $m_1$  is the number of  $n_1$ -rings,  $m_2$  is the number of  $n_2$ -rings. For example, *d6r* has descriptors  $[4^6, 6^2]$ , because it is defined by two equivalent six-rings that are connected through six four-rings.[16]

Zeolite framework types are labeled by a 3-capital letter code. For instance, **FAU** stands for faujasite and **CHA** for chabazite, rendering to the rules set by the Structure Commission of the International Zeolite Association (IZA).

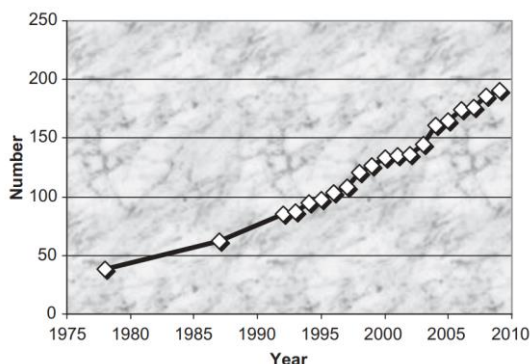


**Figure 2.2.** Increase of zeolite structure codes since the 1970s (from [17]).

253 different framework types are assigned with a three-letter code, all of which can be found on the website of the IZA (<http://www.iza-structure.org/databases>). **Figure 2.2** shows the exponential rise of discovered zeolite

structure since the first systematic listing in the years the 1970s.[18,19] New codes have been approved every year since 1992.

## 2.2 Pore structure classification

Arrangement of the building units in zeolite frameworks results in the generation of cavities and channels of various dimensions. These are responsible for the molecular sieving and confinement effect that occur during molecules' processing.[2,12]

According to their intrinsic crystalline pores, zeolites are generally classified as:

*Small pore zeolites:* 8 MR pore apertures (8 T atoms) having free diameters of 0.30–0.45 nm

*Medium pore zeolites:* 10 MR pore apertures, 0.45–0.60 nm in free diameter

*Large pore zeolites:* 12 MR pore apertures, 0.60–0.80 nm

*Extra large-pore:* >12 MR pore apertures, 0.80–2.0 nm

The team of Virginia Polytechnique Institute obtained the first extra-large pore material VPI an aluminophosphate with 18 MR pores. Later on, a silicate (UTD-1) with 14 MR was synthesized.[20] The quest to synthesize extra-large pore zeolites continued and zeolites with 24[21], 28[22], and 30 MR[23] have been discovered. The majority of these materials are Ge-silicates with limited (hydro)thermal stability.[24]

The general classification of pores in zeolites recommended by IUPAC and based on the pore width is summarized in **Table 2.1**.[12,25]

**Table 2.1. Classification of pores in zeolites.**

definition	typical material	ring size	pore diameter (nm)
ultra-large pore	VPI-5	>14	0.80–2.00
large pore	FAU	12	0.60–0.80
medium pore	ZSM-5	10	0.45–0.60
small pore	CHA	8	0.30–0.45

Multiple pores with different dimensions can exist in zeolites, which results in materials having a 1-, 2-, or 3-dimensional system of channels. The multiple pore system can be linked or not.

### 2.2.1 Zeolite structures employed in the present study

Three types of zeolite structures are used throughout this work.

#### 2.2.1.1 SSZ-13

SSZ-13 is a type of high-silica industrially used zeolite with chabazite (CHA) topology. Chabazite has a framework structure consisting of a stacked sequence of 6-rings in the order AABBC, forming double 6-rings at each apex of the rhombic unit cell (**Figure 2.3**). Thus, a specific cage (0.67 x 1.1 nm<sup>2</sup> in size) named after the mineral's name is formed (*cha*). The zeolite possesses a three-dimensional system of eight-membered ring (aperture 0.38 x 0.38 nm<sup>2</sup>) channels.



Figure 2.3. Chabazite (CHA) composite building units (from [26]).

### 2.2.1.2 ZSM-5

ZSM-5 is a high-silica pentasil type zeolite with an MFI-type framework topology. The building units are the *mfi* ( $5^45^4$ ), *cas* ( $5^26^2$ ), and *tes* ( $5^4$ ), *mel* ( $4^15^26^2$ ) polyhedral (Figure 2.4). These units, connected by sharing of corners or faces, form 10-membered rings. The resulting framework contains two intersecting channels, one parallel to  $[010]$ , and the other is sinusoidally parallel to  $[100]$ , forming both the 10-ring openings. Since the straight channels along  $[010]$  are connected to each other via the sinusoidal channels along  $[100]$ , by navigating alternately along the  $[010]$  and  $[100]$  channels, a molecule can also diffuse in the  $[001]$  direction. The effective diameter of the 10-rings of the  $[010]$  channel is  $0.53 \times 0.56 \text{ nm}^2$ , and that of the 10-rings of the  $[100]$  sinusoidal channel, about  $0.51 \times 0.55 \text{ nm}^2$ .



Figure 2.4. Composite building units in the MFI-type framework (from [26]).

### 2.2.1.3 Zeolite L

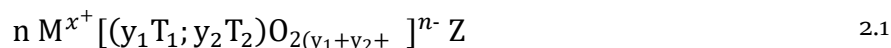
The framework topology of zeolite L (LTL-type), is built entirely from cancrinite cages (*can*) presented in Figure 2.5.[17] The resulting framework consists two types on channels running parallel to the *c*-axis. The one-dimensional 12-ring channel system of the *ltl* cages connected by a three-dimensional channel system of eight-membered rings ( $0.34 \times 0.56 \text{ nm}^2$ ). The eight-ring opening is strongly compressed and they do not allow diffusion. The framework can be considered to allow only one-dimensional diffusion along the 12 MR channels having  $0.71 \times 0.71 \text{ nm}^2$  aperture. The diameter of *ltl* cages is 1.2 nm.



Figure 2.5. LTL framework type composite building units (from [26]).

## 2.3 Zeolite composition

The framework composition of zeolites depends on the synthesis conditions. As cations in the pores are exchangeable and occluded water, organics or salts can vary, zeolites are often defined according to their framework composition. The structural formula of zeolites (the chemical composition of the unit cell) is best described by a general formula presented in eq. 2.1:



The expression in eq. 2.1. represents the framework composition and the species in the micropores. [27]

- M is an extra-framework cation with a charge of x
- T<sub>1</sub> and T<sub>2</sub> are tetrahedral elements Si and Al
- Z is water, molecules, ion pairs.

The total number of tetrahedra per unit cell is  $y_1 + y_2$ , and  $x/(y_1 + y_2)$  gives the Si/Al ratio, which can vary from 1 to infinity. The low limit of the framework ratio was observed by Löwenstein. In his work, which is frequently referred to as *Löwenstein's rule*, he postulated that framework distribution is not entirely random.[28] The rule describes that the -Al-O-Al- linkages are not favored because of the electrostatic repulsions between the negative charges, and the maximum substitution of silicon is 50 %. Bicuculite with Si/Al = 0.5 is an exception, and some computational studies predict violations of this rule in H-SSZ-13.[3,29]

Depending on their Si/Al ratio, zeolites can be classified into three classes, namely low (Si/Al = 1.0~1.5), medium (Si/Al = 2~5), and high Si/Al ratios (Si/Al = 10~100), as well as pure silica zeotypes.[30] The increase of the Si/Al ratio beyond the values observed in the naturally made materials was accomplished by employing organic structure-directing agents (OSDA), that serve as templates for zeolite pores. This allowed synthesizing all-silica molecular sieves by introducing OSDAs the number of charge balancing cations per unit cell is substantially decreased, and thus the Si/Al ratio of the framework is increased.[20] Increasing the Si/Al ratio improves the hydrothermal stability and the hydrophobicity increases.[14]

Direct synthesis often does not lead to the formation of zeolites with desired properties for a specific application. Post-synthesis modification methods enable modifying the framework composition, crystal size, and pore system, thus adapting the material to a particular application.[32]

## 3 Zeolite synthesis

### 3.1 History of zeolite synthesis

First attempts of zeolite synthesis date back to the middle of the 19<sup>th</sup> century to reproduce natural zeolites; however, identification methods like XRD were absent. In 1948 Richard M. Barrer synthesized the first synthetic analog of mordenite and a novel synthetic zeolite without a natural counterpart, much later identified as KFI.[33] In the early 1950s, Robert M. Milton and coworker Donald W. Breck (Union Carbide) found an easy method to prepare zeolites with large apertures and high adsorption capacity and discovered numerous commercially important zeolites, A, X and Y.[33] He utilized highly reactive alkaline aluminosilicate gels and low synthesis temperature (between 80 and 150 °C).[27,34]

At around the same time, Barrer and co-workers achieved systematic synthesis in the temperature range 60–450 °C from reaction mixtures with a composition of (2.2):



by varying the  $y$ ,  $x$ , and  $z$  parameters of the mixture and the nature of the base (hydroxide of Li, Na, K, Rb, Cs, Ca, Sr, Ba,  $\text{NH}_4$ , etc.). In the next twenty years, the majority of zeolites with  $\text{Si}/\text{Al} \leq 5$  now known were formed. That includes zeolite A with no natural counterpart, zeolite L, erionite, offretite, mordenite, and zeolites X and Y, the latter two having the same framework topology as natural faujasite.

In the 1960s Barrer and Patrick J. Denny were the first to replace the inorganic bases with organic ones; through this, they observed the increase of the  $\text{Si}/\text{Al}$  ratio. Since the pioneering work of Barrer and Milton, the hydrothermal synthesis from an aqueous solution has become the basic route for zeolite synthesis.[34,35] To this day, the relation between the initial synthesis variables and the structure formed is not fully understood. Nevertheless, good control of zeolite properties is achieved, and the number of new topologies continues to grow.[36] Theoretical predictions hypothesize four million zeolite topologies are still undiscovered.[37] Zeolites' properties can be manipulated, enabling the practice of *pore engineering*, which in turn contributes to endless possibilities of tailoring these materials for chemical reactions.[38]

### 3.2 Basic principles of zeolite synthesis

Generally, zeolites can be synthesized from aqueous media, a synthesis gel in hydrothermal conditions, *i.e.*, an autoclave is heated to a certain temperature under autogenous pressure (**Figure 2.6**).[39] The synthesis gel includes silicon and aluminum sources, solvents, templates, or structure-directing agents (SDAs), and a mineralizer. The reaction temperatures are between 90–170 °C, and the solution pH is typically alkaline from 9 to 14. Zeolites rarely form under acid hydrothermal conditions.[40] However, Shi *et al.* recently synthesized high silica MFI type zeolite in acidic conditions ( $\text{pH} = 2.3\text{--}5.0$ ).[41] Autoclaves should be filled 30 and 70 % vol to maintain the liquid phase.[36,42] The complex chemical process that involves the transformation of the synthesis gel into a microporous crystalline aluminosilicate can be denoted as *zeolitization*. [40]

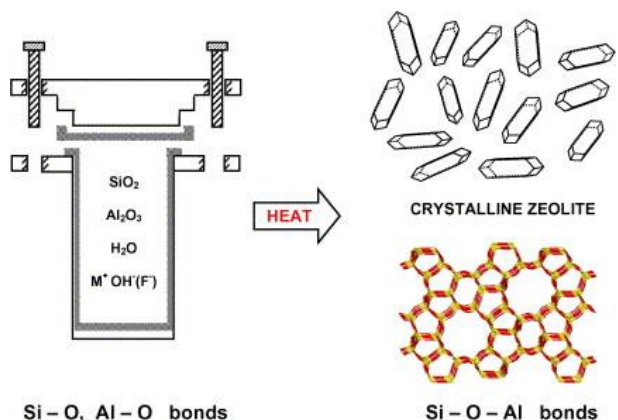


**Figure 2.6.** Hydrothermal synthesis of zeolites (from [43]).

Water is a common solvent used in zeolite synthesis; it acts as a reactant and reaction media, and it is as well low cost, non-toxic has good thermal stability and conductivity.[31] Zeolites formation takes place in conditions where water is present in considerable amounts because the open framework of zeolites must be stabilized during growth, and this happens by being filled with guest molecules.[40] Bibby and Dale showed that it is possible to grow zeolites in non-aqueous media, such as alcohol (solvothetical synthetic route).[35]

Mineralizer in the synthesis gel increases the solubility of the aluminosilicate species and transport them to the structure-directing agent. The most frequent mineralizing agent is  $\text{OH}^-$ . The hydroxyl anion promotes the solubility of silicon and aluminum sources and conducts the development of solvated silicate and aluminate anions  $[\text{Si}(\text{OH})_4^-]$ ,  $[\text{Al}(\text{OH})_4^-]$ .

F<sup>-</sup> can also be employed as a mineralizing agent, as high silica zeolites are prepared in F<sup>-</sup> media, and they present a reduced number of defects than the materials synthesized in OH<sup>-</sup> media.[36] The fluoride synthesis route lowers the pH of the synthesis since it is performed near neutral or slightly alkaline pH. The physicochemical properties of a zeolite obtained by OH and F mineralizer routes differ substantially in terms of catalytic activity.[44]

Alkali-metal hydroxides like NaOH and KOH in the synthesis gel lead to the formation of low silica zeolites since the large amounts of positive charges are balanced by the large number of aluminum atoms in the framework.[36] On contrary, to the use of organic structure-directing agents (OSDA), like amine or quaternary ammonium salt, the Si/Al ratio is increased. As OSDAs introduce fewer positive charges in the framework, less aluminum is needed to balance the charge.

Many new routes of zeolites have emerged with the quest of zeolites with tailored properties, such as solvothermal synthesis, ionothermal synthesis, microwave-assisted hydrothermal synthesis, micro emulsion-based hydrothermal synthesis, dry gel conversion synthesis, and combinatorial synthesis.[35]

Temperature and time influence the type of product that will be crystallized. The pressure does not play an important role in zeolite formation. In contrast, the temperature has a strong effect on zeolite nucleation and growth, and the desired zeolite phase can typically only be obtained in a specific temperature range. The increase of the temperature increases both the nucleation rate and the linear growth rate. The extending of synthesis time, in general, increases the crystallinity of the product, but after a certain limit, it could result in phase transformation.[35,40] The framework composition can be further modified by secondary synthesis or post-synthetic treatments.

### 3.2.1 Zeolite nucleation and growth

A simplified description of the zeolite formation includes two main stages, nucleation and crystal growth. Zeolite synthesis proceeds through spontaneous nucleation, followed by nuclei's growth exceeding a critical size when the process is not reversible.[45] The nucleation takes place during the induction period, which encompasses all events between the start of the reaction and a point when crystalline products are first observed.[35]

Nucleation is defined by a series of equilibrium and condensation steps in which atoms or molecules of the reactant phase rearrange into a nucleus or critical nuclei of the product phase large enough to have the ability to grow irreversibly.[46] It's expected that the crystallization process occurring in the hydrothermal zeolite precipitation is similar to those known to occur in simpler organic or inorganic systems.[47] Nucleation can be homogeneous or heterogeneous. Homogeneous nucleation is characterized as being directed by the supersaturation in the solution, while heterogeneous nucleation is catalyzed by a foreign surface/material.[47]

Works by Subotić *et al.* have pointed to the probability that the nucleus form from the amorphous gel matrix and become viable growing crystals as the gel phase dissolves. [48,49]

Nucleation involves many equilibria and condensation steps that lead to the supersaturation level inducing the formation of the nuclei.[31] In zeolite yielding systems, nucleation and growth are considered consecutive steps but often they occur simultaneously.[31]

Crystal growth is a process in which an atom or a molecule incorporates onto the surface of the crystal, causing an increase in size.[46] The model proposed by Kossel[50] and commonly used by the zeolite chemists, depicts a crystal surface made of cubic units, which form layers of monoatomic height, limited by edges (steps). The area between steps is referred to as a terrace, and it can contain clusters, vacancies, and single adsorbed growth units.

### 3.3 Post-synthetic treatment and modifications of zeolites

Historical development of post-synthesis modification methods is starting in the mid-1960s, and the development of these methods will continue as long as new microporous materials are developed. Secondary or post-synthetic (*ex situ*) treatment often provides a more practical route to modify the zeolites to acquire desirable framework compositions and other properties that could not be achieved by direct synthesis. The research in this area is driven by the demand for a more efficient petroleum cracking catalyst.[32,51] These treatments include ion exchange, preparation of metal-supported zeolites, dealumination, silication, reinsertion of heteroatoms into zeolite[32], acid leaching, high temperature steaming, chemical treatments with chalets or fluoride compounds, and the combinations of these treatments.[51-53]

Each post-synthesis treatment method modifies the properties of zeolites in a different way. Acid solution and high-temperature steaming can selectively dealuminate a zeolite structure; however, the high-temperature steaming doesn't remove debris generated by it from the crystal, while during acid leaching, it is washed away.

The fluorosilicate treatment can deplete aluminum centered acid sites. The treatments can sometimes generate mesopores or secondary pore system. Hydroxyl nests can be annealed, and silicon, aluminum, or other metal ions can be introduced into the framework to alter the catalytic properties and improve stability.

Therefore, the post-synthesis treatments target control active site properties and distribution to maximize the zeolite catalyst's performance.[54]

## 4 Hierarchical zeolites

Despite having many advantages and presence in the chemical processes, zeolites have their limitations. Their major problem is reduced accessibility to the active sites when the reactants have similar or larger dimensions than the micropore opening.[55] As depicted in **Figure 2.7**, bulky molecules cannot access zeolite micropores and only react on pore mouths. A fall in molecular diffusivity occurs from “intercrystalline” (diffusion of molecules outside the catalyst) to “Knudsen” (mesopore diffusion) to “configurational” (micropore diffusion).[56] Additionally, diffusion problems can cause a poor usage of zeolite crystals since the outer surface is used more effectively and the interior remains catalytically inactive.

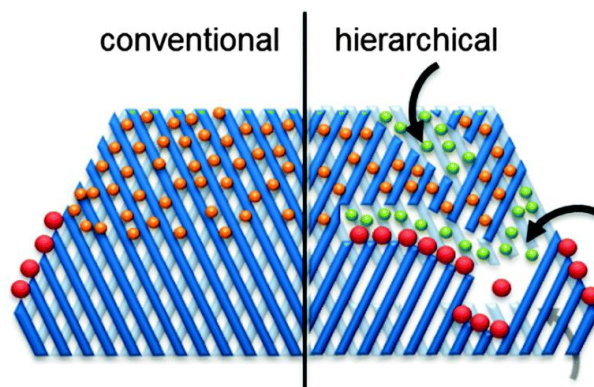


**Figure 2.7. Schematic presentation of diffusion limitation in conventional and hierarchical zeolites. The secondary porosity enhances the number of pore mouths enabling better access to green and red spheres to and within the pores (from [57]).**

Hierarchically porous structures are of key importance to achieve optimal properties and performance of the zeolite material. Significant progress has been made in the last decade in rationalizing the synthesis of hierarchically porous materials. These materials exhibit a multimodal hierarchically porous structure comprising

interconnected pores with different sizes from micro (< 2 nm) to meso (2–50 nm) and macropores (> 50 nm).[58] This means another level of pore network is implemented to increase the diffusivity, which may be formed in the crystal (intracrystalline) or between crystal particles (intercrystalline).[55]

The key interest in the production of hierarchical zeolites is driven by two drawbacks of the conventional zeolites:

- Diffusion limitations of larger molecules, which cannot, due to their size, enter micropores of zeolites but can access solely the external surface.
- Shortening the diffusion path length of molecules through the micropore system of zeolites.

The introduction of meso- and macropores in zeolite structure contributes to the intra-crystalline diffusion rate and thus improve adsorption and desorption, resulting in improved catalyst lifetime.[59] Bulky molecules can only utilize the external surface for catalytic conversion. Even if the reactants are small enough in size to enter the micropores of zeolites their mass transport could be enhanced if their diffusion is extended through the implementation of mesopores.[60] Introducing mesopores in the zeolite structure should avoid sacrificing the valuable properties of selectivity and catalytic activities. This way, reactants, and products can promptly transit the microporous domains, therefore maximally utilize the active sites throughout the entire catalyst.[61]

Diffusion limitations also stirred scientific research towards the synthesis of extra-large pore zeolites, yet they do not meet industrial applications' requirements because of low thermal/hydrothermal stability. Shortening of the diffusion path inside the micropores can also be achieved by decreasing the size of the zeolite particles (*nanosized* zeolites).[61,62] The synthesis of nanosized zeolites is not well developed on an industrial scale; their small size introduces problems post-synthesis processing and separation from the synthesis gel.

In late 1980 a new family of ordered mesoporous materials was discovered, molecular sieves MCM-41, in attempts to alleviate diffusion limitations of conventional zeolites; however, their structure is amorphous, which causes them lower acidity and low hydrothermal stability.[63,64]

The main applications of hierarchically porous materials are in the field of catalysis, adsorption, separation, sensors, energy, and life sciences. In catalysis, hierarchical zeolites show higher accessibility to bulky molecules and higher diffusion rates of reactants and products.[58]

## 4.1 Synthesis of hierarchical zeolites

The preparation of hierarchical zeolite is based on crystallization, aggregation, etching, and their combinations. These strategies can be divided into *bottom-up* and *top-down* approaches, summarized in **Figure 2.8**. Through bottom-up approaches, additional porosity is generated by careful design and optimized crystallization procedure, where sacrificial porogens are often used. Top-down approaches are based on the selective extraction of framework atoms from the zeolites.[59]

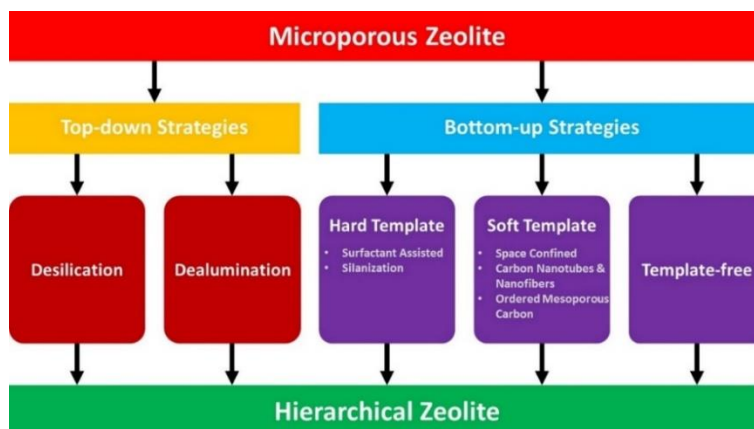


**Figure 2.8.** Schematic representation of top-down and bottom-up strategies used in the synthesis of hierarchical zeolites (from [65]).

### 4.1.1 Bottom-up approach

Bottom-up preparation strategies can be summed up to three different methods: i.) hard templating, ii.) soft-templating, and iii.) non-templating methods.[59] These methods create hierarchical zeolites during the synthesis and are considered constructive ways to build hierarchical zeolites.

The templating approach is based on finding a sacrificial porogen that directs the zeolite growth without becoming an essential part of the framework. It can be removed without the loss of the zeolite structure. The secondary template can be 'hard' or 'soft', depending on their more or less rigid nature.[60] The non-templated approach is based on the growth of nanozeolitic aggregates that assemble to form a mesoporous network.

Effective application of bottom-up approaches in the industry is still limited due to the necessity of using high quantities of organic templates, which brings about significant production costs and important environmental issues due to template removal.[66] This can be overcome by introducing cheaper mesopore templates and/or reducing their amount during the synthesis and recycling them post-synthesis.[66]

#### 4.1.1.1 Dual Templating

The dual-templating method uses the same principle that is used to synthesize microporous zeolites, *i.e.*, using a sacrificial frame of the mesoscale to direct the growth of zeolite without becoming the essential part of the framework and which can be removed without losing the final structure.[60]

##### 4.1.1.1.1 Hard templating

The method is based on the utilization of templates in a solid-state during the preparation process. Different types of commonly used hard templates (porogens) are carbonaceous, biological, and polymeric species. Their utilization requires the fulfillment of the following properties: i.) their surface properties should be compatible with the chemical properties of the reaction mixture, ii.) stability at the synthesis temperature, and iii.) the zeolite structure needs to remain stable after the removal of the hard template.

The hard template's physical characteristics, shape, and size control the pore size and the pore size distribution very effectively. However, this preparation procedure is limited to laboratory applications due to the price of the hard template, and their removal after synthesis is challenging, often damaging the zeolite framework.[66]

##### 4.1.1.1.2 Soft templating

Soft templating involves using namely, surfactant molecules to direct the formation of mesopores and even both micropores and mesopores during hydrothermal synthesis. Primary soft templating uses on-purpose designed

surfactants to form intra- or intercrystalline mesopores, which are usually not commercially available. They are prepared prior to the zeolite synthesis, which makes the method expensive and difficult to commercialize.

The secondary soft templating method is based on commercially available surfactants like cetyltrimethylammonium bromide (CTAB), which is added to the synthesis mixture after aging. The surfactant then directs the self-assembly of crystals formed during the zeolite hydrothermal synthesis to generate additional mesopores.[59]

#### **4.1.1.2 Non-templating**

This preparation method is based on nanocrystals' self-assembly effect or the generation of mesopores by excessive crystal twinning during synthesis often induced by growth modifiers. This method is done normally either by hydrothermal or dry gel conversion. It requires control over zeolite crystallization, involving the formation of nanoparticle precursors.[67] Nanocrystal assembly favors nucleation over crystal growth. Hierarchical ZSM-5 can be obtained in various crystal sizes and morphologies by controlling the synthesis conditions (concentration and pH) or the sequence of preparing aluminate and silicate mixtures.[68]

### **4.1.2 Top-down approach**

Top-down approaches include a variety of post-synthetic treatments of already synthesized zeolites. This treatment approaches the preparation of hierarchically porous materials by introducing secondary porosity by grafting additional porous material to the original porous materials. Mesopores are created in a secondary reaction after the zeolite has been synthesized and the template is removed through calcination.[60]

Principally top-down approaches are destructive. Part of the zeolite crystal is sacrificed to form mesopores.[60] Methods include steaming[69], acid[69] or base leaching[70], irradiation[71], and swelling agents[72] and strong oxidation agents[73]. Some of these methods are more readily implemented on an industrial scale.[74]

#### **4.1.2.1 Dealumination**

Barrer and M. B. Makki were the first to remove framework aluminum from clinoptilolite by acid treatment without causing structural disintegration and therefore successfully made dealumination.[75] In 1967 C.V. McDaniel and P. K. Maher reported a method to increase the thermal stability of high alumina zeolite Y.[76] Dealumination has been routinely used as industrial technology. Steaming and acid leaching are used to prepare ultra-stable Y zeolites with mesopores for the FCC (fluid catalytic cracking) process.[77]

Dealumination methods like steaming and acid leaching are the most common methods used to treat zeolites.[56] Dealumination through hydrolysis of Al-O-Si bonds forms defect sites leaving extra-framework alumina (EFAl) behind. Removing alumina from the framework also happens during calcination, especially for less stable zeolites. When the aluminum atoms are partly extracted from the framework to generate EFAl, Si/Al ratio in bulk doesn't change as these species remain in the channels.[66] Mild treatment with acid can be employed to remove the EFAl species without further extraction of Al from the framework.[78]

Generally, the extraction of aluminum increases the Si/Al ratio and enhances the mesoporosity.[65] It has been shown that extracting aluminum neutralizes the framework charge, which results in stabilizing the remaining aluminum framework against further dealumination.[79]

Steaming zeolite is conventionally performed at high temperatures (500 °C) in a humid atmosphere; during the steaming, some Al atoms are released from the framework due to the breaking of Al-O-Si bonds, and defects are formed. Extraction depends on the temperature and the type of zeolite. Extracted aluminum remains on the zeolite surface and in the pores as extra-framework Al (EFAl), while less stable Si mobilizes to the regions with depleted Al, generating Si-rich domains.[55] Steaming causes improved mobility of framework atoms compared

to heat treatments without the use of steam. The treatment itself doesn't cause a change in Si/Al ratio as aluminum stays as debris in or on the zeolite. Mild acid treatment can be used to free the mesopores by removing the debris.[65] Dealumination by steaming and acid leaching generated isolated cavities in zeolite Y rather than interconnected mesopores.[80,81]

Severe acid treatments are used to hydrolyze Si-O-Al bonds, which readily remove aluminum from the framework and increases the Si/Al ratio. The treatment's success depends on the type of zeolite, acid, and the pH of the prepared solution.[55,65] Dealumination by acid treatment can also be combined with microwave irradiation as a heating method.[82] It often leads to a reduction of tetrahedral Al species and an increased number of Lewis acid sites.[83]

Overall, the dealumination changes Si/Al ratio and therefore, the acidic properties of the zeolite along with mesopore formation within the framework, and it is often linked with partial loss of crystallinity and amorphization. Often the mesopores formed are not connected or not connected to the outer surface.[55]

#### **4.1.2.2 Desilication**

The alkaline assisted silicon preferential leaching of the zeolite framework has become an attractive method due to the experimental simplicity and efficiency of obtaining hierarchical zeolites.[74] The generated mesopores by base treatment are interconnected and accessible from the external surface.[84]

Base leaching was first patented in the 1960s by D. A. Young to increase zeolite performance in adsorption and catalysis.[85] In the late 1980s, Aouali *et al.* studied dealumination of zeolite Y and discovered structural collapse upon using the alkaline solution on a zeolite with Si/Al of 18.[86] However, the high interest in controlled preferential silicon removal was promoted by the works of J. Perez-Ramirez published during the last 15 years.[70,74,84,87-90]

Desilication hydrolyzes Si-O-Si bonds selectively; thus Si is preferentially removed from the framework, and mesopores are formed. The process starts at the boundaries of the zeolite crystals, so the zeolite crystal morphology plays a role in the desilication process.[83]

Desilication is limited to a range of molar ratios (Si/Al = 25-50) in which an optimal introduction of intracrystalline mesopores is achieved.[87] Which is also one of the main drawbacks of this post-synthetic method. At higher ratios (Si/Al > 50), the uncontrolled extraction of silicon occurs, which results in the formation of larger pores.[91] The schematic process of mesopore formation during desilication is depicted in **Figure 2.9a**. For lower Si/Al ratios, silicon extraction is hampered due to the regulatory effect of the framework aluminum, resulting in limited mesopore creation.[87] At lower values of Si/Al, negatively charged  $\text{AlO}_4^-$  prevents the extraction, and aluminum is considered as a pore-directing agent during alkaline leaching.[55,60] Combining these pieces of knowledge with the preferential dealumination conditions, a general strategy can be proposed (**Figure 2.9b**).

The dissolution degree and mesopore volume creation are determined by the intensity and the length of the desilication treatment.[60] Amorphization and loss of micropore volume are frequently observed upon severe desilication.[60] Desilication produces interconnected mesopores but fails to create abundant mesopores in large crystals.[74]

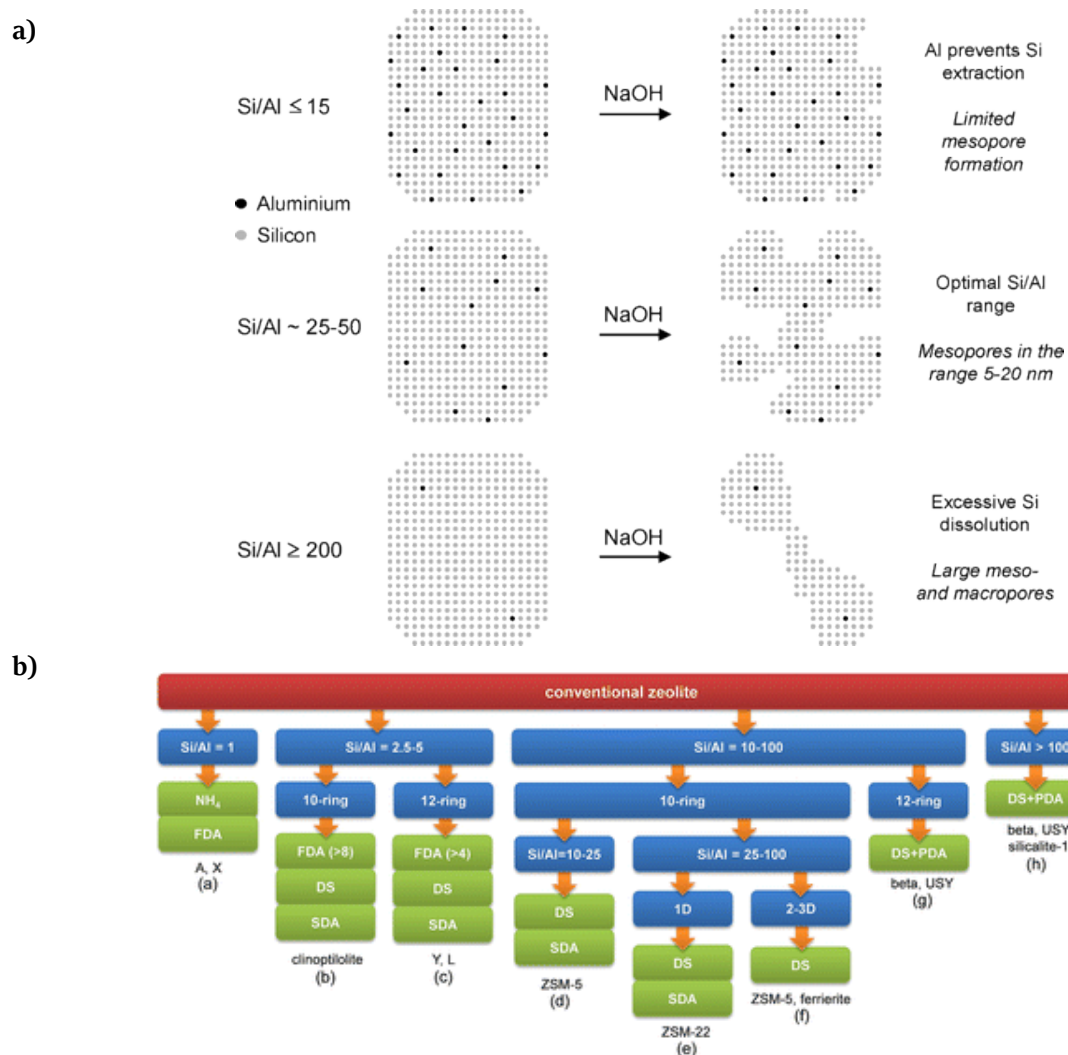


Figure 2.9. a) Simplified representation of aluminum content influences the desilication treatment with NaOH solution and the schematic mechanism of pore formation (from [87]). b) Overview of post-synthetic treatments (green) to change any conventional zeolite (red) into a hierarchical. Important features to take into account are Si/Al ratio and micropore dimensionality (blue) (from [92]). Treatment codes: FDA – framework dealumination, NH<sub>4</sub> – ion exchange, DS – desilication, SDA – selective dealumination, PDA – pore directing agents.

An important feature of desilicated zeolites is preserving the intrinsic Brønsted sites of the intact part of the zeolite framework, in contrast to zeolites modified by dealumination methods.[38] However, upon desilication, a large amount of extra framework aluminum species is generated, which increases the number of Lewis acid sites.[38,93]

Newer methods combine desilication with recrystallization; the dissolved zeolite is recrystallized thus reassembling the dissolved and dispersed species into a mesoporous phase. Recrystallization is normally done in hydrothermal conditions in the presence of a surfactant; hollow ZSM-5 was prepared in this way.[55,94]

Both dealumination and desilication methods lead to changes in the Si/Al ratio of the parent zeolite, leading to changes in the composition and distribution of silicon and aluminum altering zeolite acidic properties. Developing a method to treat zeolites that preserves the native chemical composition is desired.[95]

### 4.1.2.3 Fluoride-medium treatment

Fluoride anion is often employed as a mineraliser in the synthesis of high-silica zeolites having fewer defects than their counterparts synthesized in alkaline conditions. This was first reported by E.M. Flanigen and R.L. Patton.[96–98]

Fluorine treatment has been used to promote the catalytic activity in alumina catalysts for the acid-catalyzed reaction. The incorporation of fluorine enhances the acidic properties by replacing surface O, or OH. It increases both protonic and non-protonic sites' acidity since fluorine is more electronegative than oxygen. The fluorine incorporation occurs via two standard methods: impregnation and vapor-phase fluorination. Impregnation is done by saturating the catalyst with an aqueous solution containing HF, BF<sub>3</sub>, HBF<sub>4</sub>, NH<sub>4</sub>F, NH<sub>4</sub>BF<sub>4</sub>, or NH<sub>4</sub>SiF<sub>6</sub>, and the impregnated catalyst is then dried at higher temperatures.[99]

Loading the zeolite catalyst with fluoride compounds is usually executed with NH<sub>4</sub>F solutions and applied to MFI, MOR, and Beta type zeolites.[100–102] Reporting strengthening and increasing the concentrations of acid sites,[100] or their reduction[103], depending on the conditions applied. Extraction with F<sub>2</sub> has been used to dealuminate zeolite Y.[104] Direct fluorination is reported to increase low aluminum zeolites' activity by enhancing the Brønsted acidity and improving the activity.[105]

Solutions of HF are commonly used to etch silicon wafers for the semiconductor industry.[106] Hydrofluoric acid was discovered in 1771 by a Swedish pharmaceutical chemist Carl Scheele, who noticed the glass-etching properties of the fumes developed while heating fluorspar in sulfuric acid.[107] HF reacts with both aluminum and silicon.[108] In 1987 the work of Ghosh and Kydd showed the etching with concentrated HF solution (1.5 M) decreased the selectivity of Al dissolution and did not significantly change the Si/Al ration of mordenite zeolite.[109] While diluted solutions of HF acid ( $\leq 0.25$  M) preferentially extracted aluminum from mordenite and therefore change the framework composition without affecting its crystallinity.[109] Wloch etched ZSM-5 in an acetone solution of HF; the use of a non-aqueous solution improves the evolution of gaseous SiF<sub>4</sub> to leave the reaction medium before its decomposition can take place.[110,111] Use of solvents containing hydroxyl groups (*e.g.*, water and alcohol) leads to the decomposition of SiF<sub>4</sub> and the formation of amorphous silicic acids that may deposit on the surface of the zeolite crystals during etching.[111]

Etching ZSM-5 with different concentrations of HF (0.5–2 M) improved its catalytic activity in methanol to gasoline reaction (MTG).[112,113] Li *et al.* used a diluted HF solution to de-agglomerate IZM-2 nanocrystals without affecting the original framework.[114] Intergrowth boundaries are rich in defects; the acid targets these areas primarily.[115] The removal of intergrowths formed during the crystallization of ZSM-5 by NH<sub>4</sub>F/HF (buffered) solutions is shown in **Figure 2.10**. NH<sub>4</sub>F/HF treatments cause fragmentation of zeolite crystals, and small parts of the crystals are removed by the preferential dissolution of the defect zones. Furthermore, large pores penetrating deep into the crystals can be created, which leads to easier access to the micropores similar effect as the reduction in crystal size.[116]

Since the use of diluted HF, solutions tend to increase the Si/Al ratio, but the use of concentrated HF solutions can remove Si and Al from the framework without significant changes to the framework ratio, suggests that HF equilibrium can be shifted to allow unbiased extraction of Si and Al from the framework.[106,117] In contrast to other hydrogen halide acids, HF in water has a weak acid behavior, it doesn't fully dissociate in water solution.[118]

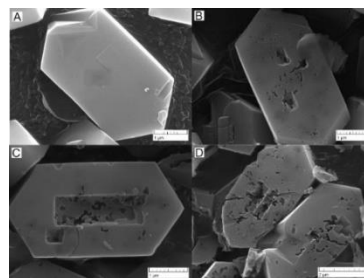


**Figure 2.10.** SEM images of ZSM-5 crystals treated with NH<sub>4</sub>F/HF solutions (from [95]).

HF dissolution in water can be expressed with two equilibria:



Different species are present in solutions of HF in water,  $\text{H}^+$ ,  $\text{F}^-$ ,  $\text{HF}_2^-$  and non-dissociated HF molecule[117] At 25 °C, the equilibrium constant of equation 2.3 is  $6.85 \times 10^{-4}$  M, and equation 2.4 is 3.963 M.[119] The equilibrium of eq. 2.3 can be shifted to the left and of eq. 2.4 to the right by adding a strong electrolyte like  $\text{NH}_4\text{F}$ . This shift in equilibrium increases the generation of undissociated HF species and hydrogen bifluoride species ( $\text{HF}_2^-$ ). HF can dimerize to  $(\text{HF})_n$  in solutions with a concentration higher than 1 M and the dimers can lose one proton, forming  $(\text{HF})_n\text{F}^-$ . [119–121] In **Figure 2.11**, the third equilibrium is added to account for the existence of dimer species in the solution.



The equilibrium constant of  $\text{H}_2\text{F}_2$  in equation 2.5 is 2.71 M,[106] which according to Knotter is another reactive species in the Si dissolution.

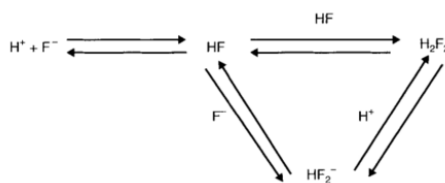


**Figure 2.11. Equilibrium reactions between fluoride species present in the aqueous solution of HF (from [106]).**

Knotter also argues, however, that  $\text{HF}_2^-$  is the only active etching species in the aq. solution of HF, since  $\text{HF}_2^-$  bond is  $180^\circ$ , its configuration allows it unrestricted access to Si in oppose to  $\text{H}_2\text{F}_2$ , having a square shape structure and bonds of  $90^\circ$ ; this is schematically depicted in **Figure 2.12**.

It is necessary to break all four siloxane bonds in order to break down the network and release the silicon from the glass.  $\text{HF}_2^-$  adsorbs on the surface silanol groups and HF on the vicinal silanol groups.

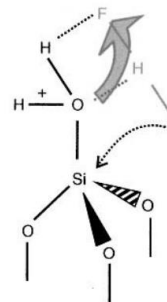


**Figure 2.12. Elimination of  $\text{OH}^-$  assisted by  $\text{HF}_2^-$  (from [119]).**

The adsorption of HF and  $\text{HF}_2^-$  increases the electronic density on the bridging oxygen in the siloxane unit, making them more basic, which leads to siloxane bonds being broken by adsorption of  $\text{H}^+$ . [122] In the only F<sup>-</sup> containing solutions, the dissolution of Si does not occur. [122,123] This is likely due to competition between  $\text{OH}^-$  ions and  $\text{F}^-$  ions for adsorption sites. [124]

Judge did find that there is a linear relationship in the rate of  $\text{SiO}_2$  etching of semiconductor wafers and concentrations of HF and  $\text{HF}_2^-$  species and the reaction rate of  $\text{HF}_2^-$  is several times higher than HF. [123] In buffered etching solutions ( $\text{NH}_4\text{F}/\text{HF}$ ), increasing the concentration of  $\text{NH}_4\text{F}$  leads to lowered activity of  $\text{HF}_2^-$  species because of the coordination with  $\text{NH}_4^+$ , and the etching reaction is dominated by HF alone. [125,126]

Etching rate data of solutions with different HF and  $\text{HF}_2^-$  concentrations show higher reactivity of  $\text{HF}_2^-$  compared to HF. Although many reports support this finding, Kline and Fogler came to an opposite conclusion, claiming only HF molecules are reactive. They also supported the catalytic role of  $\text{H}^+$  in the  $\text{SiO}_2$  dissolution. [127–129]

These findings explain why an increase of HF concentration leads to non-preferential extraction of framework atoms during zeolite etching.[95,109,130] Using more concentrated solutions of HF or buffered  $\text{NH}_4\text{F}/\text{HF}$  solutions shifts the equilibrium towards the generation of  $\text{HF}_2^-$ , and etches framework atoms, Si and Al indiscriminately.[95]

Ngoye *et al.* compared the porosities introduced by alkaline and fluoride leaching on ZSM-5 catalyst, and the fluoride treatment created some macropores without changing the physicochemical properties of the parent material, while alkaline treatment introduced mesopores interconnected with the existing micropores but at the same time generated many Lewis sites and silanol groups.[131] Meng *et al.*[113] and Ji *et al.*[132] applied  $\text{NH}_4\text{F}/\text{HF}$  solutions to treat ZSM-5 to improve their catalytic activity in MTG reaction and the cracking of n-hexane, respectively. This method was applied to other zeolite frameworks, FER, Mordenite, SAPO-34, referenced in **Table 2.2**.

Valtchev and co-workers have developed this approach further to obtain zeolites with enhanced pore volume.[133] This patent presents a novel method to obtain hierarchical zeolites by contacting the zeolite material with an aqueous solution of  $\text{NH}_4\text{F}$  and thoroughly washing, then drying the obtained products. The method is based on the double hydrolysis of  $\text{NH}_4\text{F}$  that generates *in situ* a limited amount of HF in equilibrium with  $\text{F}^-$  and  $\text{HF}_2^-$ . [115] The chemical equilibria involved in the dissolution of  $\text{NH}_4\text{F}$  in water is shown in **Figure 2.13**.

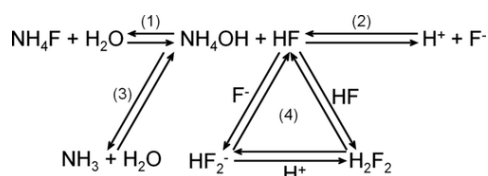


**Figure 2.13. Chemical equilibria involving dissolution of  $\text{NH}_4\text{F}$  in water (from [115]).**

The solution of  $\text{NH}_4\text{F}$  is can be tuned to be non-selective towards Si or Al. Therefore, it etches the zeolite without altering the framework composition and sacrificing the micropores contribution, which leads to improved diffusivity and catalytic activity.[115,134–136] Thus the retained acidity is accompanied by improved accessibility to the zeolite micropores. Just like the  $\text{NH}_4\text{F}/\text{HF}$  solutions remove defects and intergrowths, the same effect has been observed with  $\text{NH}_4\text{F}$  solutions etching ZSM-5 crystals, shown in **Figure 2.14**.

Washing the product thoroughly is important to avoid any exchange of  $\text{F}^-$  with the framework and to remove all the reaction products from the zeolite surface and cavities.  $\text{F}^-$  might replace  $\text{SiO}^-$  in the zeolite framework.[137]

Zeolite framework is often built by units that are inaccessible even to small molecules. Thus, the 6 MR window of a sodalite cage has an opening diameter of 0.25 nm.[138] The latest research of etching FAU zeolite with  $\text{NH}_4\text{F}$  showed that the accessibility to the micropores could be improved by opening some of the sodalite cages in the zeolite framework.[139] Most

recently, the fluoride method for wet etching has been extended to etching with aqueous solutions of  $\text{NH}_4\text{HF}_2$ . [140–142] It has been shown by Qin *et al.* that defects induced by treatment with oxalic acid leads to the formation of small irregular mesopores upon the following with  $\text{NH}_4\text{F}$  dissolution, which makes the zeolite dissolution go beyond the limits set by the zeolite structure.[136]

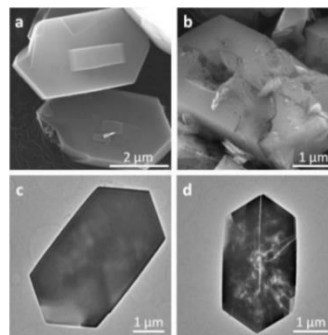


**Figure 2.14. SEM micrographs of ZSM-5 crystals treated with 40 wt/%  $\text{NH}_4\text{F}$  aqueous solution (from [115]).**

Overview of work published regarding fluoride etching of zeolites is presented in **Table 2.2**, including  $\text{NH}_4\text{F}$ , and  $\text{NH}_4\text{HF}_2$ , and combinations thereof. Works that don't include washing step after the treatment are not listed since these are considered impregnation methods.

Table 2.2. Published work on zeolite etching with fluorine compounds.

Year	Author	Framework (catalyst)	Etchant	Si/Al	Catalytic reaction	Syn. conditions	Comment	Ref
2020	Feng <i>et al.</i>	FAU (NaY)	0.3 M NH <sub>4</sub> HF <sub>2</sub>	2.7	N/A	treatment at 95 °C (6h)	Increases the Si/Al ratio to 4.7. $V_{\text{micro}} \downarrow$ , $V_{\text{meso}} \uparrow$ . Many mesopores with wide pore size distribution. Increased capacity for toluene adsorption.	[142]
2020	Haw <i>et al.</i>	CHA (NH <sub>4</sub> -SSZ-13)	H <sub>2</sub> O <sub>2</sub> /NH <sub>4</sub> F	7.8	N/A	US assisted synthesis, 22 °C, 15–90 min	$V_{\text{micro}} \uparrow$ , $V_{\text{meso}} \uparrow$ (but not substantial). No changes reported in Si/Al. Sponge like morphology created after treatment.	[143]
2020	Liu <i>et al.</i>	FAU (H-USY)	5–25 wt/% NH <sub>4</sub> F	2.7, 5.5	isobutane/1-butene alkylation	l/s = 6, 5 min treatment at 5–6 °C	$V_{\text{micro}} \downarrow$ , $V_{\text{meso}} \uparrow$ , small dealumination, *rel. cryst. (RC) $\downarrow$ with NH <sub>4</sub> F conc. increase. Zeolite with higher Si/Al ratio is more sensitive to NH <sub>4</sub> F leaching, more severe structural amorphization. NH <sub>4</sub> F modification the acid properties, Lewis acid sites (LAS) conc. on the modified zeolites was reduced.	[144]
2020	Liu <i>et al.</i>	MOR (Na-MOR)	25 wt/% NH <sub>4</sub> F	9.5	dimethyl ether carbonylation	l/s = 20, 10 min 20, 50, 80 °C	$V_{\text{micro}}$ , RC, Brønsted acid sites (BAS) preserved, except at treatment at 80 °C. Slight dealumination at all temp. $V_{\text{meso}} \uparrow$ increases in all cases.	[145]
2020	Qin <i>et al.</i>	MOR (NH <sub>4</sub> -MOR)	40 wt/% NH <sub>4</sub> F	6.5	dealkylation of 1,3,5-triisopropylbenzene (TiPBz)	l/s = 16, 50 °C, 2 min, mechanical stirring and US	$V_{\text{meso}} \uparrow$ , Si/Al, $V_{\text{micro}}$ , acidity preserved, defect removal improved conversion	[136]
2020	Tekla <i>et al.</i>	ERI (H-ERI)	NH <sub>4</sub> F/HF	3.5	dealkylation of TiPBz	15 min, 25 °C treatment, calcination	$V_{\text{meso}} \uparrow$ , Si/Al, $V_{\text{micro}}$ , acidity preserved, small improvements of conversion	[146]
2020	Todorova <i>et al.</i>	MFI (ZSM-5)	NH <sub>4</sub> F/HF		<i>m</i> -xylene and toluene transformation	20 min treatment, 25 °C, calcination	$V_{\text{micro}} \downarrow$ , $V_{\text{meso}} \uparrow$ , no observed changes in catalytic activity	[147]
2019	Bolshakov <i>et al.</i>	MFI (ZSM-5-TPA <sup>a</sup> , ZSM-5-PET <sup>b</sup> )	0.2–5 M NH <sub>4</sub> F	21	n-hexadecane hydroconversion	l/s = 69, 175 °C, 6h, calcination	30–50 % Al atoms removed without structural degradation or EFAI	[148]

							formation by template stabilization (TPA, PET)	
2019	Feng <i>et al.</i>	FAU (NaY)	0.1–0.5 M NH <sub>4</sub> HF <sub>2</sub>	2.7	N/A	l/s = 20, 95 °C, 6h	Synthesis conditions as [142]. 0.1 M NH <sub>4</sub> HF <sub>2</sub> leads to increased RC, V <sub>micro</sub> ↑, V <sub>meso</sub> ↑. Higher conc. (0.2, 0.3 M) leads to decreased <i>rel. cryst.</i> , V <sub>micro</sub> ↓, V <sub>meso</sub> ↑. 0.5 M NH <sub>4</sub> HF <sub>2</sub> V <sub>micro</sub> ↓, V <sub>meso</sub> ↓. General dealumination reported.	[140]
2019	Feng <i>et al.</i>	FAU (USY)	NH <sub>4</sub> HF <sub>2</sub> -NaOH NH <sub>4</sub> HF <sub>2</sub> -NH <sub>4</sub> OH	2.7	N/A	l/s = 20, 95 °C, 6h	V <sub>micro</sub> ↑, V <sub>meso</sub> ↑. Small increase of Si/Al. Additional OH <sup>-</sup> treatment, etching with OH <sup>-</sup> more likely to start around NH <sub>4</sub> HF <sub>2</sub> generated mesopores.	[141]
2019	Janiszewska <i>et al.</i>	MFI (H-Sil-1)	1 M NH <sub>4</sub> F	∞	acetalization of glycerol with acetone	l/s = 100, 60 °C, 1h, repeated twice, calcination	RC↑, V <sub>meso</sub> ↑, increased acidity and glycerol conversion	[149]
2019	Přech <i>et al.</i>	MFI	40 wt/% NH <sub>4</sub> F	30–35	<i>m</i> -xylene isomerization dealkylation of TiPBz	50 °C, US bath, l/s = 20, 5–140 min, calcination	layered ZSM-5 dissolve similarly to conventional ZSM-5, preserved acidity	[150]
2019	Qin <i>et al.</i>	MFI (NH <sub>4</sub> -ZSM-5)	40 wt/% NH <sub>4</sub> F	21	ethanol to hydrocarbon conversion	50 °C, 60 min, mechanical stirring and US	V <sub>meso</sub> ↑, BAS↓, high cat. Activity and stability due to house-of-cards post etching morphology	[135]
2019	Ren <i>et al.</i>	FAU (NH <sub>4</sub> -USY)	NH <sub>4</sub> F-NaOH	2.9	hydrocracking reaction of naphthalene	90 °C, 8h, steaming, desilication	partial amorphization, V <sub>micro</sub> ↓, V <sub>meso</sub> ↑, Si/Al↓, increased acidity and activity	[151]
2019	Suárez <i>et al.</i>	BEA (H-BEA)	NH <sub>4</sub> F/HF	19	isomerization/disproportionation of <i>m</i> -xylene	25–40 °C, 5–30 min, calcination	V <sub>micro</sub> ↓ V <sub>meso</sub> ↑, Si/Al↑, sponge like crystals (TEM), lowered cat. activity, increase LAS	[152]
2018	Ji <i>et al.</i>	MFI (ZSM-5)	NH <sub>4</sub> F/HF	25	n-hexane cracking to light alkenes	25 °C, 10 min, calcination	S <sub>BET</sub> ↑, V <sub>meso</sub> ↑, V <sub>micro</sub> ↑, RC↑, preserved acidity, increased cat. activity, lowered coke contents	[132]
2017	Kalvachev <i>et al.</i>	MOR (Na,K-MOR)	NH <sub>4</sub> F/HF	9.7	<i>m</i> -xylene isomerization	5–20 min, NH <sub>4</sub> <sup>+</sup> exchange, calcination	V <sub>meso</sub> ↑, Si/Al preserved, improved cat. activity	[153]

2017	Meng <i>et al.</i>	MFI (H-ZSM-5)	NH <sub>4</sub> F/HF	25	methanol to gasoline	25 °C, 10 min	$V_{\text{meso}} \uparrow$ , $V_{\text{micro}}$ and RC small losses, improved cat. lifetime	[113]
2017	Popova <i>et al.</i>	MOR (Na,K-MOR)	NH <sub>4</sub> F/HF	9	glycerol esterification	5–20 min, NH <sub>4</sub> <sup>+</sup> exchange, calcination	increased total pore volume, higher cat. activity	[154]
2017	Qin <i>et al.</i>	FAU (NH <sub>4</sub> -Y-54)	25 wt/% NH <sub>4</sub> F	2.6	dealkylation of TiPBz, hydroconversion of n-octane	l/s = 6, US, 0 °C, 1–20 min	$V_{\text{micro}} \uparrow$ due to the opening of some sodalite cages in FAU framework	[139]
2016	Chen <i>et al.</i>	CHA (SAPO-34)	NH <sub>4</sub> F/HF	/	methanol-to-olefin (MTO)	25 °C, US, 30–60 min, calcination	formation of large meso-, macropores, improved selectivity to C <sub>3</sub> H <sub>6</sub> , however reduced activity	[155]
2016	Chen <i>et al.</i>	CHA (TEA-SAPO-34)	NH <sub>4</sub> F/HF	Si/Al/P 1/6.7/6.9	MTO	25 °C, US, 15–30 min, calcination	$V_{\text{meso}}$ moderate increase, limited surface etching, dissolution of Si rich areas, BAS $\downarrow$ , improved cat. activity	[156]
2016	Du <i>et al.</i>	MFI (Ti-silicalite-1)	NH <sub>4</sub> F/HF	Si/Ti 20.4	oxidation of dibenzothiophene	25 °C, 15 min, US	$V_{\text{micro}}$ and $V_{\text{meso}} \uparrow$ , Si/Ti $\uparrow$ , improved cat. activity	[157]
2016	Guesh <i>et al.</i>	FAU (H-Y)	NH <sub>4</sub> CH <sub>3</sub> CO <sub>2</sub> -NH <sub>4</sub> F	2.6	photocatalysis	80 °C, 30 min, calcination	Al selectively removed from the surface, significantly higher photocatalytic activity	[158]
2016	Li <i>et al.</i>	MFI (NH <sub>4</sub> -ZSM-5)	FeF <sub>3</sub> /NH <sub>4</sub> HF <sub>2</sub>	25	MTO	92 °C, 24h, calcination	selective extraction of defect rich areas, indiscriminate extraction of Si and Al, high dispersion of Fe, improved MTO activity and reduced coke contents	[159]
2016	Qin <i>et al.</i>	MFI, MOR	NH <sub>4</sub> F	/	<i>m</i> -xylene isomerization, dealkylation of TiPBz	/	NH <sub>4</sub> F removes defect zones in zeolite crystals revealing crystal imperfections, <i>i.e.</i> “mosaic structure”	[115]
2016	Todorova <i>et al.</i>	MOR (Na, K-MOR)	NH <sub>4</sub> F/HF	9	<i>m</i> -xylene isomerization	25 °C, 5–20 min, NH <sub>4</sub> <sup>+</sup> exchange, calcination	improved cat. activity	[160]
2015	Hammond <i>et al.</i>	MFI (TS-1)	H <sub>2</sub> O <sub>2</sub> /NH <sub>4</sub> HF <sub>2</sub>	N/A	epoxidation	80 °C, 4h	extraction of framework Ti, no substantial changes in the porosity or acidity, increased selectivity in epoxidation	[161]

2015	Lakiss <i>et al.</i>	MFI (H-ZSM-5)	NH <sub>4</sub> F/HF	19	ethanol to hydrocarbons	/	hierarchical nanosized catalyst showed significant improvement in cat. activity despite coke poisoning	[134]
2015	Li <i>et al.</i>	MFI (H-ZSM-5)	Ga(NO <sub>3</sub> ) <sub>3</sub> /NH <sub>4</sub> HF <sub>2</sub>	15	MTO propanal to hydrocarbons	92 °C, 24 h, calcination	removing defect zones, decreased acidity, Ga deposition on zeolite, improved lifetime in MTO	[162]
2014	Chen <i>et al.</i>	FER (Na-En <sup>d</sup> -FER)	NH <sub>4</sub> F/HF	8.1	N/A	25 °C, 10–20 min, calcination, ion-exchange	high crystallinity, Si/Al↑	[163]
2014	Ngoye <i>et al.</i>	MFI (H-ZSM-5)	NH <sub>4</sub> F/HF	19	methycyclohexane transformation	25 °C, 6 min	NH <sub>4</sub> F/HF creates macropores while retaining other physicochemical properties, increased cat. Lifetime and coke contents	[131]
2013	Burel <i>et al.</i>	MFI (silicalite-1)	1 M NH <sub>4</sub> F	∞	/	170 °C, 24 h, calcination	decrease of siloxy framework defects	[164]
2013	Qin <i>et al.</i>	MFI (NH <sub>4</sub> -ZSM-5)	NH <sub>4</sub> F/HF	19	<i>m</i> -xylene isomerization	25–65 °C, 6–15 min	indiscriminate Si and Al extraction due to buffering HF with NH <sub>4</sub> F, improved cat. activity and retained acidity	[95]
2012	Tang <i>et al.</i>	MFI (H-ZSM-5)	NH <sub>4</sub> F	14	butene cracking	85 °C, 1 h, calcination	RC↑, Si/Al↑, V <sub>micro</sub> ↑, V <sub>meso</sub> ↓, BAS and LAS↓, increased cat. activity	[165]
2011	Na <i>et al.</i>	MFI (TS-1)	NH <sub>4</sub> F	Si/Ti 57	epoxidation of olefines	100 °C, 12 h, calcination	removal of silanol defects in nanosized samples, preserved cryst. due to SDA, conversion of bulky olefins increased	[166]
2010	Feng <i>et al.</i>	MFI (H-ZSM-5)	0.01–1 M NH <sub>4</sub> F	46	cracking of naphtha	35 °C, 4 h	S <sub>BET</sub> ↑, V <sub>meso</sub> ↑, V <sub>micro</sub> ↑, RC ↑, BAS and LAS↑, increased cat. activity	[167]

N/A = not available, \*RC = relative crystallinity, <sup>a</sup>TPA = tetrapropyl ammonium, <sup>b</sup>PET = pentaerythritol, <sup>c</sup>TEA = tetraethylammonium hydroxide, <sup>d</sup>En = ethylenediamine,

## 5 Applications of zeolites

Zeolite applications are entrenched in various areas such as adsorbents and gas separations, laundry detergents, oil refining, and petrochemical industries, agriculture, and horticulture.[11] China and Cuba are the largest consumers of natural zeolites; their usage is estimated to 3 million tons per year with a primary reason to enhance cement strengthness.[11] In the USA, Western and Eastern Europe, and Japan, the consumption of natural zeolites is 0.2 million tons per year. They are used as nutrient release agents, odor control in pet litter, soil conditioner for the golf course, and ion exchangers for water purification.[11]

Zeolites are used as cation exchangers in detergents, about 1.4 million tons of zeolite A are synthesized each year to remove or encapsulate  $\text{Ca}^{2+}$  and  $\text{Mg}^{2+}$  cations that make water “hard”. Phosphates which are usually used, are declining in popularity because they cause algal bloom in lakes and rivers.[168]

Zeolites are used to treat wastewater from various sources, natural, industrial, agricultural, and municipal wastewater. In water purifications processes, natural zeolites are used to remove metals from industrial wastewater, ammonium ions ( $\text{NH}_4^+$ ) from municipal wastewater. The addition of clinoptilolite to sewage sludge enhances the nitrification process.[15]

Pavelić *et al.* in their study identified that clinoptilolite zeolites when mechanically activated act as anticancer agents *in vivo* animal studies and *in vitro* culture cell models.[15] Zeolites also found a way in other medical applications, such as commercially available clotting agents (Hemosorb, QuikClot), and in dialysis machines, they are used to remove ammonia from the blood.[169]

Overall, the zeolites are remarkable materials with a vast variety of uses, environmental pollution control,[170] photocatalyzed oxidation reaction,[171] hydrogen storage,[172] and many more.

### 5.1 Catalysis

Although their use in catalysis is not the largest by volume use, it has the highest market value, where they are employed in FCC, hydrocracking, paraffin isomerization, and aromatic alkylation.[11,173] FAU-type zeolite accounts for more than 95 % of the catalysis market; it is used in the FCC process to manufacture gasoline from crude oil.

MFI-type zeolites are the second-most-used zeolite catalyst; they are added to improve yield in the FCC process.[11] Followed by mordenite and zeolite beta.[173] Of 253 reported zeolite frameworks, 18 are reported to be used in 25 different commercial operations.[174] Other notable zeolites and zeotypes in commercial applications are LTA, AEL, FER, LTL, MWW, and TON. And SAPO-34 has also been successfully commercialized in the MTO process in 2005.[175] AEL is used in the process of long-chain alkane hydroisomerization and Beckmann rearrangement.[176]

Hydrophobic zeolites like silicalite, hydrophobic Y, and beta have become increasingly interesting for the market in the adsorption of organic materials such as automobile exhaust cleanup.[11] Zeolites are the center of well-established technologies for producing key petrochemical intermediates like light ( $\text{C}_2\text{-C}_4$ ) olefins and BTX (benzene, toluene, xylene) aromatics.[177] In recent decades new technologies are emerging to produce valuable petrochemicals from alternative sources to oil, such as natural gas and non-edible biomass. Zeolites are pivotal here since the methanol-to-olefin (MTO) process is an example of a new catalytic route to light olefins from natural gas or biomass.[177] Non-oxidative methane-dehydroaromatization (MDA) is another interesting process involving the production of aromatic petrochemicals from raw materials by converting methane mostly to benzene. Deactivation of catalysts is a considerable concern for many processes producing light olefins and BTX petrochemical intermediates.

Zeolite is a highly efficient acid or red-ox catalysts for the production of fine chemicals in electrophilic aromatic substitution, isomerization, hydroxyalkylation, epoxidation, and other important reactions industrially. BEA, MFI, FAU, and MOR zeolites are of great interest in producing valuable fine chemicals.[178]

The reality of limited and declining resources of crude oil made developments in the use of zeolites as catalysts to provide known hydrocarbon cracking and oxidation chemistry more efficient, and revelation of new catalytic processes for acquisition and modification of hydrocarbons are of importance.[179,180] Progress is already being made for engineering the properties of zeolites to acclimate the challenges related to biomass and biofuels valorization.[181] Significant work is being carried out to obtain novel classes of zeolite catalysts modifying their properties for the biomass valorization process; this includes hierarchical zeolites.[182]

### 5.1.1 Properties of zeolites enabling catalysis

#### 5.1.1.1 Zeolites as solid acids

The presence of exchangeable framework cations gives zeolites their interesting catalytic properties. Protonic ( $H^+$ ) exchange leads to the active sites in zeolites, Brønsted acid sites zeolite specific bridging hydroxyl groups. They are viewed as a resonance between bridging hydroxyls (I) and terminal silanols (II) (Figure 2.15). Particularly a “fully bridged oxygen with a weakly bound proton” and a “silanol group with a weak Lewis acid interaction”. By Brønsted and Lewis acid definitions, Brønsted acids are proton donors and Lewis acids are electron acceptors

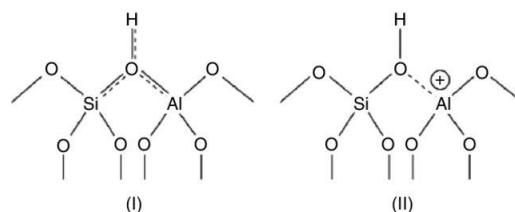


Figure 2.15. Brønsted acid sites as a resonance model between (I) and (II) (from [183]).

The acidic OH groups are further activated by the presence of neighboring-accepting  $Al^{3+}$  Lewis centers. This weakens the strength of the OH bond and increases the acidity. The number of bridging hydroxyls should, in theory, correspond to the number of framework aluminum atoms; however, this number is lowered during exchange and activation.

#### 5.1.1.2 Shape Selective Catalysis

Shape selectivity of zeolites results from their crystal structure or framework topology. This structure-activity connection was first identified by Weisz and Frillette in 1960.[184] The term shape selectivity refers to the fact that zeolites can be shape and size-selective. The shape selectivity of zeolites is exercised for reactants, products, and intermediates.[15]



Figure 2.16. Illustration of reactant shape selectivity.

For example, product selectivity occurs when products of the reaction formed within the zeolite micropores are restricted from diffusing away from the reaction site due to the incompatibilities caused by the micropores' shape/size. The same can occur with reactants, those too big to enter the zeolite micropores are excluded from the reaction (Figure 2.16).

The drawback, however, is this also results in pore blocking and catalyst deactivation by coke formation.

### 5.1.2 Catalytic applications of hierarchical zeolites

Accessibility of acid sites plays an important role in zeolites' catalytic performance.[185] The generation of mesopores in zeolite crystals results in a higher external surface area, and the intercrystalline diffusion path is shortened. The combination of micropores and mesopores provide beneficial effects to the catalytic performance

since mesopores ensure optimal accessibility and transport and micropores the shape selectivity.[69] For reactions taking place outside the micropores, mesopores increase the external surface area.[186]

The introduction of mesopores leads to increased catalytic activity; this is observed for cracking of large molecules such as polyethylene and hexadecane, but also in the alkylation of aromatic compounds.[186] Change of selectivity results from increased diffusivity of products away from the reaction site, by reducing the retention time and the chance of going through another reaction.

For catalytic applications, a material with ideal acidic properties would be found between ensuring high concentration and stretch of acid sites and high accessibility to the acid sites by introducing mesopores.[185]

Microporous structures during catalysis usually suffer from pore mouth blockage as a result of coke deposition, which results in catalyst deactivation. The formation of coke is unavoidable; therefore, it is essential to minimize coke formation. Hierarchical zeolites exhibit increased catalyst lifetime owed to their high resistance to deactivation.[187,188]

Extraction methods tend to change the Si/Al ratio and distribution during mesopore formation. This complicates the cause and effect interpretation of the catalytic data, so extensive material characterization is important.[60] Destructive methods are very attractive for industrial purposes, they are easily used for commercial zeolites.[66]

## 6 References

- [1] C. Colella, Natural zeolites, in: J. Čejka, H. van Bekkum (Eds.), *Studies in Surface Science and Catalysis*, Elsevier, 2005: pp. 13–40. [https://doi.org/10.1016/S0167-2991\(05\)80004-7](https://doi.org/10.1016/S0167-2991(05)80004-7).
- [2] M. Guisnet, J.-P. Gilson, *Zeolites for Cleaner Technologies*, Imperial College Press, 2002.
- [3] J. Weitkamp, L. Puppe, *Catalysis and zeolites: fundamentals and applications*, Springer, Berlin, 2010.
- [4] A.F. Masters, T. Maschmeyer, Zeolites – From curiosity to cornerstone, *Microporous and Mesoporous Materials*. 142 (2011) 423–438. <https://doi.org/10.1016/j.micromeso.2010.12.026>.
- [5] P. Bai, M.Y. Jeon, L. Ren, C. Knight, M.W. Deem, M. Tsapatsis, J.I. Siepmann, Discovery of optimal zeolites for challenging separations and chemical transformations using predictive materials modeling, *Nat Commun*. 6 (2015) 1–9. <https://doi.org/10.1038/ncomms6912>.
- [6] J. Li, A. Corma, J. Yu, Synthesis of new zeolite structures, *Chem. Soc. Rev*. 44 (2015) 7112–7127. <https://doi.org/10.1039/C5CS00023H>.
- [7] N.E.R. Zimmermann, M. Haranczyk, History and Utility of Zeolite Framework-Type Discovery from a Data-Science Perspective, *Crystal Growth & Design*. 16 (2016) 3043–3048. <https://doi.org/10.1021/acs.cgd.6b00272>.
- [8] A. Corma, A. Martinez, Zeolites and Zeotypes as catalysts, *Adv. Mater*. 7 (1995) 137–144. <https://doi.org/10.1002/adma.19950070206>.
- [9] Y. Li, L. Li, J. Yu, Applications of Zeolites in Sustainable Chemistry, *Chem*. 3 (2017) 928–949. <https://doi.org/10.1016/j.chempr.2017.10.009>.
- [10] P. Payra, P.K. Dutta, P.K. Dutta, Zeolites: A Primer, *Handbook of Zeolite Science and Technology*. (2003) 13–36. <https://doi.org/10.1201/9780203911167-7>.
- [11] T. Maesen, Chapter 1 - The Zeolite Scene – An Overview, in: J. Čejka, H. van Bekkum, A. Corma, F. Schüth (Eds.), *Studies in Surface Science and Catalysis*, Elsevier, 2007: pp. 1–12. [https://doi.org/10.1016/S0167-2991\(07\)80789-0](https://doi.org/10.1016/S0167-2991(07)80789-0).
- [12] J. B.Nagy, P. Bodart, I. Hannus, I. Kiricsi, Synthesis, characterization and use of zeolitic microporous materials, DecaGen Ltd., 1998.
- [13] L. Gómez-Hortigüela, M.Á. Cambor, Introduction to the Zeolite Structure-Directing Phenomenon by Organic Species: General Aspects, in: L. Gómez-Hortigüela (Ed.), *Insights into the Chemistry of Organic Structure-Directing Agents in the Synthesis of Zeolitic Materials*, Springer International Publishing, Cham, 2018: pp. 1–41. [https://doi.org/10.1007/430\\_2017\\_8](https://doi.org/10.1007/430_2017_8).
- [14] S.M. Auerbach, K.A. Carrado, P.K. Dutta, *Handbook of Zeolite Science and Technology*, CRC Press, 2003.
- [15] M. Moshoeshoe, M.S. Nadiye-Tabbiruka, V. Obuseng, A Review of the Chemistry, Structure, Properties and Applications of Zeolites, *American Journal of Materials Science*. 7 (2017) 196–221.
- [16] Inamuddin, M. Luqman, eds., *Ion Exchange Technology II: Applications*, Springer Netherlands, 2012. <https://doi.org/10.1007/978-94-007-4026-6>.
- [17] R.W. Broach, Zeolite Types and Structures, in: *Zeolites in Industrial Separation and Catalysis*, John Wiley & Sons, Ltd, 2010: pp. 27–59. <https://doi.org/10.1002/9783527629565.ch2>.
- [18] W.H. Baur, R.X. Fischer, eds., *Zeolite Structure Codes ABW to CZP*, Springer-Verlag, Berlin/Heidelberg, 2000. <https://doi.org/10.1007/b72483>.
- [19] W.M. Meier, D.H. Olson, Zeolite Frameworks, in: *Molecular Sieve Zeolites-I*, American Chemical Society, 1974: pp. 155–170. <https://doi.org/10.1021/ba-1971-0101.ch014>.
- [20] C.C. Freyhardt, M. Tsapatsis, R.F. Lobo, K.J. Balkus, M.E. Davis, A high-silica zeolite with a 14-tetrahedral-atom pore opening, *Nature*. 381 (1996) 295–298. <https://doi.org/10.1038/381295a0>.
- [21] C. Zhang, E. Kapaca, J. Li, Y. Liu, X. Yi, A. Zheng, X. Zou, J. Jiang, J. Yu, An Extra-Large-Pore Zeolite with 24×8×8-Ring Channels Using a Structure-Directing Agent Derived from Traditional Chinese Medicine, *Angewandte Chemie*. 130 (2018) 6596–6600. <https://doi.org/10.1002/ange.201801386>.
- [22] J. Jiang, J.L. Jorda, J. Yu, L.A. Baumes, E. Mugnaioli, M.J. Diaz-Cabanas, U. Kolb, A. Corma, Synthesis and Structure Determination of the Hierarchical Meso-Microporous Zeolite ITQ-43, *Science*. 333 (2011) 1131–1134. <https://doi.org/10.1126/science.1208652>.
- [23] J. Sun, C. Bonneau, A. Cantin, A. Corma, M.J. Diaz-Cabanas, M. Moliner, D. Zhang, M. Li, X. Zou, The ITQ-37 mesoporous chiral zeolite, *Nature*. 458 (2009) 1154–1157. <https://doi.org/10.1038/nature07957>.

- [24] W.-W. Zi, Z. Gao, J. Zhang, B.-X. Zhao, X.-S. Cai, H.-B. Du, F.-J. Chen, An Extra-Large-Pore Pure Silica Zeolite with  $16 \times 8 \times 8$ -Membered Ring Pore Channels Synthesized using an Aromatic Organic Directing Agent, *Angewandte Chemie International Edition*. 59 (2020) 3948–3951. <https://doi.org/10.1002/anie.201915232>.
- [25] K. Kaneko, Determination of pore size and pore size distribution 1. Adsorbents and catalysts, *Journal of Membrane Science*. 96 (1994) 59–89.
- [26] *Database of Zeolite Structures*, <http://www.iza-structure.org/databases/> (accessed November 24, 2020).
- [27] J.-L. Guth, H. Kessler, Synthesis of Aluminosilicate Zeolites and Related Silica-Based Materials, in: J. Weitkamp, L. Puppe (Eds.), *Catalysis and Zeolites: Fundamentals and Applications*, Springer, Berlin, Heidelberg, 1999: pp. 1–52. [https://doi.org/10.1007/978-3-662-03764-5\\_1](https://doi.org/10.1007/978-3-662-03764-5_1).
- [28] W. Löwenstein; M. Löwenstein, Distribution of aluminum in the tetrahedra of silicates and aluminates, *American Mineralogist* (1954) 39 (1-2): 92–96.
- [29] R.E. Fletcher, S. Ling, B. Slater, Violations of Löwenstein’s rule in zeolites, *Chem. Sci*. 8 (2017) 7483–7491. <https://doi.org/10.1039/C7SC02531A>.
- [30] R. Xu, W. Pang, J. Yu, Q. Huo, J. Chen, *Chemistry of Zeolites and Related Porous Materials: Synthesis and Structure*, Singapore, Hoboken, N.J., John Wiley & Sons (Asia), 2007
- [31] H. Holzapfel, *Zeolites in Chemical Engineering*, Verlag ProcessEng Engineering, 2011.
- [32] C.-Y. Chen, S.I. Zones, Post-Synthetic Treatment and Modification of Zeolites, in: J. Čejka, A. Corma, S. Zones (Eds.), *Zeolites and Catalysis*, Wiley-VCH Verlag GmbH & Co. KGaA, Weinheim, Germany, 2010: pp. 155–170. <https://doi.org/10.1002/9783527630295.ch6>.
- [33] S. Kulprathipanja, *Zeolites in Industrial Separation and Catalysis*, John Wiley & Sons, 2010.
- [34] E.M. Flanigen, Chapter 2 Zeolites and molecular sieves: An historical perspective, in: H. van Bekkum, E.M. Flanigen, P.A. Jacobs, J.C. Jansen (Eds.), *Studies in Surface Science and Catalysis*, Elsevier, 2001: pp. 11–35. [https://doi.org/10.1016/S0167-2991\(01\)80243-3](https://doi.org/10.1016/S0167-2991(01)80243-3).
- [35] J. Yu, Chapter 3 - Synthesis of Zeolites, in: J. Čejka, H. van Bekkum, A. Corma, F. Schüth (Eds.), *Studies in Surface Science and Catalysis*, Elsevier, 2007: pp. 39–103. [https://doi.org/10.1016/S0167-2991\(07\)80791-9](https://doi.org/10.1016/S0167-2991(07)80791-9).
- [36] FEZA School on Zeolites, M.C. Martínez Sánchez, J. Pérez Pariente, *Zeolites and ordered porous solids: fundamentals and applications: the 3rd FEZA School on Zeolites*, Valencia, Spain, July 8–9, 2011, Editorial Universitat Politècnica de València, Valencia, 2011.
- [37] D.J. Earl, M.W. Deem, Toward a Database of Hypothetical Zeolite Structures, *Ind. Eng. Chem. Res.* 45 (2006) 5449–5454. <https://doi.org/10.1021/ie0510728>.
- [38] J. Pérez-Ramírez, C.H. Christensen, K. Egeblad, C.H. Christensen, J.C. Groen, Hierarchical zeolites: enhanced utilisation of microporous crystals in catalysis by advances in materials design, *Chem. Soc. Rev.* 37 (2008) 2530–2542. <https://doi.org/10.1039/B809030K>.
- [39] R. Mallada, Hydrothermal Synthesis of Zeolite, in: E. Drioli, L. Giorno (Eds.), *Encyclopedia of Membranes*, Springer Berlin Heidelberg, 2014: pp. 1–2. [https://doi.org/10.1007/978-3-642-40872-4\\_953-1](https://doi.org/10.1007/978-3-642-40872-4_953-1).
- [40] K. Byrappa, M. Yoshimura, 6 - Hydrothermal Synthesis and Growth of Zeolites, in: K. Byrappa, M. Yoshimura (Eds.), *Handbook of Hydrothermal Technology*, William Andrew Publishing, Norwich, NY, 2001: pp. 315–414. <https://doi.org/10.1016/B978-081551445-9.50007-6>.
- [41] D. Shi, K.-G. Haw, C. Kouvatas, L. Tang, Y. Zhang, Q. Fang, S. Qiu, V. Valtchev, Expanding the Synthesis Field of High-Silica Zeolites, *Angew.Chem. Int. Ed.* 2020, 59,19576–19581. <https://doi.org/10.1002/anie.202007514>.
- [42] J.C. Jansen, Chapter 5A The preparation of oxide molecular sieves A. Synthesis of zeolites, in: H. van Bekkum, E.M. Flanigen, P.A. Jacobs, J.C. Jansen (Eds.), *Studies in Surface Science and Catalysis*, Elsevier, 2001: pp. 175–227. [https://doi.org/10.1016/S0167-2991\(01\)80246-9](https://doi.org/10.1016/S0167-2991(01)80246-9).
- [43] C.S. Cundy, P.A. Cox, The hydrothermal synthesis of zeolites: Precursors, intermediates and reaction mechanism, *Microporous and Mesoporous Materials*. 82 (2005) 1–78. <https://doi.org/10.1016/j.micromeso.2005.02.016>.
- [44] Z. Qin, L. Lakiss, L. Tosheva, J.-P. Gilson, A. Vicente, C. Fernandez, V. Valtchev, Comparative Study of Nano-ZSM-5 Catalysts Synthesized in OH<sup>-</sup> and F<sup>-</sup> Media, *Advanced Functional Materials*. 24 (2014) 257–264. <https://doi.org/10.1002/adfm.201301541>.
- [45] R.M. Barrer, Zeolites: Their Nucleation and Growth, in: M.L. Occelli, H.E. Robson (Eds.), *Zeolite Synthesis*, American Chemical Society, Washington, DC, 1989: pp. 11–27. <https://doi.org/10.1021/bk-1989-0398.ch002>.

- [46] P. Cubillas, M.W. Anderson, Synthesis Mechanism: Crystal Growth and Nucleation, in: J. Čejka, A. Corma, S. Zones (Eds.), *Zeolites and Catalysis*, Wiley-VCH Verlag GmbH & Co. KGaA, 2010: pp. 1–55. <https://doi.org/10.1002/9783527630295.ch1>.
- [47] Nucleation, growth, and seeding in zeolite synthesis, *Verified Syntheses of Zeolitic Materials*. (2001) 21–23. <https://doi.org/10.1016/B978-044450703-7/50100-9>.
- [48] B. Subotić, Influence of Autocatalytic Nucleation on Zeolite Crystallization Processes, in: *Zeolite Synthesis*, American Chemical Society, 1989: pp. 110–123. <https://doi.org/10.1021/bk-1989-0398.ch008>.
- [49] A. Katović, B. Subotić, I. Šmit, Lj.A. Despotović, M. Čurić, Role of Gel Aging in Zeolite Crystallization, in: *Zeolite Synthesis*, American Chemical Society, 1989: pp. 124–139. <https://doi.org/10.1021/bk-1989-0398.ch009>.
- [50] W. Kossel, Zur Energetik von Oberflächenvorgängen, *Annalen Der Physik*. 413 (1934) 457–480. <https://doi.org/10.1002/andp.19344130502>.
- [51] R. Szostak, Chapter 6 Secondary synthesis methods, in: H. van Bekkum, E.M. Flanigen, P.A. Jacobs, J.C. Jansen (Eds.), *Studies in Surface Science and Catalysis*, Elsevier, 2001: pp. 261–297. [https://doi.org/10.1016/S0167-2991\(01\)80248-2](https://doi.org/10.1016/S0167-2991(01)80248-2).
- [52] R. Szostak, Chapter 5 Modified Zeolites, in: H. van Bekkum, E.M. Flanigen, J.C. Jansen (Eds.), *Studies in Surface Science and Catalysis*, Elsevier, 1991: pp. 153–199. [https://doi.org/10.1016/S0167-2991\(08\)63603-4](https://doi.org/10.1016/S0167-2991(08)63603-4).
- [53] V. Valtchev, S. Mintova, Hierarchical zeolites, *MRS Bulletin*. 41 (2016) 689–693. <https://doi.org/10.1557/mrs.2016.171>.
- [54] V. Valtchev, G. Majano, S. Mintova, J. Pérez-Ramírez, Tailored crystalline microporous materials by post-synthesis modification, *Chem. Soc. Rev.* 42 (2012) 263–290. <https://doi.org/10.1039/C2CS35196J>.
- [55] D. Kerstens, B. Smeyers, J.V. Waeyenberg, Q. Zhang, J. Yu, B.F. Sels, State of the Art and Perspectives of Hierarchical Zeolites: Practical Overview of Synthesis Methods and Use in Catalysis, *Adv. Mater.* (2020) 2004690. <https://doi.org/10.1002/adma.202004690>.
- [56] A. Feliczak-Guzik, Hierarchical zeolites: Synthesis and catalytic properties, *Microporous and Mesoporous Materials*. 259 (2018) 33–45. <https://doi.org/10.1016/j.micromeso.2017.09.030>.
- [57] T. Ennaert, J.V. Aelst, J. Dijkmans, R.D. Clercq, W. Schutyser, M. Dusselier, D. Verboekend, B.F. Sels, Potential and challenges of zeolite chemistry in the catalytic conversion of biomass, *Chem. Soc. Rev.* 45 (2016) 584–611. <https://doi.org/10.1039/C5CS00859J>.
- [58] X.-Y. Yang, L.-H. Chen, Y. Li, J.C. Rooke, C. Sanchez, B.-L. Su, Hierarchically porous materials: synthesis strategies and structure design, *Chem. Soc. Rev.* 46 (2017) 481–558. <https://doi.org/10.1039/C6CS00829A>.
- [59] W. Schwieger, A.G. Machoke, B. Reiprich, T. Weissenberger, T. Selvam, M. Hartmann, Chapter 4: Hierarchical Zeolites, in: *Zeolites in Catalysis*, 2017: pp. 103–145. <https://doi.org/10.1039/9781788010610-00103>.
- [60] K. Möller, T. Bein, Mesoporosity – a new dimension for zeolites, *Chem. Soc. Rev.* 42 (2013) 3689–3707. <https://doi.org/10.1039/C3CS35488A>.
- [61] S. Mitchell, A.B. Pinar, J. Kenvin, P. Crivelli, J. Kärger, J. Pérez-Ramírez, Structural analysis of hierarchically organized zeolites, *Nature Communications*. 6 (2015) 8633. <https://doi.org/10.1038/ncomms9633>.
- [62] A. Corma, M.J. Díaz-Cabañas, J. Martínez-Triguero, F. Rey, J. Rius, A large-cavity zeolite with wide pore windows and potential as an oil refining catalyst, *Nature*. 418 (2002) 514–517. <https://doi.org/10.1038/nature00924>.
- [63] C.T. Kresge, W.J. Roth, The discovery of mesoporous molecular sieves from the twenty year perspective, *Chem. Soc. Rev.* 42 (2013) 3663–3670. <https://doi.org/10.1039/C3CS60016E>.
- [64] M. Dusselier, M.E. Davis, Small-Pore Zeolites: Synthesis and Catalysis, *Chem. Rev.* 118 (2018) 5265–5329. <https://doi.org/10.1021/acs.chemrev.7b00738>.
- [65] X. Jia, W. Khan, Z. Wu, J. Choi, A.C.K. Yip, Modern synthesis strategies for hierarchical zeolites: Bottom-up versus top-down strategies, *Advanced Powder Technology*. 30 (2019) 467–484. <https://doi.org/10.1016/j.apt.2018.12.014>.
- [66] R. Chal, C. Gérardin, M. Bulut, S. van Donk, Overview and Industrial Assessment of Synthesis Strategies towards Zeolites with Mesopores, *ChemCatChem*. 3 (2011) 67–81. <https://doi.org/10.1002/cctc.201000158>.
- [67] K. Zhang, M.L. Ostraat, Innovations in hierarchical zeolite synthesis, *Catalysis Today*. 264 (2016) 3–15. <https://doi.org/10.1016/j.cattod.2015.08.012>.
- [68] A. Petushkov, S. Yoon, S.C. Larsen, Synthesis of hierarchical nanocrystalline ZSM-5 with controlled particle size and mesoporosity, *Microporous and Mesoporous Materials*. 137 (2011) 92–100. <https://doi.org/10.1016/j.micromeso.2010.09.001>.

- [69] S. van Donk, A.H. Janssen, J.H. Bitter, K.P. de Jong, Generation, Characterization, and Impact of Mesopores in Zeolite Catalysts, *Catalysis Reviews*. 45 (2003) 297–319. <https://doi.org/10.1081/CR-120023908>.
- [70] J.C. Groen, J.A. Moulijn, J. Pérez-Ramírez, Desilication: on the controlled generation of mesoporosity in MFI zeolites, *J. Mater. Chem.* 16 (2006) 2121–2131. <https://doi.org/10.1039/B517510K>.
- [71] S. Abelló, J. Pérez-Ramírez, Accelerated generation of intracrystalline mesoporosity in zeolites by microwave-mediated desilication, *Phys. Chem. Chem. Phys.* 11 (2009) 2959–2963. <https://doi.org/10.1039/B819543A>.
- [72] W.J. Roth, J. Čejka, Two-dimensional zeolites: dream or reality?, *Catal. Sci. Technol.* 1 (2011) 43–53. <https://doi.org/10.1039/CoCY00027B>.
- [73] C.C. Pavel, R. Palkovits, F. Schüth, W. Schmidt, The benefit of mesopores in ETS-10 on the vapor-phase Beckmann rearrangement of cyclohexanone oxime, *Journal of Catalysis*. 254 (2008) 84–90. <https://doi.org/10.1016/j.jcat.2007.11.020>.
- [74] D. Verboekend, J. Pérez-Ramírez, Design of hierarchical zeolite catalysts by desilication, *Catal. Sci. Technol.* 1 (2011) 879–890. <https://doi.org/10.1039/C1CY00150G>.
- [75] R.M. Barrer, M.B. Makki, Molecular Sieve Sorbents from Clinoptilolite, *Can. J. Chem.* 42 (1964) 1481–1487. <https://doi.org/10.1139/v64-223>.
- [76] H.K. Beyer, Dealumination Techniques for Zeolites, in: *Post-Synthesis Modification I*, Springer, Berlin, Heidelberg, 2002: pp. 203–255. [https://doi.org/10.1007/3-540-69750-0\\_3](https://doi.org/10.1007/3-540-69750-0_3).
- [77] R. Bai, Y. Song, Y. Li, J. Yu, Creating Hierarchical Pores in Zeolite Catalysts, *TRECHEM.* 1 (2019) 601–611. <https://doi.org/10.1016/j.trechm.2019.05.010>.
- [78] S. van Donk, J.H. Bitter, A. Verberckmoes, M. Versluijs-Helder, A. Broersma, K.P. de Jong, Physicochemical Characterization of Porous Materials: Spatially Resolved Accessibility of Zeolite Crystals, *Angewandte Chemie*. 117 (2005) 1384–1387. <https://doi.org/10.1002/ange.200460966>.
- [79] L.H. Ong, M. Dömök, R. Olindo, A.C. van Veen, J.A. Lercher, Dealumination of HZSM-5 via steam-treatment, *Microporous and Mesoporous Materials*. 164 (2012) 9–20. <https://doi.org/10.1016/j.micromeso.2012.07.033>.
- [80] A.H. Janssen, A.J. Koster, K.P. de Jong, Three-Dimensional Transmission Electron Microscopic Observations of Mesopores in Dealuminated Zeolite Y, *Angewandte Chemie International Edition*. 40 (2001) 1102–1104. [https://doi.org/10.1002/1521-3773\(20010316\)40:6<1102::AID-ANIE11020>3.0.CO;2-6](https://doi.org/10.1002/1521-3773(20010316)40:6<1102::AID-ANIE11020>3.0.CO;2-6).
- [81] J. Zečević, C.J. Gommès, H. Friedrich, P.E. de Jongh, K.P. de Jong, Mesoporosity of Zeolite Y: Quantitative Three-Dimensional Study by Image Analysis of Electron Tomograms, *Angewandte Chemie International Edition*. 51 (2012) 4213–4217. <https://doi.org/10.1002/anie.201200317>.
- [82] X. Fan, Y. Jiao, Chapter 5 - Porous Materials for Catalysis: Toward Sustainable Synthesis and Applications of Zeolites, in: G. Szekely, A. Livingston (Eds.), *Sustainable Nanoscale Engineering*, Elsevier, 2020: pp. 115–137. <https://doi.org/10.1016/B978-0-12-814681-1.00005-9>.
- [83] E. Koohsaryan, M. Anbia, Nanosized and hierarchical zeolites: A short review, *Chinese Journal of Catalysis*. 37 (2016) 447–467. [https://doi.org/10.1016/S1872-2067\(15\)61038-5](https://doi.org/10.1016/S1872-2067(15)61038-5).
- [84] J.C. Groen, T. Bach, U. Ziese, A.M. Paulaime-van Donk, K.P. de Jong, J.A. Moulijn, J. Pérez-Ramírez, Creation of Hollow Zeolite Architectures by Controlled Desilication of Al-Zoned ZSM-5 Crystals, *J. Am. Chem. Soc.* 127 (2005) 10792–10793. <https://doi.org/10.1021/ja052592x>.
- [85] Y.D. Arthur, Hydrocarbon conversion process and catalyst comprising a crystalline alumino-silicate leached with sodium hydroxide, US3326797A, 1967.
- [86] Structural evolution of dealuminated Y zeolites during various chemical treatments, *Zeolites*. 8 (1988) 517–522. [https://doi.org/10.1016/S0144-2449\(88\)80229-X](https://doi.org/10.1016/S0144-2449(88)80229-X).
- [87] J.C. Groen, J.C. Jansen, J.A. Moulijn, J. Pérez-Ramírez, Optimal Aluminum-Assisted Mesoporosity Development in MFI Zeolites by Desilication, *J. Phys. Chem. B*. 108 (2004) 13062–13065. <https://doi.org/10.1021/jp047194f>.
- [88] J.C. Groen, L.A.A. Peffer, J.A. Moulijn, J. Pérez-Ramírez, On the introduction of intracrystalline mesoporosity in zeolites upon desilication in alkaline medium, *Microporous and Mesoporous Materials*. 69 (2004) 29–34. <https://doi.org/10.1016/j.micromeso.2004.01.002>.
- [89] J.C. Groen, L.A.A. Peffer, J.A. Moulijn, J. Pérez-Ramírez, Mechanism of Hierarchical Porosity Development in MFI Zeolites by Desilication: The Role of Aluminium as a Pore-Directing Agent, *Chemistry – A European Journal*. 11 (2005) 4983–4994. <https://doi.org/10.1002/chem.200500045>.

- [90] J.C. Groen, W. Zhu, S. Brouwer, S.J. Huynink, F. Kapteijn, J.A. Moulijn, J. Pérez-Ramírez, Direct Demonstration of Enhanced Diffusion in Mesoporous ZSM-5 Zeolite Obtained via Controlled Desilication, *J. Am. Chem. Soc.* 129 (2007) 355–360. <https://doi.org/10.1021/ja0657370>.
- [91] Dissolution of high-silica zeolites in alkaline solutions II. Dissolution of ‘activated’ silicalite-1 and ZSM-5 with different aluminum content, *Microporous Materials*. 8 (1997) 159–169. [https://doi.org/10.1016/S0927-6513\(96\)00082-X](https://doi.org/10.1016/S0927-6513(96)00082-X).
- [92] D. Verboekend, T.C. Keller, M. Milina, R. Hauert, J. Pérez-Ramírez, Hierarchy Brings Function: Mesoporous Clinoptilolite and L Zeolite Catalysts Synthesized by Tandem Acid–Base Treatments, *Chem. Mater.* 25 (2013) 1947–1959. <https://doi.org/10.1021/cm4006103>.
- [93] J.C. Groen, J.A. Moulijn, J. Pérez-Ramírez, Decoupling mesoporosity formation and acidity modification in ZSM-5 zeolites by sequential desilication–dealumination, *Microporous and Mesoporous Materials*. 87 (2005) 153–161. <https://doi.org/10.1016/j.micromeso.2005.07.050>.
- [94] C. Dai, A. Zhang, M. Liu, X. Guo, C. Song, Hollow ZSM-5 with Silicon-Rich Surface, Double Shells, and Functionalized Interior with Metallic Nanoparticles and Carbon Nanotubes, *Advanced Functional Materials*. 25 (2015) 7479–7487. <https://doi.org/10.1002/adfm.201502980>.
- [95] Z. Qin, L. Lakiss, J.-P. Gilson, K. Thomas, J.-M. Goupil, C. Fernandez, V. Valtchev, Chemical Equilibrium Controlled Etching of MFI-Type Zeolite and Its Influence on Zeolite Structure, Acidity, and Catalytic Activity, *Chem. Mater.* 25 (2013) 2759–2766. <https://doi.org/10.1021/cm400719z>.
- [96] E.M. Flanigen, R.L. Patton, Silica polymorph and process for preparing same, US4073865A, 1978. <https://patents.google.com/patent/US4073865A/en> (accessed April 29, 2019).
- [97] H. Kessler, Chapter 3 - Synthesis of high-silica zeolites and phosphate-based materials in the presence of fluoride, in: H. Robson, K.P. Lillerud (Eds.), *Verified Syntheses of Zeolitic Materials*, Elsevier Science, Amsterdam, 2001: pp. 25–26. <https://doi.org/10.1016/B978-044450703-7/50101-0>.
- [98] S.I. Zones, S.-J. Hwang, S. Elomari, I. Ogino, M.E. Davis, A.W. Burton, The fluoride-based route to all-silica molecular sieves; a strategy for synthesis of new materials based upon close-packing of guest–host products, *Comptes Rendus Chimie*. 8 (2005) 267–282. <https://doi.org/10.1016/j.crci.2004.12.009>.
- [99] A.K. Ghosh, R.A. Kydd, Fluorine-Promoted Catalysts, *Catalysis Reviews*. 27 (1985) 539–589. <https://doi.org/10.1080/01614948508064233>.
- [100] R.L.V. Mao, T.S. Le, M. Fairbairn, A. Muntasar, S. Xiao, G. Denes, ZSM-5 zeolite with enhanced acidic properties, *Applied Catalysis A: General*. 185 (1999) 41–52. [https://doi.org/10.1016/S0926-860X\(99\)00132-5](https://doi.org/10.1016/S0926-860X(99)00132-5).
- [101] K.A. Becker, S. Kowalak, Catalytic properties of H mordenite modified with fluorine, *J. Chem. Soc., Faraday Trans. 1*. 81 (1985) 1161–1166. <https://doi.org/10.1039/F19858101161>.
- [102] R.B. Borade, A. Clearfield, Effect of fluoride ions on the acidic and catalytic properties of beta zeolite, *J. Chem. Soc., Faraday Trans.* 91 (1995) 539–547. <https://doi.org/10.1039/FT9959100539>.
- [103] T. Xu, H. Liu, Q. Zhao, S. Cen, L. Du, Q. Tang, Conversion of chloromethane to propylene over fluoride-treated H-ZSM-35 zeolite catalysts, *Catalysis Communications*. 119 (2019) 96–100. <https://doi.org/10.1016/j.catcom.2018.10.029>.
- [104] N.A. Sánchez, J.M. Saniger, J.-B. d’Espinoze de la Caillerie, A.L. Blumenfeld, J.J. Fripiat, Reaction of HY Zeolite with Molecular Fluorine, *Journal of Catalysis*. 201 (2001) 80–88. <https://doi.org/10.1006/jcat.2001.3226>.
- [105] B.M. Lok, F.P. Gortsema, C.A. Messina, H. Rastelli, T.P.J. Izod, Zeolite Modification—Direct Fluorination, in: *Intrazeolite Chemistry*, American Chemical Society, 1983: pp. 41–58. <https://doi.org/10.1021/bk-1983-0218.ch003>.
- [106] D.M. Knotter, The Chemistry of Wet Etching, in: *Handbook of Cleaning in Semiconductor Manufacturing*, John Wiley & Sons, Ltd, 2011: pp. 95–141. <https://doi.org/10.1002/9781118071748.ch3>.
- [107] J.R. Partington, Chemistry in Scandinavia. II. Scheele, in: J.R. Partington (Ed.), *A History of Chemistry: Volume Three*, Macmillan Education UK, London, 1962: pp. 205–236. [https://doi.org/10.1007/978-1-349-00309-9\\_6](https://doi.org/10.1007/978-1-349-00309-9_6).
- [108] P. Walker, W.H. Tarn, *CRC Handbook of Metal Etchants*, CRC Press, 1990.
- [109] A. Ghosh, R.A. Kydd, Acidity and activity of fluorinated mordenites, *Journal of Catalysis*. 103 (1987) 399–406. [https://doi.org/10.1016/0021-9517\(87\)90131-X](https://doi.org/10.1016/0021-9517(87)90131-X).
- [110] J. Wloch, Effect of surface etching of ZSM-5 zeolite crystals on the rate of n-hexane sorption, *Microporous and Mesoporous Materials*. 62 (2003) 81–86. [https://doi.org/10.1016/S1387-1811\(03\)00395-0](https://doi.org/10.1016/S1387-1811(03)00395-0).

- [111] J. Wloch, Diffusion of n-hexane into the etched ZSM-5 crystals, *Studies in Surface Science and Catalysis*. 154 (2004) 2049–2055. [https://doi.org/10.1016/S0167-2991\(04\)80745-6](https://doi.org/10.1016/S0167-2991(04)80745-6).
- [112] F. Meng, Y. Wang, S. Wang, Methanol to gasoline over zeolite ZSM-5: improved catalyst performance by treatment with HF, *RSC Adv.* 6 (2016) 58586–58593. <https://doi.org/10.1039/C6RA14513B>.
- [113] F. Meng, X. Wang, S. Wang, Y. Wang, Fluoride-treated HZSM-5 as a highly stable catalyst for the reaction of methanol to gasoline, *Catalysis Today*. 298 (2017) 226–233. <https://doi.org/10.1016/j.cattod.2017.04.019>.
- [114] Y. Li, H. Zheng, Y. Yun, D. Bernin, M. Edén, X. Zou, F. Gao, De-agglomeration of IZM-2 zeolite crystals by post-synthetic treatment, *Microporous and Mesoporous Materials*. 225 (2016) 185–191. <https://doi.org/10.1016/j.micromeso.2015.12.021>.
- [115] Z. Qin, G. Melinte, J.-P. Gilson, M. Jaber, K. Bozhilov, P. Boullay, S. Mintova, O. Ersen, V. Valtchev, The Mosaic Structure of Zeolite Crystals, *Angewandte Chemie*. 128 (2016) 15273–15276. <https://doi.org/10.1002/ange.201608417>.
- [116] F.C. Meunier, D. Verboekend, J.-P. Gilson, J.C. Groen, J. Pérez-Ramírez, Influence of crystal size and probe molecule on diffusion in hierarchical ZSM-5 zeolites prepared by desilication, *Microporous and Mesoporous Materials*. 148 (2012) 115–121. <https://doi.org/10.1016/j.micromeso.2011.08.002>.
- [117] K.W. Kolasinski, The Composition of Fluoride Solutions, *J. Electrochem. Soc.* 152 (2005) J99–J104. <https://doi.org/10.1149/1.1952787>.
- [118] J.H. Simons, Hydrogen Fluoride and its Solutions., *Chem. Rev.* 8 (1931) 213–235. <https://doi.org/10.1021/cr60030a004>.
- [119] D.M. Knotter, Etching Mechanism of Vitreous Silicon Dioxide in HF-Based Solutions, *J. Am. Chem. Soc.* 122 (2000) 4345–4351. <https://doi.org/10.1021/ja993803z>.
- [120] P. Mctigue, T. Odonnell, B. Verity, The Determination of Fluoride-Ion Activities in Moderately Concentrated Aqueous Hydrogen-Fluoride, *Aust. J. Chem.* 38 (1985) 1797. <https://doi.org/10.1071/CH9851797>.
- [121] H.N. Farrer, F.J.C. Rossotti, Proton-fluoride association in sodium perchlorate media, *Journal of Inorganic and Nuclear Chemistry*. 26 (1964) 1959–1965. [https://doi.org/10.1016/0022-1902\(64\)80020-8](https://doi.org/10.1016/0022-1902(64)80020-8).
- [122] G.A.C.M. Spierings, Wet chemical etching of silicate glasses in hydrofluoric acid based solutions, *J Mater Sci.* 28 (1993) 6261–6273. <https://doi.org/10.1007/BF01352182>.
- [123] J.S. Judge, A Study of the Dissolution of SiO<sub>2</sub> in Acidic Fluoride Solutions, *J. Electrochem. Soc.* 118 (1971) 1772–1775. <https://doi.org/10.1149/1.2407835>.
- [124] K. Osseo-Asare, Etching Kinetics of Silicon Dioxide in Aqueous Fluoride Solutions: A Surface Complexation Model, *J. Electrochem. Soc.* 143 (1996) 1339. <https://doi.org/10.1149/1.1836640>.
- [125] H. Proksche, G. Nagorsen, D. Ross, The Influence of NH<sub>4</sub>F on the Etch Rates of Undoped SiO<sub>2</sub> in Buffered Oxide Etch, *J. Electrochem. Soc.* 139 (1992) 521. <https://doi.org/10.1149/1.2069249>.
- [126] H. Kikuyama, M. Waki, I. Kawanabe, M. Miyashita, T. Yabune, N. Miki, J. Takano, T. Ohmi, Etching Rate and Mechanism of Doped Oxide in Buffered Hydrogen Fluoride Solution, *J. Electrochem. Soc.* 139 (1992) 2239. <https://doi.org/10.1149/1.2221208>.
- [127] W.E. Kline, H.S. Fogler, Dissolution of silicate minerals by hydrofluoric acid, *Ind. Eng. Chem. Fund.* 20 (1981) 155–161. <https://doi.org/10.1021/i100002a008>.
- [128] W.E. Kline, H.S. Fogler, Dissolution kinetics: Catalysis by strong acids, *Journal of Colloid and Interface Science*. 82 (1981) 93–102. [https://doi.org/10.1016/0021-9797\(81\)90127-2](https://doi.org/10.1016/0021-9797(81)90127-2).
- [129] S.T. Tso, J.A. Pask, Reaction of Glasses with Hydrofluoric Acid Solution, *Journal of the American Ceramic Society*. 65 (1982) 360–362. <https://doi.org/10.1111/j.1151-2916.1982.tb10471.x>.
- [130] J.R. Schlup, R.W. Vaughan, Nuclear magnetic resonance investigation of fluorinated oxide catalysts: II. Fluorinated alumina and aluminosilicates, *Journal of Catalysis*. 99 (1986) 304–315. [https://doi.org/10.1016/0021-9517\(86\)90355-6](https://doi.org/10.1016/0021-9517(86)90355-6).
- [131] F. Ngoye, L. Lakiss, Z. Qin, S. Laforge, C. Canaff, M. Tarighi, V. Valtchev, K. Thomas, A. Vicente, J.P. Gilson, Y. Pouilloux, C. Fernandez, L. Pinard, Mitigating coking during methylcyclohexane transformation on HZSM-5 zeolites with additional porosity, *Journal of Catalysis*. 320 (2014) 118–126. <https://doi.org/10.1016/j.jcat.2014.10.001>.
- [132] Y. Ji, H. Yang, W. Yan, Catalytic cracking of n-hexane to light alkene over ZSM-5 zeolite: Influence of hierarchical porosity and acid property, *Molecular Catalysis*. 448 (2018) 91–99. <https://doi.org/10.1016/j.mcat.2018.01.027>.

- [133] V. Valtchev, J.-P. Gilson, Z. Qin, Method for the preparation of synthetic crystalline zeolite materials with enhanced total pore volume, WO2016005783 A1, 2016.
- [134] L. Lakiss, F. Ngoye, C. Canaff, S. Laforge, Y. Pouilloux, Z. Qin, M. Tarighi, K. Thomas, V. Valtchev, A. Vicente, L. Pinard, J.-P. Gilson, C. Fernandez, On the remarkable resistance to coke formation of nanometer-sized and hierarchical MFI zeolites during ethanol to hydrocarbons transformation, *Journal of Catalysis*. 328 (2015) 165–172. <https://doi.org/10.1016/j.jcat.2014.12.030>.
- [135] Z. Qin, L. Pinard, M.A. Benghalem, T.J. Daou, G. Melinte, O. Ersen, S. Asahina, J.-P. Gilson, V. Valtchev, Preparation of Single-Crystal “House-of-Cards”-like ZSM-5 and Their Performance in Ethanol-to-Hydrocarbon Conversion, *Chem. Mater.* 31 (2019) 4639–4648. <https://doi.org/10.1021/acs.chemmater.8b04970>.
- [136] Z. Qin, L. Hafiz, Y. Shen, S.V. Daele, P. Boullay, V. Ruaux, S. Mintova, J.-P. Gilson, V. Valtchev, Defect-engineered zeolite porosity and accessibility, *J. Mater. Chem. A*. 8 (2020) 3621–3631. <https://doi.org/10.1039/C9TA11465C>.
- [137] X. Liu, U. Ravon, A. Tuel, Evidence for F<sup>-</sup>/SiO<sup>-</sup> Anion Exchange in the Framework of As-Synthesized All-Silica Zeolites, *Angewandte Chemie International Edition*. 50 (2011) 5900–5903. <https://doi.org/10.1002/anie.201101237>.
- [138] SOD: Framework Type, (n.d.). <http://europa.iza-structure.org/IZA-SC/framework.php?STC=SOD>.
- [139] Z. Qin, K.A. Cychoz, G. Melinte, H. El Siblani, J.-P. Gilson, M. Thommes, C. Fernandez, S. Mintova, O. Ersen, V. Valtchev, Opening the Cages of Faujasite-Type Zeolite, *J. Am. Chem. Soc.* 139 (2017) 17273–17276. <https://doi.org/10.1021/jacs.7b10316>.
- [140] A. Feng, Y. Yu, L. Mi, Y. Cao, Y. Yu, L. Song, Synthesis and characterization of hierarchical Y zeolites using NH<sub>4</sub>HF<sub>2</sub> as dealumination agent, *Microporous and Mesoporous Materials*. (2019). <https://doi.org/10.1016/j.micromeso.2019.01.039>.
- [141] A. Feng, Y. Yu, L. Mi, Y. Cao, Y. Yu, L. Song, Structural, textural and toluene adsorption properties of NH<sub>4</sub>HF<sub>2</sub> and alkali modified USY zeolite, *Microporous and Mesoporous Materials*. 290 (2019) 109646. <https://doi.org/10.1016/j.micromeso.2019.109646>.
- [142] A. Feng, L. Mi, Y. Yu, Y. Cao, Y. Yu, L. Song, Development of intracrystalline mesoporosity in NH<sub>4</sub>HF<sub>2</sub>-etched NaY zeolites by surfactant-templating and its effect on toluene adsorption, *Chemical Engineering Journal*. 390 (2020) 124529. <https://doi.org/10.1016/j.cej.2020.124529>.
- [143] K.-G. Haw, S. Moldovan, L. Tang, Z. Qin, Q. Fang, S. Qiu, V. Valtchev, A sponge-like small pore zeolite with great accessibility to its micropores, *Inorg. Chem. Front.* 7 (2020) 2154–2159. <https://doi.org/10.1039/DoQ100261E>.
- [144] J. Liu, N. Ding, X. Hong, S. Zhou, X. Zhou, J.A. Wang, L. Chen, Isobutane/1-butene Alkylation Performance of Ammonium Fluoride-Modified HUSY Zeolite, *Catal Lett.* (2020). <https://doi.org/10.1007/s10562-020-03187-y>.
- [145] S. Liu, Z. Cheng, Y. Li, J. Sun, K. Cai, S. Huang, J. Lv, S. Wang, X. Ma, Improved Catalytic Performance in Dimethyl Ether Carbonylation over Hierarchical Mordenite by Enhancing Mass Transfer, *Ind. Eng. Chem. Res.* 59 (2020) 13861–13869. <https://doi.org/10.1021/acs.iecr.0c01156>.
- [146] J. Tekla, L. Lakiss, V. Valtchev, K.A. Tarach, M. Jabłońska, V. Girman, A. Szymocha, A. Kowalczyk, K. Góra-Marek, J.-P. Gilson, Increasing the catalytic performance of erionite by hierarchization, *Microporous and Mesoporous Materials*. 299 (2020) 110088. <https://doi.org/10.1016/j.micromeso.2020.110088>.
- [147] T. Todorova, P. Shestakova, T. Petrova, M. Popova, H. Lazarova, Y. Kalvachev, Fluoride etching of AlZSM-5 and GaZSM-5 zeolites, *J Mater Sci.* 55 (2020) 13799–13814. <https://doi.org/10.1007/s10853-020-05030-6>.
- [148] A. Bolshakov, N. Kosinov, D.E.R. Hidalgo, B. Mezari, A.J.F. van Hoof, E.J.M. Hensen, Mild dealumination of template-stabilized zeolites by NH<sub>4</sub>F, *Catal. Sci. Technol.* 9 (2019) 4239–4247. <https://doi.org/10.1039/C9CY00593E>.
- [149] E. Janiszewska, J. Kowalska-Kuś, K. Góra-Marek, A. Szymocha, K. Nowińska, S. Kowalak, Modification of silicalite-1 with ammonium compounds aimed at preparation of acidic catalyst for acetalization of glycerol with acetone, *Applied Catalysis A: General*. 581 (2019) 1–10. <https://doi.org/10.1016/j.apcata.2019.05.012>.
- [150] J. Přeč, K.N. Bozhilov, J. El Fallah, N. Barrier, V. Valtchev, Fluoride etching opens the structure and strengthens the active sites of the layered ZSM-5 zeolite, *Microporous and Mesoporous Materials*. 280 (2019) 297–305. <https://doi.org/10.1016/j.micromeso.2019.02.023>.
- [151] S. Ren, B. Meng, X. Sui, H. Duan, X. Gao, H. Zhang, P. Zeng, Q. Guo, B. Shen, Preparation of Mesoporous Zeolite Y by Fluorine-alkaline Treatment for Hydrocracking Reaction of Naphthalene, *Ind. Eng. Chem. Res.* (2019). <https://doi.org/10.1021/acs.iecr.9b00422>.

- [152] N. Suárez, J. Pérez-Pariente, C. Márquez-Álvarez, M. Grande Casas, A. Mayoral, A. Moreno, Preparation of mesoporous Beta zeolite by fluoride treatment in liquid phase. Textural, acid and catalytic properties, *Microporous and Mesoporous Materials*. 284 (2019) 296–303. <https://doi.org/10.1016/j.micromeso.2019.04.049>.
- [153] Y. Kalvachev, T. Todorova, D. Nihtianova, H. Lazarova, M. Popova, Fluoride etching of mordenite and its influence on catalytic activity, *J Mater Sci*. 52 (2017) 5297–5308. <https://doi.org/10.1007/s10853-017-0769-3>.
- [154] M. Popova, H. Lazarova, Y. Kalvachev, T. Todorova, Á. Szegedi, P. Shestakova, G. Mali, V.D.B.C. Dasireddy, B. Likozar, Zr-modified hierarchical mordenite as heterogeneous catalyst for glycerol esterification, *Catalysis Communications*. 100 (2017) 10–14. <https://doi.org/10.1016/j.catcom.2017.06.009>.
- [155] X. Chen, D. Xi, Q. Sun, N. Wang, Z. Dai, D. Fan, V. Valtchev, J. Yu, A top-down approach to hierarchical SAPO-34 zeolites with improved selectivity of olefin, *Microporous and Mesoporous Materials*. 234 (2016) 401–408. <https://doi.org/10.1016/j.micromeso.2016.07.045>.
- [156] X. Chen, A. Vicente, Z. Qin, V. Ruaux, J.-P. Gilson, V. Valtchev, The preparation of hierarchical SAPO-34 crystals via post-synthesis fluoride etching, *Chem. Commun*. 52 (2016) 3512–3515. <https://doi.org/10.1039/C5CC09498D>.
- [157] S. Du, X. Chen, Q. Sun, N. Wang, M. Jia, V. Valtchev, J. Yu, A non-chemically selective top-down approach towards the preparation of hierarchical TS-1 zeolites with improved oxidative desulfurization catalytic performance, *Chem. Commun*. 52 (2016) 3580–3583. <https://doi.org/10.1039/C5CC10232D>.
- [158] K. Guesh, C. Márquez-Álvarez, Y. Chebude, I. Díaz, Enhanced photocatalytic activity of supported TiO<sub>2</sub> by selective surface modification of zeolite Y, *Applied Surface Science*. 378 (2016) 473–478. <https://doi.org/10.1016/j.apsusc.2016.04.029>.
- [159] M. Li, Y. Zhou, C. Ju, Y. Fang, Remarkable increasing of ZSM-5 lifetime in methanol to hydrocarbon reaction by post engineering in fluoride media, *Applied Catalysis A: General*. 512 (2016) 1–8. <https://doi.org/10.1016/j.apcata.2015.12.001>.
- [160] T. Todorova, Y. Kalvachev, H. Lazarova, M. Popova, Catalytic activity of modified mordenite in the reaction of m-xylene transformation, *Comptes Rendus de l'Académie Bulgare Des Sciences*. 69 (2016) 1283–1291.
- [161] C. Hammond, G. Tarantino, Switching off H<sub>2</sub>O<sub>2</sub> Decomposition during TS-1 Catalysed Epoxidation via Post-Synthetic Active Site Modification, *Catalysts*. 5 (2015) 2309–2323. <https://doi.org/10.3390/catal5042309>.
- [162] M. Li, Y. Zhou, I.N. Oduro, Y. Fang, Comparative study on the catalytic conversion of methanol and propanal over Ga/ZSM-5, *Fuel*. 168 (2016) 68–75. <https://doi.org/10.1016/j.fuel.2015.11.076>.
- [163] X. Chen, T. Todorova, A. Vimont, V. Ruaux, Z. Qin, J.-P. Gilson, V. Valtchev, In situ and post-synthesis control of physicochemical properties of FER-type crystals, *Microporous and Mesoporous Materials*. 200 (2014) 334–342. <https://doi.org/10.1016/j.micromeso.2014.07.057>.
- [164] L. Burel, A. Tuel, Nanozeolites: New strategies for designing ultra small silicalite crystals with very few framework defects, *Microporous and Mesoporous Materials*. 174 (2013) 90–99. <https://doi.org/10.1016/j.micromeso.2013.02.033>.
- [165] Z. Tang, P. Zhang, W. Han, G. Lu, J. Lu, Butene catalytic cracking to ethylene and propylene on fluorinated ZSM-5-based catalyst, *Reac Kinet Mech Cat*. 108 (2013) 231–239. <https://doi.org/10.1007/s11144-012-0512-7>.
- [166] K. Na, C. Jo, J. Kim, W.-S. Ahn, R. Ryoo, MFI Titanosilicate Nanosheets with Single-Unit-Cell Thickness as an Oxidation Catalyst Using Peroxides, *ACS Catal*. 1 (2011) 901–907. <https://doi.org/10.1021/cs2002143>.
- [167] X. Feng, G. Jiang, Z. Zhao, L. Wang, X. Li, A. Duan, J. Liu, C. Xu, J. Gao, Highly Effective F-Modified HZSM-5 Catalysts for the Cracking of Naphtha To Produce Light Olefins, *Energy Fuels*. 24 (2010) 4111–4115. <https://doi.org/10.1021/ef100392d>.
- [168] F. Collins, A. Rozhkovskaya, J.G. Outram, G.J. Millar, A critical review of waste resources, synthesis, and applications for Zeolite LTA, *Microporous and Mesoporous Materials*. 291 (2020) 109667. <https://doi.org/10.1016/j.micromeso.2019.109667>.
- [169] L. Bacakova, M. Vandrovцова, I. Kopova, I. Jirka, Applications of zeolites in biotechnology and medicine – a review, *Biomater. Sci*. 6 (2018) 974–989. <https://doi.org/10.1039/C8BM00028J>.
- [170] G. Delahay, B. Coq, Pollution abatement using zeolites: state of the art and further needs, in: *Zeolites for Cleaner Technologies*, Published by Imperial College Press and distributed by World Scientific Publishing Co., 2002: pp. 345–374. [https://doi.org/10.1142/9781860949555\\_0016](https://doi.org/10.1142/9781860949555_0016).
- [171] F. Blatter, H. Sun, S. Vasenkov, H. Frei, Photocatalyzed oxidation in zeolite cages, *Catalysis Today*. 41 (1998) 297–309. [https://doi.org/10.1016/S0920-5861\(98\)00021-2](https://doi.org/10.1016/S0920-5861(98)00021-2).

- [172] J. Weitkamp, M. Fritz, S. Ernst, Zeolites as media for hydrogen storage, in: R. von Ballmoos, J.B. Higgins, M.M.J. Treacy (Eds.), *Proceedings from the Ninth International Zeolite Conference*, Butterworth-Heinemann, 1993: pp. 11–19. [https://doi.org/10.1016/B978-1-4832-8383-8\\_50086-6](https://doi.org/10.1016/B978-1-4832-8383-8_50086-6).
- [173] S.F. Abdo, S.T. Wilson, Chapter 9: Zeolites in Industrial Catalysis, in: *Zeolites in Catalysis*, 2017: pp. 310–350. <https://doi.org/10.1039/9781788010610-00310>.
- [174] W. Vermeiren, J.-P. Gilson, Impact of Zeolites on the Petroleum and Petrochemical Industry, *Top Catal.* 52 (2009) 1131–1161. <https://doi.org/10.1007/s11244-009-9271-8>.
- [175] J.Q. Chen, A. Bozzano, B. Glover, T. Fuglerud, S. Kvisle, Recent advancements in ethylene and propylene production using the UOP/Hydro MTO process, *Catalysis Today*. 106 (2005) 103–107. <https://doi.org/10.1016/j.cattod.2005.07.178>.
- [176] F. Di Renzo, F. Fajula, Introduction to molecular sieves: trends of evolution of the zeolite community, in: J. Čejka, H. van Bekkum (Eds.), *Studies in Surface Science and Catalysis*, Elsevier, 2005: pp. 1–12. [https://doi.org/10.1016/S0167-2991\(05\)80003-5](https://doi.org/10.1016/S0167-2991(05)80003-5).
- [177] A. Martínez, M.A. Arribas, S. Moussa, Chapter 10: Application of Zeolites in the Production of Light Olefins and BTX Petrochemical Intermediates, in: *Zeolites in Catalysis*, 2017: pp. 351–408. <https://doi.org/10.1039/9781788010610-00351>.
- [178] M. Opanasenko, Chapter 11: Zeolites for Fine Chemistry, in: *Zeolites in Catalysis*, 2017: pp. 409–440. <https://doi.org/10.1039/9781788010610-00409>.
- [179] C.J. Rhodes, Properties and applications of Zeolites, *Science Progress*. 93 (2010) 223–284. <https://doi.org/10.3184/003685010X12800828155007>.
- [180] A.B. Lovins, ed., *Winning the Oil Endgame: Innovation for Profits, Jobs, and Security*, 1. ed, Rocky Mountain Inst, Snowmass, Colo, 2004.
- [181] D.P. Serrano, J.A. Melero, G. Morales, J. Iglesias, P. Pizarro, Progress in the design of zeolite catalysts for biomass conversion into biofuels and bio-based chemicals, *Catalysis Reviews*. 60 (2018) 1–70. <https://doi.org/10.1080/01614940.2017.1389109>.
- [182] D.P. Serrano, J.A. Melero, J.M. Coronado, P. Pizarro, G. Morales, Chapter 12: Biomass Conversion over Zeolite Catalysts, in: *Zeolites in Catalysis*, 2017: pp. 441–480. <https://doi.org/10.1039/9781788010610-00441>.
- [183] E. Kianfar, Comparison and assessment of zeolite catalysts performance dimethyl ether and light olefins production through methanol: a review, *Reviews in Inorganic Chemistry*. 39 (2019) 157–177. <https://doi.org/10.1515/revic-2019-0001>.
- [184] P.B. Weisz, V.J. Frilette, Intracrystalline and molecular-shape-selective catalysis by zeolite salts, *J. Phys. Chem.* 64 (1960) 382–382. <https://doi.org/10.1021/j100832a513>.
- [185] J. Datka, K. Tarach, K. Góra-Marek, Acidic Properties of Hierarchical Zeolites, in: *Mesoporous Zeolites*, John Wiley & Sons, Ltd, 2015: pp. 461–496. <https://doi.org/10.1002/9783527673957.ch14>.
- [186] M.S. Holm, E. Taarning, K. Egeblad, C.H. Christensen, Catalysis with hierarchical zeolites, *Catalysis Today*. 168 (2011) 3–16. <https://doi.org/10.1016/j.cattod.2011.01.007>.
- [187] D.P. Serrano, J. Aguado, J.M. Escola, Hierarchical zeolites: materials with improved accessibility and enhanced catalytic activity, in: *Catalysis*, Royal Society of Chemistry, Cambridge, 2011: pp. 253–283. <https://doi.org/10.1039/9781849732772-00253>.
- [188] M. Milina, S. Mitchell, P. Crivelli, D. Cooke, J. Pérez-Ramírez, Mesopore quality determines the lifetime of hierarchically structured zeolite catalysts, *Nat Commun.* 5 (2014) 3922. <https://doi.org/10.1038/ncomms4922>.



# 3

## Materials and methods

<b>1</b>	<b>POST-SYNTHETIC MODIFICATIONS .....</b>	<b>41</b>
1.1	ZEOLITE L FLUORIDE ETCHING .....	41
1.1.1	<i>Sample notation</i> .....	42
1.2	SSZ-13 FLUORIDE ETCHING.....	42
1.3	CHROMIC ACID ETCHING .....	43
1.3.1	<i>Sample notation</i> .....	44
1.4	CALCINATION .....	44
<b>2</b>	<b>CHARACTERIZATION TECHNIQUES.....</b>	<b>44</b>
2.1	X-RAY DIFFRACTION .....	44
2.2	TEXTURAL ANALYSIS BY N <sub>2</sub> PHYSISORPTION.....	46
2.3	THERMAL ANALYSIS BY THERMOGRAVIMETRY .....	48
2.4	CHEMICAL COMPOSITION BY ICP-AES.....	49
2.5	CRYSTAL MORPHOLOGY BY ELECTRON MICROSCOPY .....	49
2.5.1	<i>Scanning Electron Microscopy (SEM)</i> .....	49
2.5.2	<i>Transmission Electron Microscopy (TEM)</i> .....	49
2.5.3	<i>Energy Dispersive X-ray Spectroscopy (EDX)</i> .....	50
2.6	LOCAL STRUCTURE BY SOLID-STATE NUCLEAR MAGNETIC RESONANCE.....	50
2.6.1	<sup>27</sup> Al NMR spectroscopy.....	51
2.6.2	<sup>29</sup> Si NMR spectroscopy.....	51
2.7	ACIDITY CHARACTERIZATION BY FOURIER TRANSFORMED INFRARED SPECTROSCOPY .....	52
2.8	CATALYSIS.....	53
2.8.1	<i>Dealkylation of 1,3,5-triisopropylbenzene</i> .....	53
2.8.2	<i>Dehydration of n-propanol</i> .....	53
<b>3</b>	<b>REFERENCES .....</b>	<b>54</b>

# 1 Post-synthetic modifications

## 1.1 Zeolite L fluoride etching

Zeolite L sample ( $\text{Si}/\text{Al} = 3.0$ ) is purchased from *Tosoh* (Japan). The parent material is ion exchanged with a 0.5 M  $\text{NH}_4\text{Cl}$  solution at 60 °C for 3 h, and the procedure is repeated three times. The zeolite is then washed thoroughly with double distilled water and dried at 60 °C overnight. The sample is denoted as  $\text{NH}_4\text{-L}$  in chapter 4 and  $\text{NH}_4\text{-LTL}$  in chapter 6.

The post-synthetic etchings are performed as follows:

- I. 1 g of  $\text{NH}_4\text{-L}$  is dispersed in 20 g of 20 wt/% (weight percent)  $\text{NH}_4\text{F}$  at room temperature ( $T$ ) and stirred from 3 to 480 minutes. This series of samples is denoted L-I- $x$ , where  $x$  is the treatment time ( $t$ ) in minutes. Samples L-I-60-60, and L-I-60-80 are treated at 60 and 80 °C, respectively, for 60 min.
- II. 1 g of  $\text{NH}_4\text{-L}$  zeolite is dispersed in 20 g of 40 wt/%  $\text{NH}_4\text{F}$  at room temperature and stirred from 20 to 90 minutes. This series of samples is denoted L-II- $x$ , where  $x$  is the treatment time in minutes. Samples L-II-60-60, and L-II-60-80 are treated at 60 and 80 °C, respectively, for 60 min.
- III. 1 g of  $\text{NH}_4\text{-L}$  zeolite is dispersed in 20 g of 1 wt/%  $\text{NH}_4\text{HF}_2$  at room temperature and stirred from 5 to 180 minutes. This series of samples is denoted L-III- $x$ , where  $x$  is the treatment time in minutes. Samples L-III-60-60 and L-III-60-80 are treated at 60 and 80 °C, respectively, for 60 min.
- IV. 1 g of  $\text{NH}_4\text{-L}$  zeolite is dispersed in 20 g of 2 wt/%  $\text{NH}_4\text{HF}_2$  at room temperature and stirred from 2 to 60 minutes. This series of samples is denoted L-IV- $x$ , where  $x$  is the treatment time in minutes. Sample L-IV-60-60 is treated at 60 °C for 60 min.

All products are filtered, thoroughly washed with hot double distilled water, then dried at 60 °C overnight.

### 1.1.1 Sample notation

Sample	$c(\text{NH}_4\text{F})$ wt/%	$T$ °C	$t$ min
L-I-3	20	25	3
L-I-5	20	25	5
L-I-10	20	25	10
L-I-15	20	25	15
L-I-20	20	25	20
L-I-60	20	25	60
L-I-120	20	25	120
L-I-240	20	25	240
L-I-360	20	25	360
L-I-480	20	25	480
L-I-60-60	20	60	60
L-I-60-80	20	80	60
L-II-20	40	25	20
L-II-40	40	25	40
L-II-90	40	25	90
L-II-60-60	40	60	60
L-II-60-80	40	80	60
Sample	$c(\text{NH}_4\text{HF}_2)$ wt/%	$T$ °C	$t$ min
L-III-5	1	25	5
L-III-10	1	25	10
L-III-15	1	25	15
L-III-40	1	25	40
L-III-120	1	25	120
L-III-180	1	25	180
L-III-60-60	1	60	60
L-III-60-80	1	80	60
L-IV-2	2	25	2
L-IV-5	2	25	5
L-IV-10	2	25	10
L-IV-60	2	25	60
L-IV-60-60	2	60	60

## 1.2 SSZ-13 fluoride etching

$\text{NH}_4\text{-SSZ-13}$  is purchased from *ACS Materials* (USA). The  $\text{NH}_4\text{F}$  crystals are purchased from *Sigma Aldrich*, and solutions are freshly made prior to the treatment. The parent sample ( $\text{NH}_4\text{-SSZ-13}$ ) is etched with a 40 wt/% ammonium fluoride ( $\text{NH}_4\text{F}$ ) solution in a temperature-controlled bath. The effects of the following parameters are studied: liquid-solid ratio (l/s), temperature, and time.

After  $\text{NH}_4\text{F}$  etching, the solid is recovered by filtration on a cellulose membrane and washed thoroughly with hot water (heated to 90 °C) to remove all leftover products. Samples are dried overnight at 60 °C, carefully ground, and further analyzed.

The sample code employed is CHA-Liquid/Solid-Temperature-Time.

Series I: Liquid/Solid ratio of 8

1 g of  $\text{NH}_4\text{-SSZ-13}$  is mixed with 8 ml of 40 wt/%  $\text{NH}_4\text{F}$  at 0, 25, and 50 °C.

$T$ [°C]	$t$ [min]	
	5	20
0	CHA-8-0-5	CHA-8-0-20
25	CHA-8-25-5	CHA-8-25-20
50	CHA-8-50-5	CHA-8-50-20

Series II: Liquid/Solid ratio of 20

1 g of  $\text{NH}_4\text{-SSZ-13}$  is mixed with 20 ml of 40 wt/%  $\text{NH}_4\text{F}$  at 0, 25, and 50 °C.

$T$ [°C]	$t$ [min]	
	5	20
0	CHA-20-0-5	CHA-20-0-20
25	CHA-20-25-5	CHA-20-25-20
50	CHA-20-50-5	CHA-20-50-20

Series III: Liquid/Solid ratio of 100

1 g of  $\text{NH}_4\text{-SSZ-13}$  is mixed with 100 ml of 40 wt/%  $\text{NH}_4\text{F}$  at 0, 25, and 50 °C.

$T$ [°C]	$t$ [min]	
	5	20
0	CHA-100-0-5	CHA-100-0-20
25	CHA-100-25-5	CHA-100-25-20
50	CHA-100-50-5	CHA-100-50-20

### 1.3 Chromic acid etching

Industrial samples of LTL, SSZ-13, and MFI-55 (Sud Chemie) are subjected to chromic acid etching. The  $\text{CrO}_3$  crystals are purchased from VWR and solutions are made freshly beforehand of the treatment. The parent sample ( $\text{NH}_4\text{-LTL}$ ,  $\text{NH}_4\text{-CHA}$ , and  $\text{NH}_4\text{-MFI}$ ) is etched with 0.1–10 wt/% solutions of  $\text{CrO}_3$ . The etching reaction is made at room temperature with mild agitation. The liquid-solid ratio is 20 and duration 60 min for all reactions; except for sample LTL-0.1-30 which is treated for 30 minutes.

After the etching reaction, the solids were recovered by suction filtration and washed thoroughly with water. Samples are dried overnight at 60 °C, carefully ground, and further analyzed.

### 1.3.1 Sample notation

The parent zeolite is noted with the structure code, for instance, CHA (parent). The sample code employed of etched materials includes ZEOLITE TYPE-Concentration. For example, 1 g of NH<sub>4</sub>-SSZ-13 mixed with 0.1 wt/% CrO<sub>3</sub> at 25 °C for 60 minutes is noted as sample CHA-0.1. MFI- and LTL-type zeolite etched with chromic acid were coded similarly. The CrO<sub>3</sub> concentrations (wt/%) employed are 0.1, 0.5, 1, 2 and 10.

## 1.4 Calcination

LTL type and SSZ-13 type zeolites are calcined under static air, SSZ-13 are calcined for 6h in 550 °C and LTL are calcined at 550 °C for 4h.

## 2 Characterization techniques

### 2.1 X-ray diffraction

#### Principle:

X-rays are waves in the range of 10–10<sup>-3</sup> nm in the electromagnetic spectrum. When they interact with matter, they are either scattered (diffracted) or adsorbed. XRD experiments measure the intensity of the X-rays scattered by electrons in the object. The waves that emit from the object caused by the X-ray beam can undergo interference, which can be constructive or destructive, depending on the phase relationship between emitted waves.[1] This technique gives information about long-range ordering and phase purity of zeolites.[2]

The powder X-ray diffraction (PXRD) is used to study zeolite crystallinity. Each reflection in a powder X-ray diffraction pattern observed in a polycrystalline material at a given  $2\theta$  angle, measured with a wavelength of  $\lambda$ , is related to the distance  $d$  of the lattice planes as described by the Bragg's law, expressed in eq. 3.1 and depicted in **Figure 3.1**:

$$n \lambda = 2 d_{(hkl)} \sin \theta \quad 3.1$$

$$n = 1, 2, \dots$$

here:

$\lambda$  is the wavelength of the X-rays;

$d$  is the distance between two lattice planes;

$\theta$  is the angle between the incoming X-rays and the normal to the reflecting lattice plane;

$n$  is the integer called the order of the reflection

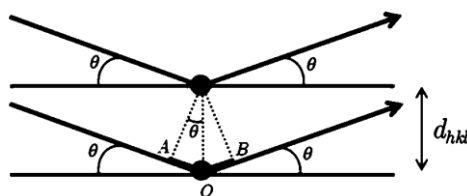


**Figure 3.1. Bragg's law.**

For the constructive interference to occur, the beams' path difference must be an integer number of wavelengths,  $n \lambda$ . The planes from which these reflections are described by Miller (**Figure 3.2**).

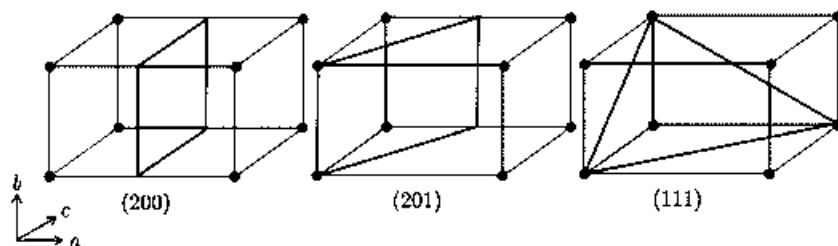


**Figure 3.2. Miller planes examples.**

Each plane has three different values,  $h$ ,  $k$ , and  $l$  describing their orientation in the unit cell. Distance between each plane is given  $d_{hkl}$ . For positive interference to occur, the Bragg equation must be satisfied, and the  $hkl$  planes must lie at a correct angle for the incident radiation. Bragg's law can be satisfied when the set of planes lie on the Ewald reflecting sphere (**Figure 3.3**).

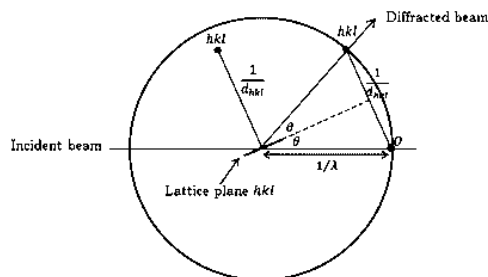


**Figure 3.3. The Ewald sphere.**

Powder X-ray diffraction (PXRD) is a compelling analytical tool. When several crystallites of different orientations are irradiated by the X-ray beam simultaneously, several Miller planes may be in a correct orientation, and each crystallite will give an individual diffraction pattern.

Atoms' positions and unit cell dimensions make the unique structure of different zeolites reflected in characteristic positions and relative intensities in the XRD patterns. The PXRD pattern is unique to a particular structure; the method can be used for fingerprinting crystalline materials.

IZA maintains on its website crystallographic data and XRD patterns for known structure types; these are as well published in the *Collection of Simulated XRD Powder Patterns for Zeolites* (Elsevier). The 5<sup>th</sup> edition of the book published in 2007 contains 218 calculated patterns of zeolite materials representing 174 framework topologies.[3] Reflecting on the almost exponential growth of new zeolite topologies and continuous success in producing novel materials by zeolite synthesis researchers.

The simplest way to identify the structure of the particular zeolite sample is to compare the experimentally measured powder diffractogram with the published reference diffractograms. Before applying qualitative measurements, it is important to compare the composition of the sample, and the reference as differences in extra framework cations composition may lead to additional reflection or different intensities.

The integrated area of peak intensity can be used to determine the sample's relative crystallinity by normalizing their intensities to those of a reference sample. The relative crystallinity (eq. 3.2) defined in ASTM D5758-01 for ZSM-5[4] is:

$$\% \text{ XRD relative crystallinity} = \frac{S_x}{S_r} \times 100 \quad 3.2$$

Where:

$S_p$  = integrated peak area for the sample, and

$S_r$  = integrated peak area for the reference.

X-ray diffraction is based on the periodicity of the crystal lattice. Therefore information about crystal structure, crystallite size, location, and concentration of exchanged cations can be obtained. It is not possible to obtain information on properties that do not repeat periodically, like lattice defects, stacking faults, and hydroxyl groups.

#### **Experimental procedure:**

The X-ray diffraction (XRD) of powder patterns were recorded using Malvern PANalytical X'Pert PRO Diffractometer with  $\text{CuK}\alpha$  radiation ( $\lambda = 1.5418 \text{ \AA}$ , 45 kV, 40 mA). The patterns were collected over a range of 4–50°  $2\theta$  with a time per step of 0.0167°  $\text{s}^{-1}$  using a 1/4° divergence slit.

Relative crystallinity values of SSZ-13 samples are determined from the integrated peak areas between 20 and 32°  $2\theta$  [5] and compared with their parent  $\text{NH}_4$ -SSZ-13.

Relative crystallinity values of MFI-55 samples are determined from the integrated peak areas between 23.1 and 24.3°  $2\theta$  [4] and compared with their parent  $\text{NH}_4$ -MFI-55.

Relative crystallinity values are determined from peak area at 22.6, 24.2, 25.5, 27.0, 27.9, 29.0, 30.6, 33.6°  $2\theta$  for all zeolite L samples, and the parent zeolite L is used as a reference sample.[6]

## **2.2 Textural analysis by $\text{N}_2$ physisorption**

#### **Principle:**

Materials with internal pores and channels have a larger surface area than dense materials. When gas molecules enter the pores and bind to sites on the internal surface areas, adsorption occurs. Adsorption can be subdivided into physisorption and chemisorption. Physisorption or physical adsorption is generally weak due to induced or permanent dipoles; it is usually observed at low temperatures. Chemisorption involves exchanging electrons between the adsorbate (gas phase) and adsorbent (solid phase); therefore it is a much stronger interaction due to the bonds formed. Physisorption is generally completely reversible upon the decrease of partial pressure; however, chemisorbed species likely need an additional driving force (*i.e.* heat) for their removal.

Adsorption by a material is usually reported as an adsorption isotherm. The weight or volume of adsorbate is taken up as a function of the partial pressure of the adsorbate at a constant temperature. Desorption denotes the converse process, where the adsorbed amount gradually decreases. Adsorption hysteresis emerges when adsorption and desorption curves do not concur.[7]

The International Union of Pure and Applied Chemistry (IUPAC) classifies the pores by their internal width, micropore: internal width less than 2 nm, mesopore: internal width between 2 and 50 nm, macropore: internal width greater than 50 nm.[8]

The shape of physisorption isotherms depends on the exchange between the strength of fluid-wall and fluid-fluid interactions. Macropores have a distinct sorption behavior from that of mesopores and micropores. Macropores can be considered as nearly flat surfaces due to their size, while the fluid-wall interactions dominate sorption behavior in micropores. Adsorption behaviors in mesopores depend on fluid-wall interaction as well as attractive interactions between fluid molecules, which may lead to pore (capillary) condensation. [8] Pore condensation represents an occurrence where a gas condenses to a liquid-like phase.

The shape of the isotherm and maximum adsorption volume is unique to the material. Physisorption isotherms are classified into six types (**Figure 3.4**).[7] Type I isotherm is obtained when adsorption is limited to a few molecular layers, often obtained on microporous materials. The initial steep uptake at low relative pressures

corresponds to monolayer deposition inside the micropores; once the micropores are filled, the isotherm reaches saturation.

Type II and IV isotherms are found with non-porous materials or mesoporous structures. Type II is characteristic for monolayer coverage at low pressures, then continues with a plateau once all the energetically favorable sites have been covered and multilayer adsorption at higher pressures. The hysteresis effect in type IV isotherms is due to the different energy of condensation on the surface of the pore and evaporation away from the pore. When molecules of gas have a higher affinity towards each other than for the surface of the adsorbent, type III and V isotherms are found. Type VI stepwise isotherm represents layer-by-layer adsorption on a highly homogeneous non-porous surface. The main types of hysteresis loops identified by IUPAC are presented in **Figure 3.5**. Each of the characteristic hysteresis loop types is closely related to the pore structure and the adsorption mechanism.

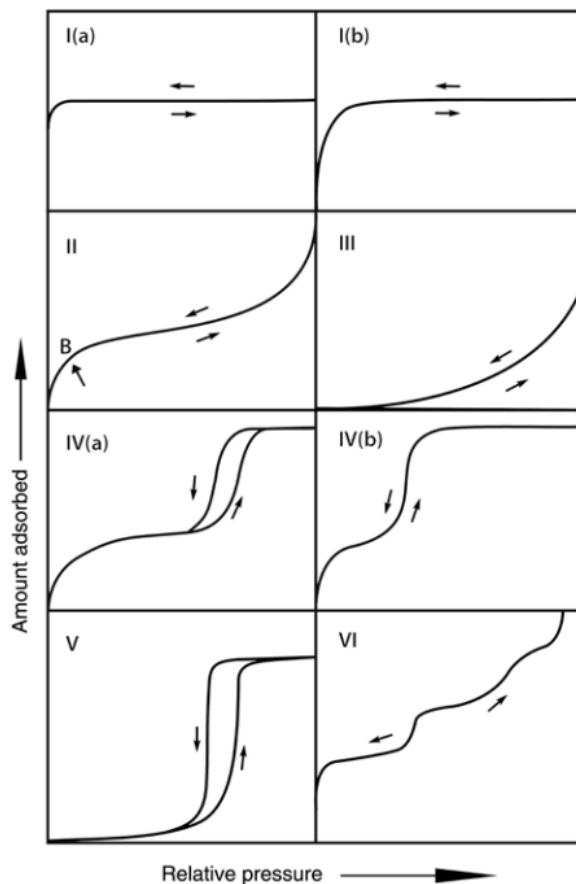


**Figure 3.4.** Classification of adsorption isotherms, according to IUPAC (from [7]).

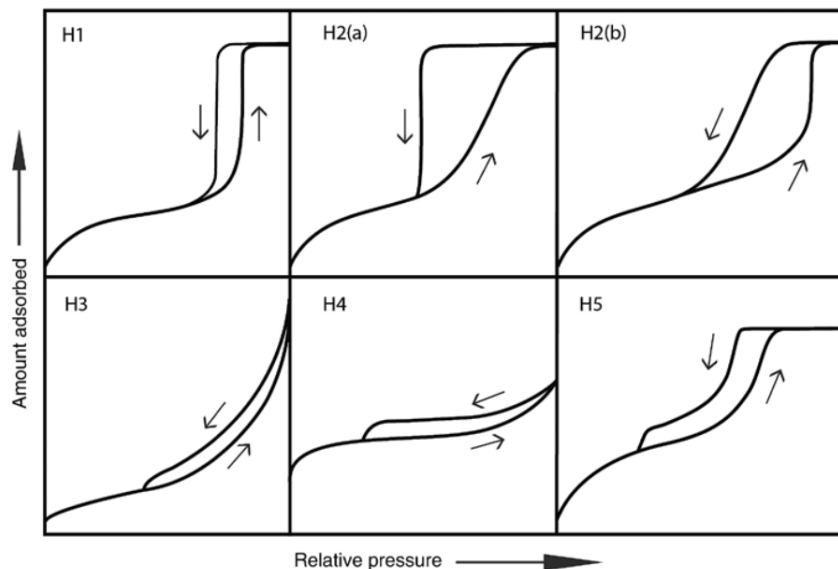


**Figure 3.5. Classification of hysteresis loops (from [7]).**

Thus the shape of the hysteresis loop can provide useful information about the mesopore structure.[9] H1 loop is found in materials that exhibit a narrow range of uniform mesopores and ink-bottle pores. H2 loops are associated with pore blocking. H3 loops are given by non-rigid aggregates of plate-like particles and not filled macropores. H4 loop is a composite of Type I and II branches, and it is often found in mesoporous zeolites and aggregated zeolite crystals. H5 loop is related to specific pore structures containing both open and partially blocked mesopores.

The Brunauer–Emmett–Teller (BET) method is the most widely used procedure for evaluating porous materials' surface area, despite its limitations for microporous adsorbents.[10]

#### **Experimental procedure:**

The N<sub>2</sub> physisorption isotherms are analyzed at -196 °C utilizing Micromeritics 3Flex high-resolution surface characterization analyzer. About 100 mg of the sample is degassed at 300 °C under vacuum overnight prior to the analysis. The isotherms are recorded using the MicroActiv analysis program for 3Flex. Micropore volume ( $V_{\text{micro}}$ ) is evaluated from non-local DFT porosity distribution using a model of N<sub>2</sub> on oxide surface with cylindrical geometry, and total pore volume ( $V_{\text{tot}}$ ) is determined by the amount of adsorbed nitrogen at  $p/p_0 = 0.98$ . Mesopore volume ( $V_{\text{meso}}$ ) is calculated by the difference in total pore volume ( $V_{\text{tot}}$ ) and micropore volume ( $V_{\text{micro}}$ ),  $V_{\text{meso}} = V_{\text{tot}} - V_{\text{micro}}$ .

## **2.3 Thermal analysis by thermogravimetry**

#### **Principles:**

Thermal analysis is used to monitor temperature-dependent properties such as dehydration, decomposition, dehydroxylation, desorption. Thermogravimetry (TG) and differential scanning calorimetry (DSC) are well-established methods for following reaction processes by measuring the thermal effects and/or weight changes. Thermogravimetry (TG) measures the change in the sample weight as a function of temperature (or time).[11] The derivative thermogravimetry (DTG) indicates the rate of mass loss by derivation ( $dm/dt$ ). Differential scanning calorimetry (DSC) follows the enthalpy changes, thermal effects of the reaction can be observed.

**Experimental procedure:**

The thermogravimetric analysis (TGA) is carried out in an air atmosphere on a SETSYS-1750 CS Evol instrument (SETARAM). Samples are heated in the air up to 800 °C. with a heating ramp of 5 °C min<sup>-1</sup> under air (40 ml min<sup>-1</sup>, 80 % N<sub>2</sub>, 20 % O<sub>2</sub>). Prior to the analysis, the samples are exposed to air with an atmosphere of 70 % humidity.

## **2.4 Chemical composition by ICP-AES**

**Principles:**

Inductively coupled plasma atomic emission spectroscopy (ICP-AES) uses plasma for atomization and excitation of the source and creating an atomic vapor from an aqueous sample. The excited atoms emit characteristic light in the ultraviolet or visible region, and the chemical composition is determined by the atomic emission lines.

**Experimental procedure:**

The Si and Al contents are determined by inductively coupled plasma atomic emission spectroscopy (ICP-AES) on an AES 5100 VDV ICP from Agilent; all samples are digested in *aqua regia* and HF prior to the analysis.

## **2.5 Crystal morphology by electron microscopy**

**Principles:**

Electron microscopy techniques give direct imaging of the local structures and enable structural investigation of zeolites. Scanning electron microscope (SEM) is used to identify the individual phases, their dimensional relationships in aggregates containing multiple phases, or if they have differences in size or habit. Due to dramatic improvement in the resolution of modern SEM, much smaller particles and details on the surface can be revealed. Tungsten filament guns give about the resolution of 3 nm and field emission gun of about 1 nm. An energy-dispersive X-ray spectrometer (EDX) is commonly installed on the SEM, and the local chemical composition can be obtained.[12]

High-resolution transmission electron microscopy (HRTEM) gives direct local images of the crystals in real space. The electron beam interaction with a solid is very strong, and the sample can absorb electrons. Large proportions of incident electrons emerge from the sample and are dispersed as back-scattered, secondary, transmitted, scattered, and energy loss electrons. Other energy forms are also generated from the interaction with the electron beam, like X-rays, Auger electrons, cathodoluminescence, etc.

### **2.5.1 Scanning Electron Microscopy (SEM)**

Electrons from the focused electron beam partially pass their energy to electrons in the sample during scanning of the solid sample surface; these electrons are ejected from the sample as secondary electrons with low energy (<50 eV). Detector accepts these electrons with random moving directions and contributes them to the image brightness. The received intensity of the secondary electrons can be correlated to the spot on the sample, but to observe the particles' morphology, the image contrast is far more important.

### **2.5.2 Transmission Electron Microscopy (TEM)**

In the case of TEM, the electron beam is transmitted through an ultra-thin specimen. TEM operates in the 100-300 kV range of electron energies. From the interactions between electrons and atoms, crystal structure can be observed as well as dislocations and grain boundaries. Atomic resolution can be achieved with high-resolution transmission electron microscopy (HR-TEM), which enables resolving lattice fringes and determining the spacing of atomic planes.

### 2.5.3 Energy Dispersive X-ray Spectroscopy (EDX)

When the incident electron beam interacts with the solid sample, some electrons from different atom shells (K, L, M, N, etc.) are ejected. An electron from a higher energy level may migrate to fill the vacancy at the lower energy level shell, and a quantum of radiation (X-ray) will be emitted corresponding to the energy difference between the shells. EDX detects local chemical composition based on the relative intensities emitted from the sample.

#### **Experimental procedure:**

Micrographs presented in Chapter 4 are collected by scanning electron microscopy (SEM) performed on a JEOL JSM-7900F low-voltage high-resolution scanning electron microscope (SEM). Before the measurement, the sample is deposited on a sample holder using an isopropyl alcohol-based carbon conductive adhesive (tedpella) tape. Transmission electron microscopy (TEM) analysis is performed on a JEM-2100F. Prior to the measurement, a diluted colloidal suspension of the sample is sonicated for 5 min and then dropped on a carbon-film-covered 300-mesh copper electron microscope grids and dried.

Micrographs presented in Chapter 5 are collected by scanning electron microscopy (SEM); pictures are taken on a MIRA TESCAN microscope equipped with a field emission gun. Micrographs are collected under an acceleration voltage of 30 kV. Before measurement, samples are deposited on a sample holder with a conductive adhesive tape and sputtered for 30 s with platinum. Transmission electron microscopy (TEM) micrographs are taken on a JEOL ARM 200 CFeg Analytical TEM at 200keV using a high angle annular dark-field (HAADF) detector under Scanning TEM (STEM) mode. Prior to analysis, the samples are dispersed in ethanol by ultrasounds for 20–30 minutes before being transferred to a carbon support grid for measurements. EDX (energy-dispersive X-ray spectroscopy) is used to map the elements and study samples' composition. Elemental mapping is carried out at 80 kV electron beam in order to limit the electron beam damage. The STEM mode is employed for both imaging and elemental mapping using the DigiScan module from Gatan Digital Micrograph and the AnalysisStation software, respectively.

Micrographs presented in Chapter 6 are collected by scanning electron microscopy (SEM); pictures are taken on a MIRA TESCAN microscope equipped with a field emission gun. Micrographs are collected under an acceleration voltage of 30 kV. Before measurement, samples are deposited on a sample holder with a conductive adhesive tape and sputtered for 30 s with platinum.

## 2.6 Local structure by solid-state nuclear magnetic resonance

#### **Principles:**

Solid-state Nuclear Magnetic Resonance, or solid-state NMR, probes the local structure around a particular nucleus.[1] It is often found to be a complementary technique to XRD since XRD focuses on long-range ordering and NMR in the short-range environment.

The most widely used solid-state NMR experiment is the magic angle spinning (MAS). The sample is spun around the ‘magic’ angle,  $54.74^\circ$  to remove chemical shielding anisotropy, dipolar coupling, and first-order quadrupolar coupling caused by the absence of fast thermal/molecular motions in solids.[1] Spinning the sample at an angle of  $54.74^\circ$  to the axis of an external magnetic field ( $B_0$ ) achieves the maximal NMR line narrowing effect, thus a solid powdered material resembles the spectrum of a liquid.

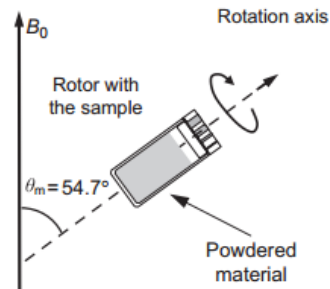


Figure 3.6. Magic angle spinning experiment scheme (from [13]).

### 2.6.1 $^{27}\text{Al}$ NMR spectroscopy

In zeolites, an aluminum atom is always connected with four silicon atoms as postulated by Löwenstein. The signal of tetrahedral aluminum ( $\text{AlO}_4$ ) in hydrated zeolite samples can be found at chemical shifts between 55 and 68 ppm.[13] Non-framework aluminum, which typically has the octahedral ( $\text{AlO}_6$ ) coordination, gives a signal at about 0 ppm. Thus, an important application of  $^{27}\text{Al}$  MAS NMR is differentiating between tetrahedral framework aluminum atoms and extraframework octahedral aluminum atoms, and their relative proportions can be directly determined from the intensities of the signals at about 60 and 0 ppm.

### 2.6.2 $^{29}\text{Si}$ NMR spectroscopy

Each silicon atom is connected via oxygen to four T atoms, which can be either silicon or aluminum which correspond to five possible distributions of Si and Al atoms around the central silicon unit  $\text{SiO}_4$  ( $Q_4$ ):  $\text{Si}(4\text{Al})$ ,  $\text{Si}(3\text{Al})$ ,  $\text{Si}(2\text{Al})$ ,  $\text{Si}(1\text{Al})$  and  $\text{Si}(0\text{Al})$ . Each type of  $\text{Si}(n\text{Al})$  ( $n = 0,1,2,3,4$ ) gives well-resolved peaks in a defined range of chemical shifts. From the analysis of chemical shift and peak intensities, the relative population of the  $\text{Si}(n\text{Al})$  units present in the zeolite can be determined. The intensity of lower frequency peaks increases upon the Si/Al ratio raise, and the Si/Al ratio of the lattice can be calculated from the peak intensities. Silicon atoms connected to OH groups located in the framework defects may overlap with  $\text{Si}[(n+1)\text{Al}]$  signals. The SiOH groups can be identified in the cross-polarization (CP) spectrum.

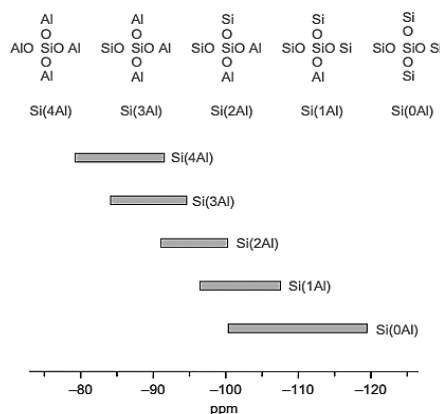


Figure 3.7.  $^{29}\text{Si}$  chemical shift of  $\text{Si}(n\text{Al})$  units in zeolites.

#### Experimental procedure:

Solid-state NMR measurements are carried out using 4 mm zirconia rotors, as the  $^{19}\text{F}$ ,  $^{27}\text{Al}$ ,  $^{29}\text{Si}$  MAS NMR spectra are recorded on a Bruker Avance 400 MHz spectrometer (magnetic field of 9.4 T). All experiments are performed with a spinning speed of 14 kHz. The chemical shifts are referenced to a 1 M  $\text{Al}(\text{NO}_3)_3$  aqueous solution, TMS and  $\text{CFCl}_3$ , for  $^{27}\text{Al}$ ,  $^{29}\text{Si}$ , and  $^{19}\text{F}$ , respectively. Exceptionally, the  $^{29}\text{Si}$  MAS NMR spectra presented in Chapter 6 are collected at a 12 kHz spinning speed, and the  $^{27}\text{Al}$  MAS NMR of MFI-55 samples are recorded on Bruker Avance 500 MHz spectrometer.

## 2.7 Acidity characterization by Fourier transformed infrared spectroscopy

### Principles:

Fourier transformed infrared (FTIR) spectroscopy is a powerful tool that provides information about molecular vibrations. Infrared spectroscopy works with the electromagnetic spectrum's infrared region and works on the principle that molecules absorb specific frequencies characteristic to their structure. Zeolites are mostly studied by transmission IR spectroscopy in the mid-infrared window (4000–400  $\text{cm}^{-1}$ ).

The technique provides helpful information by monitoring the IR vibrational mode of probe molecules (*e.g.*, CO, NO, pyridine) adsorbed on the material. This is mostly done in *in situ* cells that permit controlled degassing, activation under vacuum, and the introduction of gaseous probe molecules. The spectra obtained can be used to obtain qualitative and quantitative information. Quantitative information can be obtained by applying the Lambert-Beer adsorption law.

### Experimental procedure:

Prior to the FTIR study, the samples are pressed into self-supporting wafers (2  $\text{cm}^2$ ) and activated *in situ* at 450 °C for 2 hours under vacuum. The IR spectra (128 scans) are collected on a NICOLET 6700 fitted with a DTGS detector with a 4  $\text{cm}^{-1}$  optical resolution.

Pyridine is used to probe all sites in the zeolite L and MFI-55 samples; typically, a pressure of 1 torr pyridine is introduced in the cell to reach saturation. The wafer is then heated twice at 150 °C for 15 min to ensure a homogeneous diffusion throughout the sample. Pyridine is then stepwise (50 °C for 10 min) desorbed in the temperature range of 50–450 °C. Sample weights are normalized to 20 mg. Brønsted (B) and Lewis (L) acid site concentrations are quantified using the 1545  $\text{cm}^{-1}$  (B, extinction coefficient: 1.67  $\text{cm} \mu\text{mol}^{-1}$ ) and 1450  $\text{cm}^{-1}$  (L, extinction coefficient: 2.22  $\text{cm} \mu\text{mol}^{-1}$ ) peaks after desorption at 150 °C.[14]

2,6-di-*tert*-butylpyridine (dTBPY), on the other hand, is used to quantify the external acidity of the zeolites. The same pretreatment procedure is used as that for pyridine adsorption. 0.1 torr of dTBPY is introduced in the cell; then the wafer is heated at 150 °C for 15 min two times to ensure a homogeneous diffusion into the samples. The concentration of these Brønsted acid sites is quantified using the dTBPY 1530  $\text{cm}^{-1}$  peak area, and an extinction coefficient is calculated according to the procedure outlined by Corma *et al.* summarized by equation (3.3):

$$\epsilon_{\text{dTBPY}} = \frac{\epsilon_{\text{Py}} \cdot S_{\text{dTBPY(LTL)}}}{S_{\text{Py(LTL)}}} \quad 3.3$$

with  $\epsilon_{\text{dTBPY}}$  and  $\epsilon_{\text{Py}}$  the integrated molar extinction coefficients for dTBPY and pyridine, respectively, and  $S_{\text{dTBPY(LTL)}}$  and  $S_{\text{Py(LTL)}}$  the integrated band areas of dTBPY and pyridine, respectively, adsorbed on zeolite L.[15,16]

The Accessibility Index (ACI) is defined as the number of acid sites detected by a probe molecule divided by the total number of acid sites derived from the aluminum content. Accordingly, the pyridine ACI, is  $\text{ACI}_{\text{Py}} = (c_{\text{B}} + c_{\text{L}})/\text{Al}_{\text{ICP}}$ , as pyridine probes both Brønsted and Lewis acid sites. As dTBPY only probes Brønsted sites,  $\text{ACI}_{\text{dTBPY-B}}$  is the ratio between the Brønsted sites detected by dTBPY and the aluminum content determined by chemical analysis.[17]

SSZ-13 samples are equilibrated for 15 min at room temperature with a pressure of 1 torr  $d_3$ -acetonitrile ( $\text{CD}_3\text{CN}$ ) before recording a spectrum. Spectra are deconvoluted with the OMNIC 8.3.103 software. Quantitative results are obtained using molar absorption coefficients from the literature[18]: protonated  $\text{CD}_3\text{CN}$  on Brønsted acid sites (2297  $\text{cm}^{-1}$ ,  $\epsilon(\text{B}) = 2.05 \text{ cm} \mu\text{mol}^{-1}$ ) and coordinated on Lewis acid sites (2310  $\text{cm}^{-1}$ ,  $\epsilon(\text{L}) = 3.6 \text{ cm} \mu\text{mol}^{-1}$ ). Both integrated areas of deconvoluted bands are normalized to a wafer mass of 20 mg.

## 2.8 Catalysis

### **Principles:**

A catalytic test is conducted to test zeolite activity in a specific reaction.

### 2.8.1 Dealkylation of 1,3,5-triisopropylbenzene

#### **Experimental procedure:**

The dealkylation of 1,3,5-triisopropylbenzene (TiPBz) is performed in a tubular downflow fixed-bed reactor operating in the gas phase. A stainless-steel reactor (ID = 12.7 mm) is successively packed with inert SiC (particle size 200–300  $\mu\text{m}$ ), 30 mg (W, dried basis) catalyst (particle size 200–500  $\mu\text{m}$ ) and again with SiC, in total 400 mg of SiC, SiC/zeolite ratio 13.3. The catalysts are activated *in situ* at 450 °C for 2 hours under a dry airflow (50 ml  $\text{min}^{-1}$ ) to remove excess water and ammonia, cooled to the reaction temperature (220 °C). A stream of  $\text{N}_2$  (200 ml  $\text{min}^{-1}$ ,  $F^\circ$ ) is then diverted to a saturator maintained at 70 °C filled with TiPBz and fed to the reactor with a resulting  $W/F^\circ = 220 \text{ kg mol}^{-1} \text{ s}$ . The online analysis of the products is performed with a Varian CP-3800 gas chromatograph fitted with a flame ionization detector (FID) on an HP-Pona capillary column (50 m x 0.2 mm x 0.5  $\mu\text{m}$ ).

### 2.8.2 Dehydration of n-propanol

#### **Experimental procedure:**

The dehydration of n-propanol (nPrOH) is an acid-catalyzed test reaction that is used to evaluate the hierarchical derivative performance. It is executed in a downflow fixed-bed reactor operating in the gas phase. A quartz reactor is packed with 120 mg inert SiC (particle size 200–300  $\mu\text{m}$ ), 30 mg (W, dried basis) catalyst (particle size 200–500  $\mu\text{m}$ ), SiC/zeolite ratio 4. The catalysts are activated *in situ* at 450 °C for 4 hours under a dry airflow (50 ml  $\text{min}^{-1}$ ) to remove excess water and generate the H-form of the zeolites, cooled to the reaction temperature (205 °C). The  $\text{N}_2$  (100 ml  $\text{min}^{-1}$ ) stream is then diverted to a saturator maintained at 5 °C filled with n-propanol and fed to the reactor resulting in a  $W/F^\circ$  of 27.2  $\text{kg mol}^{-1} \text{ s}$ . The online analysis of the products is performed with a gas chromatograph Varian® 3900 gas chromatograph equipped with a WCOT CP-Wax 52 CB 2.0  $\mu\text{m}$  column (35 m x 0.25 mm) and an FID detector at 200 °C. Total coke content is determined by thermogravimetric analysis (TGA). The TGA is carried out in a SETSYS instrument (SETARAM). Samples are heated in the reconstituted (80 %  $\text{N}_2$  + 20 %  $\text{O}_2$ ) airflow to 800 °C.

### 3 References

- [1] R.E. Morris, P.K. Allan, Chapter 6: Structure Determination, in: *Zeolites in Catalysis*, 2017: pp. 194–239. <https://doi.org/10.1039/9781788010610-00194>.
- [2] A. Jentys, J.A. Lercher, *Techniques of zeolite characterization*, (n.d.) 42.
- [3] *Collection of Simulated XRD Powder Patterns for Zeolites*, Elsevier, 2007. <https://doi.org/10.1016/B978-0-444-53067-7.X5470-7>.
- [4] D32 Committee, Test Method for Determination of Relative Crystallinity of Zeolite ZSM-5 by X-Ray Diffraction, ASTM International, n.d. <https://doi.org/10.1520/D5758-01R15>.
- [5] T. Usui, Z. Liu, H. Igarashi, Y. Sasaki, Y. Shiramata, H. Yamada, K. Ohara, T. Kusamoto, T. Wakihara, Identifying the Factors Governing the Early-Stage Degradation of Cu-Chabazite Zeolite for NH<sub>3</sub>-SCR, *ACS Omega*. 4 (2019) 3653–3659. <https://doi.org/10.1021/acsomega.8b03409>.
- [6] K.A. Tarach, J. Tekla, U. Filek, A. Szymocha, I. Tarach, K. Góra-Marek, Alkaline-acid treated zeolite L as catalyst in ethanol dehydration process, *Microporous and Mesoporous Materials*. 241 (2017) 132–144. <https://doi.org/10.1016/j.micromeso.2016.12.035>.
- [7] M. Thommes, K. Kaneko, A.V. Neimark, J.P. Olivier, F. Rodriguez-Reinoso, J. Rouquerol, K.S.W. Sing, Physisorption of gases, with special reference to the evaluation of surface area and pore size distribution (IUPAC Technical Report), *Pure and Applied Chemistry*. 87 (2015) 1051–1069. <https://doi.org/10.1515/pac-2014-1117>.
- [8] S. Lowell, J.E. Shields, M.A. Thomas, M. Thommes, *Characterization of Porous Solids and Powders: Surface Area, Pore Size and Density*, Springer Netherlands, Dordrecht, 2004. <https://doi.org/10.1007/978-1-4020-2303-3>.
- [9] K.S.W. Sing, F. Rouquerol, J. Rouquerol, P. Llewellyn, Assessment of Mesoporosity, in: F. Rouquerol, J. Rouquerol, K.S.W. Sing, P. Llewellyn, G. Maurin (Eds.), *Adsorption by Powders and Porous Solids (Second Edition)*, Academic Press, Oxford, 2014: pp. 269–302. <https://doi.org/10.1016/B978-0-08-097035-6.00008-5>.
- [10] J. Rouquerol, P. Llewellyn, F. Rouquerol, Is the bet equation applicable to microporous adsorbents?, in: P.L. Llewellyn, F. Rodriguez-Reinoso, J. Rouquerol, N. Seaton (Eds.), *Studies in Surface Science and Catalysis*, Elsevier, 2007: pp. 49–56. [https://doi.org/10.1016/S0167-2991\(07\)80008-5](https://doi.org/10.1016/S0167-2991(07)80008-5).
- [11] H.G. Karge, J. Weitkamp, eds., *Characterization II*, Springer Berlin Heidelberg, Berlin, Heidelberg, 2007. <https://doi.org/10.1007/b58179>.
- [12] W. Zhou, Chapter 8: Electron Microscopy of Zeolites, in: *Zeolites in Catalysis*, 2017: pp. 277–309. <https://doi.org/10.1039/9781788010610-00277>.
- [13] A.G. Stepanov, Chapter 4 - Basics of Solid-State NMR for Application in Zeolite Science: Material and Reaction Characterization, in: B.F. Sels, L.M. Kustov (Eds.), *Zeolites and Zeolite-Like Materials*, Elsevier, Amsterdam, 2016: pp. 137–188. <https://doi.org/10.1016/B978-0-444-63506-8.00004-5>.
- [14] C.A. Emeis, Determination of Integrated Molar Extinction Coefficients for Infrared Absorption Bands of Pyridine Adsorbed on Solid Acid Catalysts, *Journal of Catalysis*. 141 (1993) 347–354. <https://doi.org/10.1006/jcat.1993.1145>.
- [15] A. Corma, V. Fornés, L. Forni, F. Márquez, J. Martínez-Triguero, D. Moscotti, 2,6-Di-Tert-Butyl-Pyridine as a Probe Molecule to Measure External Acidity of Zeolites, *Journal of Catalysis*. 179 (1998) 451–458. <https://doi.org/10.1006/jcat.1998.2233>.
- [16] A.G. Popov, V.S. Pavlov, I.I. Ivanova, Effect of crystal size on butenes oligomerization over MFI catalysts, *Journal of Catalysis*. 335 (2016) 155–164. <https://doi.org/10.1016/j.jcat.2015.12.008>.
- [17] F. Thibault-Starzyk, I. Stan, S. Abelló, A. Bonilla, K. Thomas, C. Fernandez, J.-P. Gilson, J. Pérez-Ramírez, Quantification of enhanced acid site accessibility in hierarchical zeolites – The accessibility index, *Journal of Catalysis*. 264 (2009) 11–14. <https://doi.org/10.1016/j.jcat.2009.03.006>.
- [18] B. Wichterlová, Z. Tvarůžková, Z. Sobalik, P. Sarv, Determination and properties of acid sites in H-ferrierite: A comparison of ferrierite and MFI structures, *Microporous and Mesoporous Materials*. 24 (1998) 223–233. [https://doi.org/10.1016/S1387-1811\(98\)00167-X](https://doi.org/10.1016/S1387-1811(98)00167-X).

# 4

Comparative study of zeolite L  
etching with  $\text{NH}_4\text{F}$  and  $\text{NH}_4\text{HF}_2$   
solutions

<b>1</b>	<b>INTRODUCTION</b> .....	<b>57</b>
<b>2</b>	<b>RESULTS</b> .....	<b>59</b>
2.1	X-RAY DIFFRACTION .....	59
2.2	SCANNING ELECTRON MICROSCOPY.....	61
2.3	TRANSMISSION ELECTRON MICROSCOPY.....	62
2.4	N <sub>2</sub> PHYSISORPTION .....	63
2.5	PHYSICOCHEMICAL PROPERTIES.....	64
2.6	<sup>27</sup> AL SOLID-STATE NMR .....	65
2.7	THERMOGRAVIMETRIC ANALYSIS .....	66
2.8	ACIDITY CHARACTERIZATION BY FTIR .....	68
2.9	CATALYTIC ACTIVITY .....	72
<b>3</b>	<b>DISCUSSION</b> .....	<b>74</b>
<b>4</b>	<b>CONCLUSION</b> .....	<b>75</b>
<b>5</b>	<b>REFERENCES</b> .....	<b>76</b>

# 1 Introduction

Zeolites are widely used in the chemical industry as catalysts, molecular sieves, sorbents, and ion exchange materials.[1] Their catalytic properties are unique as their acid sites (Brønsted and Lewis) are located in confined space, providing shape selectivity during hydrocarbon conversions.

Zeolite L (LTL-type) was first synthesized by Breck and Acara, and its framework topology was determined by Baerlocher and Barrer.[2] It possesses a one-dimensional pore structure. The framework consists of cancrinite cages linked with hexagonal prisms to form columns in the c-direction; they form pores with an internal diameter of 1.2 nm and 12-member ring (MR) pore opening windows with a diameter of 0.71 nm.[3] Zeolite L is typically synthesized with  $\text{Si}/\text{Al} = 3$  using  $\text{K}^+$  as a structure-directing agent.

Zeolite L loaded with noble metals is an excellent catalyst for the low-pressure aromatization (dehydrocyclization) of paraffins ( $\text{C}_{6-8}$ ) in light naphtha; such paraffins are poorly converted on classical platinum reforming catalysts ( $\text{Pt}/\text{Al}_2\text{O}_3\text{-Cl}$ ).[4] However, due to the operating conditions of this reforming reaction (high temperature, low pressure), the catalyst suffers from deactivation by coke deposition;[5-7] the known remedy is to operate in a dual catalyst bed process, the so-called CCR (Continuous Catalyst Regeneration) pioneered by UOP.[8] Zeolite L is also claimed as active in catalytic cracking[9,10] and a hierarchical derivative in FCC gasoline hydrodesulfurization.[11,12]

A key disadvantage of zeolite L is its monodimensional pore system, especially when bulky molecules are converted. For full range naphthas, diffusion is hindered and penalizes the catalyst's activity, selectivity, and stability.[5,11] Active sites accessible for bulky molecules are available at the pore mouth and zeolite crystal surface, but they represent less than 5 % of the total active sites.[13]

Two strategies are commonly used to reduce the impact of diffusion limitations in zeolites: i) decrease of the crystal size[14], ii) introduction of larger (meso- or macro-) pores in the crystals.[15] Nanozeolites (<100 nm crystal size) have relatively high external surface area, and the portion of active sites available on the external surface is higher than that of micron-sized crystals. However, the number of zeolites that can be synthesized in nanosized form is still limited.[13,15,16] Consequently, much research is devoted to the preparation of zeolite crystals comprising larger secondary pores. The methods to introduce secondary pores can be classified into two groups, bottom-up and top-down approaches. Constructive or bottom-up processes are synthetically challenging and build hierarchical zeolites by engineering microporous and mesoporous domains utilizing complicated templating routes.[17,18] While there are some reports using commercially available and inexpensive OSDA,[19] direct synthesis of mesoporous zeolite L is extremely scarce.[12] Top-down approaches are more reproducible and favored for the commercial production of hierarchical zeolites.[20]

Destructive or top-down methods include a variety of techniques to introduce a secondary level of porosity in as-synthesized zeolites through post-synthesis modification. Post-synthesis treatments are used to modify and improve the zeolite properties that cannot be achieved through direct synthesis. These treatments include  $\text{H}_2\text{O}$  steaming or etching with various acid or base solutions that cause dealumination and/or desilication while generating secondary pores.[16,18]

Etching with buffered solutions of  $\text{NH}_4\text{F}/\text{HF}$  was shown earlier to yield hierarchical zeolites with retained chemical composition due to the formation of  $\text{HF}_2^-$  anions affording an unbiased extraction of Si and Al.[21,22] Besides avoiding the use of HF,  $\text{NH}_4\text{F}$  generates a steady source of small quantities of  $\text{HF}_2^-$  allowing easy control of the dissolution kinetics. However, the  $\text{NH}_4\text{F}$  route is based on relatively concentrated (20-40 wt/%  $\text{NH}_4\text{F}$ ) solutions.  $\text{NH}_4\text{HF}_2$  was proposed as a more ecofriendly etching solution to clean silicon dioxide from semiconductor wafer surfaces.[23] Feng *et al.* showed that an  $\text{NH}_4\text{HF}_2$  solution effectively removes non-

framework aluminum and silicon from a NaY zeolite. However, the zeolite etching with  $\text{NH}_4\text{HF}_2$  is still unexplored territory, and not much information on the particularities of zeolite dissolution is available.[24]

This work aims to compare the etching ability of  $\text{NH}_4\text{F}$  and  $\text{NH}_4\text{HF}_2$  to obtain hierarchical zeolite L crystals. This study focuses on the physicochemical properties of the parent L and its hierarchical derivatives obtained with  $\text{NH}_4\text{F}$  and  $\text{NH}_4\text{HF}_2$ , as well as their catalytic performance in the conversion of a bulky molecule.

## 2 Results

### 2.1 X-ray diffraction

The  $\text{NH}_4$ -form of zeolite L is subjected to fluoride etching. The codes used to denote different samples are provided in the experimental section. Briefly, the samples treated at 25 °C are denoted L-I-x, where x is the treatment time. The samples treated at 60/80 °C are denoted L-II-x-60/80, where x is the treatment time. The XRD analysis reveals that the treatment at 25 °C with  $\text{NH}_4\text{F}$  and  $\text{NH}_4\text{HF}_2$ , does not lead to structural changes (100 % crystallinity), whatever the fluoride concentrations. The treatment with a 20 wt/%  $\text{NH}_4\text{F}$  solution is extended up to 480 min without visible changes in the XRD crystallinity (**Figure 4.1A**). The effect of 40 wt/%  $\text{NH}_4\text{F}$  on the zeolite crystallinity is studied up to 90 min, and no change in the crystallinity is observed (**Figure 4.1B**). Our preliminary experiments indicated that an  $\text{NH}_4\text{HF}_2$  solution is more aggressive and requires the use of much more dilute solutions with respect to  $\text{NH}_4\text{F}$ . For instance, a 1 wt/%  $\text{NH}_4\text{HF}_2$  (L-III-x) solution is used in order to retain the zeolite L crystallinity (**Figure 4.2A**).

The  $\text{NH}_4\text{F}$  treatment at elevated temperatures (60 and 80 °C) had a more pronounced effect on zeolite L crystallinity. For instance, L-I-60-80 and L-II-60-80 exhibited 43 % and 18 % crystallinity, respectively, with respect to the parent zeolite. In addition, the patterns display a broad feature 15–30°  $2\theta$ , indicating amorphization, proof that under such conditions, a substantial dissolution of the zeolite framework takes place. A decrease in crystallinity is also observed for the samples treated at 60 °C. Thus, L-I-60-60 and L-II-60-60 samples showed a crystallinity of 79 % and 78 %, respectively. Samples treated with 1 wt/%  $\text{NH}_4\text{HF}_2$  at 60 and 80 °C also exhibited some loss of crystallinity, which is 91 % and 89 % for L-III-60-60 and L-III-60-80, respectively.

On the other hand, the treatment with 1 wt/%  $\text{NH}_4\text{HF}_2$  at room temperature and up to 120 min leads to materials with increased XRD crystallinity. A slight decrease in the crystallinity is observed for the sample etched 180 minutes. Room temperature treatment of zeolite L with a 2 wt/%  $\text{NH}_4\text{HF}_2$  for 10 min (L-IV-10) also yields materials with higher relative crystallinity (**Table 4.1, Figure 4.2B**). We attribute this increase in crystallinity to the dissolution of some amorphous material present on the sample and the low crystalline part of the crystals, all typical for such unbiased framework etching.[21]

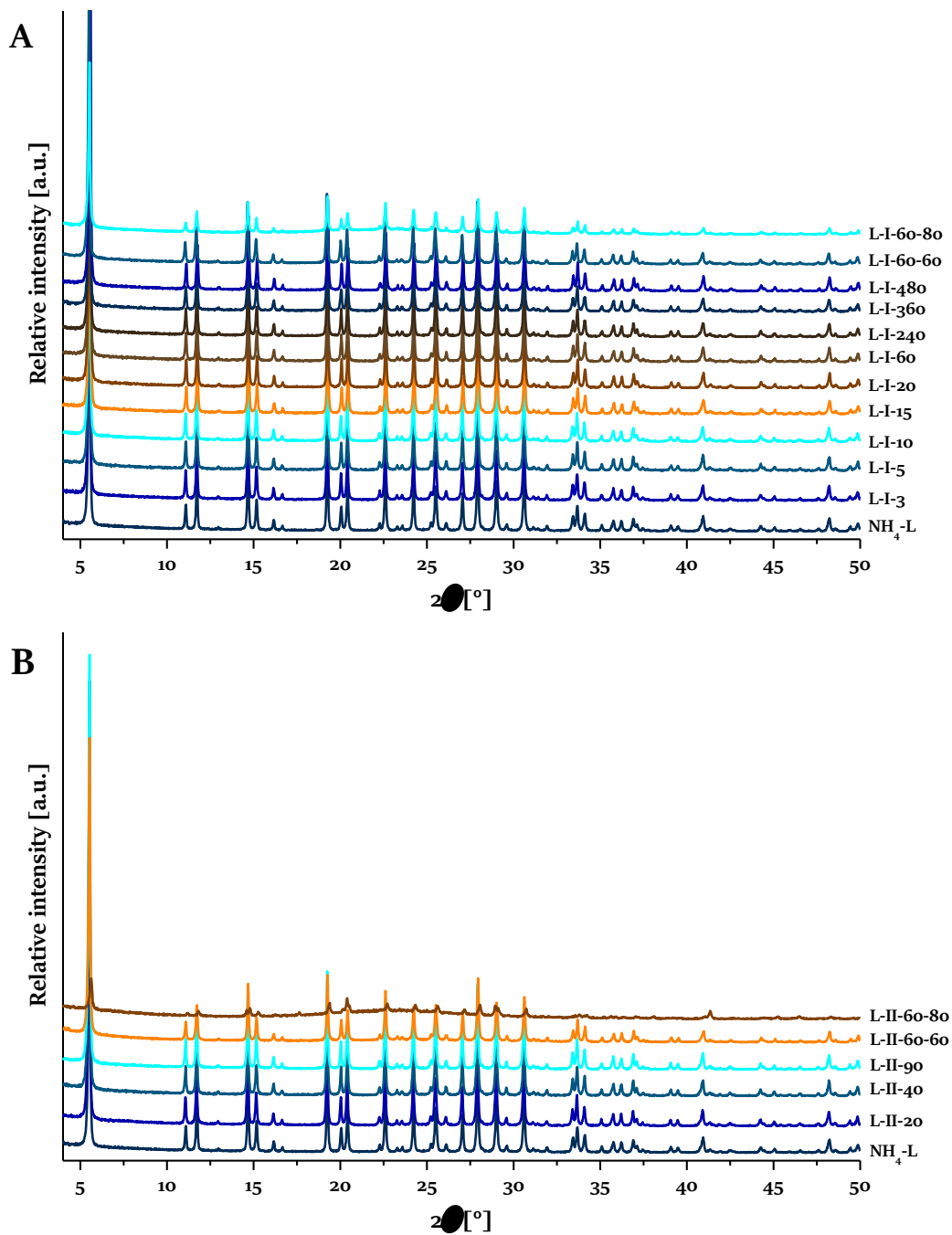


Figure 4.1. XRD patterns of zeolite L treated with 20 (A) and 40 (B) wt/%  $\text{NH}_4\text{F}$ .

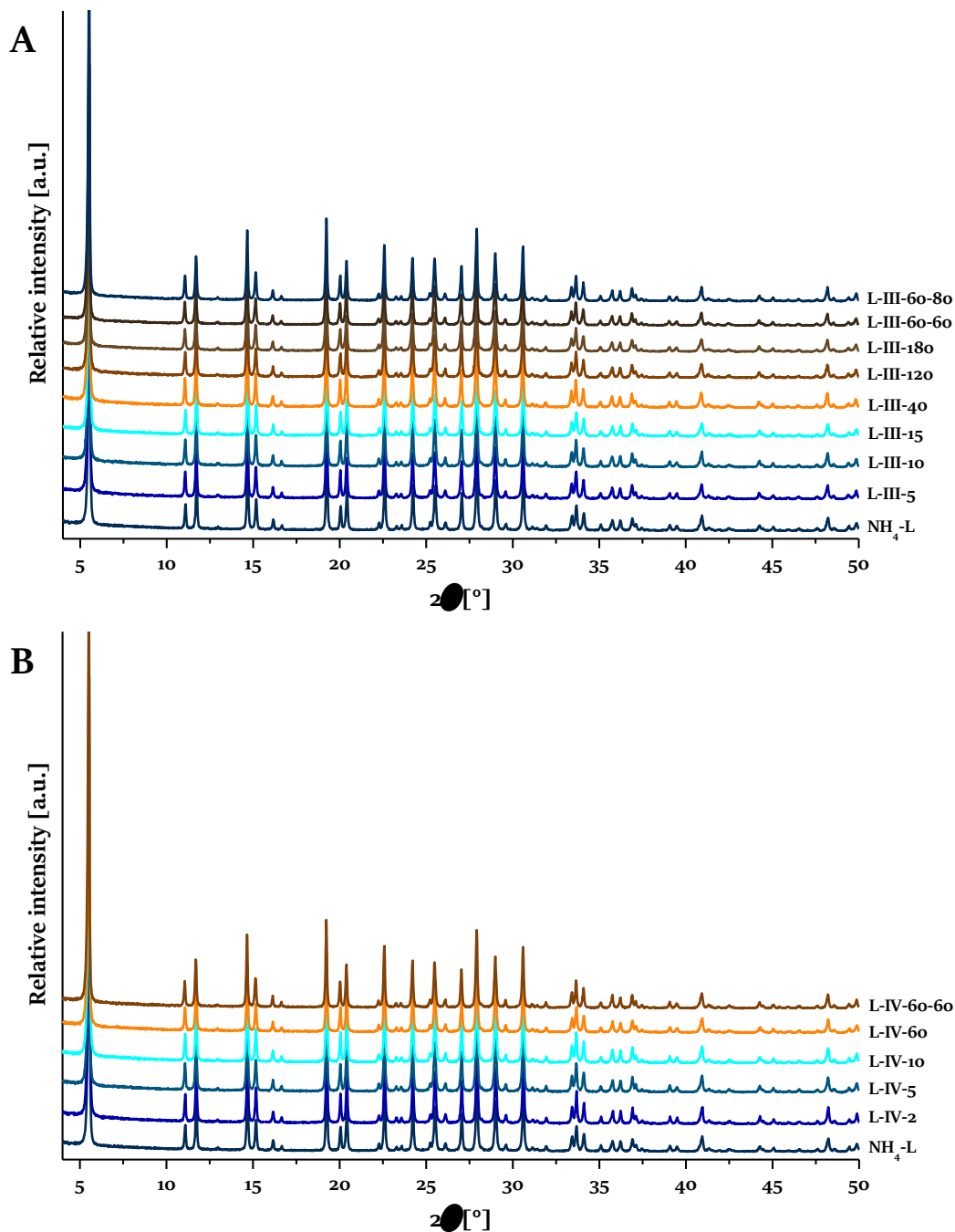


Figure 4.2. XRD patterns of zeolite L treated with 1 (A) and 2 (B) wt/%  $\text{NH}_4\text{HF}_2$ .

## 2.2 Scanning electron microscopy

The impact of fluoride etching on the morphology of zeolite L is studied with a scanning electron microscope (Figure 4.3). Typically, zeolite L exhibits a disc-like morphology with overgrown terraces on the pinacoidal face. Steps are also observed on the prismatic face, but they are not so pronounced on the basal pinacoid. This etching yields crystals with cracks and holes going deeply in the pinacoidal surface, while the sharp edges of the prismatic surface disappear, smoothing out the surface.

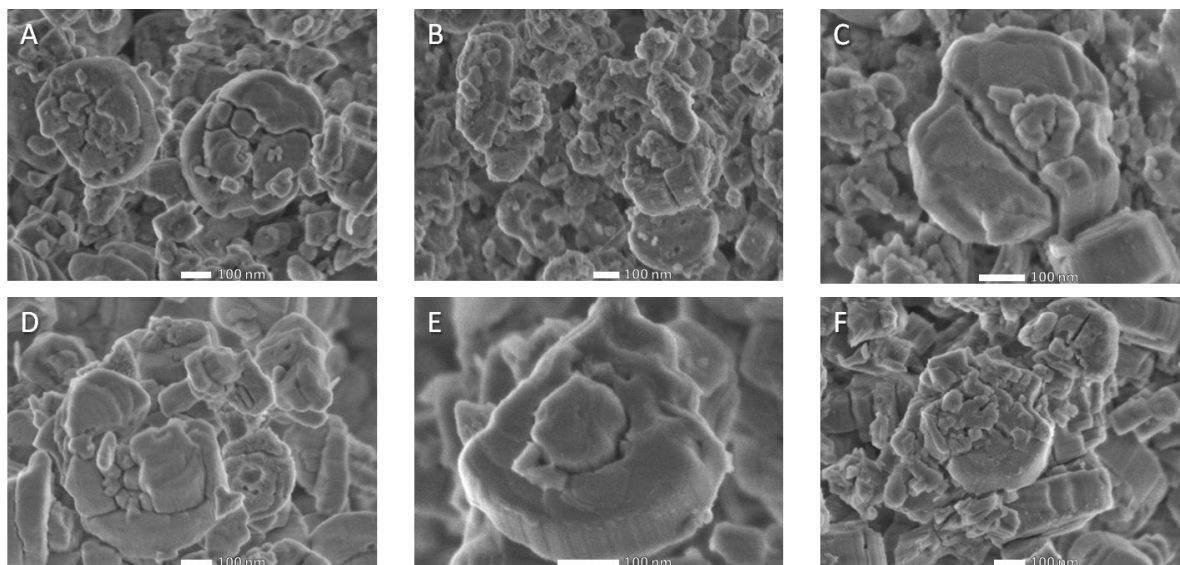


Figure 4.3. SEM micrographs of L-II-40 (A), L-II-60-60 (B), L-III-40 (C), L-III-180 (D), L-III-60-60 (E), and L-III-60-80 (F) samples.

### 2.3 Transmission electron microscopy

Transmission electron microscope (TEM) sheds more light on the most deeply etched samples and highlights details of the remaining part of the crystal (Figure 4.4). Entire crystalline domains are clearly separated from the parent crystal. TEM micrographs of the parent L zeolite and its etched derivatives are depicted in Figure 4.4A-F. The surface of the parent and the  $\text{NH}_4\text{F}$  treated zeolites (Figure 4.4A-C) appear smooth, while those treated with  $\text{NH}_4\text{HF}_2$  display rougher surfaces. Figure 3F highlights dissolution on the edges of the crystals, and Figure 4.4D-E show extended dissolution along the crystal surface with visible formation of mesopores.

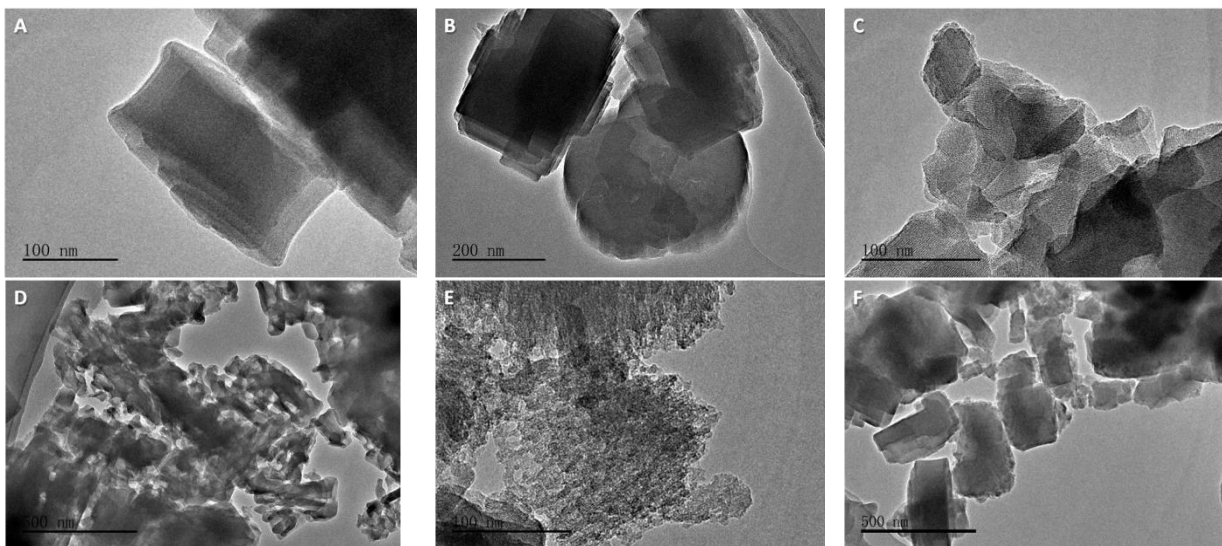


Figure 4.4. TEM micrographs of  $\text{NH}_4\text{-L}$  (A), L-I-5 (B), L-I-60 (C), L-III-180 (D), L-III-60-60 (E), and L-III-60-80 (F) samples.

## 2.4 $\text{N}_2$ physisorption

The parent zeolite and treated samples' textural properties are assessed by nitrogen physisorption (Figure 4.5).  $\text{N}_2$  isotherms of the parent zeolite and the derivatives treated with 20 wt/%  $\text{NH}_4\text{F}$  solution at room temperature exhibit a type I (a) isotherm according to the IUPAC classification. However, the fast uptake at low relative pressure characteristic of microporous materials is followed by an inclination of the isotherm, terminating with an H4 hysteresis loop in the high relative pressure region ( $\sim 0.98$ ). The latter is characteristic of the presence of textural mesopores. The surface and pore features of the derivatives produced by fluoride treatments are summarized in Table 4.1. The mesopore volume increases slightly with treatment time when 20 wt/%  $\text{NH}_4\text{F}$  is used. The micropore volume remains almost constant ( $0.17 \text{ cm}^3 \text{ g}^{-1}$ ) up to 240 min and then decreases to  $0.16 \text{ cm}^3 \text{ g}^{-1}$  after 360- and 480-min treatment. A more substantial decrease occurs after treatment at  $60^\circ\text{C}$  ( $0.14 \text{ cm}^3 \text{ g}^{-1}$ ) and  $80^\circ\text{C}$  ( $0.08 \text{ cm}^3 \text{ g}^{-1}$ ). At elevated temperatures ( $60$  and  $80^\circ\text{C}$ ), the mesopore volume is substantially increased up to  $0.20 \text{ cm}^3 \text{ g}^{-1}$ , while the micropore volume drops further to  $0.08 \text{ cm}^3 \text{ g}^{-1}$  (Table 4.1).

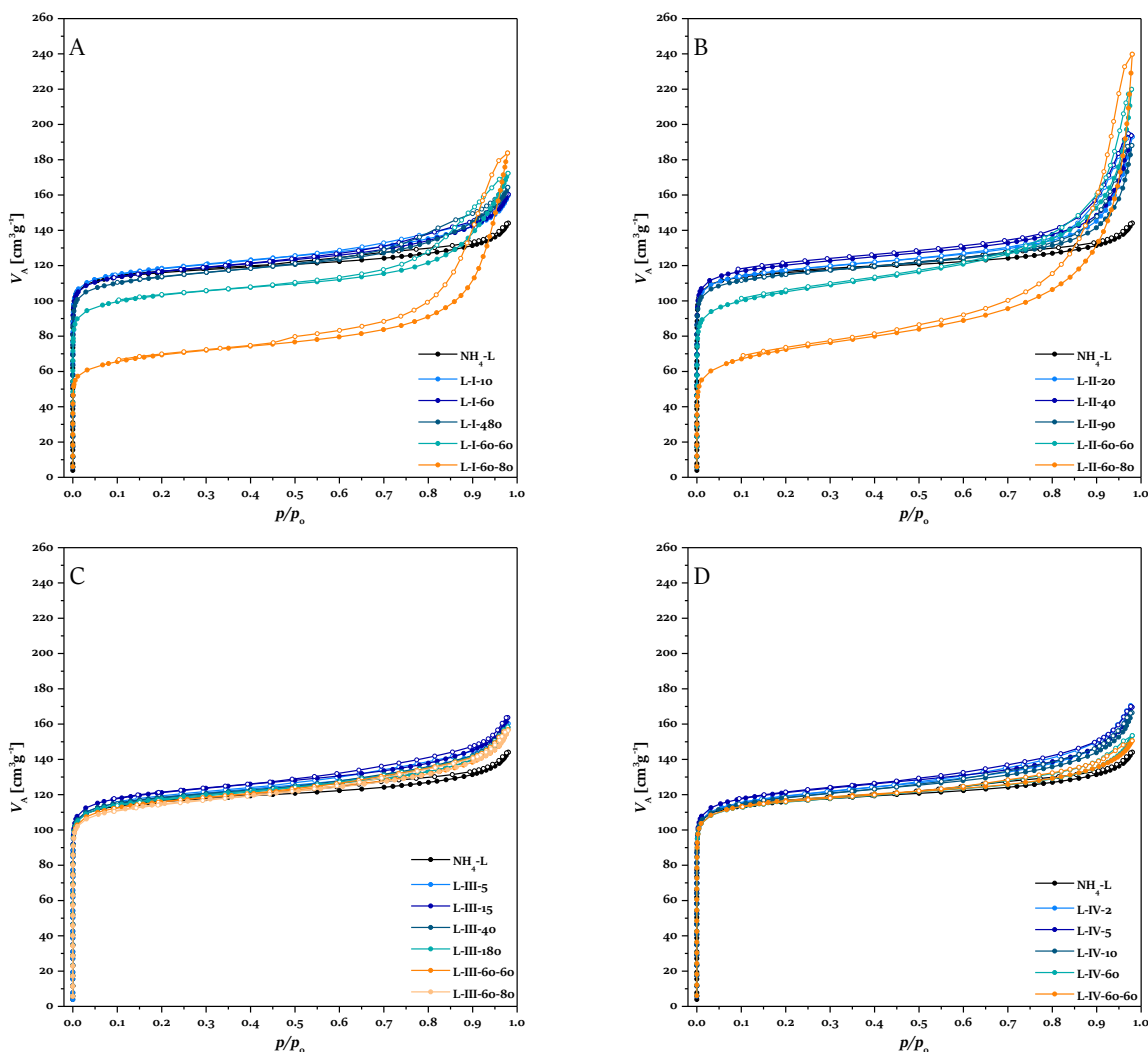


Figure 4.5.  $\text{N}_2$  adsorption isotherms of the samples treated with 20 wt/%  $\text{NH}_4\text{F}$  (A), 40 wt/%  $\text{NH}_4\text{F}$  (B), 1 wt/%  $\text{NH}_4\text{HF}_2$  (C), and 2 wt/%  $\text{NH}_4\text{HF}_2$  (D). Note: closed circles – adsorption, open circles – desorption.

## 2.5 Physicochemical properties

The use of a more concentrated (40 wt/%  $\text{NH}_4\text{F}$ ) solution results in a faster dissolution of zeolite L. The samples are treated only up to 90 minutes as after 20 min only the mesopore volume increases from 0.05 to 0.13  $\text{cm}^3 \text{g}^{-1}$ . Any further increase in the treatment time does not increase mesoporosity. The micropore volume and the crystallinity of all room temperature treated samples are retained. The sample treated at 60 °C shows a small loss of micropore volume and a substantial increase of mesopore volume. The most dramatic changes, a severe loss of crystallinity and micropore volume, are observed in the sample treated at 80 °C. As mentioned, the preliminary experiments with 20 and 40 wt/%  $\text{NH}_4\text{HF}_2$  solutions resulted in the substantial amorphization of the zeolite. Therefore, much more diluted (1 and 2 wt/%  $\text{NH}_4\text{HF}_2$ ) solutions are employed to obtain hierarchical zeolite L. The use of 1 wt/%  $\text{NH}_4\text{HF}_2$  solution did not change the surface characteristics of zeolite substantially, even after treatment at 60 and 80 °C (**Table 4.1**). The 2 wt/%  $\text{NH}_4\text{HF}_2$  solution is used at room temperature from 2 to 60 minutes, which provided materials with slightly increased micropore volume.

The chemical composition of the parent and treated samples determined by ICP-AES are presented in **Table 4.1**. The parent  $\text{NH}_4\text{-L}$  has a Si/Al ratio of 3.0, typical for zeolite L.[2,25] This composition is retained after leaching with a 20 wt/%  $\text{NH}_4\text{F}$  solution for 3 and 20 min, then slightly increases (Si/Al = 3.1) after 60 and 360 min leaching to reach Si/Al = 3.2 after 480 min. A more substantial dealumination occurs when the temperature is raised to 60 °C (Si/Al = 3.5) and 80 °C (Si/Al = 6.8), which is coupled with a substantial decrease in the micropore volume. These results are indicative of an amorphization of the L zeolite.

Samples leached with a 40 wt/%  $\text{NH}_4\text{F}$  solution show a slight increase in the Si content after 20 and 90 min treatments. Substantial dealumination occurs at 60 and 80 °C, as the Si/Al ratios raise to 3.8 and 12.7, respectively. No significant change in framework composition is recorded for L zeolite treated with 1 wt/%  $\text{NH}_4\text{HF}_2$ . A slight dealumination (Si/Al = 3.2) occurs after etching with a 2 wt/%  $\text{NH}_4\text{HF}_2$  for 2 to 10 minutes.

Table 4.1. Chemical composition and textural properties of the parent and treated zeolites.

Sample	XRD <sup>a</sup> %	Si/Al <sub>ICP</sub> mol mol <sup>-1</sup>	S <sub>BET</sub> m <sup>2</sup> g <sup>-1</sup>	V <sub>micro</sub> cm <sup>3</sup> g <sup>-1</sup>	V <sub>meso</sub> cm <sup>3</sup> g <sup>-1</sup>
NH <sub>4</sub> -L	100	3.0	452	0.17	0.05
L-I-3	100	3.0	453	0.17	0.07
L-I-5	100	3.0	464	0.18	0.07
L-I-10	100	3.0	457	0.17	0.07
L-I-15	100	3.0	454	0.17	0.08
L-I-20	100	3.0	456	0.18	0.08
L-I-60	100	3.1	453	0.17	0.08
L-I-120	100	3.1	456	0.17	0.08
L-I-240	100	3.1	453	0.17	0.09
L-I-360	94	3.1	441	0.16	0.09
L-I-480	96	3.2	441	0.16	0.09
L-I-60-60	79	3.5	333	0.14	0.12
L-I-60-80	43	6.3	227	0.08	0.20
L-II-20	103	3.1	453	0.17	0.13
L-II-40	103	3.1	464	0.18	0.13
L-II-90	103	3.1	446	0.17	0.13
L-II-60-60	78	3.8	397	0.15	0.19
L-II-60-80	18	12.7	241	0.07	0.29
L-III-5	105	3.1	461	0.17	0.07
L-III-10	105	3.1	471	0.18	0.07
L-III-15	105	3.1	472	0.18	0.07
L-III-40	105	3.1	462	0.17	0.07
L-III-120	103	3.1	471	0.18	0.08
L-III-180	90	3.1	458	0.17	0.07
L-III-60-60	89	3.0	450	0.17	0.07
L-III-60-80	91	3.0	443	0.17	0.08
L-IV-2	108	3.2	462	0.18	0.08
L-IV-5	109	3.2	471	0.18	0.08
L-IV-10	110	3.2	458	0.17	0.09
L-IV-60	92	3.0	375	0.17	0.07
L-IV-60-60	98	3.0	375	0.17	0.07

<sup>a</sup>Relative crystallinity to the reference sample measured by XRD.

## 2.6 <sup>27</sup>Al solid-state NMR

The aluminum coordination of the zeolites, studied by <sup>27</sup>Al MAS NMR, is displayed in **Figure 4.6A** and **B**. All samples are in their NH<sub>4</sub>-form, without thermal activation prior to the NMR measurement. The <sup>27</sup>Al MAS NMR spectra show a unique resonance at 59 ppm, corresponding to tetrahedrally coordinated Al. <sup>27</sup>Al MAS NMR study indicates that after a mild fluoride etching (20 wt/%), no extraframework Al is generated (**Figure 4.6A**). However, under more severe etching conditions, at a higher temperature (L-I-60-60), a small amount (ca. 1–5 %) of octahedral Al appears (**Figure 4.6B**). Increasing the NH<sub>4</sub>F concentration to 40 wt/% and at 80 °C impacts substantially the structure, as already indicated by the physisorption analysis and extra framework concentration

Al increases to 54 %. The tetrahedrally coordinated aluminum (59 ppm peak) on L-I-60-80 and L-II-60-80 samples decrease sharply, in line with their chemical analysis.

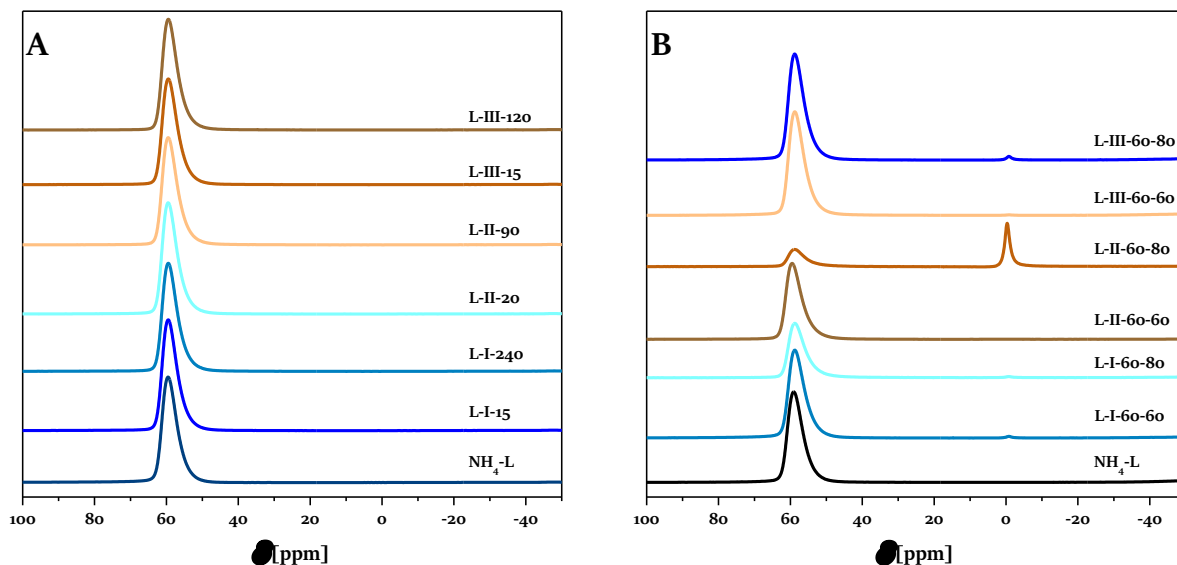


Figure 4.6. The  $^{27}\text{Al}$  MAS NMR of the parent zeolite and derivatives treated at A) room temperature and B) 60 and 80 °C, with 20 (L-I), 40 (L-II) wt/%  $\text{NH}_4\text{F}$ , and 1 wt/%  $\text{NH}_4\text{HF}_2$  (L-III) solutions.

## 2.7 Thermogravimetric analysis

Thermogravimetric (TGA) analysis monitors the mass loss upon heating of the parent  $\text{NH}_4\text{-L}$  zeolite and its fluoride-etched derivatives (Figure 4.7). All TG curves show three mass loss steps: i) 25–200 °C, attributed to the removal of loosely bound water, ii) 200–550 °C attributed to the ammonia release, iii) 550–700 °C indicative of dehydroxylation. The results are presented in Table 4.2.

Table 4.2. Thermal analysis of the parent  $\text{NH}_4\text{-L}$  zeolite and the fluoride derivatives.

Samples	$\text{H}_2\text{O}$ loss <sup>a</sup>	Ammonia loss <sup>b</sup>	Dehydroxylation <sup>c</sup>
	%	%	%
$\text{NH}_4\text{-L}$	9.94	4.80	1.81
L-I-60	10.44	5.02	1.96
L-I-480	10.03	4.95	1.83
L-I-60-60	9.95	4.80	1.81
L-I-60-80	6.83	3.05	1.47
L-II-90	10.36	4.71	1.93
L-II-60-60	10.71	4.86	1.78
L-II-60-80	7.18	2.92	1.41
L-III-15	10.67	4.97	1.81
L-III-60-60	10.45	4.75	1.97
L-III-60-80	9.23	4.93	2.00
L-IV-2	11.46	4.66	1.76
L-IV-5	11.36	5.06	1.75

Step of mass loss: <sup>a</sup> i (25–200 °C), <sup>b</sup> ii (200–550 °C), <sup>c</sup> iii (550–700 °C).

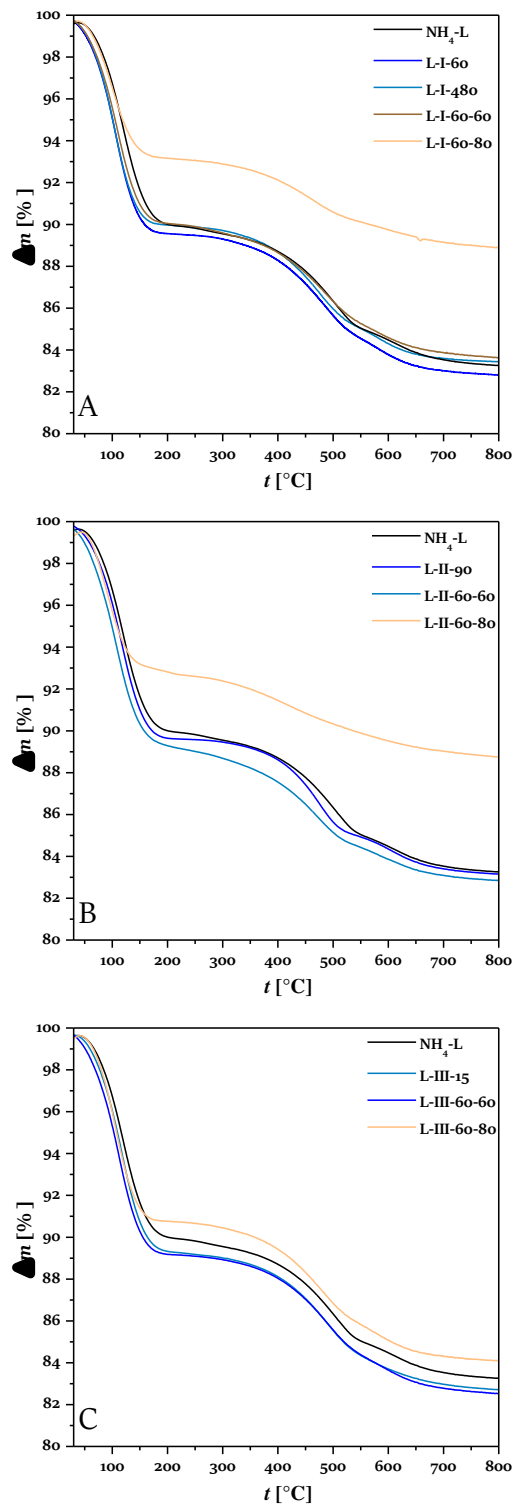


**Figure 4.7.** TG curves of the parent zeolite and the derivatives treated with 20 wt/%  $\text{NH}_4\text{F}$  (A), 40 wt/%  $\text{NH}_4\text{F}$  (B), and 1 wt/%  $\text{NH}_4\text{HF}_2$  (C).

The parent  $\text{NH}_4\text{-L}$  shows a total weight loss of 16.5 %, of which 9.9 % is a water release, 4.8 % is ammonia and 1.8 % is dehydroxylation. With a few exceptions, the total weight losses of all etched samples do not change significantly, indicating that such etchings do not modify the zeolite's intrinsic properties. However, samples

etched at higher temperatures, L-I-60-80 and L-II-60-80, have weight losses of 11.35 and 11.51 %. Their hydrophilicity and ammonia content is modified and explained by the loss of their micropore volumes ( $N_2$  physisorption, **Table 4.1**).

## 2.8 Acidity characterization by FTIR

The acidity of the parent zeolite and its etched derivatives is studied by *in situ* infrared (IR) spectroscopy of their -OH stretching vibrations (**Figure 4.8**). Full spectra of the parent zeolite L after activation is shown in **Figure 4.9**. The band at  $3746\text{ cm}^{-1}$  is assigned to Si-OH freely vibrating on the external crystal surface and the mesopore area. The parent zeolite exhibits a low-intensity peak at  $3730\text{ cm}^{-1}$ , commonly assigned to Si-OH in defects.[26]

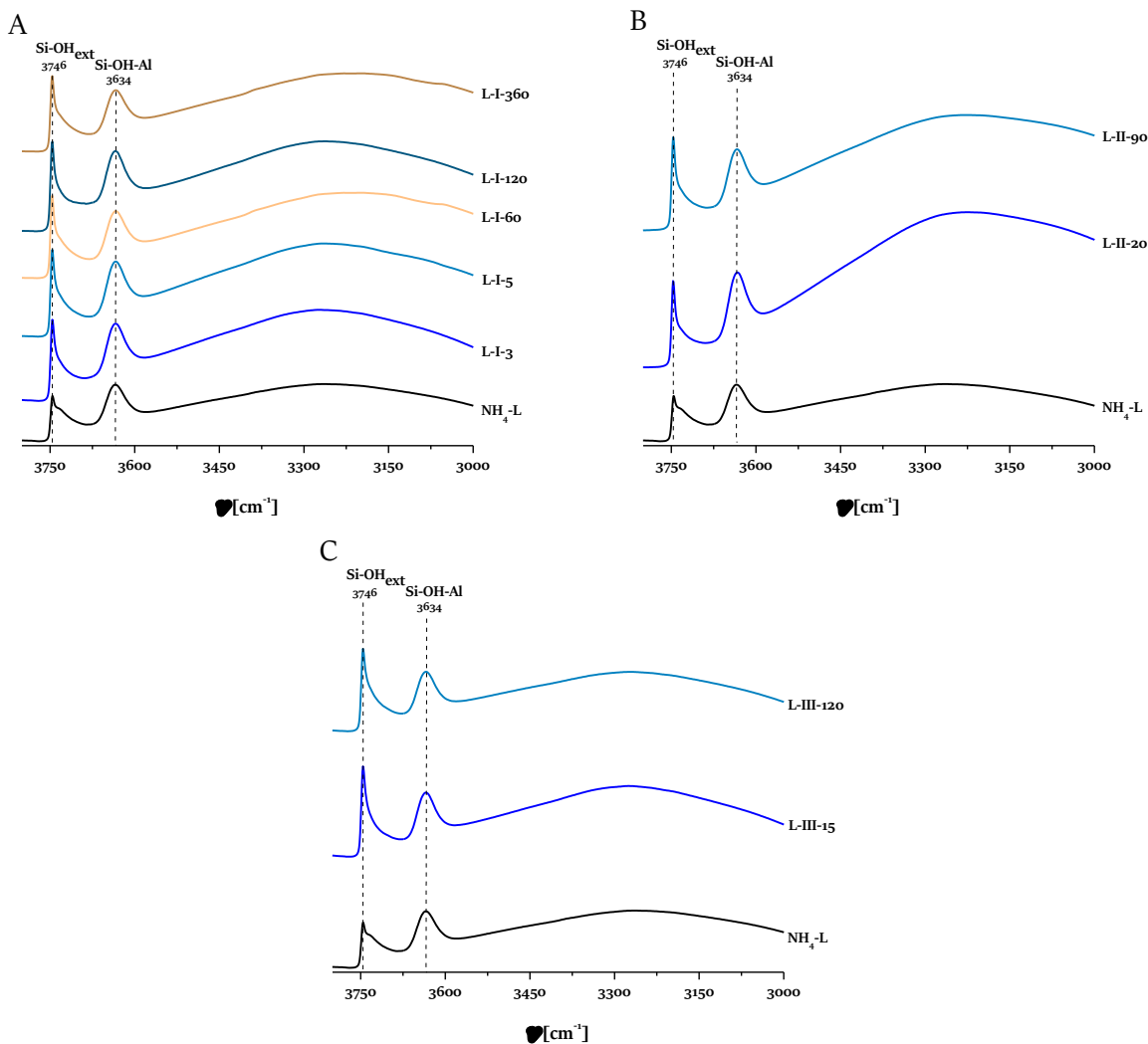


**Figure 4.8.** Room temperature IR spectra in the O-H vibrations region for the parent and some etched derivatives: 20 wt/%  $NH_4F$  (A), 40 wt/%  $NH_4F$  (B), 1 wt/%  $NH_4HF_2$  (C) solutions.

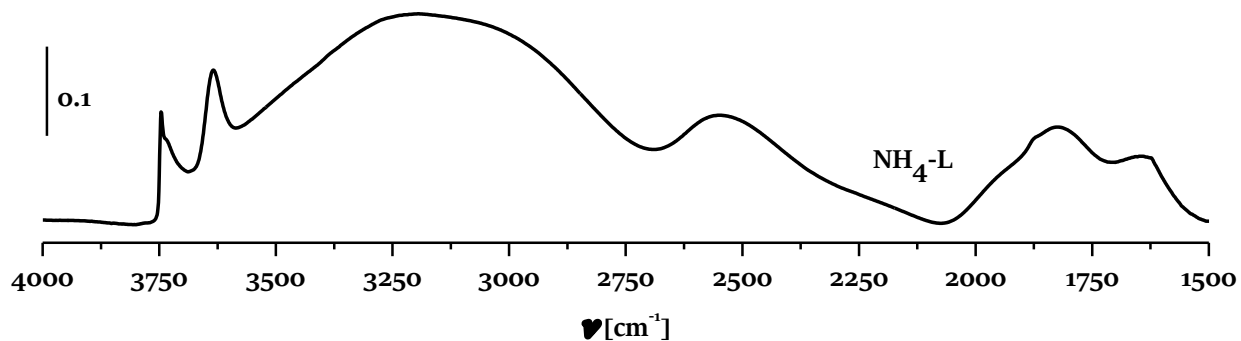


**Figure 4.9.** Room temperature IR spectra for the parent zeolite L ( $\text{NH}_4\text{-L}$ ) sample after activation.

Deconvoluted peaks in the OH region are shown in **Figure 4.10**. The band at  $3634 \text{ cm}^{-1}$  is attributed to the acidic bridging hydroxyl  $\text{Si}(\text{OH})\text{Al}$  groups and the broadband centered around  $3250 \text{ cm}^{-1}$  to hydroxyl groups located in a cancrinite cage. [27,28] IR spectra of pyridine remaining adsorbed after desorption at  $150 \text{ }^\circ\text{C}$  are used to quantify the Brønsted and Lewis acid sites, and the results are presented in **Table 4.3**. The concentrations of Brønsted and Lewis acid sites increase with respect to the parent zeolite. Sample L-II-20 exhibits the highest ( $575 \mu\text{mol g}^{-1}$ ) Brønsted acid site concentration. For the majority of the samples, the concentration of Lewis acid sites does not change substantially with the fluoride etching. This result is in agreement with the  $^{27}\text{Al}$  NMR study, which showed that the treatment does not generate extra framework aluminum, except in the cases when the zeolite is partially amorphized. Accessibility index (ACI) is defined as the number of acid sites detected by the probe molecules' adsorption divided by the total amount of acid sites in the zeolite provided by the aluminum content. [29] The increased concentrations are attributed to better accessibility of pyridine to the active sites due to the mesopore formation. The accessibility index ( $\text{ACI}_{\text{py}}$ ) of fluoride etched samples is higher with respect to the parent material.

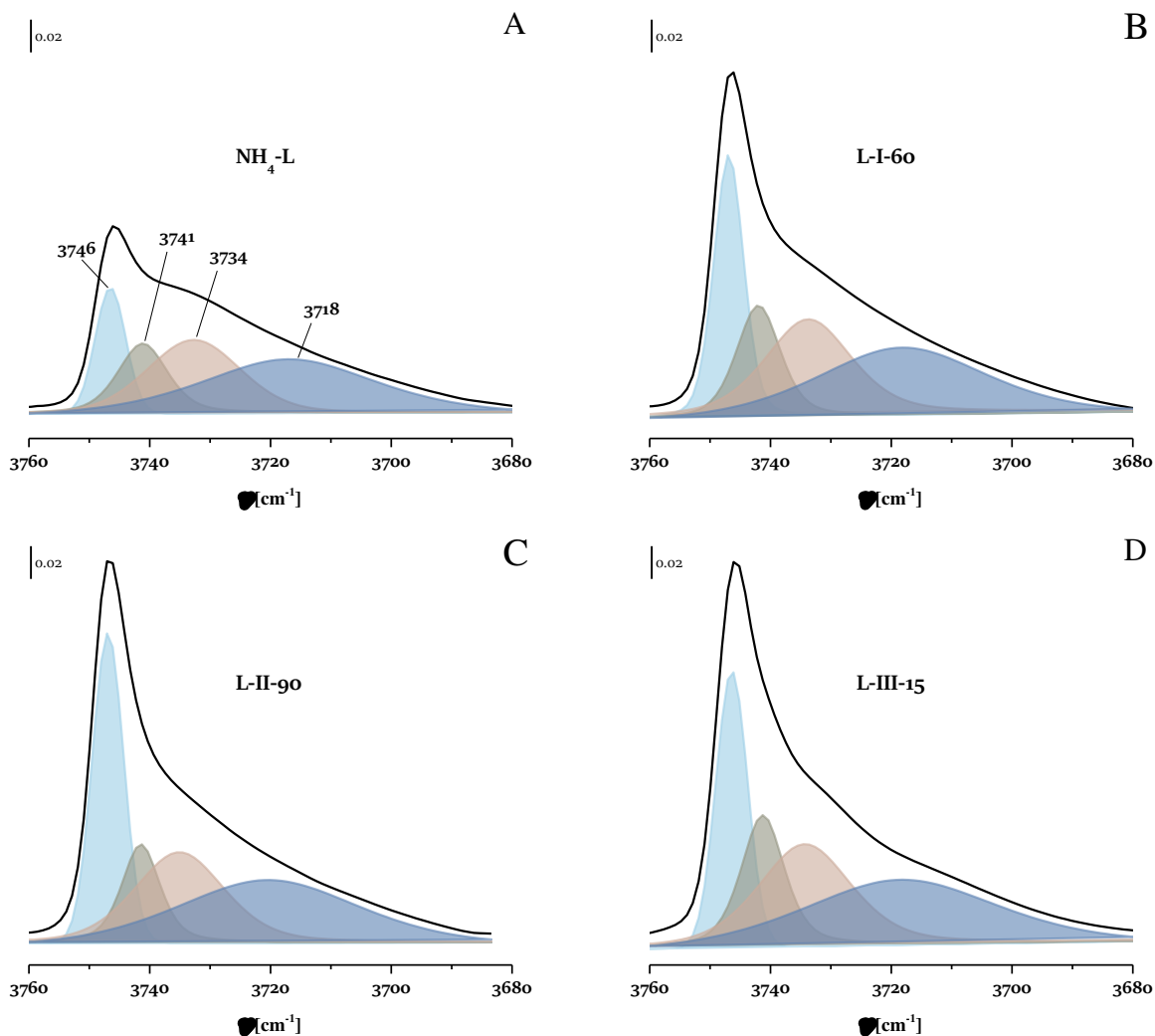


**Figure 4.10.** Deconvolution of the background spectra of activated samples: parent  $\text{NH}_4\text{-L}$  (A), L-I-60 (B), L-II-90 (C), and L-III-15 (D) in the silanol region. The spectra are baseline corrected before deconvolution.

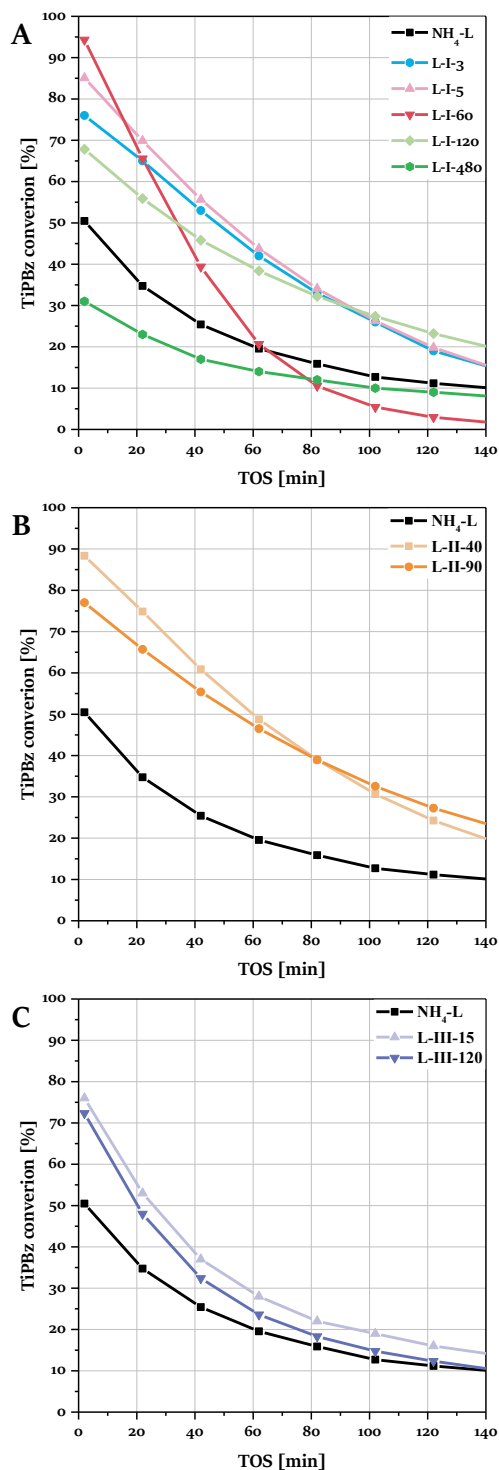
We have further studied the zeolite accessibility by employing the 2,6-di-*tert*-butylpyridine (dTBPY), a probe larger (0.80 nm) than zeolite L channel (0.71 nm).<sup>[30]</sup> The Brønsted acid site concentration is quantified using its characteristic band at  $1530\text{ cm}^{-1}$ , **Table 4.3**. The dTBPY ACI ( $\text{ACI}_{\text{dTBPY-B}}$ ) is determined for the parent and its etched derivatives. It is known that a zeolite could adsorb molecular larger than the crystallographic diameter of its channel due to the structure breathing effect and distortion of the molecule. Nevertheless, a very limited amount of dTBPY is adsorbed on the parent zeolite L, showing that it is limited to the pore mouth of zeolite L crystals. Two to three times larger amounts are adsorbed on the treated crystals. Thus, the ACI from 0.02 for the parent zeolite increased to 0.06 for the L-II-90 sample, which we attribute to the increased mesopore volume, **Table 4.1**.

Table 4.3. Concentrations of Brønsted and Lewis acid sites in the parent NH<sub>4</sub>-L and zeolite L samples evaluated by *in situ* IR spectroscopy monitoring of probe molecules.

Sample	Al <sub>ICP</sub> μmol g <sup>-1</sup>	Py-B <sup>a</sup> μmol g <sup>-1</sup>	Py-L <sup>a</sup> μmol g <sup>-1</sup>	c <sub>B</sub> + c <sub>L</sub> μmol g <sup>-1</sup>	ACI <sub>Py</sub> -	Py-B <sup>b</sup> μmol g <sup>-1</sup>	dTBPy-B <sup>c</sup> μmol g <sup>-1</sup>	ACI <sub>dTBPy-B</sub> -
NH <sub>4</sub> -L	3156	412	233	645	0.20	113	68	0.02
L-I-3	3156	476	268	744	0.24	140	/	/
L-I-5	3156	467	315	782	0.25	153	/	/
L-I-60	3076	476	319	796	0.26	127	164	0.05
L-I-120	3076	500	364	865	0.28	134	/	/
L-I-360	3076	426	299	725	0.24	145	/	/
L-I-480	3000	435	246	681	0.23	78	/	/
L-II-20	3076	575	277	852	0.28	173	/	/
L-II-90	3076	512	317	829	0.27	154	175	0.06
L-III-15	3076	430	271	700	0.23	141	153	0.05
L-III-120	3076	398	308	706	0.23	123	/	/

Determined at: <sup>a</sup>150 °C, <sup>b</sup>350 °C, <sup>c</sup>150 °C.

## 2.9 Catalytic activity



**Figure 4.11.** Conversion of 1,3,5-triisopropylbenzene (TiPBz) for the parent and some etched derivatives: 20 wt/% NH<sub>4</sub>F (A), 40 wt/% NH<sub>4</sub>F (B), 1 wt/% NH<sub>4</sub>HF<sub>2</sub> (C) solutions.

Dealkylation of TiPBz (1,3,5-triisopropylbenzene) highlights the catalytic properties of the external surface of zeolite L; this bulky molecule (kinetic diameter: 0.95 nm) does not penetrate its micropores.[31] Initial conversions (ca. 2 min time on stream) represent the state of the pristine external surface as this model reaction suffers from deactivation.

The initial conversion of TiBPz correlates well with the concentration of external acid sites. The parent zeolite, NH<sub>4</sub>-L, shows an initial conversion of 50 % while the etched derivatives are substantially higher, around 80 % conversion (**Figure 4.11**). The only exception is the 8 h etched (L-I-480) sample. Sample L-I-60 shows the highest initial conversion (94 %); however, this sample deactivates quickly, and after 60 minutes its activity drops below the other samples.

The acidity-activity relationship between the number of Brønsted active sites and the initial catalytic activity is shown in **Figure 4.12**. The plot shows that the etched mesoporous zeolites possess a higher concentration of Brønsted acid sites due to the improved accessibility and thus higher catalytic activity in the conversion of TiBPz.

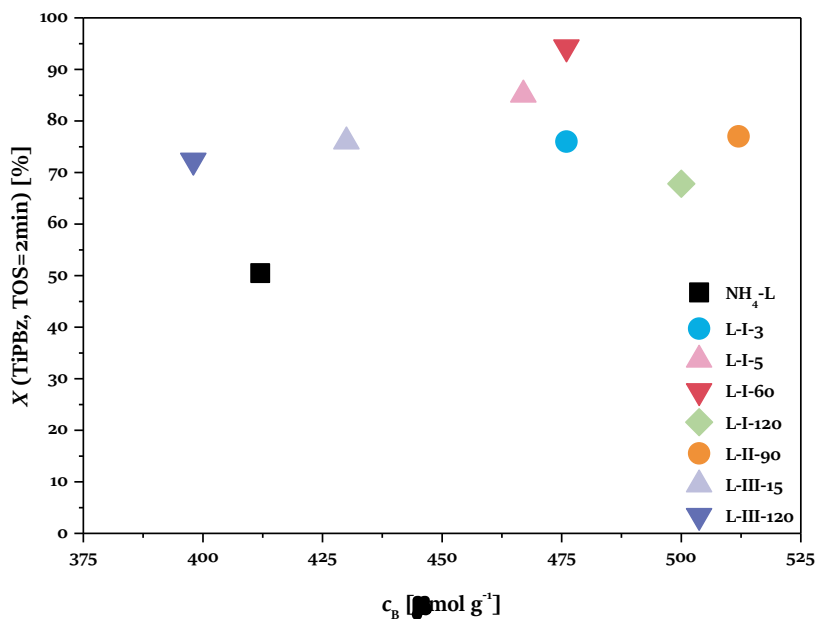


**Figure 4.12.** TiBPz initial conversion ( $X$ ) as a function of Brønsted acid sites ( $c_B$ ) concentration over hierarchical catalysts and the parent sample ( $\text{NH}_4\text{-L}$ ) after 2 min TOS.

It is worth noting that after 122 min the conversion on parent zeolite activity decreases to 10 %, while for the hierarchical zeolites, it ranges between 12 and 25 % depending on the treatment conditions. This feature is probably related to the location and toxicity of carbonaceous deposits, as observed earlier.[32] Thus the hierarchical zeolites prove to be more resistant to deactivation by coke deposition on active sites.

### 3 Discussion

Different dealumination techniques such as water vapor steaming, treatment with ammonium hexafluorosilicate and hydrochloric acid have been used to control the zeolite L framework composition and generate secondary porosity.[33] In the case of zeolite L, these techniques are not very efficient and often provoke a structural collapse. The LTL structure is retained after treatment with  $\text{SiCl}_4$ , but pore blockage occurs.[34] Here, we etched zeolite L with aqueous  $\text{NH}_4\text{F}$  and  $\text{NH}_4\text{HF}_2$  solutions at temperatures between 25 and 80 °C, to obtain hierarchical porous materials. Our previous studies showed that due to its double hydrolysis in water  $\text{NH}_4\text{F}$  generates  $\text{HF}_2^-$  in equilibrium with other products of the reaction.[21] The use of concentrated  $\text{NH}_4\text{F}$  solutions (20–50 wt/%) allows such species to be continuously generated without reaching a very high concentration of  $\text{HF}_2^-$  and thus, to better control the etching rate of the zeolite. Using an  $\text{NH}_4\text{HF}_2$  solution provides a high concentration (20–40 wt/%) of  $\text{HF}_2^-$ ; consequently, such treatment is too aggressive, and the zeolite etching is difficult to be controlled. Therefore,  $\text{NH}_4\text{HF}_2$  solutions with lower concentrations (1 and 2 wt/%) are more appropriate for generating secondary porosity in zeolites.

Zeolite L etched at room temperature with 20 and 40 wt/%  $\text{NH}_4\text{F}$  solutions shows increased X-ray crystallinity and retained micropore volume. Such a treatment generates some mesoporosity, but the mesopore contribution to the total pore volume is limited. A slight decrease in crystallinity and microporosity is observed after 360–480 min, but the negative impact is minimal. Greater structural changes are observed when  $\text{NH}_4\text{F}$  etching takes place at higher temperatures, 60 °C, and 80 °C (**Table 4.1**).

Etching at room temperature with 1 wt/%  $\text{NH}_4\text{HF}_2$  produces derivatives with high crystallinity up to 120 minutes. Similarly to the  $\text{NH}_4\text{F}$  etching, a decrease in crystallinity occurs at elevated temperatures (60 °C and 80 °C). However, the crystallinity loss is lower compared to etching with 20 and 40 wt/%  $\text{NH}_4\text{F}$  solutions. It is worth noting that no preferential dealumination of the zeolite is observed. The chemical analysis highlights that  $\text{NH}_4\text{HF}_2$  etchings are unbiased; a negligible increase in Si/Al ratio is most probably due to the dissolution of non-zeolitic alumina rich domains. In addition, the samples prepared with 1 and 2 wt/%  $\text{NH}_4\text{HF}_2$  possess a higher crystallinity than their parent zeolite. A similar effect is already reported by Feng *et al.* on zeolite Y.[24]  $\text{NH}_4\text{F}$  etching under mild conditions also leads to zeolites with higher crystallinity. We attribute this effect to the removal of low crystalline and defective parts of the zeolite as shown by Qin *et al.*[35]

The zeolites etched at room temperature retain their chemical composition, and  $^{27}\text{Al}$  MAS NMR confirms no changes in the aluminum coordination. The IR spectra of hydroxyl stretching vibrations show that the fluoride-treated samples contain more surface hydroxyls. The peak deconvolution in the silanol region revealed the presence of the peak at  $3730\text{ cm}^{-1}$  assigned to Si-OH in defects even after the treatment. No substantial changes in the intensity of the peak corresponding to the bridged hydroxyls, Si(OH)Al, is observed.

The concentration of Brønsted and Lewis acid sites is monitored by *in situ* IR spectroscopy of adsorbed pyridine. The etched samples show an increased concentration of both due to their better accessibility by the probe molecule. 2,6-di-*tert*-butylpyridine (dTBPY) is a molecule of choice to investigate the Brønsted external acidity as its kinetic diameter prevents it from penetrating the micropores. The external acid site concentration is highest for the sample prepared with 40 wt/%  $\text{NH}_4\text{F}$ .

Dealkylation of TiPBz (1,3,5-triisopropylbenzene) selectively probes the catalytic properties of the external surface of zeolite L as its kinetic diameter (0.95 nm), prevents its access to the microporosity.[31] The etching process increases the Brønsted acid site concentration on the external surface leading to a higher conversion compared to the parent zeolite L. Since the external surface of the treated zeolites does not increase substantially, we attribute the improved catalytic performances to a partial opening of zeolite channels. Namely, the extraction of

atoms at the pore mouths increases accessibility to the active sites. It should also be mentioned that unbiased chemical etching performed by  $\text{HF}_2^-$  removes defects and low crystalline parts of the samples.

## 4 Conclusion

A commercial zeolite L sample is etched by aqueous solutions of ammonium fluoride and ammonium bifluoride. The ammonium bifluoride solutions with a concentration higher than 5 % are very aggressive, making the dissolution process hard to be controlled. Lowering the  $\text{NH}_4\text{HF}_2$  concentration slows down the dissolution process and affords better control of the zeolite hierarchization. Etching with 1 and 2 wt/% of  $\text{NH}_4\text{HF}_2$  solutions provides zeolites similar to those obtained with 20 and 40 wt/%  $\text{NH}_4\text{F}$  solutions, respectively. Using  $\text{NH}_4\text{HF}_2$  solutions results in a substantial decrease in the fluoride agent used, a welcome feature for practical applications. Another advantage of  $\text{NH}_4\text{HF}_2$  solutions is the efficient generation of mesopores without causing a collapse of the structure or creating extra framework aluminum. These features of  $\text{NH}_4\text{HF}_2$  etching provide zeolites with high catalytic activity, in particular, to convert bulky hydrocarbons.

## 5 References

- [1] S.M. Auerbach, K.A. Carrado, P.K. Dutta, *Handbook of Zeolite Science and Technology*, CRC Press, 2003.
- [2] D.W. Breck, N.A. Acara, *Crystalline zeolite I*, US3216789A, 1965.
- [3] Ch. Baerlocher, R.M. Barker, The structure of the synthetic zeolite (K,Ba)-G,L, *Zeitschrift Für Kristallographie - Crystalline Materials*. 136 (1972) 245-254.
- [4] M. Breyse, J.-R. Bernard, Process for the dehydrocyclisation of paraffins at very low pressures, EP0040119A1, 1981.
- [5] A.E. Schweizer, Noble metal alkaline zeolites for catalytic reforming, US4992401A, 1991.
- [6] F. Di Renzo, F. Fajula, Introduction to molecular sieves: trends of evolution of the zeolite community, in: *Studies in Surface Science and Catalysis*, Elsevier, 2005: pp. 1-12. [https://doi.org/10.1016/S0167-2991\(05\)80003-5](https://doi.org/10.1016/S0167-2991(05)80003-5).
- [7] J.M. Newsam, B.G. Silbernagel, A.R. Garcia, M.T. Melchior, S.C. Fung, Fundamental Characteristics of the Catalyst System Platinum-Loaded Zeolite L, in: R.K. Grasselli, A.W. Sleight (Eds.), *Studies in Surface Science and Catalysis*, Elsevier, 1991: pp. 211-220. [https://doi.org/10.1016/S0167-2991\(08\)61940-0](https://doi.org/10.1016/S0167-2991(08)61940-0).
- [8] J.C. Bricker, Advanced Catalytic Dehydrogenation Technologies for Production of Olefins, *Top Catal.* 55 (2012) 1309-1314. <https://doi.org/10.1007/s11244-012-9912-1>.
- [9] H. Pan, G. Wei, H. Yuan, Q. Huo, Q. Li, X. Pan, W. Wang, X. Yu, Studies on catalytic cracking catalyst of hydrocarbons with a new type of zeolite L, in: R. Xu, Z. Gao, J. Chen, W. Yan (Eds.), *Studies in Surface Science and Catalysis*, Elsevier, 2007: pp. 1392-1398. [https://doi.org/10.1016/S0167-2991\(07\)81006-8](https://doi.org/10.1016/S0167-2991(07)81006-8).
- [10] P. Huifang, L. Xingyu, W. Guoyou, Y. Hailiang, P. Xinghong, H. Quan, Y. Pingxiang, Synthesis of La-modified ultra stable zeolite L and its application to catalytic cracking catalyst, *Pet. Sci.* 4 (2007) 75-81. <https://doi.org/10.1007/BF03187446>.
- [11] Q. Huo, T. Dou, Z. Zhao, H. Pan, Synthesis and application of a novel mesoporous zeolite L in the catalyst for the HDS of FCC gasoline, *Applied Catalysis A: General*. 381 (2010) 101-108. <https://doi.org/10.1016/j.apcata.2010.03.051>.
- [12] Q. Huo, Y. Gong, T. Dou, Z. Zhao, H. Pan, F. Deng, Novel Micro- and Mesoporous Composite Molecular Sieve Assembled by Zeolite L Nanocrystal and Its Performance for the Hydrodesulfurization (HDS) of Fluid Catalytic Cracking (FCC) Gasoline, *Energy Fuels*. 24 (2010) 3764-3771. <https://doi.org/10.1021/ef901368w>.
- [13] D.P. Serrano, J. Aguado, J.M. Escola, Hierarchical zeolites: materials with improved accessibility and enhanced catalytic activity, in: *Catalysis*, Royal Society of Chemistry, Cambridge, 2011: pp. 253-283. <https://doi.org/10.1039/9781849732772-00253>.
- [14] R. Li, N. Linares, J.G. Sutjianto, A. Chawla, J. Garcia-Martinez, J.D. Rimer, Ultrasmall Zeolite L Crystals Prepared from Highly Interdispersed Alkali-Silicate Precursors, *Angewandte Chemie International Edition*. 57 (2018) 11283-11288. <https://doi.org/10.1002/anie.201805877>.
- [15] E. Koohsaryan, M. Anbia, Nanosized and hierarchical zeolites: A short review, *Chinese Journal of Catalysis*. 37 (2016) 447-467. [https://doi.org/10.1016/S1872-2067\(15\)61038-5](https://doi.org/10.1016/S1872-2067(15)61038-5).
- [16] V. Valtchev, S. Mintova, Hierarchical zeolites, *MRS Bulletin*. 41 (2016) 689-693. <https://doi.org/10.1557/mrs.2016.171>.
- [17] K. Na, C. Jo, J. Kim, K. Cho, J. Jung, Y. Seo, R.J. Messinger, B.F. Chmelka, R. Ryoo, Directing Zeolite Structures into Hierarchically Nanoporous Architectures, *Science*. 333 (2011) 328-332. <https://doi.org/10.1126/science.1204452>.
- [18] R. Szostak, Chapter 6 Secondary synthesis methods, in: H. van Bekkum, E.M. Flanigen, P.A. Jacobs, J.C. Jansen (Eds.), *Studies in Surface Science and Catalysis*, Elsevier, 2001: pp. 261-297. [https://doi.org/10.1016/S0167-2991\(01\)80248-2](https://doi.org/10.1016/S0167-2991(01)80248-2).
- [19] X. Zhang, D. Liu, D. Xu, S. Asahina, K.A. Cychosz, K.V. Agrawal, Y.A. Wahedi, A. Bhan, S.A. Hashimi, O. Terasaki, M. Thommes, M. Tsapatsis, Synthesis of Self-Pillared Zeolite Nanosheets by Repetitive Branching, *Science*. 336 (2012) 1684-1687. <https://doi.org/10.1126/science.1221111>.
- [20] K. Zhang, S. Fernandez, J.A. Lawrence, M.L. Ostraat, Organotemplate-Free  $\beta$  Zeolites: From Zeolite Synthesis to Hierarchical Structure Creation, *ACS Omega*. 3 (2018) 18935-18942. <https://doi.org/10.1021/acsomega.8b02762>.
- [21] Z. Qin, L. Lakiss, J.-P. Gilson, K. Thomas, J.-M. Goupil, C. Fernandez, V. Valtchev, Chemical Equilibrium Controlled Etching of MFI-Type Zeolite and Its Influence on Zeolite Structure, Acidity, and Catalytic Activity, *Chem. Mater.* 25 (2013) 2759-2766. <https://doi.org/10.1021/cm400719z>.

- [22] V. Valentin, J.-P. Gilson, Q. Zhengxing, Method For The Preparation Of Synthetic Crystalline Zeolite Materials With Enhanced Pore Volume, WO 2016/005472 A1, 2015.
- [23] A. Misra, J. Prasad, J.A. Sees, L.H. Hall, Benign method for etching silicon dioxide, US6048406A, 2000.
- [24] A. Feng, Y. Yu, L. Mi, Y. Cao, Y. Yu, L. Song, Synthesis and characterization of hierarchical Y zeolites using  $\text{NH}_4\text{HF}_2$  as dealumination agent, *Microporous and Mesoporous Materials*. 280 (2019) 211–218. <https://doi.org/10.1016/j.micromeso.2019.01.039>.
- [25] R.M. Barrer, H. Villiger, The crystal structure of the synthetic zeolite L, *Zeitschrift für Kristallographie - Crystalline Materials*, 128 (1969) 352. <https://doi.org/10.1524/zkri.1969.128.3-6.352>
- [26] K.A. Tarach, J. Tekla, U. Filek, A. Szymocha, I. Tarach, K. Góra-Marek, Alkaline-acid treated zeolite L as catalyst in ethanol dehydration process, *Microporous and Mesoporous Materials*. 241 (2017) 132–144. <https://doi.org/10.1016/j.micromeso.2016.12.035>.
- [27] H.G. Karge, E. Geidel, *Vibrational Spectroscopy*. In: H.G. Karge, J. Weitkamp (eds) *Characterization I. Molecular Sieves – Science and Technology*, vol 4. Springer, Berlin, Heidelberg. <https://doi.org/inc.bib.cnrs.fr/10.1007/b94235>
- [28] E. Brunner, K. Beck, M. Koch, L. Heeribout, H.G. Karge, Verification and quantitative determination of a new type of Brønsted acid sites in H-ZSM-5 by  $^1\text{H}$  magic-angle spinning nuclear magnetic resonance spectroscopy, *Microporous Materials*. 3 (1995) 395–399. [https://doi.org/10.1016/0927-6513\(94\)00052-W](https://doi.org/10.1016/0927-6513(94)00052-W).
- [29] F. Thibault-Starzyk, I. Stan, S. Abelló, A. Bonilla, K. Thomas, C. Fernandez, J.-P. Gilson, J. Pérez-Ramírez, Quantification of enhanced acid site accessibility in hierarchical zeolites – The accessibility index, *Journal of Catalysis*. 264 (2009) 11–14. <https://doi.org/10.1016/j.jcat.2009.03.006>.
- [30] A. Corma, V. Fornés, L. Forni, F. Márquez, J. Martínez-Triguero, D. Moscotti, 2,6-Di-Tert-Butyl-Pyridine as a Probe Molecule to Measure External Acidity of Zeolites, *Journal of Catalysis*. 179 (1998) 451–458. <https://doi.org/10.1006/jcat.1998.2233>.
- [31] K.-G. Haw, J.-M. Goupil, J.-P. Gilson, N. Nesterenko, D. Minoux, J.-P. Dath, V. Valtchev, Embryonic ZSM-5 zeolites: zeolitic materials with superior catalytic activity in 1,3,5-triisopropylbenzene dealkylation, *New J. Chem.* 40 (2016) 4307–4313. <https://doi.org/10.1039/C5NJ03310A>.
- [32] L. Lakiss, F. Ngoye, C. Canaff, S. Laforge, Y. Pouilloux, Z. Qin, M. Tarighi, K. Thomas, V. Valtchev, A. Vicente, L. Pinard, J.-P. Gilson, C. Fernandez, On the remarkable resistance to coke formation of nanometer-sized and hierarchical MFI zeolites during ethanol to hydrocarbons transformation, *Journal of Catalysis*. 328 (2015) 165–172. <https://doi.org/10.1016/j.jcat.2014.12.030>.
- [33] R. Rachwalik, Z. Olejniczak, M. Hunger, B. Sulikowski, Dealumination of zeolite L:  $^1\text{H}$ ,  $^{29}\text{Si}$  and  $^{27}\text{Al}$  MAS NMR studies, XXXIX Polish Sem. on Nuclear Magnetic Resonance and its Applications, Kraków, Poland 2006, p. 79.
- [34] P. Bartl, W.F. Hölderich, A study of the dealumination methods for zeolite L, *Microporous and Mesoporous Materials*. 38 (2000) 279–286. [https://doi.org/10.1016/S1387-1811\(00\)00147-5](https://doi.org/10.1016/S1387-1811(00)00147-5).
- [35] Z. Qin, G. Melinte, J.-P. Gilson, M. Jaber, K. Bozhilov, P. Boullay, S. Mintova, O. Ersen, V. Valtchev, The Mosaic Structure of Zeolite Crystals, *Angewandte Chemie*. 128 (2016) 15273–15276. <https://doi.org/10.1002/ange.201608417>.



# 5

Preparation of hierarchical SSZ-13  
by  $\text{NH}_4\text{F}$  etching

<b>1</b>	<b>INTRODUCTION</b> .....	<b>81</b>
<b>2</b>	<b>RESULTS</b> .....	<b>83</b>
2.1	X-RAY DIFFRACTION .....	83
2.2	SCANNING ELECTRON MICROSCOPY.....	85
2.3	TRANSMISSION ELECTRON MICROSCOPY.....	87
2.4	N <sub>2</sub> PHYSISORPTION .....	87
2.5	PHYSICOCHEMICAL ANALYSIS .....	89
2.6	SOLID-STATE NMR SPECTROSCOPY.....	90
2.7	ACIDITY CHARACTERIZATION BY FTIR .....	93
2.8	CATALYTIC ACTIVITY .....	98
<b>3</b>	<b>DISCUSSION</b> .....	<b>100</b>
<b>4</b>	<b>CONCLUSION</b> .....	<b>102</b>
<b>5</b>	<b>REFERENCES</b> .....	<b>103</b>

# 1 Introduction

Chabazite, a naturally occurring mineral, was discovered in 1792 by Bosch D'Antic.[1] In 1925, Weigel and Steinhoff studied the adsorption selectivity of dehydrated chabazite.[2] Chabazite is an important member of the small pore, eight-ring zeolites, along with LTA, RHO, ERI, and DDR. The high-silica members of these zeolites have now found widespread application as size-selective adsorbents.[3]

The CHA structure contains large interconnected ellipsoidal cages (0.67 x 1.1 nm<sup>2</sup>), accessible through eight-membered ring windows (0.38 x 0.38 nm<sup>2</sup>). The cage (4<sup>12</sup>6<sup>2</sup>8<sup>6</sup>) has six octagonal windows (8<sup>6</sup>), allowing sorption from all directions[4], and can accommodate fairly large molecules. The structure features of Chabazite explain the unique selectivity to olefins in the MTO process, where the bulky aromatic molecules are prisoned in the cage, and only lower olefins (2–4 carbon atoms) can leave it.[5] In the Al-rich forms of chabazite, the windows are partially obstructed by the exchangeable cations compensating the negative surface charge.

SSZ-13 is the aluminosilicate analog of chabazite type SAPO-34, used commercially along with ZSM-5 as a methanol-to-olefin (MTO) catalyst.[6] The SAPO-34 MTO catalyst deactivates during operation, and a fluidized bed is required for continuous olefins production.[7] However, SSZ-13 deactivates faster than SAPO-34[8], and extending the lifetime of the SSZ-13 catalyst can be done by shortening the diffusion pathlength on molecules in the microporosity, either by reducing the crystallite size or generating mesopores, *i.e.*, hierarchization.[9] Copper exchanged SSZ-13 has been used as a catalyst for the last decade in NO<sub>x</sub> emission control in the ammonia selective catalytic reduction (NH<sub>3</sub>-SCR) process.[10]

Often an as-synthesized zeolite does not provide the desired material properties, and post-synthesis treatments are required to fine-tune some specific zeolite properties.[11] A wide variety of post-synthesis treatments, such as alkaline leaching,[12–14] dealumination by ammonium hexafluorosilicate,[15] nitric acid,[16] and neutron irradiation[17] have been used to prepare hierarchical SSZ-13 with mixed results since they either cause structural collapse or modify acidity.

Traditionally SSZ-13 is synthesized in the presence of N,N,N-trimethyl-1-adamantanammonium hydroxide (TMAdaOH), and the crystals are usually larger than 1 μm.[18] Nanosized SSZ-13 has been successfully synthesized via a one-pot strategy by adding hexadecyl trimethylammonium bromide (CTAB) surfactant.[6] Wu *et al.* prepared mesoporous SSZ-13 using a dual template strategy: a diquaternary-ammonium surfactant ([C<sub>22</sub>H<sub>45</sub>-N<sup>+</sup>(CH<sub>3</sub>)<sub>2</sub>-(CH<sub>2</sub>)<sub>4</sub>-N<sup>+</sup>(CH<sub>3</sub>)<sub>2</sub>-C<sub>4</sub>H<sub>9</sub>Br<sub>2</sub>] denoted as C<sub>22-4-4</sub>Br<sub>2</sub>) as sacrificial mesoporegen, along with N,N,N-trimethyl-1-adamantanammonium hydroxide (TMAdaOH).[19,20] The resulting hierarchical catalyst showed increased conversion and improved stability in the MTO reaction. Another study showed that the C<sub>22-4-4</sub>Br<sub>2</sub> mesoporegen combined with fluoride anions could yield hierarchical SSZ-13 with trimodal porosity.[21] Mesoporous SSZ-13 can also be obtained using a mono-quaternary ammonium head group (N-methyl piperidine).[22] Liu *et al.* explored biphasic/toluene media to generate mesopores in SSZ-13.[23]

Post-synthesis methods, particularly caustic leaching, generate mesopores at the expense of micropore volume. Previous studies focused on SSZ-13 desilication showed no improvement in NH<sub>3</sub>-SCR[12] or MTO reaction despite the introduction of mesopores.[13] Wardani *et al.* managed to preserve the crystallinity and micropore volume of SSZ-13 by leaving the template in the pores during desilication.[14] The activity of SSZ-13 in MTO reaction was improved by neutron irradiation; however, hydrothermal methods of post-synthesis treatment are more practical.[17] Dai *et al.* employed dealumination by nitric acid to modify the properties of SSZ-13.[16] Their method altered acidity and lowered micropore volume but extended the catalyst lifetime in the ethene-to-propene (ETP) reaction. Haw *et al.* synthesized mesoporous SSZ-13 using NH<sub>4</sub>F-H<sub>2</sub>O<sub>2</sub> solutions, retaining the intrinsic zeolite properties.[24] The use of H<sub>2</sub>O<sub>2</sub> resulted in the ultra-fast dissolution of SSZ-13 crystals and the formation of a sponge-like structure.

The sole use of  $\text{NH}_4\text{F}$  as an etching agent also allows the preparation of hierarchical zeolites.[25] The ammonium fluoride route to hierarchical zeolites was applied to various low and high silica zeolites to generate mesoporosity while preserving their Si/Al ratio, *i.e.*, acid site concentration.[26] The present study is devoted to the  $\text{NH}_4\text{F}$  etching on SSZ-13 zeolite and a comprehensive analysis of its hierarchical derivatives' physicochemical properties.

## 2 Results

### 2.1 X-ray diffraction

XRD patterns of the parent zeolite and its etched derivatives are plotted in **Figure 5.1**. Briefly, for better understanding the sample notation, the etched samples are divided to three series, I, II and III referring to the liquid-solid ratio used during the synthesis, 8, 20 and respectively. CHA-8-x-y, refers to a sample prepared with l/s of 8, x refers to the temperature of preparation, varied from 0 to 50 °C and y refers to the time of the treatment, varied from 5 to 20 min. Series I zeolites, prepared with a liquid/solid ratio of 8, showed the highest relative crystallinity of 96–90 %, except for sample CHA-8-50-20 (78 %). The latter indicates that higher temperatures promote amorphization. The temperature's impact is more pronounced when an etching solution with a higher liquid/solid ratio is employed. Thus, from the samples from series II with a liquid/solid ratio of 20, only the one prepared at 50 °C (CHA-20-50-20) showed a substantial decrease of crystallinity (77 %). Series III samples analysis further confirmed the impact of temperature. This last series of samples with liquid/solid = 100 maintain high crystallinity for the sample prepared at a temperature of 0 and 25 °C. However, the products prepared at 50 °C are examples of substantial amorphization; for instance, the relative crystallinity of CHA-100-50-5 and CHA-100-50-20 is 39 and 9 %, respectively. Thus, the elevated temperatures contribute to the amorphization of the structure. Since all the solutions have the same concentrations of 40 wt/%  $\text{NH}_4\text{F}$  in water, the liquid/solid ratio modifies the number of fluoride species available for the reaction. Rising overall fluoride content contributes to structural degradation. This effect is the most clearly demonstrated by the series with the highest liquid/sold ratio (series III), which exhibits the highest amorphization level. The amorphization is demonstrated by the decrease in the peak intensity and the appearance of a broad halo in the range of 15–30°  $2\theta$  (**Figure 5.1**).

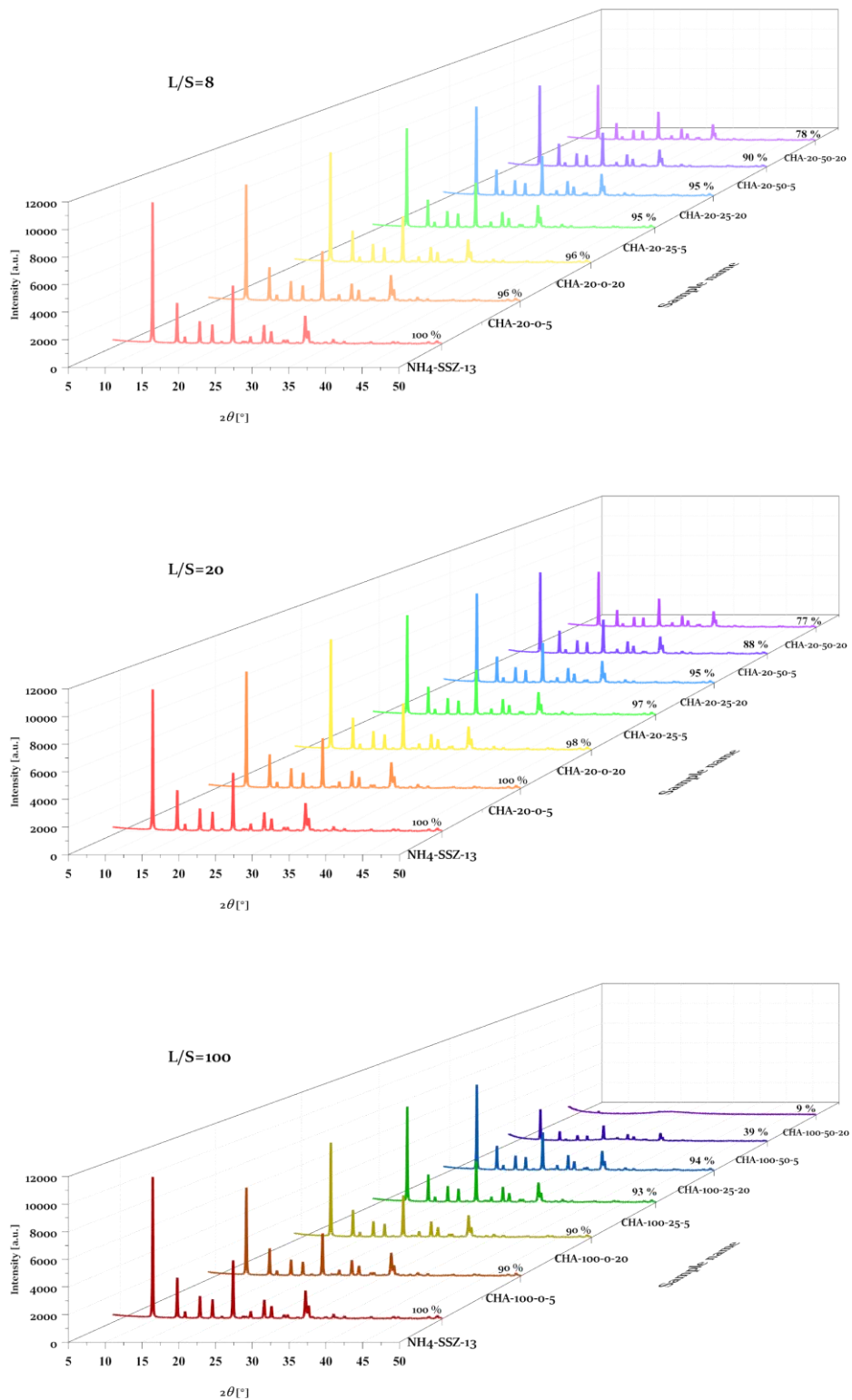
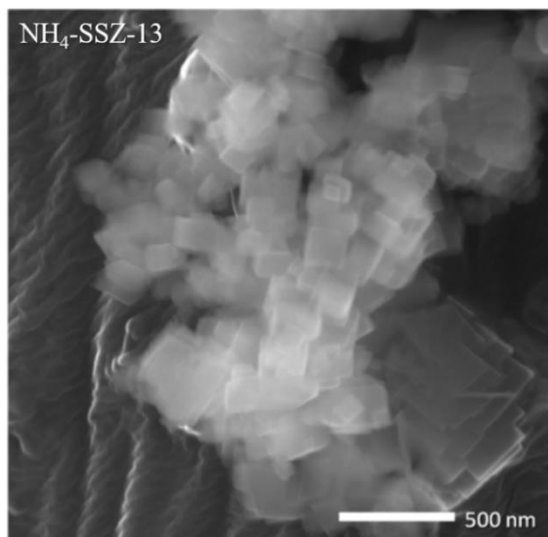


Figure 5.1. XRD patterns of etched derivatives and their parent NH<sub>4</sub>-SSZ-13. Samples prepared with a Liquid/Solid ratio of 8, 20, and 100 are plotted. The relative (to the NH<sub>4</sub>-SSZ-13 parent) crystallinity is indicated on each pattern.

## 2.2 Scanning electron microscopy

SEM shows isometric SSZ-13 crystals with a cubic appearance. Their size ranges between 100 and 500 nm as the crystallites form larger agglomerates up to 1000 nm (**Figure 5.2**). The surface of parent crystals is flat with distinguishable edges and corners. The morphology of series I crystals is almost intact with minor signs of surface etching and separated intergrowths traces (**Figure 5.3A and B**). In series II (**Figure 5.3C and D**), more visible traces of etching are apparent. CHA-20-50-20 exhibits small holes ( $\sim 10\text{--}40$  nm) on the surface penetrating the crystals. The etching also removes parts of the crystals on the surface, eliminating intergrowths, and making the surface rougher. The effects of etching are more pronounced in series III (**Figure 5.3E and F**). CHA-100-0-20 displays holes in the mesopore range, penetrating in the crystals' core. A few cubic particles characteristic of SSZ-13 are visible in CHA-100-50-20. The sample also contains very small particles, most probably amorphous, with a random morphology.



**Figure 5.2.** Representative SEM micrograph of the parent SSZ-13.

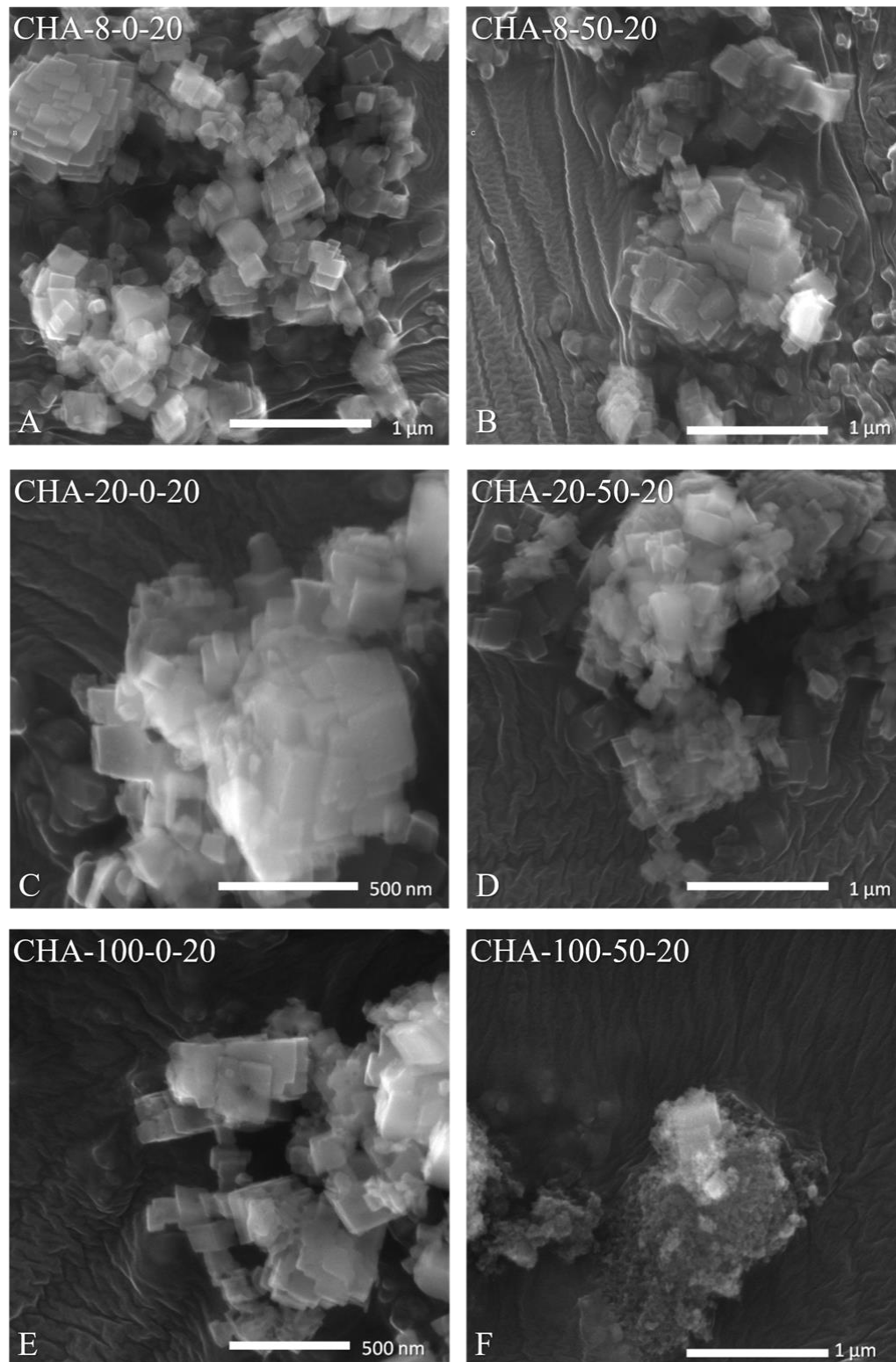
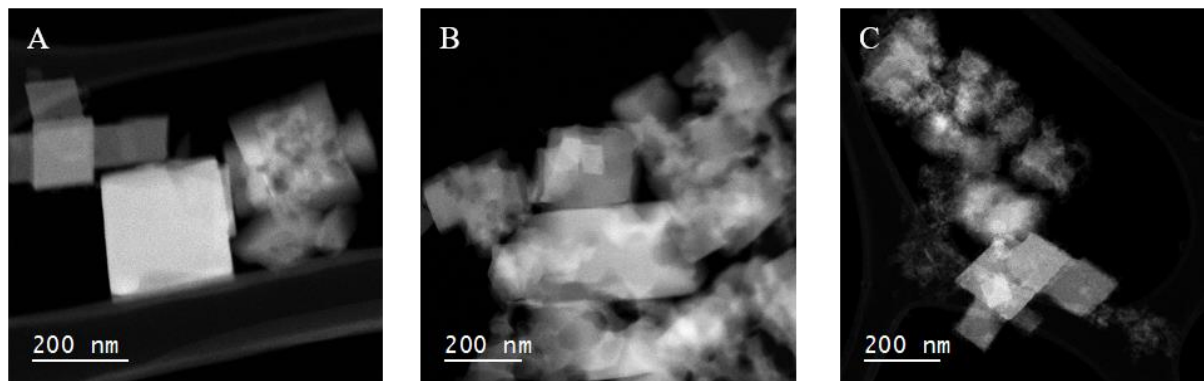


Figure 5.3. SEM micrographs of the etched samples: (A, B) series I, (C, D) series I, and (E, F) series III.

## 2.3 Transmission electron microscopy

More details of series III samples etching are observed by TEM (**Figure 5.4**). CHA-100-25-5 (**Figure 5.4A**) exhibits a mostly regular cubic-like structure, with the average edges' lengths of about 200 nm. The etching removes parts of crystals leaving porous crystals (a "swiss cheese"-like oval mesopores) with the outer edges of similar sizes as for the non-porous crystals. CHA-100-25-20 (**Figure 5.4B**) is prepared as CHA-100-25-5 but with a 20 minutes etching. Its crystals' surface is rougher and marked by pores with depths up to 100 nm covering all faces. CHA-100-50-5 specimen (**Figure 5.4C**) exhibits two types of morphologies, very small particles most likely amorphous, with a foam type of structure, similar to those observed in CHA-100-50-20 by SEM (**Figure 5.3**), and few cubic non-porous crystals.



**Figure 5.4.** STEM-HAADF micrographs of: (A) CHA-100-25-5, (B) CHA-100-25-20 and (C) CHA-100-50-5.

## 2.4 $\text{N}_2$ physisorption

$\text{N}_2$  physisorption curves are shown in **Figure 5.5**. The parent  $\text{NH}_4\text{-SSZ-13}$  displays an I (a) type isotherm characteristic of microporous materials with a steep uptake at low relative pressure. The isotherm ends with an H4 hysteresis loop, characteristic of slit-type shape pores.[27] The analysis of the  $\text{N}_2$  adsorption isotherms of the parent and its derivative is summarized in **Table 5.1**. The parent has a micropore volume of  $0.27 \text{ cm}^3 \text{ g}^{-1}$ , a mesopore volume of  $0.04 \text{ cm}^3 \text{ g}^{-1}$ , and a specific surface area of  $700 \text{ m}^2 \text{ g}^{-1}$ .

The etched samples display a high uptake in the micropore region, as they retain or even gain micropore volume compared to their parent. (**Figure 5.5**). In contrast, the severely etched samples, like CHA-100-50-5 and CHA-100-50-20, lose microporosity (**Figure 5.5E and F**). The textural changes are so profound in deeply etched samples that they exhibit a different type of isotherm. For instance, the CHA-100-50-20 isotherm has the features of type IV (a), and the hysteresis loop is an H1 type.[28]

The etched zeolites have mesopore volumes between  $0.06 \text{ cm}^3 \text{ g}^{-1}$  and  $0.98 \text{ cm}^3 \text{ g}^{-1}$ , depending on the treatment conditions. In general, the etching close to  $0^\circ \text{C}$  and at ambient temperature ( $25^\circ \text{C}$ ) generate limited mesopore volume. Upon such conditions, the mesoporosity is not created at the expense of the native microporosity. A combination of high temperature and high l/s ratio etches the samples deeply and increases mesopore volume as in CHA-100-50-5 ( $0.75 \text{ cm}^3 \text{ g}^{-1}$ ) and CHA-100-50-20 ( $0.98 \text{ cm}^3 \text{ g}^{-1}$ ). However, loss of microporosity is observed in both samples, CHA-100-50-5 having a decrease to  $0.17 \text{ cm}^3 \text{ g}^{-1}$  and CHA-100-50-20 to  $0.08 \text{ cm}^3 \text{ g}^{-1}$

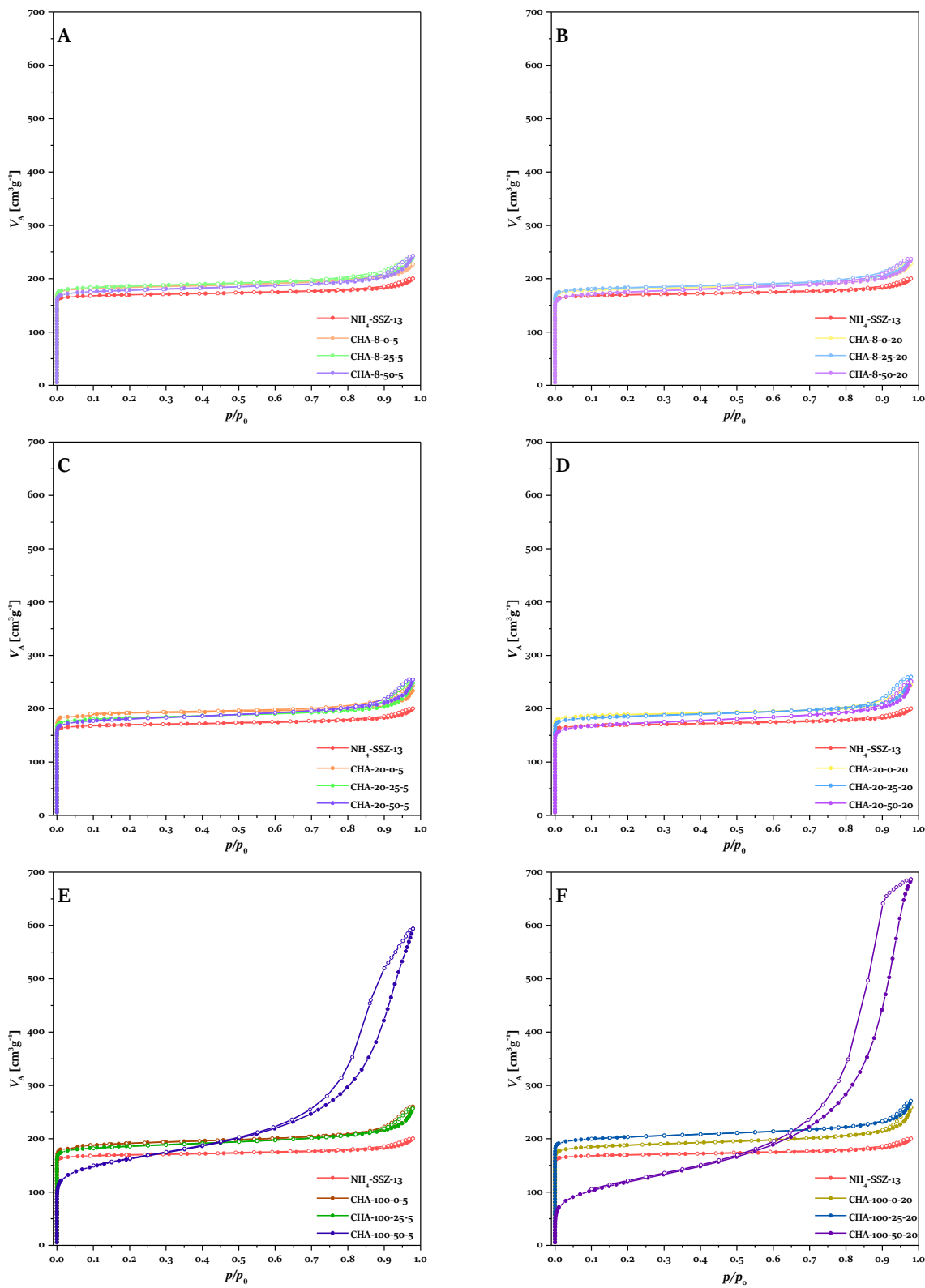


Figure 5.5.  $N_2$  physisorption isotherms of series I (A, B), series II (C, D), and series III (E, F) samples.

## 2.5 Physicochemical analysis

The parent NH<sub>4</sub>-SSZ-13 has a Si/Al<sub>ICP</sub> ratio of 9 (Table 5.2). Depending on the treatment conditions, Si/Al changes, but in series I and II, the Si/Al ratio is mostly maintained and fluctuates between 9–11 even at the highest temperature (50 °C). More significant Si/Al changes occur in series III at 50 °C treatment when Si/Al reaches 30 and 288 (Table 5.2). These materials, however, are partially or fully amorphized (Figure 5.1).

**Table 5.1. Physicochemical properties of parent and NH<sub>4</sub>F etched samples.**

	Sample	V <sub>micro</sub> cm <sup>3</sup> g <sup>-1</sup>	V <sub>meso</sub> cm <sup>3</sup> g <sup>-1</sup>	S <sub>BET</sub> m <sup>2</sup> g <sup>-1</sup>	Si/Al <sub>ICP</sub> mol mol <sup>-1</sup>	Al <sub>ICP</sub> μmol g <sup>-1</sup>
Series I	NH <sub>4</sub> -SSZ-13	0.27	0.04	700	9.0	1234
	CHA-8-0-5	0.29	0.06	758	9.1	1221
	CHA-8-25-5	0.29	0.08	765	9.0	1234
	CHA-8-50-5	0.28	0.10	728	10.2	1100
	CHA-8-0-20	0.28	0.07	745	9.0	1234
	CHA-8-25-20	0.29	0.08	752	9.7	1152
	CHA-8-50-20	0.27	0.10	700	10.6	1061
Series II	CHA-20-0-5	0.31	0.07	800	9.0	1234
	CHA-20-25-5	0.28	0.10	748	9.0	1234
	CHA-20-50-5	0.28	0.12	725	9.3	1197
	CHA-20-0-20	0.30	0.08	779	9.0	1234
	CHA-20-25-20	0.28	0.10	757	9.8	1141
	CHA-20-50-20	0.26	0.13	679	11.1	1017
Series III	CHA-100-0-5	0.30	0.11	780	9.5	1174
	CHA-100-25-5	0.29	0.11	750	9.9	1130
	CHA-100-50-5	0.17	0.75	522	29.5	400
	CHA-100-0-20	0.29	0.11	763	9.8	1141
	CHA-100-25-20	0.32	0.10	824	11.4	992
	CHA-100-50-20	0.08	0.98	309	287.9	42

The Si/Al ratios obtained by STEM-EDX analysis are shown in Figure 5.4. The Si/Al ratio observed for samples CHA-100-25-5, CHA-100-25-20, and CHA-100-50-5 differ from the ICP-AES method results. In samples CHA-100-25-5 and CHA-100-25-20, the silicon to aluminum content is 3 to 4 fold higher. CHA-100-50-5 sample has zones that are significantly depleted of Al, and the observed ratio is 1.4 to 19 folds more elevated than the ratio found by ICP-AES. The fluctuation of Si and Al content in different crystals is attributed to the different levels of amorphization. These results illustrate that the crystallinity lost is related to a preferential dealumination. Also, there is a gradient of Al concentration in deeply etched samples, as the surface and the core of a crystal can exhibit different framework compositions.

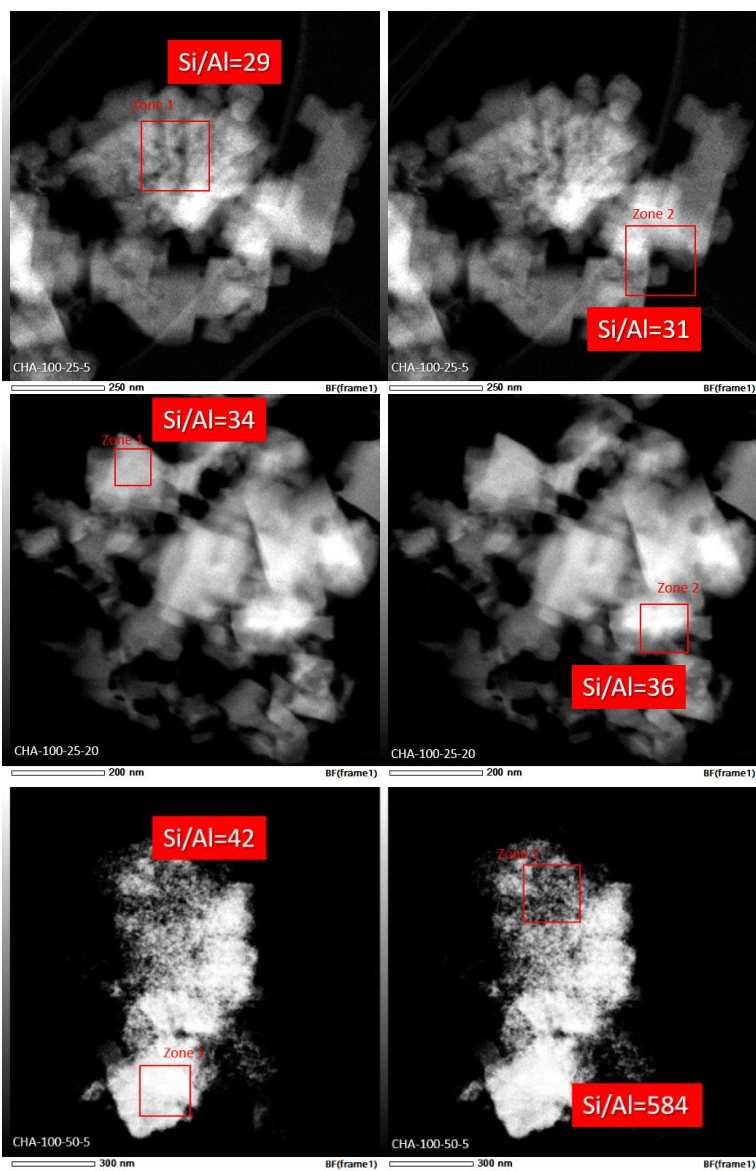
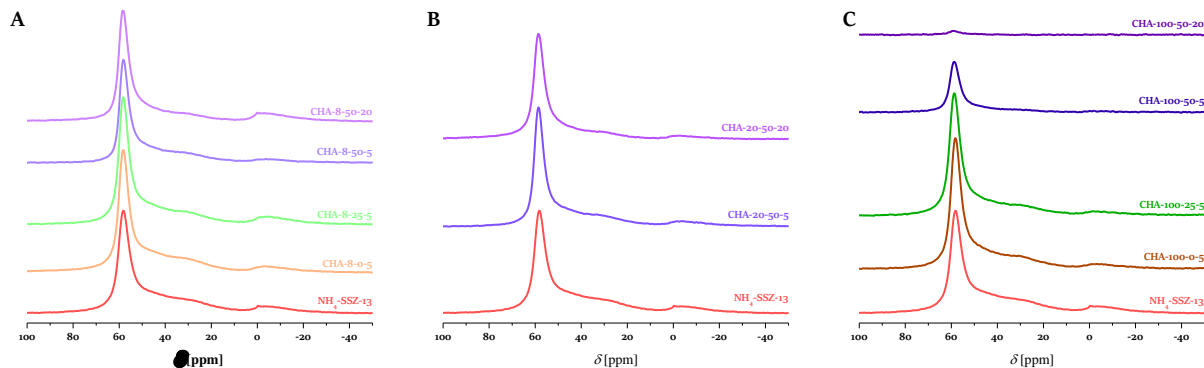


Figure 5.6. Synthesis of the STEM-EDX analyses of three types of samples: CHA-100-25-5 (top row), CHA-100-25-20 (middle row), and CHA-100-50-5 (bottom row).

## 2.6 Solid-state NMR spectroscopy

While ICP provides a bulk composition,  $^{27}\text{Al}$  MAS NMR will distinguish between framework and extra-framework aluminum. **Figure 5.7** summarizes aluminum's state in the parent and the derivatives from series I, II, and III. All spectra display three peaks, often encountered in zeolites. The peak at 58 ppm is characteristic of the framework, tetrahedrally coordinated aluminum. The broad tailing between 50 and 30 ppm is attributed to distorted tetrahedral or penta-coordinated aluminum. The low-intensity broad peak between 0 and -10 ppm is due to extraframework hexacoordinated aluminum species.



**Figure 5.7.** <sup>27</sup>Al MAS NMR spectra of the non-calcined samples from (A) series I, (B) series II, and (C) series III.

The peak intensities of zeolites in series I (**Figure 5.7A**) and II (**Figure 5.7B**) are mostly preserved. In contrast, the deeply etched samples from series III (CHA-100-50-5 and CHA-100-50-20) show a substantial decrease in peak intensities (**Figure 5.7C**). **Table 5.2** summarizes the ICP and <sup>27</sup>Al MAS NMR results. The data show an increase in extra framework Al after calcination, which is below 20 % of overall Al content for most tested samples, except CHA-8-0-5 and CHA-8-25-5. The amount of Al, which remains in tetrahedral coordination and provides a Brønsted acid site, is evaluated. As can be seen, the sample treated under mild conditions retains the number of Brønsted acid sites.

**Table 5.2.** Chemical composition of the samples obtained from ICP-AES and <sup>27</sup>Al MAS NMR data.

Sample	As-synthesized			Calcined	
	Si/Al <sub>ICP</sub> mol mol <sup>-1</sup>	Al <sub>ICP</sub> μmol g <sup>-1</sup>	Al <sup>IV</sup> <sub>NMR</sub> μmol g <sup>-1</sup>	Si/Al <sup>IV</sup> mol mol <sup>-1</sup>	Al <sup>VI</sup> %
NH <sub>4</sub> -SSZ-13	9.0	1234	1101	10.1	27.2
CHA-8-0-5	9.1	1221	1131	9.8	24.2
CHA-8-25-5	9.0	1234	1113	10.0	30.3
CHA-8-50-5	10.2	1100	1028	10.9	18.5
CHA-8-50-20	10.6	1061	923	12.2	/
CHA-20-50-5	9.3	1197	1105	10.1	/
CHA-20-0-20	9.0	1234	/	/	19.4
CHA-20-25-20	9.8	1141	/	/	17.9
CHA-20-50-20	11.1	1017	966	11.7	18.6
CHA-100-0-5	9.5	1174	1102	10.1	/
CHA-100-25-5	9.9	1130	1066	10.5	/
CHA-100-50-5	29.5	400	373	31.7	/
CHA-100-0-20	9.8	1141	/	/	17.4
CHA-100-50-20	287.9	42	42	287.9	/

<sup>29</sup>Si MAS NMR is also a reliable technique to measure the Si/Al framework composition. **Figure 5.8A** highlights the spectra of the NH<sub>4</sub>-SSZ-13 parent and one derivative (CHA-20-50-20). Both spectra exhibit three peaks at chemical shifts (δ) -111, -105, and -99 corresponding to Si(4Si, 0Al), Si(3Si, 1Al) and Si(2Si, 2Al), respectively.[29] The magnitude of resonance peaks is strongly impacted by the number of the neighboring framework atoms, and Al, as the nearest neighbor, has a strong influence on the intensity of those peaks.[30] Sample CHA-20-50-20 shows the decreased intensity of the resonance peaks corresponding to Si(4Si, 0Al), Si(3Si, 1Al). The decreasing intensity of the resonance peaks is related to a decreasing number of neighboring Al atoms.

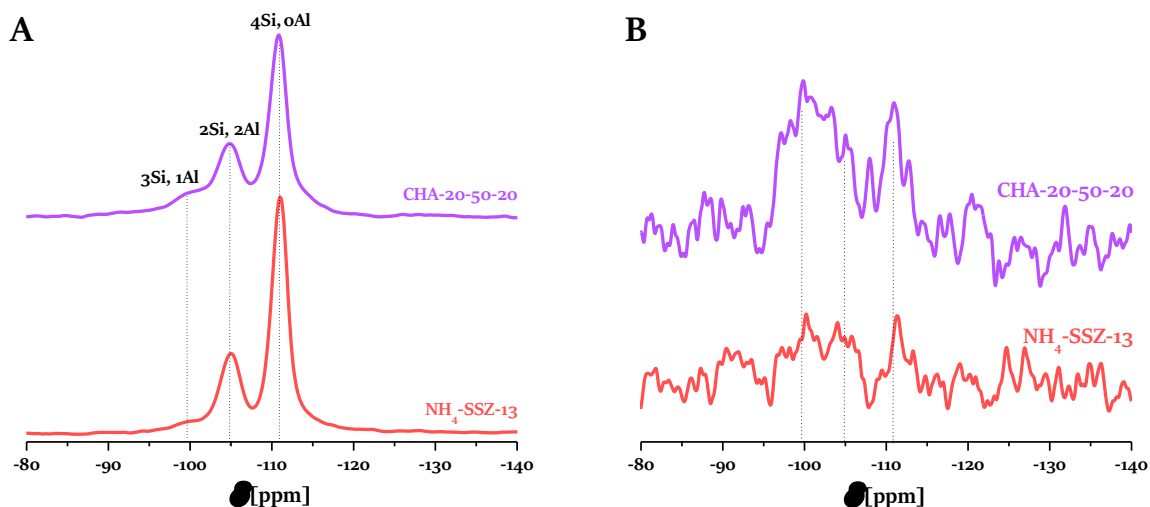


**Figure 5.8.**  $^{29}\text{Si}$  MAS NMR spectra (A) and  $^{29}\text{Si}\{^1\text{H}\}$  cross-polarization spectra (B) of  $\text{NH}_4\text{-SSZ-13}$  and one derivative,  $\text{CHA-20-50-20}$ .

$^{29}\text{Si}\{^1\text{H}\}$  cross-polarization NMR gives qualitative information on the silanol species in zeolites. The spectra of the parent and  $\text{CHA-20-50-20}$  sample are depicted in **Figure 5.8B**. The parent material exhibits resonance peaks in the area -110 to -90 ppm. In this range, there is some overlap of the peaks related to Si-O-Al and Si-O-OH. Sample  $\text{CHA-20-50-20}$  shows an increase of the peak intensity in the -110 to -90 ppm region, which is attributed to a rise in Si-OH group concentration. The extraction of a framework atom results in the formation of silanol groups highlighted by the  $^{29}\text{Si}\{^1\text{H}\}$  cross-polarization NMR spectrum changes.

$^{19}\text{F}$  MAS NMR (**Figure 5.9**) is a very sensitive technique that can detect traces (ppb) of fluor in solids and verify if the etched zeolites retain some fluorinated products from the reaction.[31] All spectra  $^{19}\text{F}$  MAS NMR show a broad peak around -103 ppm due to the rotor cap's PTFE signal. Besides, several weak peaks are observed in  $\text{CHA-100-50-20}$ ,  $\text{CHA-20-50-20}$ , and  $\text{CHA-8-50-20}$  samples. These peaks emanate from the etching reaction products, as -169, -152, -140, and -125 ppm resonances reveal the presence of  $\text{SiF}_4$ ,  $\text{Na}_2\text{SiF}_6$ ,  $(\text{NH}_4)_3\text{AlF}_6$ , and  $(\text{NH}_4)_2\text{SiF}_6$ , respectively. The peaks' intensity is low, showing the low content of these products. After calcination, the traces of fluorine compounds disappeared.

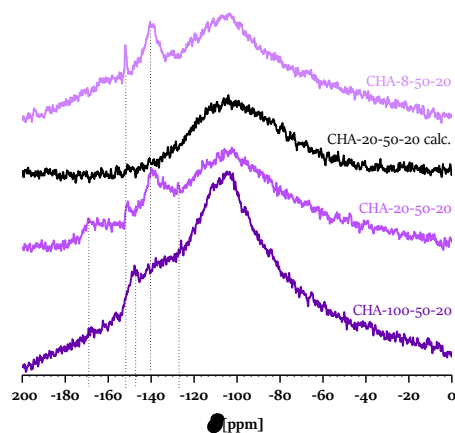


**Figure 5.9.**  $^{19}\text{F}$  MAS NMR spectra of samples  $\text{CHA-100-50-20}$ ,  $\text{CHA-20-50-20}$ ,  $\text{CHA-20-50-20}$  calcined, and  $\text{CHA-8-50-20}$ .

## 2.7 Acidity characterization by FTIR

The acidity of the etched zeolites is studied by IR spectroscopy using deuterated acetonitrile as a probe molecule.  $\text{CD}_3\text{CN}$  adsorbed on acid sites is detected in the  $2400\text{--}2200\text{ cm}^{-1}$  spectral window (**Figure 5.10**). The deconvolution of the  $2360\text{--}2180\text{ cm}^{-1}$  spectral range reveals five peaks (**Figure 5.11**), four sharp at  $2324$ ,  $2316$ ,  $2295$ ,  $2283$ ,  $2265\text{ cm}^{-1}$ , and a broad one centered at  $2214\text{ cm}^{-1}$ . The  $2283\text{ cm}^{-1}$  peak is attributed to  $\text{CD}_3\text{CN}$  interacting with silanols observed on a purely siliceous material MFI-type material.[32]

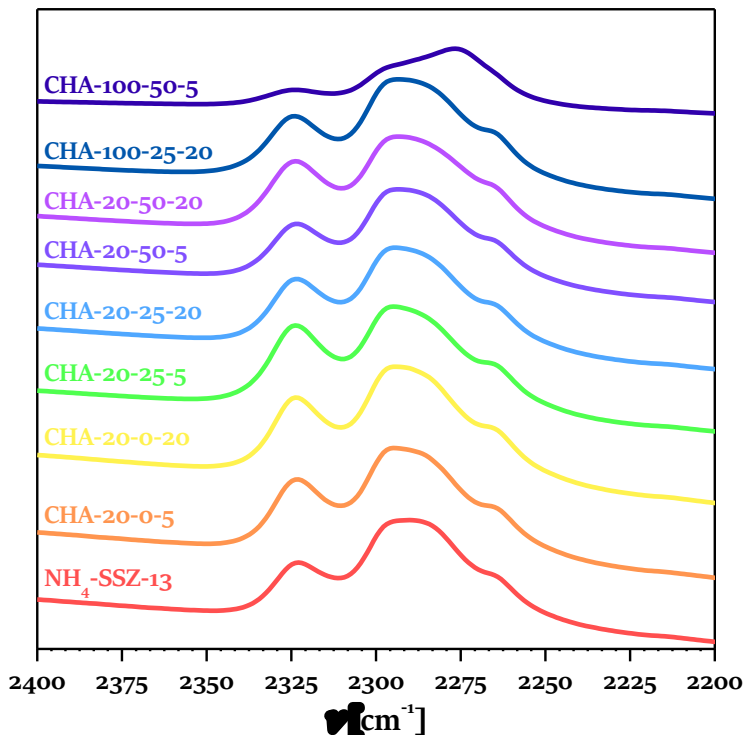


**Figure 5.10.** Bands of adsorbed acetonitrile  $2400\text{--}2200\text{ cm}^{-1}$  on parent sample ( $\text{NH}_4\text{-SSZ-13}$ ) and etched samples.

The  $2324\text{ cm}^{-1}$  peak corresponds to  $\text{CD}_3\text{CN}$  interacting with Lewis acid sites[33] while the  $2265\text{ cm}^{-1}$  corresponds to physisorbed  $\text{CD}_3\text{CN}$ . The  $2298\text{ cm}^{-1}$  peak results from  $\text{CD}_3\text{CN}$  interacting with Brønsted acid sites, while the attribution of the  $2310\text{ cm}^{-1}$  peak is a matter of debate and could be due to  $\text{CD}_3\text{CN}$  interacting with either weak Lewis acid sites[34] or weak Brønsted acid sites.[35]

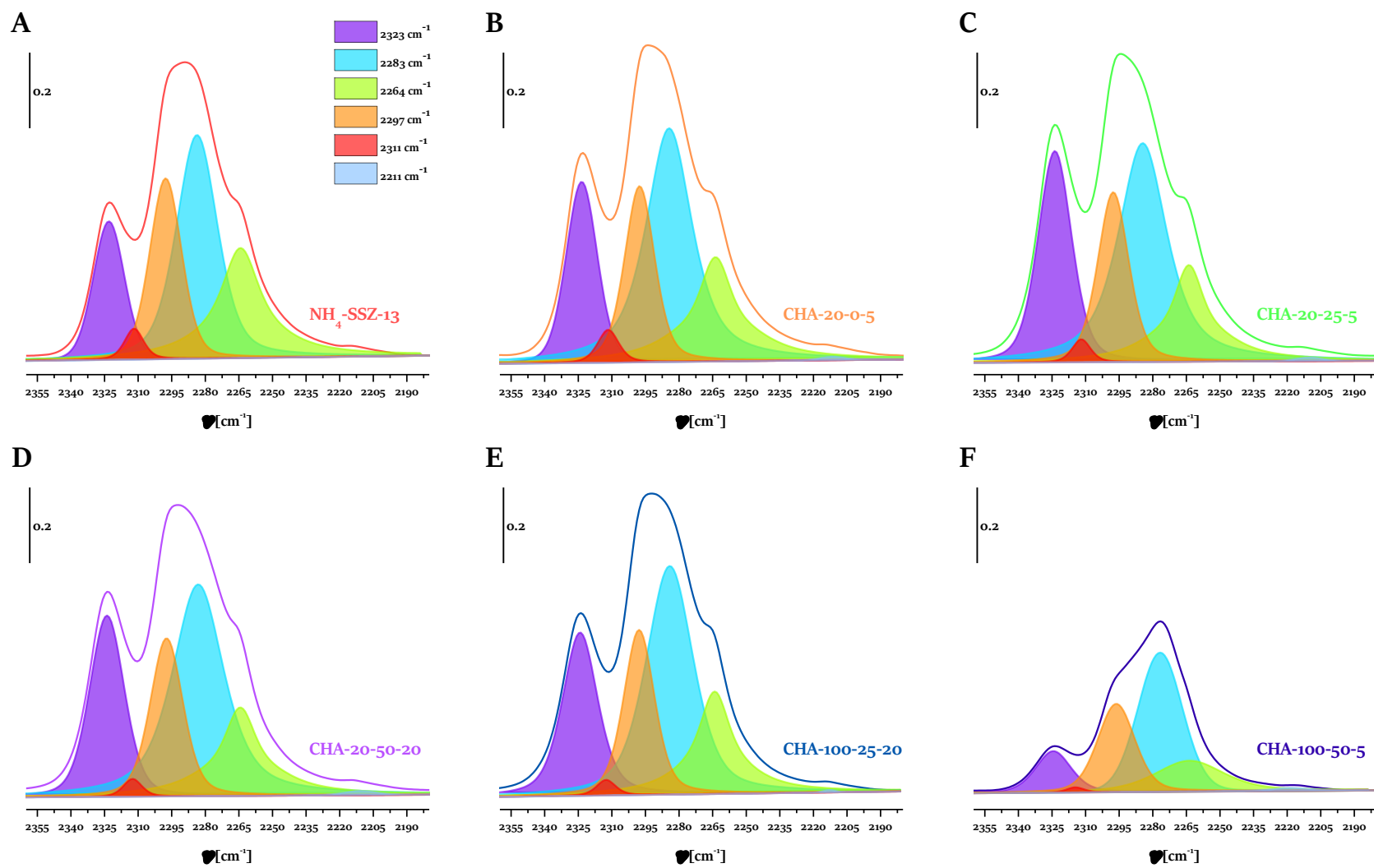


Figure 5.11. Deconvoluted bands in the range 2360–2180  $\text{cm}^{-1}$  of the parent (A) and different etched (B-F) samples.

The acid site concentrations, Brønsted ( $c_B$ ), and Lewis ( $c_L$ ) are summarized in **Table 5.3**. The Brønsted acidity is preserved on all etched samples except for some deeply etched ones from series III (CHA-100-25-20, CHA-100-50-5), where their Lewis acidity increases.

Here, we define the accessibility index (ACI) as the number of acid sites ( $c_B + c_L$ ) detected by CD<sub>3</sub>CN adsorption divided by the total amount of acid sites in the zeolite, based on the measured aluminum content ( $Al_{ICP}$ ).<sup>[36]</sup> In the parent NH<sub>4</sub>-SSZ-13, ACI is 0.47. The etched zeolites in series I and II have ACI in the range 0.52-0.61, while under more severe conditions as in series III, ACI increases to 0.70 for CHA-100-50-5. The latter zeolite, however, lost much of its Brønsted acidity.

**Table 5.3. Acid site concentrations of the parent H-SSZ-13 and its etched derivatives.**

Sample	$Al_{ICP}$ $\mu\text{mol g}^{-1}$	$c_L$ $\mu\text{mol g}^{-1}$	$c_B$ $\mu\text{mol g}^{-1}$	$c_B + c_L$ $\mu\text{mol g}^{-1}$	ACI -
H-SSZ-13	1234	176	401	577	0.47
CHA-20-0-5	1234	245	400	645	0.52
CHA-20-0-20	1234	276	396	672	0.54
CHA-20-25-5	1234	322	413	735	0.60
CHA-20-50-5	1197	205	417	622	0.52
CHA-20-25-20	1141	240	371	611	0.54
CHA-20-50-20	1017	288	330	618	0.61
CHA-100-25-20	992	251	285	536	0.54
CHA-100-50-5	400	59	222	281	0.70

The activated parent sample is studied by IR spectroscopy. The OH region's deconvolution reveals a series of bands in the 3750–3450 cm<sup>-1</sup> range (**Figure 5.12**).

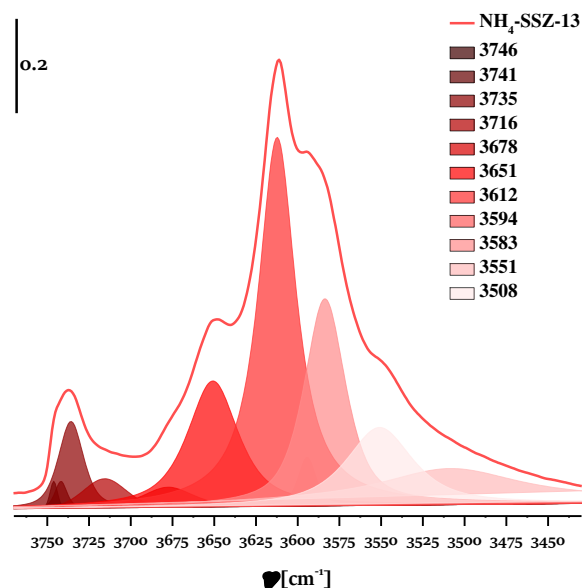


**Figure 5.12.** Unperturbed OH sites in the area  $3800\text{--}3400\text{ cm}^{-1}$  of zeolite H-SSZ-13 taken at room temperature after activation.

The etched samples showed similar spectra with the exceptions of samples CHA-20-50-20 and CHA-100-50-5, where silanol bands become more prominent (**Figure 5.13**). As the CHA structure contains one T-site and four crystallographically different oxygen atoms, four possible acid site configurations are possible.[37] Suzuki *et al.* attribute the  $\sim 3644$ ,  $\sim 3616$ ,  $\sim 3575$ , and  $\sim 3538\text{ cm}^{-1}$  bands to acidic OH groups on four non-equivalent oxygen sites in the CHA structure.[38] The complex  $3735\text{ cm}^{-1}$  band represents isolated silanols in the zeolite, while the  $3716\text{ cm}^{-1}$  band is related to vicinal silanol groups.[37] The bridged hydroxyls (Brønsted acid sites) are observed as a composite band centered around  $3612\text{ cm}^{-1}$  with a shoulder at  $3594\text{ cm}^{-1}$ . The bands  $3660\text{--}3680\text{ cm}^{-1}$  indicate the presence of an extra framework or distorted framework aluminum.[37]

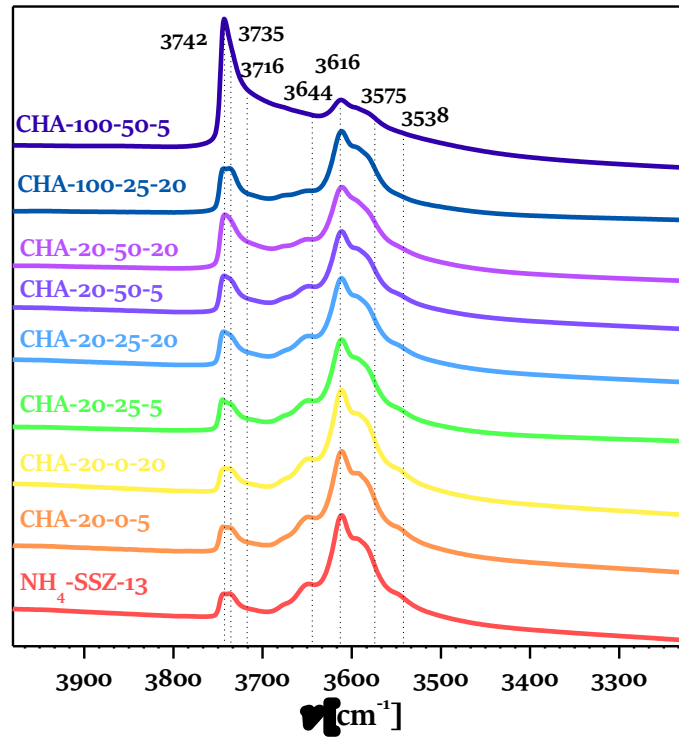
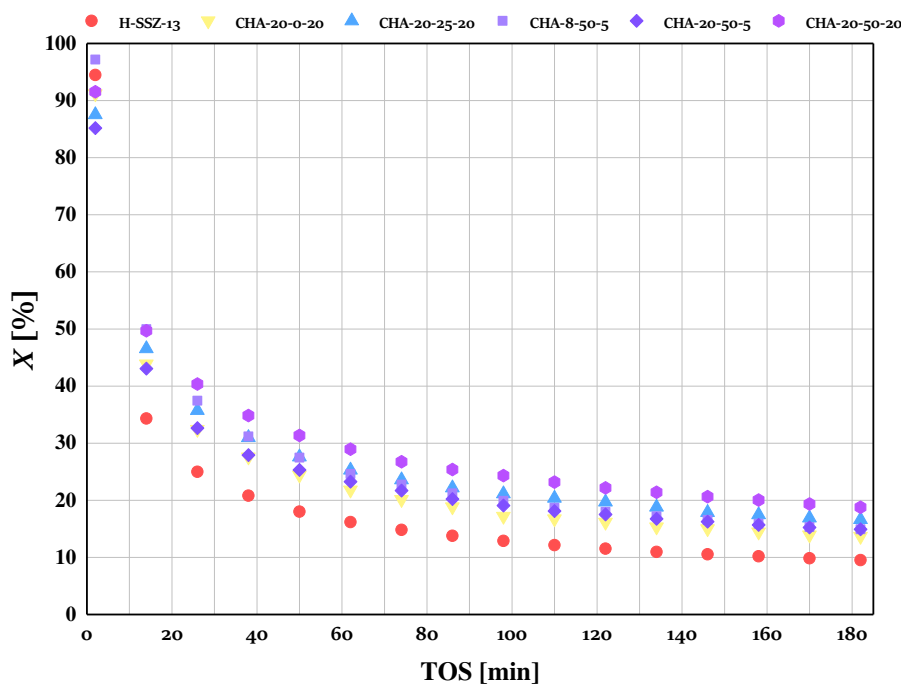


Figure 5.13. Room temperature IR spectra of the pristine surface hydroxyls of the H-SSZ-13 zeolite and its derivatives after activation ( $T = 450\text{ }^\circ\text{C}$ ).

## 2.8 Catalytic activity

The dehydration of n-propanol is a reaction catalyzed by Brønsted acid sites. We have employed this reaction to screen the catalytic properties of the hierarchical derivatives of SSZ-13. Under our conditions ( $T = 205\text{ }^{\circ}\text{C}$ ,  $P = 1\text{ bar}$ ,  $W/F^{\circ}$  of  $27.2\text{ kg mol}^{-1}\text{ s}$ ), the protonic form of the parent has an initial conversion of 94 %, but it decreases fast with time on stream (TOS) (**Figure 5.14**). After 10 minutes of TOS, the conversion falls to about 30 %. All etched samples have a similar initial conversion, between 85 and 95 %, with sample CHA-8-50-5 having the highest (97 %) initial conversion.



**Figure 5.14.** The n-propanol conversion ( $X$ [%]) with time on stream (TOS/min) for the H-SSZ-13 parent and some  $\text{NH}_4\text{F}$  etched derivatives ( $T = 205\text{ }^{\circ}\text{C}$ ,  $P = 1\text{ bar}$ ,  $W/F^{\circ} = 27.2\text{ kg mol}^{-1}\text{ s}$ ).

The parent sample exhibits significant propene selectivity, yielding also small amounts of dipropyl ether and propanal. Heavier products ( $\text{C}_{4+}$ ) are observed in the outlet gas in very small quantities  $<0.03\%$ , which is consistent with a previous study, where heavier products are yielded at higher reaction temperatures.[39] In our experiments, these products appeared in detectable amounts at temperatures above  $230\text{ }^{\circ}\text{C}$ . The parent sample's selectivity toward propene decreases with the decrease of the conversion (**Figure 5.15**). In general, the etched samples show higher selectivity to propene than the parent, as selectivity decreases in the order  $\text{CHA-20-50-20} > \text{CHA-20-50-5} > \text{CHA-8-50-5} > \text{CHA-20-25-20} > \text{CHA-20-0-20} > \text{H-SSZ-13}$ .

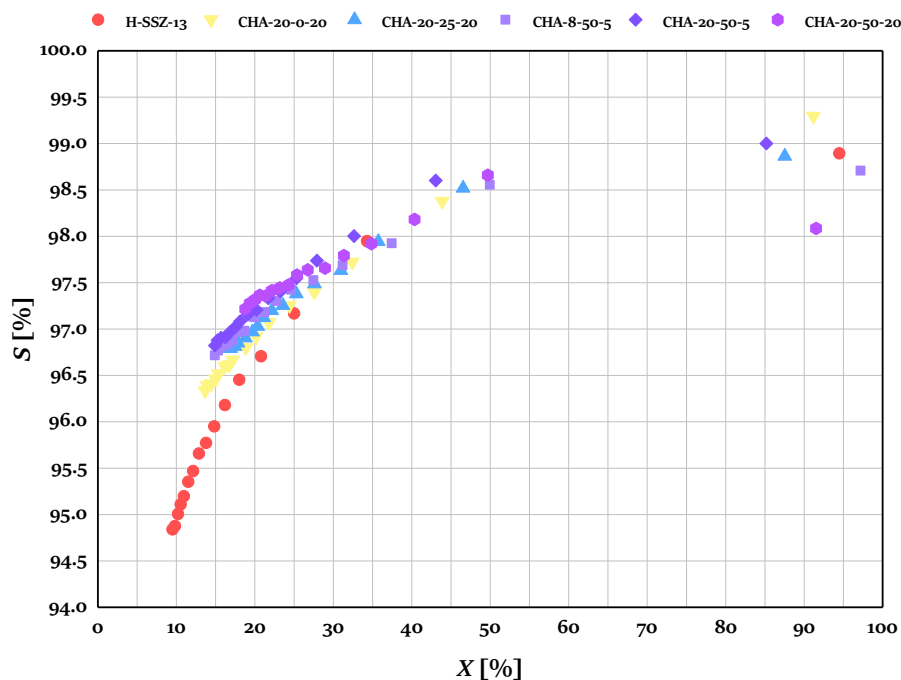


**Figure 5.15.** Propene selectivity (y-axis) as a function n-propanol conversion (x-axis) for parent and etched samples.

Coke content in the exhausted catalysts is estimated by thermogravimetric analysis (Table 5.4), as the mass loss between 200 and 800 °C is attributed to coke removal. The total coke loss of the parent sample is 11.4 %. The coke content in the etched samples is slightly higher, ranging between 12 and 14.5 %.

**Table 5.4.** Results of thermogravimetric analysis of exhausted catalysts used in n-propanol dehydration.

Sample	Total coke loss (%)
	200–800 °C
H-SSZ-13	11.4
CHA-20-0-20	12.0
CHA-20-25-20	14.5
CHA-8-50-5	13.8
CHA-20-50-5	13.9
CHA-20-50-20	13.8

### 3 Discussion

Relatively concentrated (40 wt/%)  $\text{NH}_4\text{F}$  aqueous solution is used to obtain hierarchical SSZ-13 zeolites. The etching conditions, including the liquid/solid ratio, treatment temperature, and time, are varied to obtain materials with different physicochemical properties. Hydrothermal treatment with an aqueous ammonium fluoride solution is a proven zeolite etching method.

The  $\text{NH}_4\text{F}$  etching of SSZ-13 generates mesopores in all prepared samples, including the most mildly treated one. For example, CHA-8-0-5 from series I show a slight increase in the mesopore volume ( $V_{\text{meso}} = 0.06 \text{ cm}^3 \text{ g}^{-1}$ ) compared to the parent zeolite ( $V_{\text{meso}} = 0.04 \text{ cm}^3 \text{ g}^{-1}$ ). The tuning of etching parameters allowed to increase mesoporosity and retain the basic characteristics of parent zeolite in terms of crystallinity, micropore volume, and acidity. For instance, sample CHA-20-50-20, which represents this series of samples, its mesopore volume increases to  $0.13 \text{ cm}^3 \text{ g}^{-1}$ . A much higher mesopore volume is observed in the sample subjected to partial amorphization. For instance, the CHA-100-50-20 sample reached a mesopore volume of  $0.98 \text{ cm}^3 \text{ g}^{-1}$ , but the micropore volume dropped to  $0.08 \text{ cm}^3 \text{ g}^{-1}$ .

The most significant changes in the physicochemical properties are observed for the zeolites etched at  $50^\circ\text{C}$ . Their relative crystallinity is usually below 90 % and can drop to 9 % when a liquid/solid ratio of 100 is used.  $\text{N}_2$  physisorption data matches well with XRD analysis and changes in the chemical composition analyzed by ICP-AES. The samples of series III ( $l/s = 100$ ) have a loss of micropore volume after 5 minutes of etching ( $0.17 \text{ cm}^3 \text{ g}^{-1}$ ), and after 20 minutes of etching, the micropore volume drops to  $0.08 \text{ cm}^3 \text{ g}^{-1}$  when compared with the parent zeolite ( $0.27 \text{ cm}^3 \text{ g}^{-1}$ ). In contrast, the samples prepared at lower temperatures (0 and  $25^\circ\text{C}$ ) have a well-preserved micropore volume or even higher than the parent zeolite. For instance, several samples exhibit a micropore volume from 0.28 to  $0.32 \text{ cm}^3 \text{ g}^{-1}$ . We attribute the last phenomenon to the dissolution of low crystalline or amorphous material present in the sample. The etching at  $50^\circ\text{C}$  causes amorphization, revealed by the lower intensity of the XRD peaks and a loss of micropore volume. The etching at this temperature generates amorphous material that could remain, thus causing a pore blockage.

Micrographs obtained by SEM reveal changes in the surface morphology of the etched samples (**Figure 5.3**). In the case of SSZ-13, the small intrinsic pores (0.38 nm) impose diffusion limitations to the water-fluoride species. Consequently, the etching reaction is concentrated at the crystal surface, and the dissolution rate rises at an elevated temperature ( $50^\circ\text{C}$ ). Thus, the treatment at  $50^\circ\text{C}$  (CHA-100-50-20) resulted in foam-like particles after only 20 min of treatment (**Figure 5.4C**). Micrographs from series I samples show the etching is generally started from the surface and removes parts of the crystal vulnerable to  $\text{NH}_4\text{F}$  dissolution, defect zones, and nanocrystalline domains. A similar type of dissolution in a fluoride medium has already been reported.[40,41] The number of “holes” created by  $\text{NH}_4\text{F}$  is multiplied for the series II and III samples, showing more intense zeolite dissolution at a higher  $l/s$  ratio. Finally, increasing the etching time also leads to the deeper dissolution of zeolite crystals (**Figure 5.4A and B**).

The results of chemical composition analysis (**Table 5.2**) show a non-selective extraction of framework cations. Even the most deeply treated series I and II samples have a Si/Al ratio of 11, which is not substantially different from the parent material. The changes in the framework composition of series III samples are still in this range when the treatment is performed at 0 and  $25^\circ\text{C}$ . Only samples CHA-100-50-5 and CHA-100-50-20 treated at  $50^\circ\text{C}$  show substantial dealumination related to an almost total loss of crystallinity. The EDX results imply the Al is not evenly distributed within the etched crystals. In addition, the surface of the crystals is more attacked since it contains less aluminum, particularly in the case of partially amorphous samples. Such a type of dissolution is most probably due to the diffusion limitation of water-soluble fluoride anions through the pores of SSZ-13. This is also observed in the work of Bolshakov *et al.* while treating ZSM-5 with  $\text{NH}_4\text{F}$  solution.[42]

Solid-state <sup>27</sup>Al MAS NMR is used to evaluate the state of Al in the etched samples (**Figure 5.7, Table 5.2**). Overall, the samples from series I and II show preserving of the chemical shift intensities with respect to the parent, *i.e.*, no substantial changes in the state of Al take place during the fluoride etching. Furthermore, the data collected show that the NH<sub>4</sub>F etching does not contribute to the octahedral extra framework aluminum formation. The acidity measurements show that the Brønsted acid site's concentration is preserved for the series I and II samples, further confirming the NMR data. The samples from series III have lower Brønsted acid site concentrations (**Table 5.3**). The concentration of Lewis acid sites is increased for all three series of samples, which is attributed to the etching reaction products.

The catalytic activity of parent and modified zeolites is tested in the dehydration of n-propanol. Primary alcohols undergo dehydration via the E2 elimination mechanism, where dipropyl ether are intermediates of acid-catalyzed dehydration of alcohols.[43] Here, dipropyl ether is observed as a minor product of the reaction along with propanal, while the propene is yielded with high selectivity (>90 %). Ethers normally form as major products at temperatures lower than 200 °C. Propanal formation indicates some oxidation reaction occurs along with dehydration and dehydrogenation reactions. The parent and treated samples' initial activity is similar, *i.e.*, in the range of 85–95 %, reflecting a similar number of available active sites. Differences are observed with the extension of the time on stream, where the etched samples, as a function of the treatment conditions, showed lower deactivation. Oligomers (C<sub>4+</sub>) and coke formation are most likely the cause. Oligomers are formed at the beginning of the reaction in small amounts (~0.9 %). After the first 2 min, their conversion is reduced (0.03 %). The etched samples also have a higher selectivity towards propene; this is most likely due to generated hierarchical porosity and the small changes in the Si/Al ratio. As known, the dehydrogenation reaction of n-propanol yielding dipropyl ether takes place mainly on the flat surface of the catalyst, whereas the dehydration reaction is restricted to the pores.[44] Therefore, the increased porosity in hierarchical zeolites promotes the later reaction. Zhi *et al.* described these mechanisms of dimer formation and alkoxide formation during n-propanol dehydration over ZSM-5.[45] A dehydration reaction is also inhibited by the presence of water, which is the co-product competing with alcohol reactants for BAS.[45,46]

The etched catalysts showed extended lifetime and higher coke content to the parent. The improved activity of etched derivatives is certainly related to the enhanced accessibility to active sites, together with the preserved Brønsted acidity. Previous spectroscopic data suggest the large carbonaceous species from the near-surface region of the crystals.[47,48] Thus, the deactivation is slower, with the sample having a higher external surface due to introduced mesopores.

Previous studies of NH<sub>4</sub>F or HF buffered with NH<sub>4</sub>F etching focused on medium-pore (10 MR) zeolites like MFI and FER and large-pore (12 MR) zeolites like FAU, LTL, MOR, and Beta. [41,49–52] Compared with those studies, the dissolution of the small-pore SSZ-13 shows some differences. For instance, Qin *et al.* also used 40 wt/% NH<sub>4</sub>F solutions to etch ZSM-5 upon similar experimental conditions. They reported rapid and abundant mesopore formation in the case of ZSM-5.[41] We attribute the slower dissolution rate of SSZ-13 to the small pore size. The diffusion of hydrated bifluoride ion through the 8 MR window of the chabazite cage is restrained. Thus, only the surface defects are the available sites where the dissolution can start. Consequently, the surface etching dominates the dissolution process when mild etching conditions are employed. The last statement is supported by the preserved micropore volume in most of the treated samples. The substantial micropore volume loss is only noticeable in extreme cases, *i.e.*, when the etching temperature is 50 °C, accelerating the etching reaction, and the liquid/solid ratio is high. Briefly, the dissolution rate of SSZ-13 is particularly lower compared with the larger pore zeolites.

## 4 Conclusion

Hierarchical zeolite SSZ-13 is successfully obtained by post-synthesis etching with a 40 wt/%  $\text{NH}_4\text{F}$  water solution. The effect of each parameter influencing the zeolite dissolution, *i.e.*, the temperature, liquid/solid ratio, and time, is studied, and the conditions of etching optimized. Using ambient temperature and low liquid/solid ratio (8 and 20) leads to hierarchical SSZ-13 derivatives with retained intrinsic characteristics. More precisely, the crystallinity, micropore volume, and the number of Brønsted acid sites are similar to the parent zeolite. Consequently, these hierarchical materials showed improved catalytic stability in the dehydration of n-propanol. Solely an extended treatment at 50 °C resulted in a partial amorphization of the zeolite and alteration of its physicochemical properties.

The results of this study revealed some particularities of the dissolution of small-pore zeolites in a fluoride medium. The dissolution rate is lower, although a relatively concentrated  $\text{NH}_4\text{F}$  solution is used, which is attributed to the constrained diffusion of hydrated bifluoride ions through the small pore channels. Consequently, the mesopore generation always starts from the crystal surface and penetrates further into the crystal's bulk. This particularity of SSZ-13  $\text{NH}_4\text{F}$  etching is probably valid for all small pore zeolites.

## 5 References

- [1] C. Colella, Natural zeolites, in: J. Čejka, H. van Bekkum (Eds.), *Studies in Surface Science and Catalysis*, Elsevier, 2005: pp. 13–40. [https://doi.org/10.1016/S0167-2991\(05\)80004-7](https://doi.org/10.1016/S0167-2991(05)80004-7).
- [2] A.F. Masters, T. Maschmeyer, Zeolites – From curiosity to cornerstone, *Microporous and Mesoporous Materials*. 142 (2011) 423–438. <https://doi.org/10.1016/j.micromeso.2010.12.026>.
- [3] Eight-Ring Zeolites, in: *Diffusion in Nanoporous Materials*, Wiley-Blackwell, 2012: pp. 561–606. <https://doi.org/10.1002/9783527651276.ch16>.
- [4] L.S. Dent, J.V. Smith, Crystal Structure of Chabazite, a Molecular Sieve, *Nature*. 181 (1958) 1794–1796. <https://doi.org/10.1038/1811794b0>.
- [5] V. Van Speybroeck, K. Hemelsoet, K. De Wispelaere, Q. Qian, J. Van der Mynsbrugge, B. De Sterck, B.M. Weckhuysen, M. Waroquier, Mechanistic Studies on Chabazite-Type Methanol-to-Olefin Catalysts: Insights from Time-Resolved UV/Vis Microspectroscopy Combined with Theoretical Simulations, *ChemCatChem*. 5 (2013) 173–184. <https://doi.org/10.1002/cctc.201200580>.
- [6] Z. Li, M.T. Navarro, J. Martínez-Triguero, J. Yu, A. Corma, Synthesis of nano-SSZ-13 and its application in the reaction of methanol to olefins, *Catal. Sci. Technol.* 6 (2016) 5856–5863. <https://doi.org/10.1039/C6CY00433D>.
- [7] P. Tian, Y. Wei, M. Ye, Z. Liu, Methanol to Olefins (MTO): From Fundamentals to Commercialization, *ACS Catal.* 5 (2015) 1922–1938. <https://doi.org/10.1021/acscatal.5b00007>.
- [8] F. Bleken, M. Bjørgen, L. Palumbo, S. Bordiga, S. Svelle, K.-P. Lillerud, U. Olsbye, The Effect of Acid Strength on the Conversion of Methanol to Olefins Over Acidic Microporous Catalysts with the CHA Topology, *Top Catal.* 52 (2009) 218–228. <https://doi.org/10.1007/s11244-008-9158-0>.
- [9] E. Koohsaryan, M. Anbia, Nanosized and hierarchical zeolites: A short review, *Chinese Journal of Catalysis*. 37 (2016) 447–467. [https://doi.org/10.1016/S1872-2067\(15\)61038-5](https://doi.org/10.1016/S1872-2067(15)61038-5).
- [10] A.M. Beale, F. Gao, I. Lezcano-Gonzalez, C.H.F. Peden, J. Szanyi, Recent advances in automotive catalysis for NO<sub>x</sub> emission control by small-pore microporous materials, *Chem. Soc. Rev.* 44 (2015) 7371–7405. <https://doi.org/10.1039/C5CS00108K>.
- [11] V. Valtchev, G. Majano, S. Mintova, J. Pérez-Ramírez, Tailored crystalline microporous materials by post-synthesis modification, *Chem. Soc. Rev.* 42 (2012) 263–290. <https://doi.org/10.1039/C2CS35196J>.
- [12] R. Oord, I.C. ten Have, J.M. Arends, F.C. Hendriks, J. Schmidt, I. Lezcano-Gonzalez, B.M. Weckhuysen, Enhanced activity of desilicated Cu-SSZ-13 for the selective catalytic reduction of NO<sub>x</sub> and its comparison with steamed Cu-SSZ-13, *Catal. Sci. Technol.* 7 (2017) 3851–3862. <https://doi.org/10.1039/C7CY00798A>.
- [13] L. Sommer, D. Mores, S. Svelle, M. Stöcker, B.M. Weckhuysen, U. Olsbye, Mesopore formation in zeolite H-SSZ-13 by desilication with NaOH, *Microporous and Mesoporous Materials*. 132 (2010) 384–394. <https://doi.org/10.1016/j.micromeso.2010.03.017>.
- [14] M.K. Wardani, G.T.M. Kadja, A.T.N. Fajar, Subagio, I.G.B.N. Makertihartha, M.L. Gunawan, V. Suendo, R.R. Mukti, Highly crystalline mesoporous SSZ-13 zeolite obtained via controlled post-synthetic treatment, *RSC Advances*. 9 (2019) 77–86. <https://doi.org/10.1039/C8RA08979E>.
- [15] H.S. Shin, I.J. Jang, N.R. Shin, S.H. Kim, S.J. Cho, Dealumination and characterization of chabazite for catalytic application, *Research on Chemical Intermediates*. 37 (2011) 1239–1246. <https://doi.org/10.1007/s11164-011-0390-z>.
- [16] W. Dai, X. Sun, B. Tang, G. Wu, L. Li, N. Guan, M. Hunger, Verifying the mechanism of the ethene-to-propene conversion on zeolite H-SSZ-13, *Journal of Catalysis*. 314 (2014) 10–20. <https://doi.org/10.1016/j.jcat.2014.03.006>.
- [17] L. Sommer, A. Krivokapić, S. Svelle, K.P. Lillerud, M. Stöcker, U. Olsbye, Enhanced Catalyst Performance of Zeolite SSZ-13 in the Methanol to Olefin Reaction after Neutron Irradiation, *J. Phys. Chem. C*. 115 (2011) 6521–6530. <https://doi.org/10.1021/jp109696z>.
- [18] S.I. Zones, Zeolite SSZ-13 and its method of preparation, US4544538A, 1985.
- [19] L. Wu, V. Degirmenci, P.C.M.M. Magusin, B.M. Szyja, E.J.M. Hensen, Dual template synthesis of a highly mesoporous SSZ-13 zeolite with improved stability in the methanol-to-olefins reaction, *Chem. Commun.* 48 (2012) 9492–9494. <https://doi.org/10.1039/C2CC33994C>.
- [20] L. Wu, V. Degirmenci, P.C.M.M. Magusin, N.J.H.G.M. Lousberg, E.J.M. Hensen, Mesoporous SSZ-13 zeolite prepared by a dual-template method with improved performance in the methanol-to-olefins reaction, *Journal of Catalysis*. 298 (2013) 27–40. <https://doi.org/10.1016/j.jcat.2012.10.029>.

- [21] X. Zhu, J.P. Hofmann, B. Mezari, N. Kosinov, L. Wu, B.M. Weckhuysen, S. Asahina, J. Ruiz-Martínez, Trimodal Porous Hierarchical SSZ-13 Zeolite with Improved Catalytic Performance in the Methanol-to-Olefins Reaction, (n.d.) 14.
- [22] X. Zhu, R. Rohling, G. Filonenko, B. Mezari, J.P. Hofmann, S. Asahina, E.J.M. Hensen, Synthesis of hierarchical zeolites using an inexpensive mono-quaternary ammonium surfactant as mesoporegen, *Chem. Commun.* 50 (2014) 14658–14661. <https://doi.org/10.1039/C4CC06267A>.
- [23] B. Liu, X. Zhao, W. Mao, H. Chen, L. Han, K. Zhu, X. Zhou, Pickering emulsion mediated crystallization of hierarchical zeolite SSZ-13 with enhanced NH<sub>3</sub> selective catalytic reduction performance, *Microporous and Mesoporous Materials*. 285 (2019) 202–214. <https://doi.org/10.1016/j.micromeso.2019.05.004>.
- [24] K.-G. Haw, S. Moldovan, L. Tang, Z. Qin, Q. Fang, S. Qiu, V. Valtchev, A sponge-like small pore zeolite with great accessibility to its micropores, *Inorg. Chem. Front.* 7 (2020) 2154–2159. <https://doi.org/10.1039/DoQI00261E>.
- [25] V. Valentin, J.-P. Gilson, Z. Qin, Method For The Preparation Of Synthetic Crystalline Zeolite Materials With Enhanced Pore Volume, WO 2016/005472 A1, 2015.
- [26] Z. Qin, L. Lakiss, J.-P. Gilson, K. Thomas, J.-M. Goupil, C. Fernandez, V. Valtchev, Chemical Equilibrium Controlled Etching of MFI-Type Zeolite and Its Influence on Zeolite Structure, Acidity, and Catalytic Activity, *Chem. Mater.* 25 (2013) 2759–2766. <https://doi.org/10.1021/cm400719z>.
- [27] M. Thommes, K. Kaneko, A.V. Neimark, J.P. Olivier, F. Rodriguez-Reinoso, J. Rouquerol, K.S.W. Sing, Physisorption of gases, with special reference to the evaluation of surface area and pore size distribution (IUPAC Technical Report), *Pure and Applied Chemistry*. 87 (2015) 1051–1069. <https://doi.org/10.1515/pac-2014-1117>.
- [28] K.A. Cychosz, R. Guillet-Nicolas, J. García-Martínez, M. Thommes, Recent advances in the textural characterization of hierarchically structured nanoporous materials, *Chem. Soc. Rev.* 46 (2017) 389–414. <https://doi.org/10.1039/C6CS00391E>.
- [29] G. Engelhardt, Multinuclear solid-state NMR in silicate and zeolite chemistry, *TrAC Trends in Analytical Chemistry*. 8 (1989) 343–347. [https://doi.org/10.1016/0165-9936\(89\)87043-8](https://doi.org/10.1016/0165-9936(89)87043-8).
- [30] J.M. Newsam, The influence of second-neighbor aluminums on the isotropic chemical shift of silicon-29 in a zeolite environment, *J. Phys. Chem.* 89 (1985) 2002–2005. <https://doi.org/10.1021/j100256a040>.
- [31] J.M. Griffin, J.R. Yates, A.J. Berry, S. Wimperis, S.E. Ashbrook, High-Resolution <sup>19</sup>F MAS NMR Spectroscopy: Structural Disorder and Unusual J Couplings in a Fluorinated Hydroxy-Silicate, *J. Am. Chem. Soc.* 132 (2010) 15651–15660. <https://doi.org/10.1021/ja105347q>.
- [32] C. Pazé, S. Bordiga, G. Spoto, C. Lamberti, A. Zecchina, IR spectroscopy of CH<sub>3</sub>CN–HCladducts in silicalite channels A model system for the study of acid–base reactions in zeolites, *J. Chem. Soc., Faraday Trans.* 94 (1998) 309–314. <https://doi.org/10.1039/A705380K>.
- [33] R.E. Sempels, P.G. Rouxhet, Infrared study of the adsorption of benzene and acetonitrile on silica–alumina gels: Acidity properties and surface heterogeneity, *Journal of Colloid and Interface Science*. 55 (1976) 263–273. [https://doi.org/10.1016/0021-9797\(76\)90033-3](https://doi.org/10.1016/0021-9797(76)90033-3).
- [34] B. Wichterlová, Z. Tvarůžková, Z. Sobalík, P. Sarv, Determination and properties of acid sites in H-ferrierite: A comparison of ferrierite and MFI structures, *Microporous and Mesoporous Materials*. 24 (1998) 223–233. [https://doi.org/10.1016/S1387-1811\(98\)00167-X](https://doi.org/10.1016/S1387-1811(98)00167-X).
- [35] W. Daniell, N.-Y. Topsøe, H. Knözinger, An FTIR Study of the Surface Acidity of USY Zeolites: Comparison of CO, CD<sub>3</sub>CN, and C<sub>5</sub>H<sub>5</sub>N Probe Molecules, *Langmuir*. 17 (2001) 6233–6239. <https://doi.org/10.1021/la010345a>.
- [36] F. Thibault-Starzyk, I. Stan, S. Abelló, A. Bonilla, K. Thomas, C. Fernandez, J.-P. Gilson, J. Pérez-Ramírez, Quantification of enhanced acid site accessibility in hierarchical zeolites – The accessibility index, *Journal of Catalysis*. 264 (2009) 11–14. <https://doi.org/10.1016/j.jcat.2009.03.006>.
- [37] S. Bordiga, L. Regli, D. Cocina, C. Lamberti, M. Bjørgen, K.P. Lillerud, Assessing the Acidity of High Silica Chabazite H–SSZ-13 by FTIR Using CO as Molecular Probe: Comparison with H–SAPO-34, *J. Phys. Chem. B*. 109 (2005) 2779–2784. <https://doi.org/10.1021/jp045498w>.
- [38] K. Suzuki, G. Sastre, N. Katada, M. Niwa, Ammonia IRMS-TPD measurements and DFT calculation on acidic hydroxyl groups in CHA-type zeolites, *Phys. Chem. Chem. Phys.* 9 (2007) 5980–5987. <https://doi.org/10.1039/B711961E>.

- [39] A.W. Lepore, Z. Li, B.H. Davison, G.-S. Foo, Z. Wu, C.K. Narula, Catalytic Dehydration of Biomass Derived 1-Propanol to Propene over M-ZSM-5 (M = H, V, Cu, or Zn), *Ind. Eng. Chem. Res.* 56 (2017) 4302–4308. <https://doi.org/10.1021/acs.iecr.7b00592>.
- [40] Z. Qin, J.-P. Gilson, V. Valtchev, Mesoporous zeolites by fluoride etching, *Current Opinion in Chemical Engineering.* 8 (2015) 1–6. <https://doi.org/10.1016/j.coche.2015.01.002>.
- [41] Z. Qin, G. Melinte, J.-P. Gilson, M. Jaber, K. Bozhilov, P. Boullay, S. Mintova, O. Ersen, V. Valtchev, The Mosaic Structure of Zeolite Crystals, *Angewandte Chemie.* 128 (2016) 15273–15276. <https://doi.org/10.1002/ange.201608417>.
- [42] A. Bolshakov, N. Kosinov, D.E.R. Hidalgo, B. Mezari, A.J.F. van Hoof, E.J.M. Hensen, Mild dealumination of template-stabilized zeolites by NH<sub>4</sub>F, *Catal. Sci. Technol.* 9 (2019) 4239–4247. <https://doi.org/10.1039/C9CY00593E>.
- [43] Antal Michael Jerry, M. Carlsson, X. Xu, D.G.M. Anderson, Mechanism and Kinetics of the Acid-Catalyzed Dehydration of 1- and 2-Propanol in Hot Compressed Liquid Water, *Ind. Eng. Chem. Res.* 37 (1998) 3820–3829. <https://doi.org/10.1021/ie980204c>.
- [44] H. Knözinger, The dehydration of alcohols, in: *The Hydroxyl Group* (1971), John Wiley & Sons, Ltd, 2010: pp. 641–718. <https://doi.org/10.1002/9780470771259.ch12>.
- [45] Y. Zhi, H. Shi, L. Mu, Y. Liu, D. Mei, D.M. Camaioni, J.A. Lercher, Dehydration Pathways of 1-Propanol on HZSM-5 in the Presence and Absence of Water, *J. Am. Chem. Soc.* 137 (2015) 15781–15794. <https://doi.org/10.1021/jacs.5b09107>.
- [46] O.M. Kut, R.D. Tanner, J.E. Prenosil, K. Kamholz, Catalytic Conversion of Alcohols to Olefins, in: R.G. Herman (Ed.), *Catalytic Conversions of Synthesis Gas and Alcohols to Chemicals*, Springer US, Boston, MA, 1984: pp. 361–394. [https://doi.org/10.1007/978-1-4613-2737-0\\_19](https://doi.org/10.1007/978-1-4613-2737-0_19).
- [47] D. Mores, E. Stavitski, M.H.F. Kox, J. Kornatowski, U. Olsbye, B.M. Weckhuysen, Space- and Time-Resolved In-situ Spectroscopy on the Coke Formation in Molecular Sieves: Methanol-to-Olefin Conversion over H-ZSM-5 and H-SAPO-34, *Chemistry – A European Journal.* 14 (2008) 11320–11327. <https://doi.org/10.1002/chem.200801293>.
- [48] D. Mores, J. Kornatowski, U. Olsbye, B.M. Weckhuysen, Coke Formation during the Methanol-to-Olefin Conversion: In Situ Microspectroscopy on Individual H-ZSM-5 Crystals with Different Brønsted Acidity, *Chemistry – A European Journal.* 17 (2011) 2874–2884. <https://doi.org/10.1002/chem.201002624>.
- [49] Z. Qin, K.A. Cychoz, G. Melinte, H. El Siblani, J.-P. Gilson, M. Thommes, C. Fernandez, S. Mintova, O. Ersen, V. Valtchev, Opening the Cages of Faujasite-Type Zeolite, *J. Am. Chem. Soc.* 139 (2017) 17273–17276. <https://doi.org/10.1021/jacs.7b10316>.
- [50] X. Chen, T. Todorova, A. Vimont, V. Ruaux, Z. Qin, J.-P. Gilson, V. Valtchev, In situ and post-synthesis control of physicochemical properties of FER-type crystals, *Microporous and Mesoporous Materials.* 200 (2014) 334–342. <https://doi.org/10.1016/j.micromeso.2014.07.057>.
- [51] V. Babić, L. Tang, Z. Qin, L. Hafiz, J. Gilson, V. Valtchev, Comparative Study of Zeolite L Etching with Ammonium Fluoride and Ammonium Bifluoride Solutions, *Adv. Mater. Interfaces.* (2020) 2000348. <https://doi.org/10.1002/admi.202000348>.
- [52] N. Suárez, J. Pérez-Pariente, C. Márquez-Álvarez, M. Grande Casas, A. Mayoral, A. Moreno, Preparation of mesoporous Beta zeolite by fluoride treatment in liquid phase. Textural, acid and catalytic properties, *Microporous and Mesoporous Materials.* 284 (2019) 296–303. <https://doi.org/10.1016/j.micromeso.2019.04.049>.



# 6

Chromic acid etching of zeolites

<b>1</b>	<b>INTRODUCTION .....</b>	<b>109</b>
<b>2</b>	<b>RESULTS .....</b>	<b>111</b>
2.1	X-RAY DIFFRACTION .....	111
2.2	N <sub>2</sub> PHYSISORPTION .....	113
2.3	PHYSICOCHEMICAL ANALYSIS .....	115
2.4	SCANNING ELECTRON MICROSCOPY.....	116
2.5	TRANSMISSION ELECTRON MICROSCOPY.....	117
2.5.1	<i>STEM-EDX</i> .....	118
2.6	SOLID-STATE NMR SPECTROSCOPY.....	119
2.6.1	<sup>27</sup> Al MAS NMR.....	119
2.6.2	<sup>29</sup> Si MAS NMR .....	120
2.7	ACIDITY CHARACTERIZATION BY FTIR .....	121
2.7.1	<i>CHA</i> .....	121
2.7.2	<i>MFI</i> .....	122
2.7.3	<i>LTL</i> .....	123
<b>3</b>	<b>DISCUSSION.....</b>	<b>125</b>
<b>4</b>	<b>CONCLUSION .....</b>	<b>126</b>
<b>5</b>	<b>REFERENCES .....</b>	<b>127</b>

# 1 Introduction

Dealumination by acid leaching is one of the earliest methods used for the demetallation of zeolites. Removing aluminum from the zeolite framework is first reported by Barrer and Maki in 1964.[1] They performed dealumination of clinoptilolite by refluxing in hydrochloric acid.[2] Dealumination by treating with acids increases the framework Si/Al ratio but makes minor changes to the zeolite porosity.[3] In certain zeolites the majority of the aluminum in the framework can be removed, thereby enhancing the hydrophobicity and hydrothermal stability of the zeolites.[4] For example, aluminum is completely removed from pentasil-type zeolites.[5-7] Dealumination yields defect sites denoted as “hydroxyl nest” (silanol nest), as four SiOH groups are generated per one Al removed.[2]

One of the most well-known examples is the dealumination of zeolite Y yielding an ultra-stable (US) zeolite Y derivative, which is an invaluable industrial cracking catalyst.[4] FAU-type zeolite cannot be directly synthesized with a Si/Al ratio higher than 3, at least not in an economically feasible manner.[8] Hence to obtain high-silica zeolite Y, *i.e.*, ultrastable zeolite Y (USY), dealumination methods are beneficial. The increased Si/Al ratios lead to decreased density of the acid sites, which enhances their acidity and activity in catalytic processes. However, inconsistent remarks can be found in the literature about the thermal stability of dealuminated zeolites. Zeolites containing low concentrations of aluminum are, in general, more thermally and chemically stable.[8] However, acid leaching decreased the thermal stability of mordenite[9], still, some authors claim higher thermal stability of acid leached zeolites.[10] Higher concentrations of framework defects deteriorate zeolites’ thermal stability.[10] The mechanism description was provided by Kerr, who showed the presence of water during thermal treatment plays a major role in ultra stabilization.[11]

However, dealumination can sometimes prompt structure and significant porosity losses.[12] The acid site loss, mesopores with broad range distribution, the formation of inaccessible mesopores are important limitations of the dealumination process.[13] Thus, Van Nierkerk *et al.* found that dealumination by nitric acid was linked to a partial loss of crystallinity.[5]

Field of zeolite post-synthesis dealumination methods by acid leaching is expanding to various mineral and organic acids. It is contemplated that the mineral acids solubilize silica more readily than organic acids, which contributes to losses of structure.[12] Complexing agents have also been employed successfully in zeolite dealumination.[10] EDTA, acetylacetone, tartaric, and oxalic acid have been successfully applied for the dealumination of zeolites.[2]

In this chapter, we report the influence of chromic acid treatment on zeolites with various framework topologies (8 MR, 10 MR, 12 MR). The potential of this strong acid as a zeolite dealumination agent hasn’t been previously studied and the selected zeolites are chosen to study the effects of the chromic acid as a function of the pore size.

Chromium (VI) is a strongly oxidizing agent and exists only in oxo species  $\text{CrO}_3$ ,  $\text{CrO}_4^{2-}$  and  $\text{CrO}_2\text{F}_2$ .[14]  $\text{CrO}_3$  forms different ions in water depending on the pH, above 6,  $\text{CrO}_3$  forms  $\text{CrO}_4^{2-}$ , a yellow tetrahedral chromate ion. Between pH of 2 and 6,  $\text{HCrO}_4^-$  and  $\text{Cr}_2\text{O}_7^{2-}$  (dichromate) are in equilibrium. And at pH values below 1  $\text{H}_2\text{CrO}_4$  is formed. The equilibria are the subsequent[15]:



However, the existence of  $\text{HCrO}_4^-$  is a matter of debate and at low concentrations of  $\text{Cr}^{\text{VI}}$  ( $\sim 0.2$  M),  $\text{HCrO}_4^-$  is expected to be a minor species.[16] Chromium (VI) can also form deep red ions  $\text{Cr}_3\text{O}_{10}^{2-}$  and  $\text{Cr}_4\text{O}_{13}^{2-}$  at high highly concentrated solutions.[17] The structures continue the pattern set by  $\text{Cr}_2\text{O}_7^{2-}$  in having chains of  $\text{CrO}_4$  tetrahedra

sharing corners.  $\text{CrO}_3$  consists of infinite chains of corner-sharing tetrahedra  $-\text{O}-\text{CrO}_2-\text{O}-$  and there are only Van der Waals forces between the chains.[18,19] The structures are determined for solid-state salts.

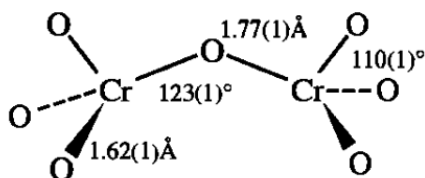


Figure 6.1. Structure of the dichromate ion found in  $\text{Rb}_2\text{Cr}_2\text{O}_7$  (from [15]).

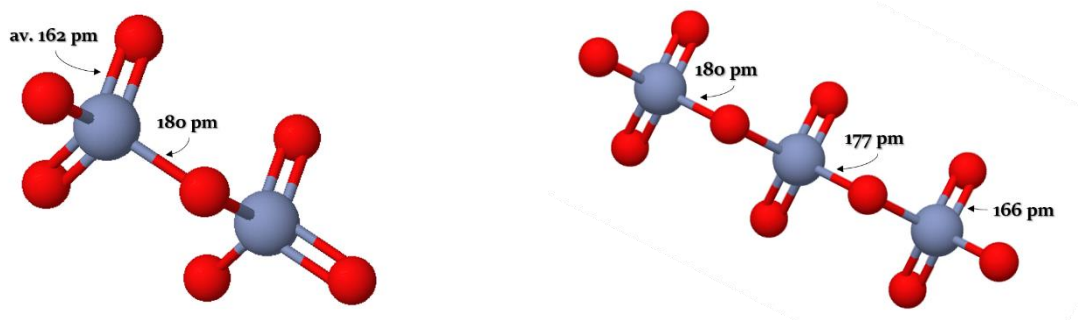


Figure 6.2. Structures of  $\text{Cr}_2\text{O}_7^{2-}$  and  $\text{Cr}_3\text{O}_{10}^{2-}$  (from [20]).

Data available indicate the possible existence of anions containing more than two chromium atoms. Polyacids including Cr (VI) can be expressed by the formula  $\text{H}_2\text{Cr}_n\text{O}_{3n+1}$ . The value of  $n$  is presumed not to exceed 4, making  $\text{Cr}_4\text{O}_{13}^{2-}$ . [20,21]

Chromium trioxide is used alone or as an additive to other acids and used as an oxidizing agent in a number of etching solutions. Specifically,  $\text{H}_3\text{PO}_4/\text{CrO}_3$  for oxide removal from  $\text{Al}_2\text{O}_3$  or preferential etching and cleaning of Si with  $\text{HF}/\text{CrO}_3$ . [22]

## 2 Results

### 2.1 X-ray diffraction

XRD patterns of parent and treated zeolites are depicted in **Figure 6.3A–C**, with relative crystallinity indicated for every pattern. Diffractograms of  $\text{NH}_4\text{-CHA}$  (**Figure 6.3A**) treated with chromic acid solutions (0.1–2 wt/%) are highly crystalline; a small loss of crystallinity is observed after treatment with 10 wt/% solutions.

Patterns of MFI treated with chromic acid are also highly crystalline (**Figure 6.3B**), showing relative crystallinity up to 99 % with samples etched with solutions of 0.1–1 wt/%. A minor decrease of crystallinity (97 %) in samples MFI-2 and MFI-10 is observed.

X-ray diffraction patterns of LTL treated with chromic acid presented in **Figure 6.3C**. Again, the zeolites treated with 0.1–1 wt/% acid solutions are highly crystalline. A small loss of crystallinity is observed after using a 2 wt/% solution, while the sample obtained with 10 wt/% solution treatment is almost entirely amorphous.

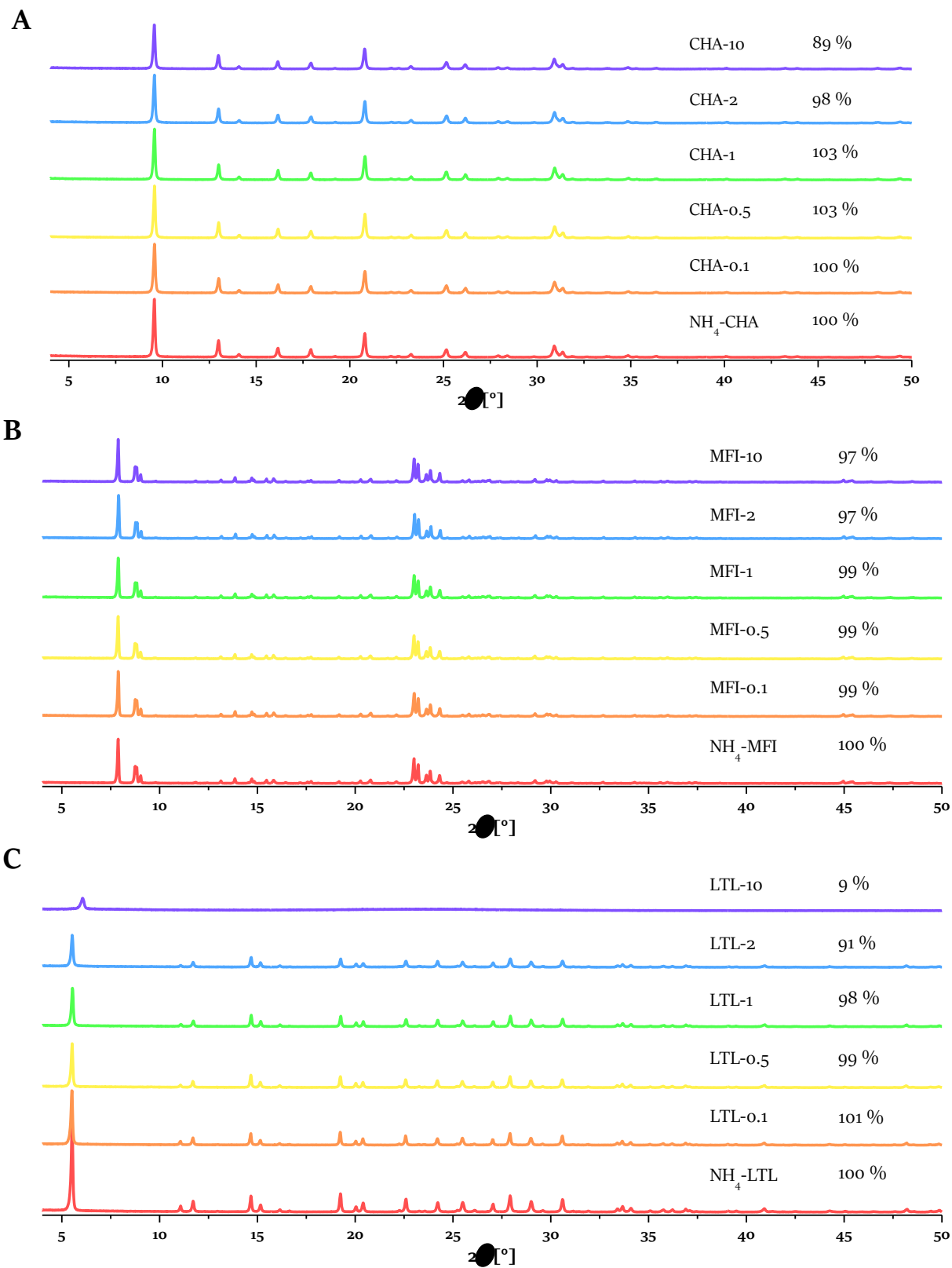


Figure 6.3. X-ray diffraction patterns of the series of A) CHA, B) MFI, and C) LTL treated samples, with relative crystallinity percentages indicated for each sample.

## 2.2 N<sub>2</sub> physisorption

Textural properties of all the samples are assessed by nitrogen physisorption, and the obtained isotherms are depicted in **Figure 6.4A–C**. All parent samples, NH<sub>4</sub>-CHA, NH<sub>4</sub>-MFI, and NH<sub>4</sub>-LTL, exhibit an I (a) type isotherm with an H<sub>4</sub> hysteresis loop. Type I (a) isotherm is characteristic for microporous materials, evident by the high uptake at the low relative pressure ( $p/p_0$ ) region, while the H<sub>4</sub> hysteresis loop characterizes slit-shape pores.

The isotherms of CHA etched derivatives (**Figure 6.4A**) show isotherm and hysteresis loop identical with the parent material. The etched samples exhibit an increase in the micropore volume adsorption, *i.e.*, revealed by the higher uptake at the low relative pressure.

The etched MFI samples (**Figure 6.4B**) exhibit isotherms similar to the parent, with samples MFI-0.5 and MFI-1 showing a small increase of micropore volume, whereas samples MFI-2 and MFI-10 lost a little bit microporosity.

All etched LTL (**Figure 6.4C**) samples show a loss of micropore volume with some differences. The samples treated with 0.1–2 wt/% solutions show minor losses, while the micropore volume loss of 10 wt/% treated sample is substantial. The samples also exhibit a small increase at the high relative pressure region, indicating the development of mesopores.

The porosity assessments of all the samples are summarized in **Table 6.1**.

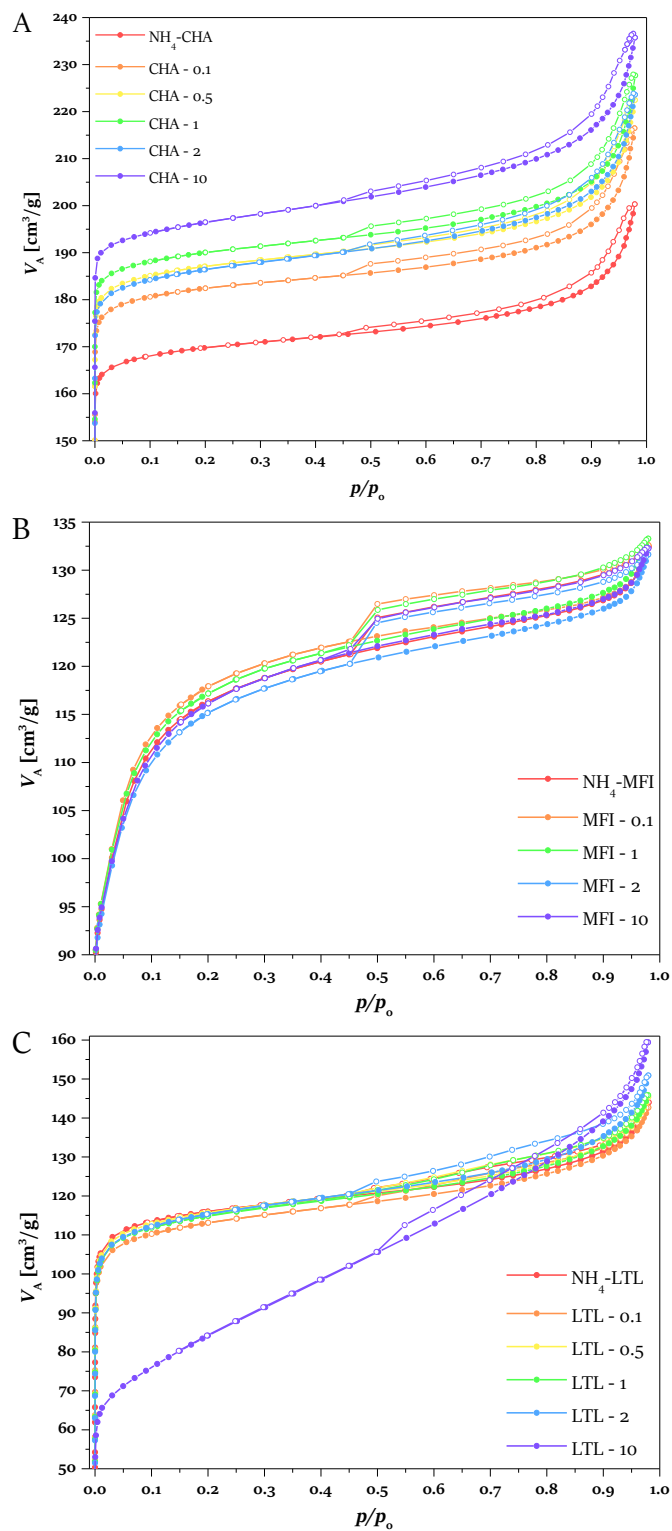


Figure 6.4.  $N_2$  physisorption isotherms of A)  $NH_4$ -CHA, B)  $NH_4$ -MFI, and C)  $NH_4$ -LTL with their etched derivatives. *Note:* the y-axis starts at higher values of  $V_A$  to highlight the changes in the micropore area.

## 2.3 Physicochemical analysis

Analysis of physisorption data and chemical analysis are summarized in **Table 6.1**. The three framework types showed different susceptibility to the chromic acid etching.

Parent CHA-type zeolite has a micropore volume of  $0.27 \text{ cm}^3 \text{ g}^{-1}$  and mesopore volume of  $0.04 \text{ cm}^3 \text{ g}^{-1}$ . The etched samples exhibit an increase of micropore volume with no present changes of the  $V_{\text{meso}}$ . The  $V_{\text{micro}}$  increases to  $0.29 \text{ cm}^3 \text{ g}^{-1}$  with a sample treated with 0.1 wt/% (CHA-0.1) and up to  $0.32 \text{ cm}^3 \text{ g}^{-1}$  for the sample treated with 10 wt/% (CHA-10). Mesopore volume in all the treated samples is  $0.04 \text{ cm}^3 \text{ g}^{-1}$ , and the external surface ( $S_{\text{BET}}$ ) slightly increases. The etched CHA samples also exhibit changes in the chemical composition measured with ICP-AES. Sample CHA-1 has a small increase of the Si/Al ratio (9.4), and the ratio increases with the raise of chromic acid concentration, as a sample treated with 10 wt/% chromic acid exhibits a Si/Al ratio of 10.5.

Parent sample MFI has a micropore volume of  $0.16 \text{ cm}^3 \text{ g}^{-1}$  and mesopore volume of  $0.04 \text{ cm}^3 \text{ g}^{-1}$ . The etched MFI samples retain the same micropore and mesopore volume despite the concentration used (0.1–10 wt/%). The specific surface area ( $S_{\text{BET}}$ ) also does not show any significant changes. The etched MFI samples, however, do show a small change in the Si/Al ratio. The Si/Al ratio of the parent sample ( $\text{NH}_4$ -MFI) is 19, while all samples treated with chromic acid solutions of 0.1–10 wt/% have a ratio of 21.

The parent sample LTL has a micropore volume of  $0.17 \text{ cm}^3 \text{ g}^{-1}$  and mesopore volume of  $0.05 \text{ cm}^3 \text{ g}^{-1}$ . The samples treated with 0.1 and 0.5 wt/% acid solutions retain these properties. While samples treated with 1–4 wt/% chromic acid show a small decrease of the micropore volume, having  $0.16 \text{ cm}^3 \text{ g}^{-1} V_{\text{micro}}$ . However, the sample treated with 10 wt/% shows a significant loss of the micropore volume, almost half of the initial value, having  $V_{\text{micro}} = 0.09 \text{ cm}^3 \text{ g}^{-1}$ . The etched LTL samples also show a small degree of preferential dealumination. The sample LTL-0.1-30 retains the Si/Al ratio of 3.0 as the parent sample; the samples treated with 0.1–2 wt/% acid solutions show a small increase of Si/Al ratio, up to 3.2; while those treated with 4 wt/% solution shows significant dealumination reaching a Si/Al = 6.1.

Table 6.1. Textural properties of the parent and treated zeolites.

Sample	$V_{\text{micro}}$ $\text{cm}^3 \text{g}^{-1}$	$V_{\text{meso}}$ $\text{cm}^3 \text{g}^{-1}$	$S_{\text{BET}}$ $\text{m}^2 \text{g}^{-1}$	Si/Al $\text{mol mol}^{-1}$
CHA	0.27	0.04	700	9.0
CHA-0.1	0.29	0.04	735	9.4
CHA-0.5	0.31	0.04	752	9.8
CHA-1	0.32	0.04	765	9.9
CHA-2	0.31	0.04	747	10.4
CHA-10	0.32	0.04	788	10.5
MFI	0.16	0.04	436	19
MFI-0.1	0.16	0.04	440	21
MFI-1	0.16	0.05	439	21
MFI-2	0.16	0.04	430	/
MFI-10	0.16	0.04	432	21
LTL	0.17	0.05	456	3.0
LTL-0.1-30	0.17	0.04	455	3.0
LTL-0.1	0.17	0.05	450	3.1
LTL-0.5	0.17	0.05	454	/
LTL-1	0.16	0.05	426	3.2
LTL-2	0.16	0.05	432	3.4
LTL-4	0.16	0.05	417	6.1
LTL-10	0.09	0.16	295	/

## 2.4 Scanning electron microscopy

The impact of chromic acid on the morphology of obtained zeolites is studied with a scanning electron microscope as representative micrographs are presented in **Figure 6.5A-F**. Samples CHA-1 (**Figure 6.5A**) and CHA-2 (**Figure 6.5B**) show pristine surfaces of the typical SSZ-13 crystal cubic crystals with well-defined edges.

MFI crystals (**Figure 6.5C-D**) are much larger in size than SSZ-13 and zeolite L, having around 5  $\mu\text{m}$  in length. The crystals have a coffin-shaped morphology with intergrown crystals, ramps, and defects appearing on the (010) surface.[23] Sample MFI-1 shows large parts of the crystals are removed; it is likely that some intergrown crystals separated during chromic acid etching.

Typically, zeolite L exhibits a disc-like morphology with overgrown terraces on the pinacoidal face (**Figure 6.5E-F**). The samples LTL-1 and LTL-2 show well-defined edges, and the faces of the crystal do not show visible traces of chromic acid etching.

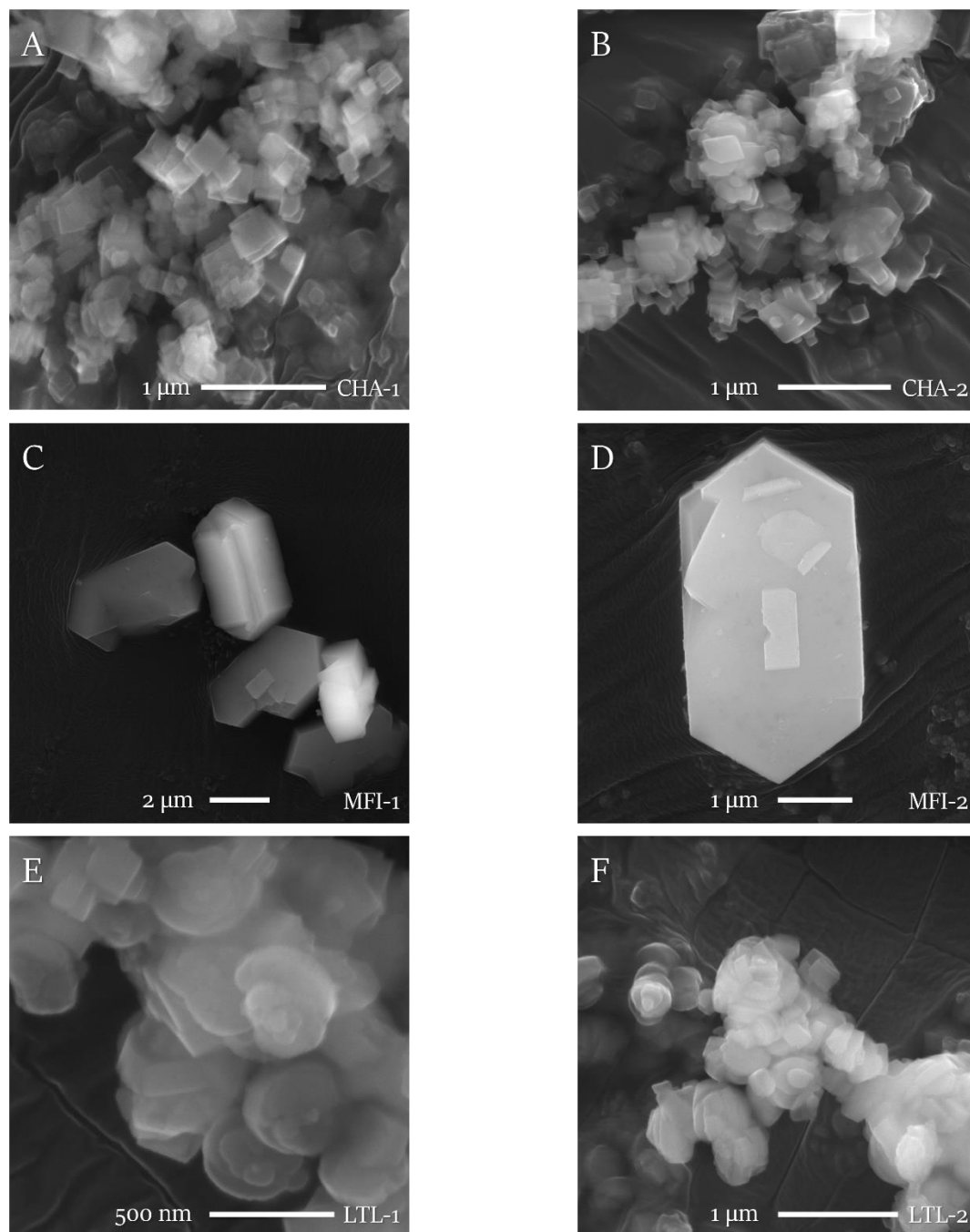


Figure 6.5. SEM micrographs of CHA (A,B), MFI(C,D) and LTL (E,F) etched samples.

## 2.5 Transmission electron microscopy

Transmission electron microscopy is employed to gather more details on the morphology of the etched samples. The LTL-0.1-30 sample exhibits the typical zeolite L morphology. However, on the crystal surface, small holes of 10–20 nm size penetrating the crystal core are observed (Figure 6.6A). Upon higher magnification (Figure 6.6B), a pore of 15 nm width starting from the crystal's surface and penetrating 50 nm in the crystal volume is visible.

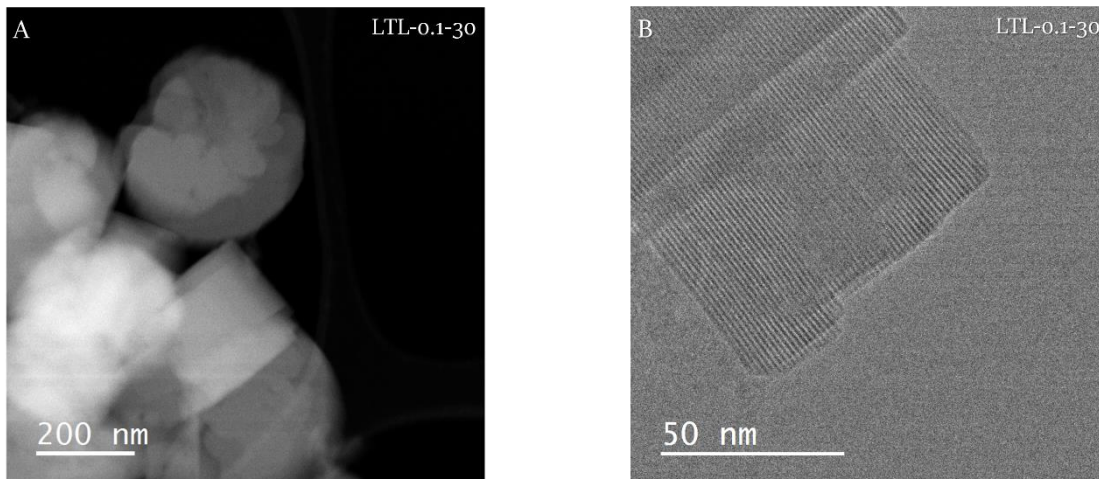


Figure 6.6. STEM micrographs of sample LTL-0.1-30 obtained by ADF (left) and BF imaging (right).

CHA-1 and CHA-2 etched samples are also studied by TEM. The samples retain the parent crystal morphology. The chromic acid etching didn't produce any noticeable changes in the porosity or morphology in these samples.

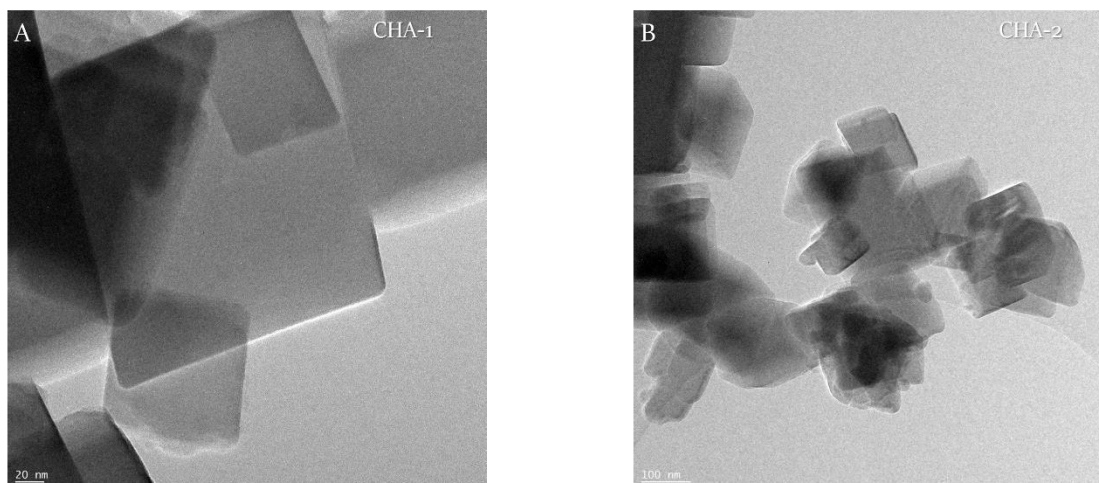
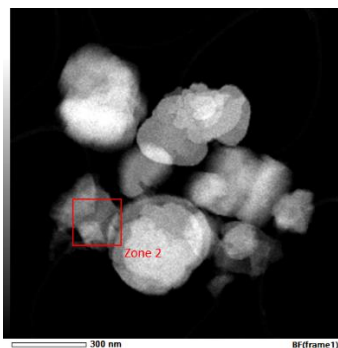


Figure 6.7. TEM micrographs of samples CHA-1 (A) and CHA-2 (B).

### 2.5.1 STEM-EDX

The results of EDX analysis are summarized in **Figure 6.8**. The surface chemical analysis results indicate that the sample LTL-0.1-30 is well washed since only small amounts of Cr are detected (0.4 wt%). The Si/Al ratio of 13 reveals that a preferential dealumination occurs on the crystal surface.



Element	wt/%
O	17.2
F	0.3
Al	5.5
Si	76.2
K	0.2
Ca	0.2
Cr	0.4
Total	100

Figure 6.8. STEM EDX results and analysis.

## 2.6 Solid-state NMR spectroscopy

### 2.6.1 $^{27}\text{Al}$ MAS NMR

$^{27}\text{Al}$  MAS NMR was performed to check the state of aluminum after the etching. The parent chabazite sample,  $\text{NH}_4\text{-CHA}$  (Figure 6.9A) exhibits three peaks related to octa-, penta- and tetra-coordinated aluminum. The etched samples exhibit the same peaks with a small increase of intensity of octacoordinated aluminum. The content of octacoordinated Al in the parent CHA sample is determined to be 10.7 % (Table 6.2); the etched samples contain a minor increase of octahedral Al, with sample CHA-10 having the highest content of 14 %.

The parent sample  $\text{NH}_4\text{-MFI}$  (Figure 6.9B) exhibits a single peak at ~60 ppm related to tetra-coordinated aluminum, the peak pointing to octahedral species is not visible from the spectra. Still, it is found it contains 1.1 % (Table 6.2). The etched samples show some increase in the  $\text{Al}^{\text{VI}}$  content, which is determined to be between 1.6 and 2.3 %.

$\text{NH}_4\text{-LTL}$  (Figure 6.9C) exhibits only the peak related to tetra-coordinated Al at ~60 ppm. The samples etched with solutions 0.1–2 wt/% have a visible increase of the octacoordinated resonance peak. The sample etched with 10 wt/% solution has a significant decrease of both resonance peaks related to octa- and tetra-coordinated Al, indicating significant preferential dealumination. Among the samples etched with 0.1–2 wt/% acid solutions, the content of  $\text{Al}^{\text{VI}}$  is 0.8–5.2 % (Table 6.2).

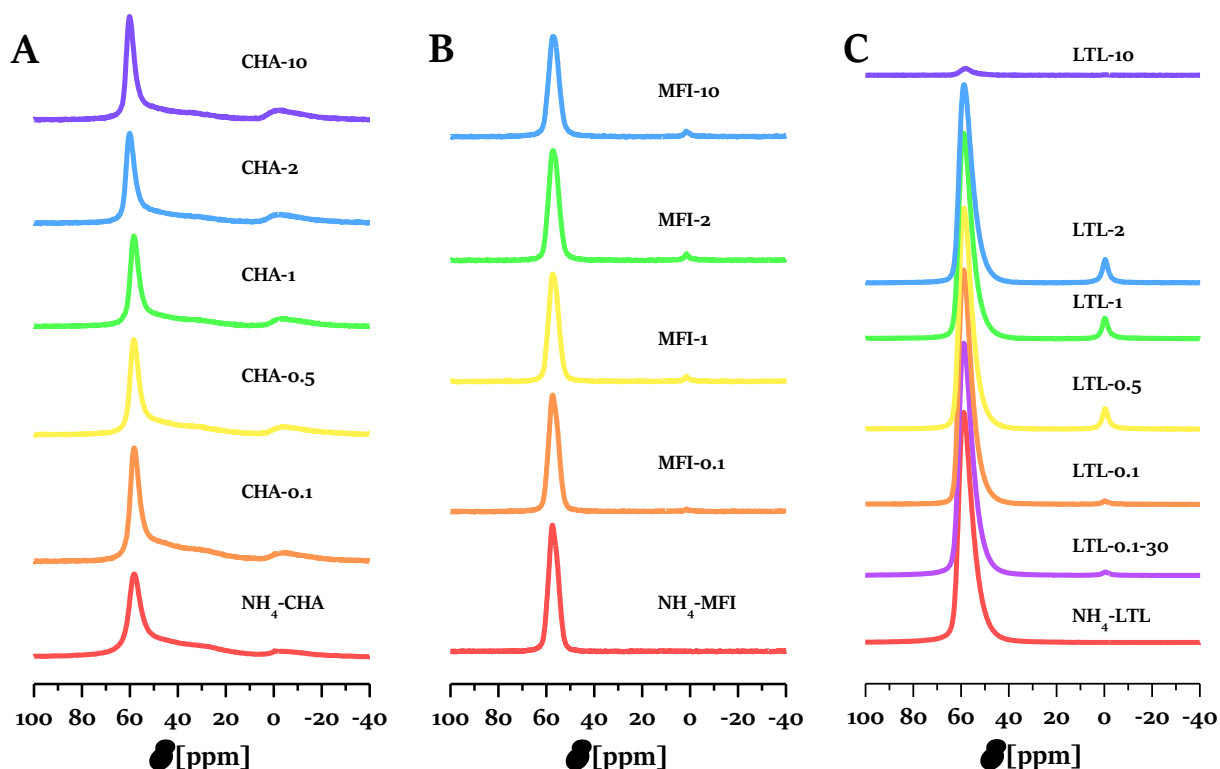


Figure 6.9.  $^{27}\text{Al}$  MAS NMR spectra of A) CHA, B) MFI, and C) LTL series of samples.

**Table 6.2.** Results of extraframework aluminum ( $\text{Al}^{\text{VI}}$ ) content expressed in percentages (%), obtained from  $^{27}\text{Al}$  MAS NMR spectra.

Sample	$\text{Al}^{\text{VI}}$ %
$\text{NH}_4$ -CHA	10.7
CHA-0.5	12.0
CHA-1	12.5
CHA-2	13.3
CHA-10	14.0
$\text{NH}_4$ -MFI	1.1
MFI-0.1	1.6
MFI-1	2.0
MFI-2	2.2
MFI-10	2.3
$\text{NH}_4$ -LTL	0.1
LTL-0.1-30	0.8
LTL-0.1	1.0
LTL-0.5	4.5
LTL-1	4.9
LTL-2	5.2
LTL-10	2.8

### 2.6.2 $^{29}\text{Si}$ MAS NMR

$^{29}\text{Si}$  MAS NMR is used to study the coordination of silicon in the zeolite framework. **Figure 6.10** depicts spectra of the parent LTL zeolite and one etched derivative, LTL-1. The both samples exhibit four peaks at chemical shifts ( $\delta$ ) -110, -106, -100, and -95 ppm corresponding to  $\text{Si}(4\text{Si}, 0\text{Al})$ ,  $\text{Si}(3\text{Si}, 1\text{Al})$ ,  $\text{Si}(2\text{Si}, 2\text{Al})$  and  $\text{Si}(1\text{Si}, 3\text{Al})$ , respectively.[24] The etched sample LTL-1 exhibits increased intensities of the peaks corresponding to  $\text{Si}(4\text{Si}, 0\text{Al})$ ,  $\text{Si}(3\text{Si}, 1\text{Al})$ , and decreased intensity of the peak corresponding to  $\text{Si}(1\text{Si}, 3\text{Al})$ .

$^{29}\text{Si}\{^1\text{H}\}$  cross-polarization NMR gives qualitative information on the silanol species in zeolites. The spectra of the parent LTL and LTL-1 samples are depicted in **Figure 6.10**. The parent sample exhibits peaks at -110, -106, -100, and -96, corresponding well to the peaks observed in **Figure 6.10**, indicating peaks related to Si-O-Al and Si-O-OH bonds overlap in the  $^{29}\text{Si}$  MAS NMR spectra for both samples. Sample LTL-1 exhibits intensity decrease of the peaks at -95 and -110 ppm related to  $\text{Si}(1\text{Si}, 3\text{OH})$  and  $\text{Si}(1\text{Si}, 0\text{OH})$  and a small increase of the peak centered at -100 corresponding to  $\text{Si}(2\text{Si}, 2\text{OH})$ . The results of  $^{29}\text{Si}\{^1\text{H}\}$  cross-polarization NMR suggest the treatment of LTL with 1 wt/% chromic acid doesn't contribute to the formation of silanol groups.

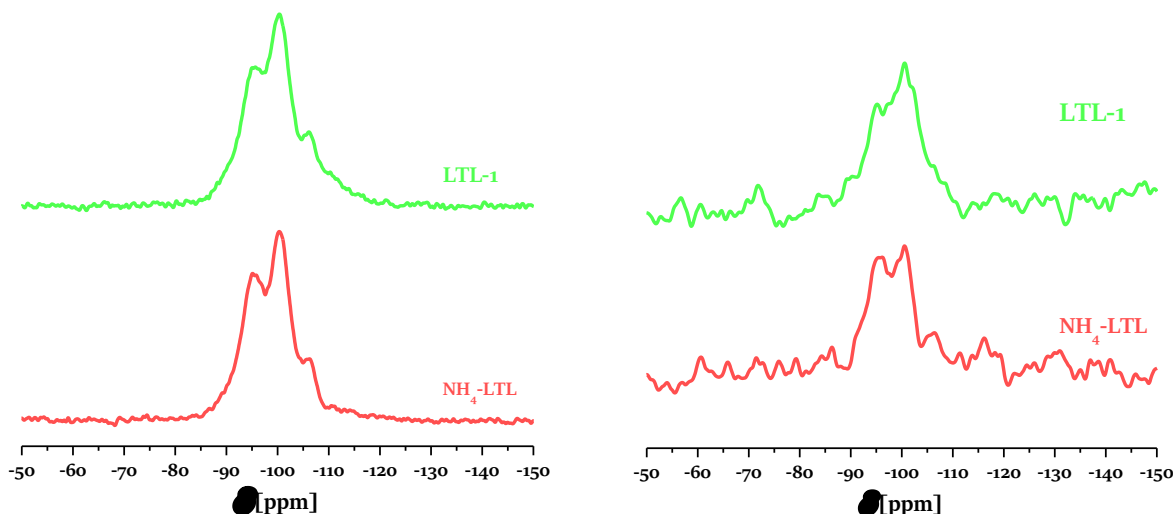


Figure 6.10.  $^{29}\text{Si}$  MAS NMR spectra of parent LTL and etched LTL-1 (left) samples and their  $^{29}\text{Si}\{^1\text{H}\}$  cross-polarization spectra (right).

$^{29}\text{Si}$  MAS NMR of both CHA samples reveals three peaks at chemical shifts ( $\delta$ ) -109, -103, and -98 ppm, corresponding to  $\text{Si}(4\text{Si}, 0\text{Al})$ ,  $\text{Si}(3\text{Si}, 1\text{Al})$ ,  $\text{Si}(2\text{Si}, 2\text{Al})$ , depicted in **Figure 6.11**. Sample CHA-1 has lower intensities of all three peaks compared to the parent sample  $\text{NH}_4\text{-CHA}$ .  $^{29}\text{Si}\{^1\text{H}\}$  cross-polarization NMR is also depicted in **Figure 6.11**. The figure shows that the parent sample ( $\text{NH}_4\text{-CHA}$ ) having some broad peaks between -110 and 90 ppm; however, sample CHA-1 shows an increase in the peak intensity at -109 ppm. This peak is related to  $\text{Si}(4\text{Si}, 0\text{OH})$ , indicating some silanols develop in the chabazite sample treated with 1 wt/%  $\text{CrO}_3$ .

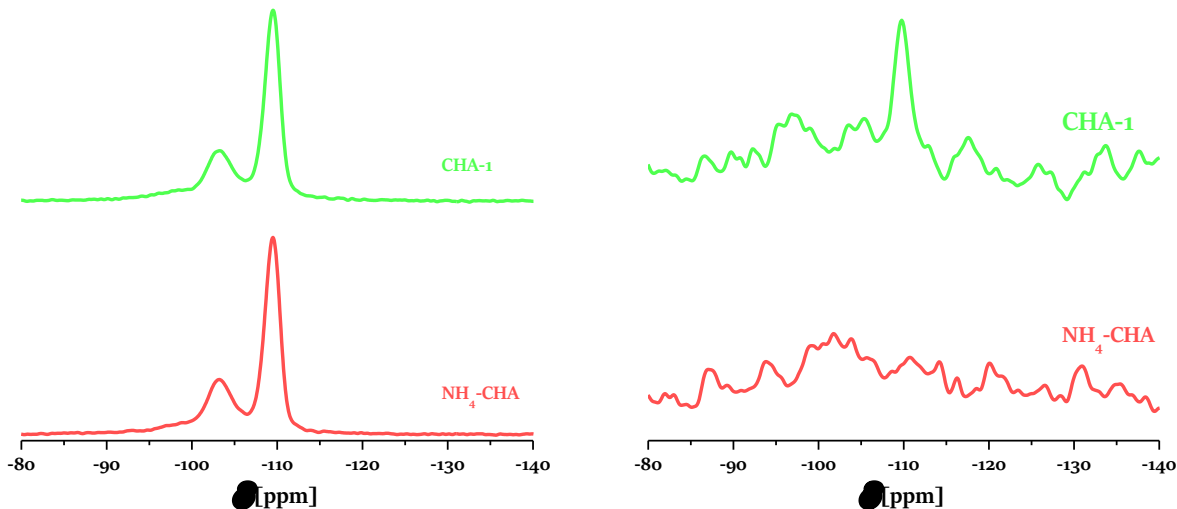


Figure 6.11.  $^{29}\text{Si}$  MAS NMR spectra of parent (CHA) and etched (CHA-1) samples (left) and their  $^{29}\text{Si}\{^1\text{H}\}$  cross-polarization spectra (right).

## 2.7 Acidity characterization by FTIR

### 2.7.1 CHA

The etched CHA-type zeolites' acidity is studied by IR spectroscopy using deuterated acetonitrile ( $\text{CD}_3\text{CN}$ ) probe molecule.  $\text{CD}_3\text{CN}$  adsorbed on acid sites is detected in the  $2400\text{--}2200\text{ cm}^{-1}$  spectral window (**Figure 6.12**). The deconvolution of the  $2360\text{--}2170\text{ cm}^{-1}$  spectral range reveals five peaks (**Table 6.3**), four sharp at 2324, 2316, 2295,

2283, 2265  $\text{cm}^{-1}$ , and a broad one centered at 2214  $\text{cm}^{-1}$ . The 2283  $\text{cm}^{-1}$  peak is attributed to  $\text{CD}_3\text{CN}$  interacting with silanols observed on a purely siliceous material MFI-type material.[25] The 2324  $\text{cm}^{-1}$  peak corresponds to  $\text{CD}_3\text{CN}$  interacting with Lewis acid sites[26] while the 2265  $\text{cm}^{-1}$  corresponds to physisorbed  $\text{CD}_3\text{CN}$ . The 2298  $\text{cm}^{-1}$  peak results from  $\text{CD}_3\text{CN}$  interacting with Brønsted acid sites, while the attribution of the 2310  $\text{cm}^{-1}$  peak is a matter of debate and could be due to  $\text{CD}_3\text{CN}$  interacting with either weak Lewis acid sites[27] or weak Brønsted acid sites.[28]

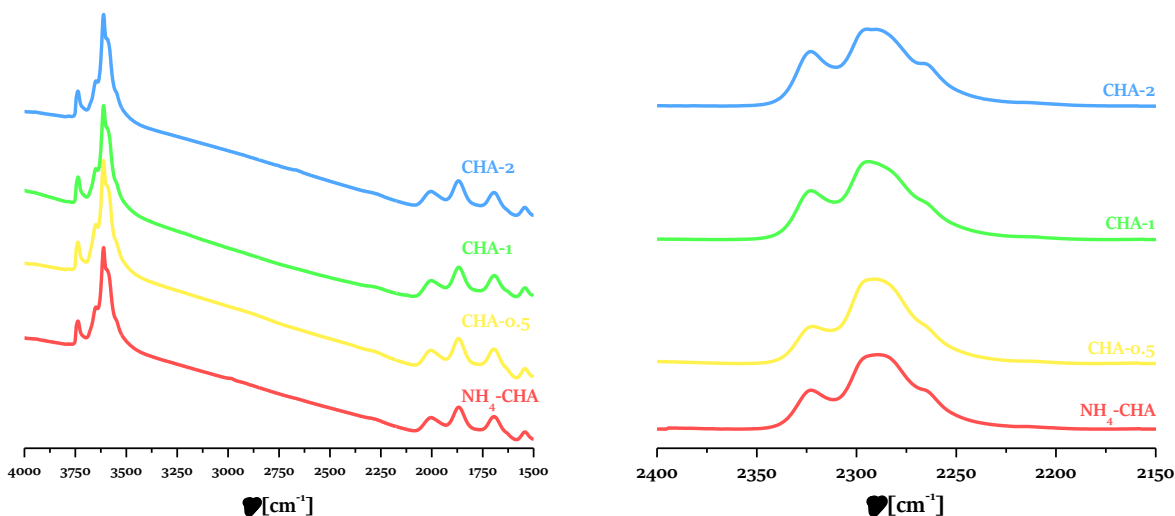


**Figure 6.12.** The room temperature IR spectra of the hydroxyl groups in activated parent CHA and etched derivatives (left). IR spectra of acid sites perturbed by interaction with  $d_3$ -acetonitrile after RT diffusion (right).

The acid site concentrations, Brønsted ( $c_B$ ), and Lewis ( $c_L$ ) are summarized in **Table 6.3**. The accessibility of Brønsted acid sites increased in all etched samples. Samples CHA-1 and CHA-2 also exhibit increased Lewis acidity, except for the sample treated with 0.5 wt/%. Here, we define the accessibility index (ACI) as the number of acid sites ( $c_B + c_L$ ) detected by  $\text{CD}_3\text{CN}$  adsorption divided by the total amount of acid sites in the zeolite, based on the measured aluminum content ( $\text{Al}_{\text{ICP}}$ ).[29] In the parent  $\text{NH}_4\text{-CHA}$ , ACI is 0.47. The etched zeolites CHA-0.5 and CHA-1 have increased ACI, 0.57 and 0.78, respectively. While CHA-2 shows decreased accessibility, which is related to the substantial dealumination and increased amount of extraframework Al in this sample

**Table 6.3.** Concentrations of Brønsted and Lewis acid sites in the parent  $\text{NH}_4\text{-CHA}$  and CHA samples evaluated by *in situ* IR spectroscopy monitoring of probe molecules.

Sample	$\text{Al}_{\text{ICP}}$ $\mu\text{mol g}^{-1}$	$c_B$ $\mu\text{mol g}^{-1}$	$c_L$ $\mu\text{mol g}^{-1}$	$c_B + c_L$ $\mu\text{mol g}^{-1}$	$\text{ACI}_{\text{CD}_3\text{CN}}$ -
CHA	1234	401	176	577	0.47
CHA-0.5	1141	503	158	661	0.57
CHA-1	1141	654	247	901	0.78
CHA-2	1080	447	269	716	0.41

## 2.7.2 MFI

The *in situ* infrared (IR) spectroscopy in the hydroxyls range (3500–3700  $\text{cm}^{-1}$ ) of the parent MFI shows two bands, 3744  $\text{cm}^{-1}$  and 3610  $\text{cm}^{-1}$  (**Figure 6.13**). The band at 3744  $\text{cm}^{-1}$  is assigned to Si-OH, freely vibrating on the external crystal surface and the mesopore area. The parent sample also exhibits a low-intensity peak at 3730  $\text{cm}^{-1}$  assigned to Si-OH in defects.[30] The band at 3610  $\text{cm}^{-1}$  is attributed to the acidic bridging hydroxyl Si(OH)Al

groups. The etched samples MFI-0.5, MFI-1, and MFI-2 exhibit the same peak; only sample MFI-2 shows a small intensity decrease of the Si(OH)Al band.

Pyridine adsorbed on acid sites is detected in the 1700–1400  $\text{cm}^{-1}$  spectral window (**Figure 6.13**). The band centered at 1570  $\text{cm}^{-1}$  is related to pyridine interacting with Brønsted acid sites, while the band at 1462  $\text{cm}^{-1}$  is related to Lewis acid sites.

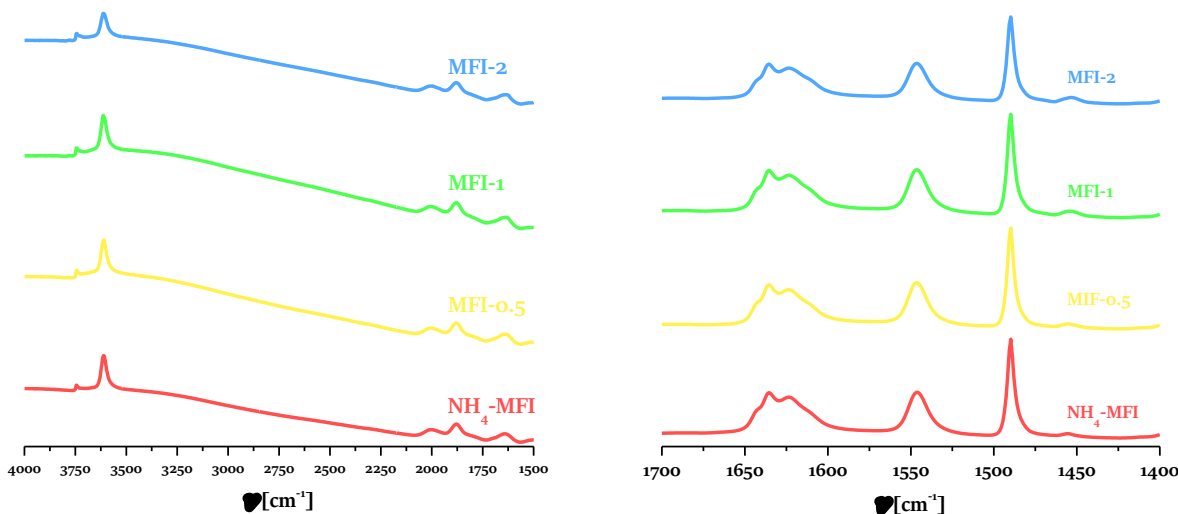


**Figure 6.13.** The room temperature IR spectra of the hydroxyl groups in activated parent MFI and its etched derivatives (left). IR spectra of acid sites perturbed by interaction with pyridine after desorption at 200 °C (right).

IR spectra of pyridine remaining adsorbed after desorption at 200 °C are used to quantify the Brønsted and Lewis acid sites, and the results are presented in **Table 6.4**. The concentrations of Brønsted and Lewis acid sites increase with respect to the parent zeolite. Sample MFI-1 exhibits the highest concentration of BAS, 431  $\mu\text{mol g}^{-1}$ , while sample MFI-0.5 has equal concentration as the parent sample, and MFI-2 has lower. The parent sample has a low LAS concentration, 19  $\mu\text{mol g}^{-1}$ . The etched samples MFI-1 and MFI-2 show increased concentration of LAS, up to 30  $\mu\text{mol g}^{-1}$ . Accessibility index (ACI) is defined as the number of acid sites detected by the probe molecule adsorption divided by the total amount of acid sites in the zeolite provided by the aluminum content.[29] The samples MFI-0.5 and MFI-1 show increased accessibility to the acid sites.

**Table 6.4.** Concentrations of Brønsted and Lewis acid sites in the parent and etched MFI samples evaluated by *in situ* pyridine IR spectroscopy monitoring.

Sample	$\text{Al}_{\text{ICP}}$ $\mu\text{mol g}^{-1}$	$c_{\text{B}}$ $\mu\text{mol g}^{-1}$	$c_{\text{L}}$ $\mu\text{mol g}^{-1}$	$c_{\text{B}} + c_{\text{L}}$ $\mu\text{mol g}^{-1}$	$\text{ACI}_{\text{py}}$ -
$\text{NH}_4$ -MFI	612	418	19	437	0.71
MFI-0.5	556	418	23	441	0.79
MFI-1	556	431	30	461	0.83
MFI-2	556	362	30	392	0.71

### 2.7.3 LTL

The acidity of the parent zeolite and its etched derivatives is studied by *in situ* infrared (IR) spectroscopy of their -OH stretching vibrations (**Figure 6.14**). The band at 3746  $\text{cm}^{-1}$  is assigned to Si-OH, freely vibrating on the external crystal surface and the mesopore area. The parent zeolite exhibits a low-intensity peak at 3730  $\text{cm}^{-1}$ ,

commonly assigned to Si-OH in defects.[30] The band at  $3634\text{ cm}^{-1}$  is attributed to the acidic bridging hydroxyl Si(OH)Al groups and the broadband centered around  $3250\text{ cm}^{-1}$  to hydroxyl groups located in the cancrinite cage.[31,32]

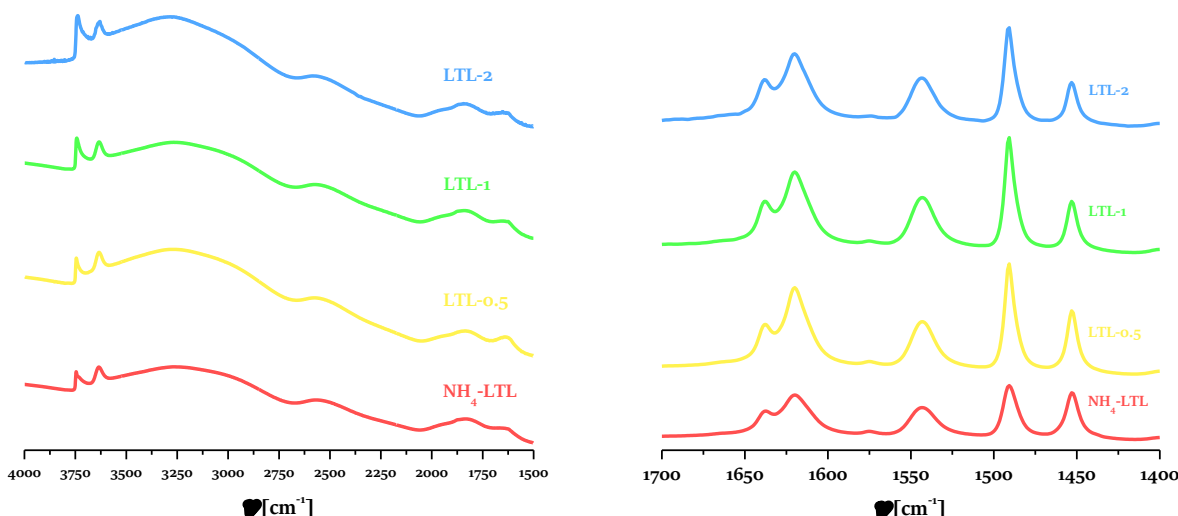


**Figure 6.14.** The room temperature IR spectra of the hydroxyl groups in activated parent zeolite L and its etched derivatives (left). IR spectra of acid sites perturbed by interaction with pyridine after desorption at  $150\text{ }^{\circ}\text{C}$  (right).

IR spectra of pyridine remaining adsorbed after desorption at  $150\text{ }^{\circ}\text{C}$  are used to quantify the Brønsted and Lewis acid sites, and the results are presented in **Table 6.5**. The concentrations of Brønsted and Lewis acid sites increase with respect to the parent zeolite. Etched samples LTL-0.5, LTL-1, and LTL-2 show increased BAS concentration in regard to the parent LTL. The concentrations of LAS in samples LTL-0.5 and LTL-2 are lower, despite the presence of extraframework Al, determined by  $^{27}\text{Al}$  MAS NMR (**Figure 6.9**).

Accessibility index (ACI) is defined as the number of acid sites detected by the probe molecule adsorption divided by the total amount of acid sites in the zeolite provided by the aluminum content.[29] The accessibility index ( $\text{ACI}_{\text{Py}}$ ) of chromic acid-etched samples is higher with respect to the parent material.

**Table 6.5.** Concentrations of Brønsted and Lewis acid sites in the parent and etched zeolite L samples evaluated by *in situ* pyridine IR spectroscopy monitoring.

Sample	$\text{Al}_{\text{ICP}}$ $\mu\text{mol g}^{-1}$	$c_{\text{B}}$ $\mu\text{mol g}^{-1}$	$c_{\text{L}}$ $\mu\text{mol g}^{-1}$	$c_{\text{B}} + c_{\text{L}}$ $\mu\text{mol g}^{-1}$	$\text{ACI}_{\text{Py}}$ -
$\text{NH}_4\text{-LTL}$	3156	412	233	645	0.20
LTL-0.5	3076	507	194	701	0.23
LTL-1	3000	469	245	714	0.24
LTL-2	2859	435	167	602	0.21

### 3 Discussion

Chromic acid in a wide range of concentrations is applied for etching of different types of industrially available zeolites, SSZ-13 (NH<sub>4</sub>-CHA), MFI-55 (NH<sub>4</sub>-MFI), and zeolite L (NH<sub>4</sub>-LTL). The concentration of chromic acid is varied (0.1–10 wt%), while the reaction's temperature and time remained the same. The chosen industrial zeolites have different framework topology, pore size, and Si/Al ratios. The selected zeolites are chosen to study the effects of chromic acid as a function of the pore size.

Almost all the zeolites withstand the reaction with chromic acid quite well and mostly retain their crystallinity. MFI type zeolite has the highest values of relative crystallinity even after etching with 10 wt% concentrated acid (rel. cryst. 97 %). While sample CHA-10 has relative crystallinity of 89 %, and LTL-10 is almost fully amorphized. LTL-10 is almost fully amorphized and suffers from a substantial loss of micropore volume, almost half the value of the parent zeolite L. The amorphization likely occurs in LTL-10 is due to a combination of its low Si/Al ratio and the large pores. Other LTL samples obtained from chromic acid etching (0.1–1 wt%) are well crystalline, having 98–101 % relative crystallinity. Samples obtained with 2 and 10 wt% concentrated acids have a loss of relative crystallinity, having 91 and 9 %. However, all the LTL samples obtained suffer from micropore volume loss, evident from the N<sub>2</sub> physisorption isotherms presented in **Figure 6.4**. For instance, MFI samples obtained from 2 and 10 wt%, even though highly crystalline, also suffer from micropore volume loss. All the modified CHA samples exhibit an increase in their micropore volume. It is likely that the anions yielded in the chromic acid are too large to enter the 8 MR of the chabazite framework. The crystals are only etched from the external surface, which also causes an increase in the measured external surface ( $S_{\text{BET}}$ ).

The chromic acid etching causes preferential dealumination shown by chemical composition analysis, removing Al from the framework and leading to increased Si/Al ratio. Though in most cases, it is far from a substantial increase in the Si/Al ratio. The CHA-10 has a 10.5 Si/Al ratio, while for the parent CHA it is 9.0. The MFI-10 sample has Si/Al = 21, while the parent MFI has a Si/Al = 19. Only sample LTL-4 has a significant increase in the Si/Al ratio, it is 6.1, which is double the Si/Al ratio of the parent LTL. Dealumination of LTL is also confirmed by <sup>27</sup>Al MAS NMR (**Figure 6.9C**). LTL-10 shows significant intensity loss of the peak related to tetrahedral aluminum, *i.e.*, framework aluminum. Other LTL samples obtained with chromic acid of lower concentrations 0.1–2 wt% show the formation of extraframework aluminum. The same effect is observed with CHA and MFI samples; however, LTL has the highest increase of Al<sup>VI</sup>, which for sample LTL-2 is 5.2 %. CHA and MFI etched samples have an Al<sup>VI</sup> increase of up to 2.3 %, even for the most concentrated acid solutions.

<sup>29</sup>Si MAS NMR is employed to study the effect of chromic acid treatment on the short-range ordering in the zeolites. The dealumination of the zeolite framework leads to the formation of silanol defects. The <sup>29</sup>Si{<sup>1</sup>H} cross-polarization spectra of LTL-1 doesn't show a spectacular increase of the silanol defects in respect to the parent LTL sample (**Figure 6.10**). CHA-1 sample does show a clear signal related to silanol defects detected in its <sup>29</sup>Si{<sup>1</sup>H} cross-polarization spectra (**Figure 6.11**).

The acidity measurements show the Brønsted acid site's concentration is preserved to a great extent, which is expected since the studied samples' dealumination is mild. CHA samples show higher concentrations of BAS, which we attribute to the dissolution of low crystalline parts in the sample. MFI etched samples (MFI-0.5, MFI-1) show higher accessibility index values and higher BAS concentrations despite having a lowered concentration of framework aluminum, detected by ICP-AES.

## 4 Conclusion

Commercial zeolites with CHA, MFI, and LTL framework topology are subjected to etching with chromic acid solutions with concentrations ranging between 0.1 and 10 wt/%. Results indicate that according to the size of the pore opening, 8 MR and 10 MR zeolites are more resistant to etching with chromic acid than 12 MR zeolite.

The chromic acid etching doesn't introduce substantial secondary porosity. The treatment leads to a small increase of the Si/Al ratio, indicating some preferential dealumination. The acidity of the samples is well preserved as measure by *in situ* FTIR spectroscopy. The acid treatment leads to the formation of extraframework Al species; however, if a dilute acid is used, the yielded Al<sup>VI</sup> species are usually around 1 %.

## 5 References

- [1] R.M. Barrer, M.B. Makki, Molecular Sieve Sorbents from Clinoptilolite, *Can. J. Chem.* 42 (1964) 1481–1487. <https://doi.org/10.1139/v64-223>.
- [2] H.K. Beyer, Dealumination Techniques for Zeolites, in: *Post-Synthesis Modification I*, Springer, Berlin, Heidelberg, 2002: pp. 203–255. [https://doi.org/10.1007/3-540-69750-0\\_3](https://doi.org/10.1007/3-540-69750-0_3).
- [3] Z. Qin, J.-P. Gilson, V. Valtchev, Mesoporous zeolites by fluoride etching, *Current Opinion in Chemical Engineering*. 8 (2015) 1–6. <https://doi.org/10.1016/j.coche.2015.01.002>.
- [4] L. Zhang, A.N.C. van Laak, P.E. de Jongh, K.P. de Jong, Textural Characterization of Mesoporous Zeolites, in: J. Čejka, A. Corma, S. Zones (Eds.), *Zeolites and Catalysis*, Wiley-VCH Verlag GmbH & Co. KGaA, Weinheim, Germany, 2010: pp. 237–282. <https://doi.org/10.1002/9783527630295.ch9>.
- [5] M.J. Van Niekerk, J.C. Fletcher, C.T. O’Conner, Characterization of dealuminated large-pore mordenites, *Journal of Catalysis*. 138 (1992) 150–163. [https://doi.org/10.1016/0021-9517\(92\)90014-9](https://doi.org/10.1016/0021-9517(92)90014-9).
- [6] E.B. Lami, F. Fajula, D. Anglerot, T. Des Courieres, Single step dealumination of zeolite beta precursors for the preparation of hydrophobic adsorbents, *Microporous Materials*. 1 (1993) 237–245. [https://doi.org/10.1016/0927-6513\(93\)80067-5](https://doi.org/10.1016/0927-6513(93)80067-5).
- [7] B. Kraushaar, J.H.C. Van Hooff, A new method for the preparation of titanium-silicalite (TS-1), *Catal Lett.* 1 (1988) 81–84. <https://doi.org/10.1007/BF00772769>.
- [8] M.-C. Silaghi, C. Chizallet, P. Raybaud, Challenges on molecular aspects of dealumination and desilication of zeolites, *Microporous and Mesoporous Materials*. 191 (2014) 82–96. <https://doi.org/10.1016/j.micromeso.2014.02.040>.
- [9] H.K. Beyer, I.M. Belenykaja, I.W. Mishin, G. Borbely, Structural Peculiarities and Stabilisation Phenomena of Aluminium Deficient Mordenites, *Studies in Surface Science and Catalysis*. 18 (1984) 133–140. [https://doi.org/10.1016/S0167-2991\(09\)61148-4](https://doi.org/10.1016/S0167-2991(09)61148-4).
- [10] V. Valtchev, G. Majano, S. Mintova, J. Pérez-Ramírez, Tailored crystalline microporous materials by post-synthesis modification, *Chem. Soc. Rev.* 42 (2012) 263–290. <https://doi.org/10.1039/C2CS35196J>.
- [11] G.T. Kerr, Intracrystalline rearrangement of constitutive water in hydrogen zeolite Y, *J. Phys. Chem.* 71 (1967) 4155–4156. <https://doi.org/10.1021/j100871a079>.
- [12] C.-Y. Chen, S.I. Zones, Post-Synthetic Treatment and Modification of Zeolites, in: J. Čejka, A. Corma, S. Zones (Eds.), *Zeolites and Catalysis*, Wiley-VCH Verlag GmbH & Co. KGaA, Weinheim, Germany, 2010: pp. 155–170. <https://doi.org/10.1002/9783527630295.ch6>.
- [13] W. Khan, X. Jia, Z. Wu, J. Choi, A.C.K. Yip, Incorporating Hierarchy into Conventional Zeolites for Catalytic Biomass Conversions: A Review, *Catalysts*. 9 (2019) 127. <https://doi.org/10.3390/catal9020127>.
- [14] F.A. Cotton, G.F.R.S. Wilkinson, *Advanced Inorganic Chemistry*, 3rd ed., Interscience Publishers, Toronto, 1972.
- [15] F.A. Cotton, G.F.R.S. Wilkinson, *Advanced Inorganic Chemistry*, 6th ed., Interscience Publishers, Toronto, 1999.
- [16] J.D. Ramsey, L. Xia, M.W. Kendig, R.L. McCreery, Raman spectroscopic analysis of the speciation of dilute chromate solutions, *Corrosion Science*. 43 (2001) 1557–1572. [https://doi.org/10.1016/S0010-938X\(00\)00145-1](https://doi.org/10.1016/S0010-938X(00)00145-1).
- [17] C. Kasper, The structure of the chromic acid plating bath: The theory of chromium deposition, *BUR. STAN. J. RES.* 9 (1932) 353. <https://doi.org/10.6028/jres.009.026>.
- [18] A.F. Wells, *Structural Inorganic Chemistry*, 4th ed., Oxford University Press, London, 1975.
- [19] J.S. Stephens, D.W.J. Cruickshank, The crystal structure of  $(\text{CrO}_3)_\infty$ , *Acta Crystallographica Section B*. 26 (1970) 222–226. <https://doi.org/10.1107/S0567740870002182>.
- [20] C.E. Housecraft, A.G. Sharpe, *Inorganic Chemistry*, 3rd ed., Pearson Education Limited, Harlow, England, 2008.
- [21] R. Šarmaitis, V. Dikinis, V. Rézaitė, Equilibrium in Solutions of Chromic Acid, *Plating and Surface Finishing*. (1996) 6.
- [22] P. Walker, W.H. Tarn, *CRC Handbook of Metal Etchants*, CRC Press, 1990.
- [23] M.B.J. Roeffaers, R. Ameloot, M. Baruah, H. Uji-i, M. Bulut, G. De Cremer, U. Müller, P.A. Jacobs, J. Hofkens, B.F. Sels, D.E. De Vos, Morphology of Large ZSM-5 Crystals Unraveled by Fluorescence Microscopy, *J. Am. Chem. Soc.* 130 (2008) 5763–5772. <https://doi.org/10.1021/ja7113147>.
- [24] G. Engelhardt, Multinuclear solid-state NMR in silicate and zeolite chemistry, *TrAC Trends in Analytical Chemistry*. 8 (1989) 343–347. [https://doi.org/10.1016/0165-9936\(89\)87043-8](https://doi.org/10.1016/0165-9936(89)87043-8).

- [25] C. Pazé, S. Bordiga, G. Spoto, C. Lamberti, A. Zecchina, IR spectroscopy of CH<sub>3</sub>CN–HCl adducts in silicalite channels: A model system for the study of acid–base reactions in zeolites, *J. Chem. Soc., Faraday Trans. 94* (1998) 309–314. <https://doi.org/10.1039/A705380K>.
- [26] R.E. Sempels, P.G. Rouxhet, Infrared study of the adsorption of benzene and acetonitrile on silica–alumina gels: Acidity properties and surface heterogeneity, *Journal of Colloid and Interface Science*. 55 (1976) 263–273. [https://doi.org/10.1016/0021-9797\(76\)90033-3](https://doi.org/10.1016/0021-9797(76)90033-3).
- [27] B. Wichterlová, Z. Tvarůžková, Z. Sobalík, P. Sarv, Determination and properties of acid sites in H-ferrierite: A comparison of ferrierite and MFI structures, *Microporous and Mesoporous Materials*. 24 (1998) 223–233. [https://doi.org/10.1016/S1387-1811\(98\)00167-X](https://doi.org/10.1016/S1387-1811(98)00167-X).
- [28] W. Daniell, N.-Y. Topsøe, H. Knözinger, An FTIR Study of the Surface Acidity of USY Zeolites: Comparison of CO, CD<sub>3</sub>CN, and C<sub>5</sub>H<sub>5</sub>N Probe Molecules, *Langmuir*. 17 (2001) 6233–6239. <https://doi.org/10.1021/la010345a>.
- [29] F. Thibault-Starzyk, I. Stan, S. Abelló, A. Bonilla, K. Thomas, C. Fernandez, J.-P. Gilson, J. Pérez-Ramírez, Quantification of enhanced acid site accessibility in hierarchical zeolites – The accessibility index, *Journal of Catalysis*. 264 (2009) 11–14. <https://doi.org/10.1016/j.jcat.2009.03.006>.
- [30] K.A. Tarach, J. Tekla, U. Filek, A. Szymocha, I. Tarach, K. Góra-Marek, Alkaline-acid treated zeolite L as catalyst in ethanol dehydration process, *Microporous and Mesoporous Materials*. 241 (2017) 132–144. <https://doi.org/10.1016/j.micromeso.2016.12.035>.
- [31] H.G. Karge, E. Geidel, Vibrational Spectroscopy, in: H.G. Karge, J. Weitkamp (Eds.), *Characterization I: -/-*, Springer, Berlin, Heidelberg, 2004: pp. 1–200. <https://doi.org/10.1007/b94235>.
- [32] E. Brunner, K. Beck, M. Koch, L. Heeribout, H.G. Karge, Verification and quantitative determination of a new type of Brønsted acid sites in H-ZSM-5 by <sup>1</sup>H magic-angle spinning nuclear magnetic resonance spectroscopy, *Microporous Materials*. 3 (1995) 395–399. [https://doi.org/10.1016/0927-6513\(94\)00052-W](https://doi.org/10.1016/0927-6513(94)00052-W).

# 7

## Conclusions and prospects

# 1 Conclusions

Zeolites are important industrial catalysts; their unique shape-selectivity is the basis of important applications, but also a pitfall limiting their efficiency. Overcoming or decreasing the diffusion limitations in zeolites is important to improve their catalytic and separation performance. The present Ph.D. thesis reports work on the preparation of zeolites with increased porosity via post-synthesis methods of modification. The work aims to create secondary porosity (mesopores) connected to the native microporosity without altering the intrinsic zeolite properties. Three zeolite types (LTL, CHA, MFI) are studied to achieve this goal by optimizing already published methods and novel etching solutions.

**The Ph.D. thesis includes 7 chapters:** a short introduction to the goals of the study (Chapter 1), a literature overview (Chapter 2), a technical part including the materials and methods (Chapter 3).

**Chapter 4** compares the etching abilities of  $\text{NH}_4\text{F}$  and  $\text{NH}_4\text{HF}_2$  solutions in the hierarchization of zeolite L. Etching with an aqueous  $\text{NH}_4\text{F}$  solution is an established method for demetallation of zeolites. Our study showed that  $\text{NH}_4\text{F}$  can be replaced with  $\text{NH}_4\text{HF}_2$ . The latter can be used in much lower concentration since it is a steadier source of the  $\text{HF}_2^-$  anions, which are shown to dissolve Si and Al from zeolites indiscriminately. The most important finding of our study can be summarized as follows:

- The etching with 1 and 2 wt/%  $\text{NH}_4\text{HF}_2$  yields hierarchical derivatives similar to those obtained with 20 and 40 wt/%  $\text{NH}_4\text{F}$ .
- The etched samples generally have preserved microporosity and crystallinity, while mesopores are generated.
- The Si/Al ratio is mostly preserved, and the  $\text{NH}_4\text{HF}_2$  and  $\text{NH}_4\text{F}$  solutions don't contribute to EFAl formation, except in cases when samples are prepared at elevated temperatures.
- The zeolite acidity is preserved while showing high accessibility to probe molecules due to the generated mesopores.
- The catalytic activity and catalyst lifetime in the dealkylation of TiPBz is improved, which is attributed to preserved acidity and generated mesopores.

**The results show that a substantial decrease in the fluoride agent used can be achieved by using the  $\text{NH}_4\text{HF}_2$  in low concentrations, 1–2 wt/%, a welcome feature for practical applications. Lowering the  $\text{NH}_4\text{HF}_2$  concentration also slows down the dissolution process and better controls the zeolite hierarchization.**

**Chapter 5** focuses on optimizing the concentrated ammonium fluoride solution in etching a small pore SSZ-13 zeolite (CHA-type). Yielding a hierarchical SSZ-13 through post-synthesis methods has also been shown to be a challenging task. The optimization of SSZ-13 etching is done through  $\text{NH}_4\text{F}$  (40 wt/%) etching varying the liquid-solid ratio, time, and temperature. The  $\text{NH}_4\text{F}$  etching of SSZ-13 generates mesopores in all prepared samples, including the most mildly treated one. The tuning of etching parameters allowed to increase mesoporosity and retain the basic characteristics of parent zeolite in terms of crystallinity, micropore volume, and acidity. The most important results can be summarized as follows:

- Using ambient temperature and low liquid/solid ratio (8 and 20) leads to hierarchical SSZ-13 derivatives with retained intrinsic characteristics.
- Etching at 50 °C causes amorphization, revealed by the lower intensity of the XRD peaks and a loss of micropore volume.

- The results of chemical composition analysis show a non-selective extraction of framework cations. Even the most deeply treated samples treated with 1/s of 8 and 20 have a Si/Al ratio of 11, which is not substantially different from the parent material.
- The EDX results imply the Al is not evenly distributed within the etched crystals. In addition, the surface of the crystals is more attacked since it contains less aluminum, particularly in the case of partially amorphous samples.
- The acidity measurements show that the Brønsted acid site's concentration is preserved, further confirming the NMR data.
- The catalytic activity of parent and modified zeolites is tested in the dehydration of n-propanol. The parent and treated samples' initial activity is similar, reflecting a similar number of available active sites, however, differences are observed with the extension of the time on stream, where the etched samples, as a function of the treatment conditions, showed lower deactivation.
- The etched catalysts showed extended lifetime and higher coke content to the parent. The improved activity of etched derivatives is attributed to the enhanced accessibility to active sites, together with the preserved Brønsted acidity.

**The results of this study revealed some particularities of the dissolution of small-pore zeolites in a fluoride medium. The dissolution rate is lower, although a relatively concentrated  $\text{NH}_4\text{F}$  solution is used, which is attributed to the constrained diffusion of hydrated bifluoride ions through the small pore channels. Consequently, the mesopore generation always starts from the crystal surface and penetrates further into the crystal's bulk. This particularity of SSZ-13  $\text{NH}_4\text{F}$  etching is probably valid for all small pore zeolites.**

**Chapter 6** brings about a novel etching method applicable to conventional zeolites. In the present study, we used three different zeolites (CHA, MFI, LTL) with 8, 10, and 12 MR pore openings and etched them with chromic acid solutions in concentrations ranging 0.1–10 wt/%. Almost all the zeolites withstand the reaction with chromic acid quite well and mostly retain their crystallinity, with the exception of some severely etched LTL samples.

- The chromic acid etching causes preferential dealumination shown by chemical composition analysis, removing Al from the framework and leading to increased Si/Al ratio. Though in most cases, it is far from a substantial increase in Si/Al ratio.
- The etched sample show formation of extra framework aluminum species as observed by  $^{27}\text{Al}$  MAS NMR, but to a limited extent.
- The acidity measurements show the Brønsted acid sites' concentration is preserved to a great extent, which is a consequence of relatively mild dealumination.

**Overall, the results indicate that according to the size of the pore opening, 8 MR and 10 MR zeolites are more resistant to etching with chromic acid than 12 MR zeolite. Chromic acid in its aqueous solution forms large anions, most likely too big to enter the 8 MR windows of the SSZ-13 zeolite.**

## 2 Prospects

The etching with  $\text{NH}_4\text{HF}_2$  solutions should be expanded to other zeolite types, including medium and small pore zeolites.

The work presented in chapter 5 reveals the difficulties associated with diffusion limitation during wet etching. The  $\text{NH}_4\text{F}$  etching of small pore zeolites needs further elucidation in terms of dissolution profile, type of generated mesopores, and micro-mesopore connectivity.

The pioneering work on chromic acid etching opens the door for its application in post-synthesis treatments of zeolites. This topic needs further developments and deeper analysis of the experimental parameters, *e.g.*, the chromic acid concentration, time, and temperature etching on zeolite properties.

# Annexes

## Appendix A

### TABLE OF FIGURES

FIGURE 2.1. EXAMPLES OF ZEOLITE BUILDING UNITS AND FRAMEWORK TYPES.	6
FIGURE 2.2. INCREASE OF ZEOLITE STRUCTURE CODES SINCE THE 1970s (FROM [17]).	6
FIGURE 2.3. CHABAZITE (CHA) COMPOSITE BUILDING UNITS (FROM [26]).	8
FIGURE 2.4. COMPOSITE BUILDING UNITS IN THE MFI-TYPE FRAMEWORK (FROM [26]).	8
FIGURE 2.5. LTL FRAMEWORK TYPE COMPOSITE BUILDING UNITS (FROM [26]).	8
FIGURE 2.6. HYDROTHERMAL SYNTHESIS OF ZEOLITES (FROM [43]).	10
FIGURE 2.7. SCHEMATIC PRESENTATION OF DIFFUSION LIMITATION IN CONVENTIONAL AND HIERARCHICAL ZEOLITES. THE SECONDARY POROSITY ENHANCES THE NUMBER OF PORE MOUTHS ENABLING BETTER ACCESS TO GREEN AND RED SPHERES TO AND WITHIN THE PORES (FROM [57]).	12
FIGURE 2.8. SCHEMATIC REPRESENTATION OF TOP-DOWN AND BOTTOM-UP STRATEGIES USED IN THE SYNTHESIS OF HIERARCHICAL ZEOLITES (FROM [65]).	14
FIGURE 2.9. A) SIMPLIFIED REPRESENTATION OF ALUMINUM CONTENT INFLUENCES THE DESILICATION TREATMENT WITH NaOH SOLUTION AND THE SCHEMATIC MECHANISM OF PORE FORMATION (FROM [87]). B) OVERVIEW OF POST-SYNTHETIC TREATMENTS (GREEN) TO CHANGE ANY CONVENTIONAL ZEOLITE (RED) INTO A HIERARCHICAL. IMPORTANT FEATURES TO TAKE INTO ACCOUNT ARE Si/Al RATIO AND MICROPORE DIMENSIONALITY (BLUE) (FROM [92]). TREATMENT CODES: FDA – FRAMEWORK DEALUMINATION, NH <sub>4</sub> – ION EXCHANGE, DS – DESILICATION, SDA – SELECTIVE DEALUMINATION, PDA – PORE DIRECTING AGENTS.	17
FIGURE 2.10. SEM IMAGES OF ZSM-5 CRYSTALS TREATED WITH NH <sub>4</sub> F/HF SOLUTIONS (FROM [95]).	18
FIGURE 2.11. EQUILIBRIUM REACTIONS BETWEEN FLUORIDE SPECIES PRESENT IN THE AQUEOUS SOLUTION OF HF (FROM [106]).	19
FIGURE 2.12. ELIMINATION OF OH <sup>-</sup> ASSISTED BY HF <sub>2</sub> <sup>-</sup> (FROM [119]).	19
FIGURE 2.13. CHEMICAL EQUILIBRIA INVOLVING DISSOLUTION OF NH <sub>4</sub> F IN WATER (FROM [115]).	20
FIGURE 2.14. SEM MICROGRAPHS OF ZSM-5 CRYSTALS TREATED WITH 40 WT/% NH <sub>4</sub> F AQUEOUS SOLUTION (FROM [115]).	20
FIGURE 2.15. BRØNSTED ACID SITES AS A RESONANCE MODEL BETWEEN (I) AND (II) (FROM [183]).	27
FIGURE 2.16. ILLUSTRATION OF REACTANT SHAPE SELECTIVITY.	27
FIGURE 3.1. BRAGG'S LAW.	44
FIGURE 3.2. MILLER PLANES EXAMPLES.	45
FIGURE 3.3. THE EWALD SPHERE.	45
FIGURE 3.4. CLASSIFICATION OF ADSORPTION ISOTHERMS, ACCORDING TO IUPAC (FROM [7]).	47
FIGURE 3.5. CLASSIFICATION OF HYSTERESIS LOOPS (FROM [7]).	48
FIGURE 3.6. MAGIC ANGLE SPINNING EXPERIMENT SCHEME (FROM [13]).	51
FIGURE 3.7. <sup>29</sup> Si CHEMICAL SHIFT OF Si(NAl) UNITS IN ZEOLITES.	51
FIGURE 4.1. XRD PATTERNS OF ZEOLITE L TREATED WITH 20 (A) AND 40 (B) WT/% NH <sub>4</sub> F.	60
FIGURE 4.2. XRD PATTERNS OF ZEOLITE L TREATED WITH 1 (A) AND 2 (B) WT/% NH <sub>4</sub> HF <sub>2</sub> .	61
FIGURE 4.3. SEM MICROGRAPHS OF L-II-40 (A), L-II-60-60 (B), L-III-40 (C), L-III-180 (D), L-III-60-60 (E), AND L-III-60-80 (F) SAMPLES.	62
FIGURE 4.4. TEM MICROGRAPHS OF NH <sub>4</sub> -L (A), L-I-5 (B), L-I-60 (C), L-III-180 (D), L-III-60-60 (E), AND L-III-60-80 (F) SAMPLES.	62
FIGURE 4.5. N <sub>2</sub> ADSORPTION ISOTHERMS OF THE SAMPLES TREATED WITH 20 WT/% NH <sub>4</sub> F (A), 40 WT/% NH <sub>4</sub> F (B), 1 WT/% NH <sub>4</sub> HF <sub>2</sub> (C), AND 2 WT/% NH <sub>4</sub> HF <sub>2</sub> (D). NOTE: CLOSED CIRCLES – ADSORPTION, OPEN CIRCLES – DESORPTION.	63
FIGURE 4.6. THE <sup>27</sup> Al MAS NMR OF THE PARENT ZEOLITE AND DERIVATIVES TREATED AT A) ROOM TEMPERATURE AND B) 60 AND 80 °C, WITH 20 (L-I), 40 (L-II) WT/% NH <sub>4</sub> F, AND 1 WT/% NH <sub>4</sub> HF <sub>2</sub> (L-III) SOLUTIONS.	66
FIGURE 4.7. TG CURVES OF THE PARENT ZEOLITE AND THE DERIVATIVES TREATED WITH 20 WT/% NH <sub>4</sub> F (A), 40 WT/% NH <sub>4</sub> F (B), AND 1 WT/% NH <sub>4</sub> HF <sub>2</sub> (C).	67

FIGURE 4.8. ROOM TEMPERATURE IR SPECTRA IN THE O-H VIBRATIONS REGION FOR THE PARENT AND SOME ETCHED DERIVATIVES: 20 WT/% NH <sub>4</sub> F (A), 40 WT/% NH <sub>4</sub> F (B), 1 WT/% NH <sub>4</sub> HF <sub>2</sub> (C) SOLUTIONS.	68
FIGURE 4.9. ROOM TEMPERATURE IR SPECTRA FOR THE PARENT ZEOLITE L (NH <sub>4</sub> -L) SAMPLE AFTER ACTIVATION.	69
FIGURE 4.10. DECONVOLUTION OF THE BACKGROUND SPECTRA OF ACTIVATED SAMPLES: PARENT NH <sub>4</sub> -L (A), L-I-60 (B), L-II-90 (C), AND L-III-15 (D) IN THE SILANOL REGION. THE SPECTRA ARE BASELINE CORRECTED BEFORE DECONVOLUTION.	70
FIGURE 4.11. CONVERSION OF 1,3,5-TRISOPROPYLBENZENE (TIPBz) FOR THE PARENT AND SOME ETCHED DERIVATIVES: 20 WT/% NH <sub>4</sub> F (A), 40 WT/% NH <sub>4</sub> F (B), 1 WT/% NH <sub>4</sub> HF <sub>2</sub> (C) SOLUTIONS.	72
FIGURE 4.12. TIPBz INITIAL CONVERSION (X) AS A FUNCTION OF BRØNSTED ACID SITES (C <sub>B</sub> ) CONCENTRATION OVER HIERARCHICAL CATALYSTS AND THE PARENT SAMPLE (NH <sub>4</sub> -L) AFTER 2 MIN TOS.	73
FIGURE 5.1. XRD PATTERNS OF ETCHED DERIVATIVES AND THEIR PARENT NH <sub>4</sub> -SSZ-13. SAMPLES PREPARED WITH A LIQUID/SOLID RATIO OF 8, 20, AND 100 ARE PLOTTED. THE RELATIVE (TO THE NH <sub>4</sub> -SSZ-13 PARENT) CRYSTALLINITY IS INDICATED ON EACH PATTERN.	84
FIGURE 5.2. REPRESENTATIVE SEM MICROGRAPH OF THE PARENT SSZ-13.	85
FIGURE 5.3. SEM MICROGRAPHS OF THE ETCHED SAMPLES: (A, B) SERIES I, (C, D) SERIES II, AND (E, F) SERIES III.	86
FIGURE 5.4. STEM-HAADF MICROGRAPHS OF: (A) CHA-100-25-5, (B) CHA-100-25-20 AND (C) CHA-100-50-5.	87
FIGURE 5.5. N <sub>2</sub> PHYSISORPTION ISOTHERMS OF SERIES I (A, B), SERIES II (C, D), AND SERIES III (E, F) SAMPLES.	88
FIGURE 5.6. SYNTHESIS OF THE STEM-EDX ANALYSES OF THREE TYPES OF SAMPLES: CHA-100-25-5 (TOP ROW), CHA-100-25-20 (MIDDLE ROW), AND CHA-100-50-5 (BOTTOM ROW).	90
FIGURE 5.7. <sup>27</sup> Al MAS NMR SPECTRA OF THE NON-CALCINED SAMPLES FROM (A) SERIES I, (B) SERIES II, AND (C) SERIES III.	91
FIGURE 5.8. <sup>29</sup> Si MAS NMR SPECTRA (A) AND <sup>29</sup> Si{ <sup>1</sup> H} CROSS-POLARIZATION SPECTRA (B) OF NH <sub>4</sub> -SSZ-13 AND ONE DERIVATIVE, CHA-20-50-20.	92
FIGURE 5.9. <sup>19</sup> F MAS NMR SPECTRA OF SAMPLES CHA-100-50-20, CHA-20-50-20, CHA-20-50-20 CALCINED, AND CHA-8-50-20.	92
FIGURE 5.10. BANDS OF ADSORBED ACETONITRILE 2400–2200 CM <sup>-1</sup> ON PARENT SAMPLE (NH <sub>4</sub> -SSZ-13) AND ETCHED SAMPLES.	93
FIGURE 5.11. DECONVOLUTED BANDS IN THE RANGE 2360–2180 CM <sup>-1</sup> OF THE PARENT (A) AND DIFFERENT ETCHED (B-F) SAMPLES.	94
FIGURE 5.12. UNPERTURBED OH SITES IN THE AREA 3800–3400 CM <sup>-1</sup> OF ZEOLITE H-SSZ-13 TAKEN AT ROOM TEMPERATURE AFTER ACTIVATION.	96
FIGURE 5.13. ROOM TEMPERATURE IR SPECTRA OF THE PRISTINE SURFACE HYDROXYLS OF THE H-SSZ-13 ZEOLITE AND ITS DERIVATIVES AFTER ACTIVATION (T = 450 °C).	97
FIGURE 5.14. THE N-PROPANOL CONVERSION (X/%) WITH TIME ON STREAM (TOS/MIN) FOR THE H-SSZ-13 PARENT AND SOME NH <sub>4</sub> F ETCHED DERIVATIVES (T = 205 °C, P = 1 BAR, W/F° = 27.2 KG MOL <sup>-1</sup> S).	98
FIGURE 5.15. PROPENE SELECTIVITY (Y-AXIS) AS A FUNCTION N-PROPANOL CONVERSION (X-AXIS) FOR PARENT AND ETCHED SAMPLES.	99
FIGURE 6.1. STRUCTURE OF THE DICHROMATE ION FOUND IN Rb <sub>2</sub> Cr <sub>2</sub> O <sub>7</sub> (FROM [15]).	110
FIGURE 6.2. STRUCTURES OF Cr <sub>2</sub> O <sub>7</sub> <sup>2-</sup> AND Cr <sub>3</sub> O <sub>10</sub> <sup>2-</sup> (FROM [20]).	110
FIGURE 6.3. X-RAY DIFFRACTION PATTERNS OF THE SERIES OF A) CHA, B) MFI, AND C) LTL TREATED SAMPLES, WITH RELATIVE CRYSTALLINITY PERCENTAGES INDICATED FOR EACH SAMPLE.	112
FIGURE 6.4. N <sub>2</sub> PHYSISORPTION ISOTHERMS OF A) NH <sub>4</sub> -CHA, B) NH <sub>4</sub> -MFI, AND C) NH <sub>4</sub> -LTL WITH THEIR ETCHED DERIVATIVES. NOTE: THE Y-AXIS STARTS AT HIGHER VALUES OF V <sub>A</sub> TO HIGHLIGHT THE CHANGES IN THE MICROPORE AREA.	114
FIGURE 6.5. SEM MICROGRAPHS OF CHA (A,B), MFI(C,D) AND LTL (E,F) ETCHED SAMPLES.	117
FIGURE 6.6. STEM MICROGRAPHS OF SAMPLE LTL-0.1-30 OBTAINED BY ADF (LEFT) AND BF IMAGING (RIGHT).	118
FIGURE 6.7. TEM MICROGRAPHS OF SAMPLES CHA-1 (A) AND CHA-2 (B).	118
FIGURE 6.8. STEM EDX RESULTS AND ANALYSIS.	119
FIGURE 6.9. <sup>27</sup> Al MAS NMR SPECTRA OF A) CHA, B) MFI, AND C) LTL SERIES OF SAMPLES.	119
FIGURE 6.10. <sup>29</sup> Si MAS NMR SPECTRA OF PARENT LTL AND ETCHED LTL-1 (LEFT) SAMPLES AND THEIR <sup>29</sup> Si{ <sup>1</sup> H} CROSS-POLARIZATION SPECTRA (RIGHT).	121
FIGURE 6.11. <sup>29</sup> Si MAS NMR SPECTRA OF PARENT (CHA) AND ETCHED (CHA-1) SAMPLES (LEFT) AND THEIR <sup>29</sup> Si{ <sup>1</sup> H} CROSS-POLARIZATION SPECTRA (RIGHT).	121

FIGURE 6.12. THE ROOM TEMPERATURE IR SPECTRA OF THE HYDROXYL GROUPS IN ACTIVATED PARENT CHA AND ETCHED DERIVATIVES (LEFT). IR SPECTRA OF ACID SITES PERTURBED BY INTERACTION WITH <i>D</i> <sub>3</sub> -ACETONITRILE AFTER RT DIFFUSION (RIGHT).	122
FIGURE 6.13. THE ROOM TEMPERATURE IR SPECTRA OF THE HYDROXYL GROUPS IN ACTIVATED PARENT MFI AND IT'S ETCHED DERIVATIVES (LEFT). IR SPECTRA OF ACID SITES PERTURBED BY INTERACTION WITH PYRIDINE AFTER DESORPTION AT 200 °C (RIGHT).	123
FIGURE 6.14. THE ROOM TEMPERATURE IR SPECTRA OF THE HYDROXYL GROUPS IN ACTIVATED PARENT ZEOLITE L AND IT'S ETCHED DERIVATIVES (LEFT). IR SPECTRA OF ACID SITES PERTURBED BY INTERACTION WITH PYRIDINE AFTER DESORPTION AT 150 °C (RIGHT).	124

#### TABLE OF FIGURES

TABLE 2.1. CLASSIFICATION OF PORES IN ZEOLITES.	7
TABLE 2.2. PUBLISHED WORK ON ZEOLITE ETCHING WITH FLUORINE COMPOUNDS.	22
TABLE 4.1. CHEMICAL COMPOSITION AND TEXTURAL PROPERTIES OF THE PARENT AND TREATED ZEOLITES.	65
TABLE 4.2. THERMAL ANALYSIS OF THE PARENT NH <sub>4</sub> -L ZEOLITE AND THE FLUORIDE DERIVATIVES.	66
TABLE 4.3. CONCENTRATIONS OF BRØNSTED AND LEWIS ACID SITES IN THE PARENT NH <sub>4</sub> -L AND ZEOLITE L SAMPLES EVALUATED BY <i>IN SITU</i> IR SPECTROSCOPY MONITORING OF PROBE MOLECULES.	71
TABLE 5.1. PHYSICOCHEMICAL PROPERTIES OF PARENT AND NH <sub>4</sub> F ETCHED SAMPLES.	89
TABLE 5.2. CHEMICAL COMPOSITION OF THE SAMPLES OBTAINED FROM ICP-AES AND <sup>27</sup> AL MAS NMR DATA.	91
TABLE 5.3. ACID SITE CONCENTRATIONS OF THE PARENT H-SSZ-13 AND ITS ETCHED DERIVATIVES.	95
TABLE 5.4. RESULTS OF THERMOGRAVIMETRIC ANALYSIS OF EXHAUSTED CATALYSTS USED IN N-PROPANOL DEHYDRATION.	99
TABLE 6.1. TEXTURAL PROPERTIES OF THE PARENT AND TREATED ZEOLITES.	116
TABLE 6.2. RESULTS OF EXTRAFRAMEWORK ALUMINUM (AL <sup>VI</sup> ) CONTENT EXPRESSED IN PERCENTAGES (%), OBTAINED FROM <sup>27</sup> AL MAS NMR SPECTRA.	120
TABLE 6.3. CONCENTRATIONS OF BRØNSTED AND LEWIS ACID SITES IN THE PARENT NH <sub>4</sub> -CHA AND CHA SAMPLES EVALUATED BY <i>IN SITU</i> IR SPECTROSCOPY MONITORING OF PROBE MOLECULES.	122
TABLE 6.4. CONCENTRATIONS OF BRØNSTED AND LEWIS ACID SITES IN THE PARENT AND ETCHED MFI SAMPLES EVALUATED BY <i>IN SITU</i> PYRIDINE IR SPECTROSCOPY MONITORING.	123
TABLE 6.5. CONCENTRATIONS OF BRØNSTED AND LEWIS ACID SITES IN THE PARENT AND ETCHED ZEOLITE L SAMPLES EVALUATED BY <i>IN SITU</i> PYRIDINE IR SPECTROSCOPY MONITORING.	124

# Appendix B

## LIST OF COMMUNICATIONS

---

### Posters

- Babić, V., Gilson, J.-P., Valtchev, V. (June 2018) Comparative study of zeolite L etching with ammonium fluoride and ammonium bifluoride solutions. Poster presented at Journée de l'Ecole Doctorale Normande de Chimie (Le Havre, France)
- Babić, V., Gilson, J.-P., Valtchev, V. (January 2019) Comparative study of zeolite L etching with ammonium fluoride and ammonium bifluoride solutions. Poster presented at 4th Euro Asia Zeolite Congress (Taormina, Italy)
- Babić, V., Gilson, J.-P., Valtchev, V. (January 2019) Dissolution behavior of ZSM-5 in  $\text{NH}_4\text{F}$  and  $\text{NH}_4\text{HF}_2$  aqueous solutions. Poster session presented 4th Euro Asia Zeolite Congress (Taormina, Italy)

### Publications

#### Related to this work

- Babić, V., Koneti, S., Moldovan, S., Nesterenko, N., Gilson, J.-P., Valtchev, V., Preparation of hierarchical SSZ-13 by  $\text{NH}_4\text{F}$  etching, Full paper published in Microporous Mesoporous Materials. (doi: 10.1016/j.micromeso.2020.110863)
- Babić, V., Hafiz, L., Tang, L., Qin, Z., Gilson, J.-P., Valtchev, V. Comparative study of zeolite L etching with ammonium fluoride and ammonium bifluoride solutions. Full paper published in Advanced Materials Interfaces. (doi: 10.1002/admi.202000348)

#### Previous

- Babić, V., Ivanda, M., Štefanić, G., Phase development in the metastable solid solutions of  $\text{ZrO}_2\text{-YO}_{1.5}$  system, Journal of Molecular Structure, 1185 (2019) 310-322

# Acknowledgments

---

These past three years spent in Caen Normandy have been a challenge and a blessing. Being a Ph.D. student in Laboratoire Catalyse et Spectrochimie (LCS) for 3 years resulted in all the work presented in this thesis and it occurred with many new experiences, challenges, and acquaintanceship. This time has had an important impact on me as a person and as a researcher. I would like to thank everyone who accompanied me on this journey.

First and foremost, I would like to thank my supervisors dr. Valentin Valtchev and prof. Jean-Pierre Gilson for the opportunity to be a part of their team and working under their supervision. Thank you, Valentin, for all the guidance, remarks during this work, and help during my arrival in France. I want to thank Jean-Pierre as well for his guidance and remarks while writing my manuscripts.

Thanks to Region of Normandy for funding this Ph.D. through their RIN 100 contract and additional prolongation due to COVID-19 confinements.

I want to thank all the students and post-docs who through their stories, advice, and tips helped me navigate this academic life. Special thanks to Valentin's students Kamilla Goldyn, Stijn Van Deale, Ana Palcic, Mariame Akouche, and Honza (Jan) Prech, and Chuanqi Zhang.

I would like to thank other teams in LCS for their help while performing my experiments, the spectroscopy group (Yoann, Alexandre, Phillipe), the NMR group (Hussein, Aurélie, Cassandre), synthesis group (Louwanda, Marie, Valerie). Thanks to Benjamin for the help with the catalytic equipment, Jaafar for the help with SEM, and Pascal for the IT support. Thanks also to all the administrative staff in LCS, Sophie, Blandine, and Robenson, you have been very kind.

I want to thank the microscopy teams for the micrographs used in this thesis. First to Lingxue Tang from Jilin Univesity for the TEM images and Zhengxing Qin from China University of Petroleum for SEM images. To, Siddardha and Simona, the team from Rouen University for TEM images, and to Maxime Debost from LCS/Crismat, for TEM images.

I want to give a big thanks to all the other LCS students and post-docs for creating a friendly and productive working environment and all the social events outside of the lab. Special thanks to Peng Peng for being my longest lunch buddy and Abdelhafid for being my travel buddy. I want to thank Houeida and Phillipe for a nice time while visiting the ESRF in Grenoble.

I would like to thank all the people I've met during my time in Normandy for their friendship, the English teachers, the Spanish speaking group, my few French friends, the people from the Balkans. People from LPC, you've welcomed me with open arms. The associations of EIC, Crous, Optic, for organizing educational and social events, helped me improve my French and get acquainted with new people and French culture, special thanks to Lydie, you're so nice.

To my Croatians (Marta, Doris, and Ante) who took a part of their own time to come to visit me in France, big thank you.

Wish you all a beautiful life.





### ***Increasing the porosity of zeolites***

Zeolites are important industrial catalysts; their unique shape-selectivity is the basis of important applications, but also a pitfall limiting their efficiency. Overcoming or decreasing the diffusion limitations in zeolites is important to improve their catalytic and separation performance. The present Ph.D. thesis reports work on the preparation of zeolites with increased porosity via post-synthesis chemical etching. The work aims to create secondary porosity (mesopores) connected to the native microporosity without altering the intrinsic zeolite properties. Three zeolite types are studied: a small pore SSZ-13 (CHA), a medium pore ZSM-5 (MFI), and a large pore zeolite L (LTL). Zeolite L study compares the etching abilities of  $\text{NH}_4\text{F}$  and  $\text{NH}_4\text{HF}_2$  solutions in the hierarchization of zeolite L. The results show that  $\text{NH}_4\text{F}$  can be replaced with  $\text{NH}_4\text{HF}_2$ . The etching with 1 and 2 wt/%  $\text{NH}_4\text{HF}_2$  solutions yield hierarchical derivatives similar to those obtained with 20 and 40 wt/%  $\text{NH}_4\text{F}$  solutions. Thus by replacing  $\text{NH}_4\text{F}$  with  $\text{NH}_4\text{HF}_2$  a substantial decrease in the used fluorine is achieved. SSZ-13 is etched with 40 wt/%  $\text{NH}_4\text{F}$ , which generates mesopores in all prepared samples. The results reveal the mesopore generation starts from the crystal surface due to the constrained diffusion of hydrated bifluoride ions through the small pore channels. Chromic acid etching of zeolites with different pore opening (8, 10, 12 MR) reveals that this dissolution process is dependent on the size of the pore opening as 8 MR and 10 MR zeolites are more resistant to etching with chromic acid than 12 MR zeolite. In general, the chromic acid does not generate substantial mesopore formation. The number of accessible acid sites in etched derivatives is close to the parent material, although some preferential dealumination is observed.

### ***Augmentation de la porosité des zéolithes***

Les zéolites sont des catalyseurs industriels importants ; leur sélectivité basée sur la forme unique de leurs pores est à l'origine de plusieurs applications importantes. Cependant, la seule présence des micropores limitent le transport de réactifs et de produits et par la suite entrave l'efficacité de zéolites. Surmonter ou réduire les limitations de diffusion dans les zéolites est important pour améliorer leurs performances catalytiques et leurs capacités séparation. Le présent sujet de doctorat rapporte la préparation de zéolites avec une porosité accrue par la méthode de post-synthèse « etching ». Ce travail vise à créer une porosité secondaire (mésopores) liée à la microporosité native sans altération des propriétés intrinsèques de zéolites. Trois types de zéolites de différentes tailles de pores sont étudiés : petit pore SSZ-13 (CHA), pore moyen ZSM-5 (MFI) et grand pore zéolite L (LTL). L'étude de la Zéolite « L » consiste sur la comparaison des capacités de solutions  $\text{NH}_4\text{F}$  et  $\text{NH}_4\text{HF}_2$  dans la création des mésopores. Les résultats obtenus montrent que  $\text{NH}_4\text{F}$  peut être remplacé par  $\text{NH}_4\text{HF}_2$ . L'utilisation des solutions de  $\text{NH}_4\text{HF}_2$  à 1 et 2 % en masse aboutit à la création d'une (mésop-) porosité similaire à celles obtenus avec des solutions de  $\text{NH}_4\text{F}$  à 20 et 40 % en masse. Ainsi, en remplaçant  $\text{NH}_4\text{F}$  par  $\text{NH}_4\text{HF}_2$ , on observe une diminution substantielle de la quantité de fluor utilisée. SSZ-13 est traité avec 40 % en masse de  $\text{NH}_4\text{F}$ , ce qui a généré des mésopores dans tous les échantillons préparés. Les résultats obtenus révèlent que la génération de mésopores commence à partir de la surface du cristal, en raison des contraintes de diffusion d'ions bifluorure hydratés à travers les petits canaux de pores. Le traitement de zéolites de différentes tailles de pores (8, 10, 12 MR) avec l'acide chromique révèle que ce processus de dissolution dépend de la taille de l'ouverture des pores car les zéolithes à 8 MR et 10 MR sont plus résistantes au traitement à l'acide chromique qu'une zéolite à 12 MR. En général, l'acide chromique ne génère pas de mésopores substantielles. Le nombre de sites acides accessibles dans les dérivés obtenus par « etching » est proche de celui du matériau d'origine, bien qu'une certaine désalumination préférentielle soit observée.